

Washington University in St. Louis

Washington University Open Scholarship

Arts & Sciences Electronic Theses and
Dissertations

Arts & Sciences

7-12-2023

Cardiovascular SARS-CoV-2 Tropism and Immunopathology

Oleksandr Dmytrenko

Washington University in St. Louis

Follow this and additional works at: https://openscholarship.wustl.edu/art_sci_etds

Recommended Citation

Dmytrenko, Oleksandr, "Cardiovascular SARS-CoV-2 Tropism and Immunopathology" (2023). *Arts & Sciences Electronic Theses and Dissertations*. 2995.

https://openscholarship.wustl.edu/art_sci_etds/2995

This Dissertation is brought to you for free and open access by the Arts & Sciences at Washington University Open Scholarship. It has been accepted for inclusion in Arts & Sciences Electronic Theses and Dissertations by an authorized administrator of Washington University Open Scholarship. For more information, please contact digital@wumail.wustl.edu.

WASHINGTON UNIVERSITY IN ST. LOUIS

Division of Biology and Biomedical Sciences
Immunology

Dissertation Examination Committee:

Kory Lavine, Chair
Michael Diamond, Co-Chair
Deborah Lenschow
Gwendalyn Randolph
Joel Schilling
Amber Stratman

Cardiovascular SARS-CoV-2 Tropism and Immunopathology
by
Oleksandr Dmytrenko

A dissertation presented to
Washington University in St. Louis
in partial fulfillment of the
requirements for the degree
of Doctor of Philosophy

August 2023
St. Louis, Missouri

© 2023, Oleksandr Dmytrenko

Table of Contents

Table of Contents	iii
List of Figures	vi
List of Tables	viii
Acknowledgements	ix
Abstract	xi
Chapter 1: Introduction to Viral-Associated Cardiac Disease	1
1.1 Introduction	1
1.2 Coxsackie Virus	2
1.2.1 Epidemiology	2
1.2.2 Virion and Replication Cycle	3
1.2.3 Disease Pathogenesis	3
1.2.4 Cardiovascular Disease	3
1.2.5 Models of Cardiovascular Disease	4
1.3 Influenza	5
1.3.1 Epidemiology	5
1.3.2 Virion and Replication Cycle	6
1.3.3 Disease Pathogenesis	7
1.3.4 Cardiovascular Disease	7
1.3.5 Models of Cardiovascular Disease	8
1.4 SARS-CoV	9
1.4.1 Epidemiology	10
1.4.2 Virion and Replication Cycle	10
1.4.3 Disease Pathogenesis	11
1.4.4 Cardiovascular Disease	12
1.4.5 Models of Cardiovascular Disease	12
1.5 SARS-CoV-2	13
1.5.1 Epidemiology	13
1.5.2 Virion and Replication Cycle	13
1.5.3 Disease Pathogenesis	14
1.5.4 Cardiovascular Disease	16
1.5.5 Models of Cardiovascular Disease	20
1.6 Conclusions	20
1.7 References	21
Chapter 2: SARS-CoV-2 Infects Human Engineered Heart Tissues and Models COVID-19 Myocarditis	34
2.1 Summary	34

2.2	Introduction	35
2.3	Results	36
2.3.1	Evidence of Cardiomyocyte Infection in Severe COVID-19 Myocarditis	36
2.3.2	SARS-CoV-2 Tropism in the Human Heart	37
2.3.3	RNA Sequencing Identified Robust Viral Transcription and Activation of Innate Immune Responses	39
2.3.4	SARS-CoV-2 Entry Into Cardiomyocytes Is Mediated by ACE2 and Endosomal Cysteine Proteases	41
2.3.5	EHTs Model COVID-19 Myocarditis	43
2.4	Discussion	45
2.4.1	Study Limitations	47
2.5	Conclusions	48
2.6	Methods	48
2.7	References	62
Chapter 3: Human Cardiac Pericytes are Susceptible to SARS-CoV-2 Infection		89
3.1	Summary	89
3.2	Introduction	90
3.3	Results	91
3.3.1	ACE2 is Expressed in Human Cardiac Pericytes In Situ	91
3.3.2	Human Cardiac Pericytes are Permissive to SARS-CoV-2 Infection	91
3.3.3	SARS-CoV-2 Infects Human Primary Cardiac Pericytes	92
3.3.4	SARS-CoV-2 Enters Cardiac Pericytes Through an Endosomal Pathway	93
3.3.5	Cardiac Pericyte Infection Elicits Inflammatory and Vasoactive Responses and Alters Endothelial Cell Transcription	95
3.3.6	SARS-CoV-2 Infection in COVID-19 Patients	98
3.4	Discussion	98
3.4.1	Study Limitations	99
3.5	Conclusions	99
3.6	Methods	100
3.7	References	114
Chapter 4: Mouse Model of Cardiomyocyte-Restricted SARS-CoV-2 Infection		135
4.1	Summary	135
4.2	Introduction	135

4.3	Results	138
4.3.1	SARS-CoV-2 Infects Cardiac Tissue in Unrestricted and Cardiac-Restricted Murine Models of Infection	138
4.3.2	Cardiac Infection with SARS-CoV-2 Leads to Left Ventricular Dysfunction and Macrophage Accumulation in the Heart	140
4.3.3	SARS-CoV-2 Causes Downregulation of Sarcomere and Metabolism Genes.	141
4.3.4	CCR2 Blockade Rescues Cardiac Dysfunction and Increases Viral Clearance During Cardiac Infection with SARS-CoV-2	142
4.4	Discussion	143
4.5	Methods	147
4.6	References	154
	Chapter 5: Conclusions and Future Directions	165
5.1	Cardiomyocytes in SARS-CoV-2 Infection	165
5.2	Cardiac Pericytes in SARS-CoV-2 Infection	167
5.3	Cardiomyocyte-Restricted Mouse Model of SARS-CoV-2 infection	169
5.4	Concluding Remarks	173
5.5	References	174

List of Figures

Figure 1.1	Cardiac complications of COVID-19	33
Figure 2.1	Specimens From Patients With Severe COVID-19 Myocarditis Show Evidence of SARS-CoV-2 Cardiomyocyte Infection	68
Figure 2.2	In situ hybridization for SARS-CoV-2 RNA in cardiac autopsy specimens	69
Figure 2.3	ACE2 expression and infectivity of hPSC-derived cells in human engineered heart tissues.	70
Figure 2.4	ACE2 is expressed in the human heart and in stem cell derived cardiomyocytes	71
Figure 2.5	SARS-CoV-2 Infects Cardiomyocytes	72
Figure 2.6	Flow cytometry gating strategies for primary human cardiac cell types and hPSC-derived endothelial cells and cardiac fibroblasts.	74
Figure 2.7	SARS-CoV-2 infects hPSC-derived cardiomyocytes but not undifferentiated hPSC lines	75
Figure 2.8	Flow cytometry gating schemes	76
Figure 2.9	Sequencing Identified Viral Transcription and Activation of Innate Immune Response in hPSC-Derived Cardiomyocytes and Tissues	77
Figure 2.10	RNA sequencing of mock and SARS-CoV-2 infected hPSC-derived cardiomyocytes, fibroblasts, macrophages, and two-dimensional tissues	79
Figure 2.11	SARS-CoV-2 entry of hPSC-derived cardiomyocytes is mediated by ACE2 and endosomal cysteine proteases	80
Figure 2.12	EHTs Recapitulate Aspects of COVID-19 Myocarditis	82
Figure 2.13	Confocal microscopy of mock and SARS-CoV-2 infected three-dimensional EHTs	84
Figure 2.14	Mechanisms of Reduced EHT Contractility	85
Figure 2.15	SARS-CoV-2 infection drives type I interferon signaling and sarcomere breakdown in hPSC-derived cardiomyocytes	87
Figure 3.1	ACE2 protein is expressed on cardiac pericytes and cardiomyocytes	118
Figure 3.2	Detection of SARS-CoV-2 in Pericytes of Inoculated Ventricular Organotypic Slices	119
Figure 3.3	Detection of SARS-CoV-2 genomic and replication intermediate RNAs in cultured cardiac slides	120

Figure 3.4	Detection of SARS-CoV-2 nucleocapsid protein within pericytes of cardiac slices	121
Figure 3.5	Detection of SARS-CoV-2 nucleocapsid protein within NG2-positive pericytes of human cardiac tissue	122
Figure 3.6	Isolation of cardiac pericytes from human hearts	124
Figure 3.7	SARS-CoV-2 Productively Infects Human Primary Cardiac Pericytes	125
Figure 3.8	Selective susceptibility of human cardiac pericytes to SARS-CoV-2 infection	126
Figure 3.9	SARS-CoV-2 enters human cardiac pericytes in ACE2- and cysteine protease-dependent manner	127
Figure 3.10	Inhibition of cysteine proteases and ACE2 decreases pericyte infection with SARS-CoV-2 for an extended period	128
Figure 3.11	Inhibition of endosomal acidification decreases pericyte infection early in replication cycle independent of cell-to-cell spread	129
Figure 3.12	SARS-CoV-2 Infection Upregulates Type I IFN Signaling, Inflammatory Pathways, and Vasoactive Genes in Cardiac Pericytes	130
Figure 3.13	SARS-CoV-2 infection reproducibly upregulates IL6 and can upregulate IL8 in cardiac pericytes	131
Figure 3.14	Inhibition of NFkB signaling decreases cell death in infected pericytes	132
Figure 3.15	Infected cardiac pericyte-conditioned medium leads to upregulation of type I interferon signaling and downregulation of thrombomodulin	133
Figure 3.16	Detection of SARS-CoV-2 in Pericytes of COVID-19 Cardiac Autopsy Specimens	134
Figure 4.1	Systemic and cardiac-restricted murine models of SARS-CoV-2 infection	160
Figure 4.2	Infection with SARS-CoV-2 leads to cardiac dysfunction and macrophage accumulation	161
Figure 4.3	Flow cytometry of cardiac immune cells from infected MYH6-hACE2 mice at dpi 8	162
Figure 4.4	SARS-CoV-2 causes downregulation of sarcomere and metabolism genes	163
Figure 4.5	CCR2 blockade rescues cardiac dysfunction and decreases viral burden in MYH6-hACE2 model	164

List of Tables

Table 2.1	Control and COVID-19 myocarditis patient demographic data	67
Table 3.1	Patient and donor Demographics	117

Acknowledgements

A Ph.D. thesis is a celebration of 4+ years of scientific research. Yet, I see it more as a culmination of decades-long work and commitment by communities that might not know they are connected but together are essential for the science to prosper. This work and I as a scientist are both products of such communities and want to take my opportunity and thank them here.

First, I want to thank my graduate school mentors. Being co-mentored is like having two parents with different personalities, knowledge and wisdoms but united in their dedication to your success. Kory Lavine, you took me in as a wide-eyed student fresh out of a small liberal arts college in 2018. You let me grow, learn, make mistakes. You taught me to focus on the primary model – the human condition – to study the relevant aspects of human disease in animals and cells. You guided me through the process and when the opportunity arose and you sensed a change in my interest (and the world around us), you took a gamble and let me plunge into the unknown world of virology and biosafety level 3 research. That plunge would not have been possible without my co-mentor, Mike Dimond, who agreed to co-mentor someone without any background in the study of pathogens in the middle of the pandemic when the resources were tight. I learned so much from you about scientific thinking, asking good questions and healthy skepticism about scientific findings that are so necessary for high-quality research work. I also want to acknowledge the tremendous effort and commitment by Adam Bailey, who took a lot of time to meticulously train me in all the intricacies of high biocontainment environment work. Adam, you changed the way I think about projects and your quote “all models are wrong, some are useful” drives a lot of what I do today. I would also like to thank my thesis committee for their guidance both scientifically and professionally. Debby Lenschow, Gwen Randolph, Amber Stratman, and Joel Schilling – you all

selflessly shared your diverse expertise and helped me grow over the last 4 years both as a scientist, a future clinician, and a human being.

I want to thank both of my laboratories, the Lavine and Diamond Labs, for your support and care, for willingness to help after hours and on weekends, for encouraging me to go on when things were hard in lab or at home. I especially want to thank Andrea and Vinay for being the best desk buddies one could have hoped for. Your advice and help during my impromptu brainstorming sessions are a big reason this work has been completed. Jamison, thank you for always being there when things got hard. And a crew of BSL3 folks: Samantha, Rita, Bradley, and Emma – hours in a PAPR created a bond that is hard to describe and even harder to break.

To my friends in St. Louis, in Minnesota, in Ukraine and all over the world – thank you for being supportive of my pursuits and for genuine interest in the science I do. Your constant inquisitiveness and curiosity gave my work meaning and made it so much more whole. You also opened my eyes to the beauty of the world around me through epic bike rides, camping under the winter stars, shared homemade food, and travel destinations that are sometimes in my (or your) own backyard. I will keep these lessons with me for the rest of my life.

Finally, I want to thank my family. None of this would have been possible without you. My parents Iryna and Andriy gave me a gift of freedom to explore my interests which ultimately landed me in the MD-PhD program. Your love and support were there – from my first time looking at human chromosomes in my mother’s lab in Ukraine to the research internships in the US. Thank you for having faith and letting me find my way in the world and in science.

Oleksandr Dmytrenko

*Washington University in St. Louis
August 2023*

ABSTRACT OF THE DISSERTATION

Cardiovascular SARS-CoV-2 Tropism and Immunopathology

by

Oleksandr Dmytrenko

Doctor of Philosophy in Biology and Biomedical Sciences

Immunology

Washington University in St. Louis, 2023

Professor Kory J. Lavine, Chair

Professor Michael S. Diamond, Co-Chair

Coronavirus Disease 2019 (COVID-19) is caused by SARS-CoV-2, a member of Coronaviridae family. This single-stranded RNA virus is transmitted through a respiratory route, binds to a host receptor ACE2 and enters lung pneumocytes, causing fulminant pulmonary disease in a subset of patients. In addition to pulmonary disease, SARS-CoV-2 can also lead to extrapulmonary manifestations, affecting brain, kidneys, blood vessels and heart. Cardiac complications are common in COVID-19 patients with both mild and severe clinical courses. However, it remains unclear which cardiac cell types are susceptible to SARS-CoV-2 and what the consequences of their infection are.

In this work, I identified human cardiomyocytes and cardiac pericytes as cells that can be targeted by SARS-CoV-2 in the heart, established models of cell type-specific viral infection in vitro and developed a novel animal model of cardiac disease caused by this virus. Cardiomyocytes are specialized muscle cells that perform primary contractile function in the heart. Pericytes are one of the cellular components of the blood vessel wall and are important for endothelial cell

homeostasis, blood vessel permeability, angiogenesis and direct modulation of blood flow. Infected human stem-cell derived cardiomyocytes produce infectious virions, release inflammatory cytokines, lose sarcomeres and contractile function and die. Human primary cardiac pericytes support productive viral replication, produce abundant inflammatory and vasoactive mediators, activate endothelial cells, and undergo cell death after being infected with SARS-CoV-2. Finally, I developed a mouse model to study SARS-CoV-2 associated cardiac disease using transgenic mice with cardiomyocyte-restricted expression of human ACE2. This model allowed me to study cardiac dysfunction as a result of cardiac infection with SARS-COV-2 isolated from the effects of pulmonary disease and associated systemic inflammation. These human ACE2-expressing mice support cardiac infection and show cardiac dysfunction, injury, and immunopathology that resembles cardiac manifestations of COVID-19. Cardiac injury observed in these animals is dependent on recruitment of CCR2⁺ cells, which maintain viral burden by impeding viral clearance.

Taken together, this thesis defines cardiovascular cell types that are susceptible to SARS-CoV-2 infection, identifies molecular consequences of such infection in vitro and in vivo and offers new insights into the mechanistic basis of cardiovascular complications seen in patients with COVID-19.

Chapter 1

Introduction to Viral-Associated Cardiac Disease

Parts of this chapter were adapted from a review published in *Viruses*:

Dmytrenko, O., Lavine, K.J., 2022. Cardiovascular Tropism and Sequelae of SARS-CoV-2 Infection. *Viruses* 14, 1137.

1.1 Introduction

Viral-associated cardiac diseases have been reported as far back as the influenza pandemic of 1918-1919¹. It is currently appreciated that a broad spectrum of viral agents contributes to etiologies of myocarditis, dilated cardiomyopathy, and heart failure. These cardiac manifestations of infection share a target organ but differ in severity, mode of transmission, underlying mechanism and immune response². Extrapulmonary manifestation of Coronavirus Disease-19 (COVID-19) caused by Severe Acute Respiratory Syndrome Coronavirus-2 (SARS-CoV-2) became apparent early during the COVID-19 pandemic. The cardiovascular system is among the most affected organ systems outside of the lungs, especially in severe clinical courses³. The main theories explaining cardiovascular disease in patients with COVID-19 are: 1) cytokine storm and immune activation caused by pulmonary disease; 2) direct infection of cardiomyocytes and other cardiac cell types by SARS-CoV-2; 3) infection-independent cardiac response to virions of SARS-CoV-2 acting as activators of immune system.

It is now recognized that cells of the cardiovascular system can be targets of SARS-CoV-2 infection and are associated with disease pathogenesis⁴. While some details are emerging, much

remains to be understood pertaining to the mechanistic basis by which SARS-CoV-2 causes cardiovascular manifestations of COVID-19. In this dissertation, I set out to characterize the contribution of direct viral infection to cardiac disease seen in patients with COVID-19.

This chapter provides a summary of viruses that are known to cause cardiac disease: coxsackie virus, influenza virus, and severe acute respiratory syndrome coronavirus (SARS). It outlines the epidemiology and pathophysiology of cardiovascular sequelae of COVID-19, focusing on direct SARS-CoV-2 infection of major cardiovascular cell types. Finally, I identify major outstanding questions in cardiovascular COVID-19 research.

1.2 Coxsackie Virus

Coxsackieviruses (CV) are members of Enterovirus genus and are comprised of two groups: A (types 1-24) and B (types 1-6). The viruses primarily affect children and cause a wide range of diseases and syndromes in humans: from cold-like disease to pneumonia, pancreatitis, meningitis, and myocarditis⁵. Only CVB1, CVB3 and CVB5 show significant cardiac tropism and thus will be reviewed here⁶.

1.2.1 Epidemiology

CVB infections occur worldwide and affect males and females equally. Like other enteroviruses, their spread is seasonal in nature and increased in summer and fall months⁷. As the variations of symptoms and associated diseases is high, their surveillance is mostly grouped by clinical presentation rather than viral serotypes that cause the disease⁸. CVBs are the predominant causative agent behind viral myocarditis, aseptic meningitis, and viral pancreatitis in children and adults, with children usually presenting with more severe disease⁹.

1.2.2 Virion and Replication Cycle

CVBs are members of Enteroviridae genus in the Picornaviridae family with an extensively characterized structure. Their virions consist of four structural viral particle (VP) proteins VP1 - VP4 that form an icosahedral non-enveloped 30 nm particle. The particle harbors a 7.5 kb sense single-strand RNA genome that encodes one open reading frame (ORF). This ORF encodes for 11 proteins, including 4 structural VP proteins, RNA-dependent RNA polymerase (3D), two proteases (2A and 3C), two proteins important for synthesis of viral RNA (2B, 2C), a primer of initiation for RNA synthesis (3AB), and a small polypeptide. Two receptors are required for CVB entry into the cell. CVB3 uses decay accelerating factor (DAF also known as CD55) and coxsackie and adenovirus receptor (CAR). CVB1 uses DAF and $\alpha\beta 6$ integrin. After entry and uncoating, RNA is translated to synthesize a single polypeptide that is subsequently cleaved into eleven components by the viral protease. The genome is replicated in the cytoplasm by the viral RNA-dependent RNA polymerase, which together with the capsid proteins assemble into new virions in autophagosomes.

1.2.3 Disease Pathogenesis

CVB members are transmitted through oral-fecal route and respiratory droplets. They enter the intestine and replicate within the intestinal wall, although the exact location for their amplification is poorly understood⁶. Most infections remain asymptomatic or are restricted to mild gastrointestinal or respiratory disease. In patients who seek medical attention, primary intestinal infection is followed by spread to its secondary organ targets causing pancreatitis, meningitis, and myopericarditis.

1.2.4 Cardiovascular Disease

As the primary cause of infectious myocarditis in the developed world, CVBs have been extensively studied in relationship to the cardiovascular disease. As a group, CVB 1-5 are

associated with 20-30% of myocarditis cases¹⁰. Patients present with fever, tachycardia, cardiomegaly, arrhythmias and conduction abnormalities. Patients with confirmed CVB infection show evidence of viral RNA and protein in cardiac tissue on post-mortem histology¹¹. The tissue is also characterized by T and B cell infiltrates. In infants, viral myocarditis often progresses to heart failure and death with mortality rates as high as 50-75%¹². In older children and adults the prognosis is better and with survival of over 75% of affected individuals and complete recovery in over 50% of patients¹³. However, the patients who do not recover frequently develop chronic cardiac disease that eventually progresses to dilated cardiomyopathy and requires heart transplantation^{14,15}.

1.2.5 Models of Cardiovascular Disease

Multiple animal models of cardiovascular disease have been developed and reviewed before¹⁶. The two primary murine models differ in the sources of virus used for the infection. Intraperitoneal administration of *in vitro* passaged CVB3 (Nancy strain) leads to viral spread to the heart, pancreas, and brain and acute myocarditis with long-term decrease in cardiac function and high mortality¹⁷⁻²⁰. Cardiac-passaged CVB3 causes acute disease of lower mortality in C57B6 mice with a strong myeloid and CD4 T cell mediated immune response in the heart²¹. In BALB/c but not C57BL/6 mice, acute disease can progress to a chronic condition with dilated cardiomyopathy seen 1.5 months after inoculation^{19,21}. The virus infects cardiomyocytes in these animals and causes cell death through apoptosis or necroptosis²²⁻²⁴. CD8⁺ cytotoxic T cells and CD4⁺ regulatory T cells (Treg) are required for successful control of infection in these models^{17,25,26}. In addition to its protective role, the adaptive immune response can cause cardiac damage in CVB3-induced myocarditis. BALB/c and A/J mice develop autoreactive antibodies

against cardiac proteins^{27,28}. A/J mice develop T cells that target cardiac myosin and are capable of inducing myocarditis in a virus-naïve animal²⁹.

Innate immune pathways also can have harmful or protective roles during viral myocarditis. As such, TLR3 action through TRIF has been recognized as an important survival element for CBV3 infection. In contrast, members of other innate signaling pathways that lead to type I interferon (IFN) production such as NOD2, IRAK4, and MyD88, contribute to disease exacerbation³⁰⁻³². However, the importance of these innate immune signaling cascades in specific cell types has not been clearly delineated.

1.3 Influenza

1.3.1 Epidemiology

Influenza infections occur worldwide and annually with the peak season occurring in the cold months of the year, corresponding to fall and winter in the US³³. Every year in the US, endemic influenza leads to symptomatic illness in 20-40 million people, 150,000-500,000 hospitalizations and 5,000 to 50,000 deaths³⁴. In contrast, pandemic influenza has occurred every 10-40 years and is associated with antigenic shift discussed below. During these seasons, 20-40% of world population get affected by the disease, and the rate of mortality and complications significantly increases. As such, the pandemics of 1918-19 (“Spanish influenza”), 1952 (“Asian influenza”), 1968 (“Hong Kong influenza”), and 2009 (A(H1N1) pdm09) occurred after viral mutation in animal hosts and showed unusually high attack rate in younger, generally healthy populations³⁵.

1.3.2 Virion and Replication Cycle

Influenza replication has been extensively studied and reviewed³⁶. Briefly, influenza viruses belong to the Orthomyxoviridae family and include four genera: Influenzavirus A, B, C, and D. Human-circulating species are Influenza A (IAV), Influenza B, and Influenza C. Influenza A includes subtypes based on antigenicity of their hemagglutinin (HA) and neuraminidase (NA) proteins: H1-H18 and N1-N11. There are no subtypes for influenza B or C. Influenza is an enveloped, segmented, single-stranded, negative sense RNA virus. The virion includes 8 segments of the genome organized around the nucleoprotein (NP), 3 RNA-dependent RNA polymerase protein components (PA, PB1 and PB2), and surface proteins hemagglutinin (HA), neuraminidase (NA) and matrix proteins 1 and 2 (M1, M2). HA binds sialic acids on host cell surface, facilitating viral entry and endocytosis. The acidic environment of the endosome opens the viral M2 channel and facilitates viral fusion with the, leading to cytoplasmic penetration of the genome. After viral entry, the genome is transcribed and translated into virion components and nonstructural protein 1 (NS1). Following virion assembly, newly generated viral particles bud from the cell and are released by NA-mediated cleavage of sialic acid³⁷.

A remarkable feature of IAV is its ability to undergo antigenic change through two independent mechanisms: antigenic shift and drift. Antigenic drift results from accumulation of point mutations due to absent proofreading by viral RNA-dependent RNA polymerase during progeny genome synthesis³⁸. Mutations that occur at the antigenic regions of HA and NA glycoproteins can alter species and organ tropism and affinity. Antigenic shift is related to the segmented nature of the virus. During the shift, a whole sequence of HA and/or NA gene gets replaced as a complete genomic segment gets swapped. These shifts are only characteristic of IAV

due to the extensive number of its animal reservoirs, which can be concomitantly infected by multiple strains of IAV and facilitate such segmental swaps³⁹.

1.3.3 Disease Pathogenesis

Influenza A and B cause acute respiratory illness in adults and children. The disease begins with abrupt high fever, myalgia, night sweats and cough. General malaise, sore throat, nausea, and headache are also common symptoms. Gastrointestinal symptoms such as vomiting and diarrhea are prevalent in children but rare in adults⁴⁰. Uncomplicated cases are usually self-limiting, resolving 10-14 days after the onset of symptoms⁴¹. Children under 5 and adults over 65 are at high risk for complicated courses of illness. Pneumonia is the most common complication and can be of bacterial, viral, or mixed origins. Cardiovascular complications include transient electrocardiographic changes, myocarditis, myocardial infarctions and cardiomyopathy (further described below). Guillain-Barre syndrome is the most common neurological complication. Some patients with advanced disease present with multiorgan failure, although such presentation is rather uncommon⁴¹.

1.3.4 Cardiovascular Disease

Cardiac effects of pandemic influenza strains such as cardiac edema and pericarditis were reported during the pandemic of 1918-1919¹. Modern long-term ecological data point to increased total mortality and cardiac-related mortality as well as increased frequency of myocardial infarctions during peak influenza season by 30-50%^{42,43}. Cardiovascular complications are more prevalent in IAV infection, but can also occur in influenza B-infected individuals⁴⁴. Myocarditis, the most common of such complications, has been relatively rare in general population but afflicts approximately 5% of hospitalized patients⁴⁵. While most cases of myocarditis occur in adults,

children can be affected as well⁴⁶. Patients start experiencing cardiac symptoms of myocarditis 2-21 days after the onset of pulmonary disease. These include dyspnea, chest pain, and excessive fatigue with exercise⁴⁷. Patients also present with echocardiographic wall motion abnormalities, abnormal electrocardiograms, late gadolinium enhancement on cardiac MRI, and elevated cardiac enzymes⁴⁸. Viral myocarditis presents a severe complication of influenza, as 20-30% of patients with myocarditis succumb to the disease, and up to 48% of those who perish from influenza have evidence of myocarditis⁴⁸. For the survivors, cardiac function tends to normalize over time, although some patients experience symptoms as far as 1.5 months after the primary infection^{45,49}. The presence of IAV in the heart can be detected in some patients by PCR and histological methods⁵⁰. Cardiac histology shows evidence of myocardial damage and cardiomyocyte cell death as well as immune cell infiltrates including T cells and macrophages^{46,51,52}.

1.3.5 Models of Cardiovascular Disease.

Multiple mouse models of influenza infection have been described. Pulmonary infection of animals leads to dissemination of the virus to the heart, spleen, thymus, liver and kidney⁵³. Severity of cardiac disease in infected animals is dependent on mouse strain and viral dose used. ICR mice infected via nebulizer with IAV PR8/34 (H1N1) strain develop myocarditis that is less severe and transient in nature compared to that caused by CVB3⁵⁴. In contrast, BALB/c animals infected intranasally with 40 plaque forming units (PFU) of the same strain present with tissue infiltration of lymphocytes and macrophages, cardiac dysfunction, remodeling and scar formation that persists chronically and leads to cardiomyopathy phenotype^{55,56}. Notably, infection of BALB/c and C57BL/6 mice with higher doses of the same viral strain causes high mortality in animals^{57,58}.

IAV tropism in the heart as well as the mechanism of cardiac injury have been openly debated. Dogma states that cardiovascular disease is caused by inflammation and cytokine release from primary pulmonary infection⁵⁹. However, new data challenging this paradigm has recently emerged. Filgueiras-Rama and colleagues showed that human induced pluripotent stem-cell (iPSC) -derived cardiomyocytes can also be infected with the virus⁶⁰. They also showed that cardiomyocytes, cardiac endothelial cells, and Purkinje cells support viral replication during mouse infection with a pathogenic strain of IAV⁶⁰. Cardiomyocyte-specific attenuation of viral replication by miRNA led to increased survival, decreased cardiac inflammation and fibrosis, and improved electrical dysfunction during a lethal model of IAV infection⁶¹. Taken together, this new evidence suggests a previously unappreciated role of direct cardiac infection by IAV in influenza-associated myocarditis.

Multiple factors have been studied in relationship to cardiac disease caused by IAV. Trypsin and trypsin-like proteases are capable of HA cleavage required for viral spread and entry. Ectopic expression of trypsin induced by IAV infection contributes to short-term cardiac pathology and is required for the progression towards the cardiomyopathy phenotype^{55,56}. IFITM3, an IFN-responsive gene that inhibits viral entry and dampens immune response, has been shown to be protective in cardiac infection by decreasing viral load, preventing cardiac fibrosis, and protecting from electric abnormalities⁶². The nature of cellular immune response in cardiac manifestations of IAV has not been characterized. While alveolar macrophages and classical dendritic cells are important for animal recovery from pulmonary IAV infection, their role in progression of myocarditis is less understood^{63,64}

1.4 SARS-CoV

Coronaviruses are a family of RNA viruses that get their name from the characteristic structural feature of spherical virion being covered with protruding spike proteins resembling a crown (or “corona”). The family is phylogenetically divided into 4 genera: alpha, beta, gamma, delta, of which alpha and beta group viruses cause disease in humans⁶⁵. Specifically, alpha-coronaviruses HCoV-229E, HCoV-NL63, HCoV-OC43, HCoV-HKU1 cause self-limiting respiratory disease, whereas beta-coronaviruses SARS-CoV, Middle Eastern Respiratory Syndrome Coronavirus (MERS-CoV) and SARS-CoV-2 lead to more severe presentations and mortality. Of these, SARS-CoV and SARS-CoV-2 have been shown to exhibit signs of direct cardiac tropism and thus are reviewed below⁶⁶.

1.4.1 Epidemiology

SARS-CoV is a member of betacoronaviruses that was the causative agent behind 2003 world outbreak of SARS⁶⁷. This virus crossed into human population from zoonotic hosts sold at animal wet markets⁶⁸. The outbreak began in the Guangdong province of China, but then spread across the world to 29 countries from a single infected patient who stayed in a hotel in Hong Kong. CDC estimates that 8,098 people contracted SARS-CoV worldwide, and 774 died from it during the outbreak in 2003⁶⁹. It was finally contained through aggressive quarantine measures for symptomatic individuals thanks to lack of asymptomatic transmission⁷⁰.

1.4.2 Virion Structure and Replication Cycle

The structure and function of SARS-CoV proteins have been extensively reviewed⁷¹. Like other members of Coronaviridae family, it is an enveloped, positive sense single stranded RNA virus. The virion of SARS-CoV consists of a lipid bilayer envelope, genomic RNA, and 4

structural proteins encoded on the 3' end of the genome: nucleocapsid, spike, envelope and membrane proteins. Nucleocapsid protein serves as a backbone for RNA genome assembly and organization. Envelope and membrane proteins anchor the outer membrane of the virion and stabilize the curvature and organization of the lipid bilayer. Trimers of the spike protein recognize the host receptor angiotensin-converting enzyme 2 (ACE2) and facilitate viral entry upon binding. The rest of the 29 kb genome encodes non-structural proteins such as polymerases, helicases, RNA-modifying enzymes and accessory proteins important in host immune response modulation. For example, nsp16 (2'-*O*-methyltransferase) and nsp15 prevent interferon induction through MDA5⁷², while PLpro inhibits IRF3 signaling⁷³. After the release of viral RNA into the host cell, reverse transcription begins to generate more sense RNA template and amplify expression of viral genes.

1.4.3 Disease Pathogenesis

SARS-CoV is transmitted via respiratory droplets from symptomatic individuals. While it affects both adults and children, the latter experience milder course of the disease⁷⁴. Patients who get infected with SARS-CoV experience a 2-10 day asymptomatic incubation period, followed by high fevers, myalgia, chills and diarrhea that progress to dyspnea at the end of the first week of disease^{75,76}. Some patients progress to acute respiratory distress syndrome (ARDS) and require ventilatory support by three weeks of infection. Pulmonary disease is the primary manifestation of SARS and characterized by diffuse alveolar damage or fibrinous pneumonia pattern on histology and multifocal airspace consolidation on imaging. Vascular thrombi, pulmonary infarcts, and evidence of endothelial damage were found in tissues of SARS-CoV-infected patients⁷⁷. The pulmonary phase of the disease lasts about 1 week in duration. Most patients recovered within 14-

18 days after the onset of symptoms, whereas under 10% of all patients and as high as 50% of older patients succumb to infection⁷⁸⁻⁸⁰. Recovery was associated with spontaneous and complete return of pulmonary functions in most individuals⁸¹.

1.4.4 Cardiovascular Disease

The number of studies investigating cardiovascular complications of SARS-CoV has been limited due to a relatively short nature of the 2003 outbreak. A study of 121 hospitalized SARS patients found that tachycardia was the most common of the cardiac sign (71% of patients), followed by hypotension (50%) and cardiomegaly without signs of heart failure (10%). Arrhythmias and echocardiographic findings were not common⁸². Furthermore, no echocardiographic evidence for a change in systolic function was seen at 30-day follow up of infected individuals⁸³. Myocardial infarction was seen in a small number of patients from case reports⁸⁴. Autopsy findings identified the presence of SARS-CoV RNA in 35% of patients with SARS diagnosis, and this was accompanied by macrophage-predominant immune accumulation with a distinct lack of T cells. Macrophage accumulation was more severe in patients with evidence of viral RNA in the heart and was distinct from lymphocyte-predominant infiltration characteristic of coxsackie virus infection described above⁸⁵. The nature and role of these macrophages in pathophysiology of SARS-associated cardiac disease remains unknown. Furthermore, the nature of infected cells in humans and consequences of such infection have not been extensively studied.

1.4.5 Models of cardiovascular disease.

While multiple animal models of SARS-CoV infection have been developed, most have focused on pulmonary disease⁸⁶. One study describes evidence for viral spread from the primary site of pulmonary infection to the cardiac tissue in wild-type C57BL/6 mice⁸⁵. Such spread was

dependent on global expression of ACE2 and led to downregulation of the receptor in the heart. However, no further functional, histological, or immunological characterization of murine cardiac infection was performed.

1.5 SARS-CoV-2

1.5.1 Epidemiology

SARS-CoV-2 was identified as a causative agent behind the ongoing COVID-19 pandemic within a month of the first reports describing a novel severe pulmonary syndrome in China in 2019⁸⁷. The virus spilled into human population most likely from an animal host that has not been identified. The main suspects included bats, pangolins, raccoon dogs and civet cats⁸⁸. However, no strain that is evolutionarily close enough to the human SARS-CoV-2 has been isolated from these animals to date⁸⁹. The outbreak started in the Hubei province in China and quickly spread beyond that area, first in China and then worldwide. Unlike SARS-CoV, SARS-CoV-2 can be transmitted from asymptomatic individuals, complicating its containment with isolation measures alone⁹⁰. The virus infects people of all ages with severe disease being more common in older populations⁹¹. Pediatric infections and severe disease have been reported as well⁹². As of April 2023, there has been over 750 million cases and almost 7 million deaths attributed to COVID-19 worldwide⁹³. The pandemic is currently under partial control through a combination of isolation measures, vaccination, herd immunity as well as improved therapeutics and treatment protocols^{94,95}.

1.5.2 Virion Structure and Replication Cycle

The virion structure of SARS-CoV-2 is similar to SARS-CoV. The genomes of these viruses share 79% of sequence with major differences localized to the S gene⁹⁶. SARS-CoV-2 uses

ACE2 as a host cell receptor for entry⁸⁷, although other putative entry factors have been identified such as CD147, LFA-1, heparan sulfate, AXL, LDLRAD3, CD209/DC-SIGN/CLEC4L, CLEC4G/LSECTin, and KREMEN1⁹⁷⁻⁹⁹. Unlike SARS-CoV, SARS-CoV-2 circulated in the population long enough to encounter significant evolutionary pressure from natural and vaccination-acquired immunity. As such, several new strains have emerged since 2020. Among them, variants alpha, beta, gamma, delta, and omicron harbor changes in S protein, which confer increased transmissibility and resistance to pre-existing antibody immunity^{100,101}. These changes led to several consecutive surges of cases in the population and contributed to significant morbidity and mortality of COVID-19⁹³. The variants tend to sequentially outcompete each other on the global scale, with omicron subvariants (e.g., XBB.1.5) being dominant at the time of this writing in April 2023.

1.5.3 Disease Pathogenesis

The virus is transmitted via respiratory and potentially aerosol routes from both symptomatic and asymptomatic individuals. Infection sets in within first 14 days after exposure, with most cases presenting 4-5 days after contact with infected host¹⁰². Patients infected with the omicron variant tended to develop symptoms slightly earlier, around 3 days after exposure¹⁰³.

Infection begins with upper respiratory tract and can spread to the lower respiratory tract in patients who develop moderate to severe disease. Patients present with productive cough, fever, shortness of breath, headache, myalgias, and severe malaise. Moreover, 20-40% of those show signs of gastrointestinal distress, such as vomiting and diarrhea. However, presenting symptoms vary depending on the causative variant of SARS-CoV-2. As such, patients infected with omicron and delta variant experience nasal discharge and congestion, sore throats, and sneezing as most

common early symptoms¹⁰⁴. Loss of taste and smell is a wide-spread unique feature of COVID-19, happening in up to 57% of patients with infected with the omicron variant¹⁰⁴. Pneumonia and ARDS are the most common severe complications in adult patients and often require hospitalization, advanced levels of care, and mechanical support¹⁰⁵. Other complications suggest extensive extrapulmonary involvement. These include thromboembolic events including deep vein thrombosis and pulmonary embolism, cardiovascular disease such as myocarditis and myocardial infarction, acute kidney injury, hyperglycemia, Guillain-Barre syndrome and stroke³. In children, multisystem inflammatory syndrome (MIS-C) has been among the common complications. It is similar to other hyperinflammatory diseases in pediatric populations, such as Kawasaki disease and toxic shock syndrome, and is characterized by sustained high fevers, dermatologic manifestations, and cardiac collapse⁹².

Clinical outcomes vary greatly by age and geographic location. Before the development of effective vaccines, the mortality rate worldwide was about 0.539% with the lowest rate in 7 year old patients (0.0023%) and increasing exponentially with age reaching 20% in 90 year old individuals¹⁰⁶. Hospitalized patients experienced higher overall mortality at 11%¹⁰⁷. Wide-spread vaccination, better hospital protocols and availability as well as novel therapeutic approaches decreased mortality over the years of this pandemic¹⁰⁸.

Most of the survivors of SARS-CoV-2 infection fully recover. However, long-term complications of COVID-19, defined as persistent symptoms 3 months after the onset of illness, have been commonly reported¹⁰⁹. Post-acute COVID symptoms have been seen weeks following initial infection in young and otherwise healthy individuals that had mild acute COVID-19 symptoms^{110,111}. Dry cough and breathlessness, fatigue, exercise intolerance, mental fog, and

cardiac dysfunction are among the signs and symptoms that characterize Post-Acute COVID-19 syndrome (PACS), also known as “long COVID”, “long-haul COVID”, post-acute sequelae of SARS-CoV-2 (PASC), and Persistent Post-COVID-19 Syndrome (PPCS)¹¹².

1.5.4 Cardiovascular Disease

Cardiac complications of COVID-19 occur in 20-44% of acutely hospitalized patients and constitute an independent risk factor for COVID-19 mortality^{102,113–115}. During acute infection, cardiac manifestations include myocardial injury (elevated serum troponin levels), myocarditis, pericarditis, heart failure, acute coronary syndromes, and arrhythmias (**Figure 1.1**)^{102,116–123}. Vascular involvement is particularly evident and often presents as acute venous (deep vein thrombosis, pulmonary embolism) and arterial thrombosis (stroke, critical limb ischemia) (**Figure 1.1**). Among patients presenting with chest pain and/or heart failure, cardiac magnetic resonance imaging has revealed signs of myocardial and pericardial inflammation (delayed contrast enhancement, T1 mapping, T2 signal)¹²⁴. Surprisingly, MRI evidence of cardiac inflammation was reported in patients who had seemingly recovered, highlighting an underappreciated cardiac component of this disease even in its milder forms¹²⁴.

Long-term sequelae of COVID-19 infection are now being identified in patients who remain symptomatic beyond the acute phase. An array of cardiovascular symptoms have been described in this population including fatigue, exertional dyspnea, chest pain, and palpitations¹⁰⁹. Remarkably, only 30% of patients report full recovery of symptoms 6 months after infection^{125,126}. While much remains to be learned regarding the epidemiology and natural history of cardiovascular PACS, these early observations signify that cardiovascular damage is a potential long-lasting feature of COVID-19 in select individuals.

The underlying cause(s) of the cardiovascular manifestations of acute COVID-19 and PACS remain a topic of considerable debate. Direct viral infection of cardiovascular cell types, systemic inflammation, and microvascular thrombosis have each been implicated in the pathogenesis of acute COVID-19. Patients with acute COVID-19 display numerous systemic derangements including marked increases in circulating inflammatory mediators^{127,128}, activation of the complement cascade¹²⁹, impaired fibrinolysis¹³⁰, platelet activation and aggregation¹³¹. While associations between systemic inflammation and acute cardiovascular sequelae of COVID-19 exist¹³², a causative relationship has yet to be rigorously established. Much less is known regarding the pathology of PACS. Cardiac MRI findings compatible with myocarditis were only observed in a subset of individuals¹³³ and increasing evidence may point towards involvement of the vasculature¹³⁴ and autonomic nervous system^{135,136}.

Postmortem analysis of patients who succumbed from acute COVID-19 has revealed evidence of cardiac involvement without clinically apparent features of heart failure or myocarditis. Myocardial necrosis, myocarditis, and microthrombi in capillaries, arterioles, and small arteries were apparent in approximately 35% of cases. Abundant interstitial macrophages were present in the majority of cases and multifocal lymphocytic myocarditis in a smaller fraction of the cases¹³⁷⁻¹⁴⁰. SARS-CoV-2 RNA was detected within the myocardium by multiple techniques and co-localized with rare interstitial cells and cardiomyocytes¹³⁸. The precise identity of interstitial cells with detectable SARS-CoV-2 RNA is unknown. It is important to note that the majority of autopsy samples are collected after extended periods of hospitalization beyond the phase of active viral replication. Thus, these analyses might underestimate the extent of viral infection.

Pathological analyses have been performed on patients with clinical diagnoses of myocarditis and heart failure. While these biopsy and autopsy studies have small numbers of subjects, they each have reported macrophage and lymphocyte infiltration and evidence of interstitial cell and cardiomyocyte SARS-CoV-2 infection. Intriguingly, interstitial cells adjacent to areas of microthrombi contained SARS-CoV-2 RNA^{141,142}. Within the systemic vasculature, endotheliitis with associated viral inclusions and genomes have been observed^{143,144}. Collectively, these studies implicate SARS-CoV-2 infection as a possible pathological mechanism contributing to cardiac and vascular manifestations of COVID-19.

Several studies have established that extrapulmonary sites are susceptible to SARS-CoV-2 infection^{145,146}. Cellular tropism outside of the lung seems to be dictated by ACE2 expression and the ability of the virus to gain access to extrapulmonary tissues. Whether SARS-CoV-2 enters the heart and vasculature through hematological seeding or immune cell trafficking of virions remains unclear. Among myocardial cell types, cardiomyocytes and pericytes express ACE2 mRNA. Cardiac fibroblasts and vascular smooth muscle cells may also express ACE2, albeit to a lesser degree^{147,148}.

Susceptible cell types

Cardiomyocytes are the most abundant cell type in the heart by volume. These specialized muscle cells evolved to perform repeated rhythmic contractions, ensuring consistent blood supply in the body. Human pluripotent stem cell-derived cardiomyocytes (hPSC-CMs), human cardiac slices, and isolated cardiomyocytes are readily infected by SARS-CoV-2^{141,149–155}. ACE2 serves as the cardiomyocyte cell surface receptor for SARS-CoV-2. Cardiomyocyte infection can be abrogated by neutralizing ACE2 antibodies or genetic disruption of *ACE2*. Infected

cardiomyocytes form syncytia in culture through a spike dependent mechanism that can be mitigated by furin inhibitors or mutation of the spike furin cleavage site (R682S)¹⁵³. Whether SARS-CoV-2 propagates within the myocardium by directly spreading between adjacent cells through syncytia and bypasses traditional cell entry and exit mechanisms is not yet clear. Most importantly, the functional consequences of such infection *in vitro* and *in vivo* remained elusive.

Pericytes are vascular mural cells that envelop endothelial cells of blood vessels and play a critical role in vascular development, integrity, and modulation. These cells do not have access to the lumen of the blood vessel but are rather associated with the endothelial cells on the basolateral side¹⁵⁶. Such endothelial cell-pericyte interaction are crucial in recruitment and stabilization of the endothelial cells during angiogenesis and remodeling of blood vessels^{157,158}, enhancement of tight junction formation and ultimate prevention of microvascular leakiness¹⁵⁹. In addition to affecting endothelial cells, pericytes can directly modulate blood vessel tone and change blood flow of small blood vessels^{160,161}, suggesting another potential role in cardiovascular maintenance. Pericytes also contribute to regeneration of injuries in multiple organs¹⁶². Their ability to differentiate into multiple cell types upon stimulation *in vitro* and *in vivo* suggests their multipotent nature¹⁶³. Pericyte dysfunction has been implicated in a number of diseased states, including diabetic retinopathy¹⁶⁴, Alzheimer's disease¹⁶⁵, and renal fibrosis¹⁶⁶.

Cardiac pericytes are believed to originate from epicardial cells during embryogenesis¹⁶⁷. These cells cover cardiac microvasculature at the ratio of 1 per 2-3 endothelial cells¹⁶⁸. Similar to findings in other organs, pericyte depletion leads to leakiness of coronary microvasculature as well as increased inflammation and cardiac dysfunction during ischemic injury¹⁶⁹. These cells have been further implicated in direct modulation of coronary capillary blood flow during injury¹⁶⁰.

In the context of viral infection, the role of pericytes is only beginning to emerge. Existing studies have been focused primarily on brain infection and suggest permissiveness of human brain pericytes to Mayaro, Chikungunya and Zika viruses^{170,171}. Recently, human brain pericytes have been shown to be susceptible to SARS-CoV-2 and can underline neuropathology of COVID-19¹⁷². However, the role of cardiac pericytes in cardiovascular manifestations of COVID-19 remained understudied.

1.5.5 Models of cardiovascular disease.

Reliable animal models of cardiovascular disease associated with COVID-19 are lacking, as the field has primarily focused on pulmonary illness¹⁷³. Hamsters, which are naturally susceptible to SARS-CoV-2, offer some insights into effects of the virus on the heart¹⁷⁴. During pulmonary infection, cardiac spread of the virus is observed together with acute cardiac injury and inflammatory response¹⁷⁵. Chronically, SARS-COV-2 infection leads to increased ventricular wall thickening, cardiac enlargement and fibrosis¹⁷⁶. Mice have shown only mild cardiac viral titers during the pulmonary infection and have not been extensively studied¹⁷⁷. None of the models have been evaluated for immune response, the nature of infected cardiac cells, or cardiac dysfunction. Moreover, pulmonary disease in these animals can confound interpretation of any cardiac findings. Thus, the consequences of direct infection of the heart cannot be easily separated from the effects of systemic inflammation or abnormal circulation due to pulmonary disease. More targeted small animal models are required for better understanding of cardiovascular effects of SARS-CoV-2.

1.6 Conclusions

Extrapulmonary manifestations of COVID-19 include cardiovascular disease and have an array of presentations. Whether SARS-CoV-2 exerts most of its effect on the heart through direct

infection as does CVB3, or through a systemic inflammatory response as does IAV is not known. Moreover, the consequences of the immune response of viral involvement in the heart are not understood. Interestingly, coronaviruses cause uncharacteristic macrophage-predominant, lymphocyte-poor immune accumulation in cardiac tissue, unlike the response seen in CVB3 and IAV infections. It is not clear what role these cells play in pathophysiology of COVID-19 and if they can be targeted for therapeutic purposes.

The data chapters of this thesis focus on outlining the consequences of direct cardiac infection by SARS-CoV-2. In my studies, I investigated the mode of entry of SARS-CoV-2 into human cardiomyocytes, its effect on contractility in 3D organoid structure and on integrity of sarcomere structure. Our group was the first to show that cardiac pericytes can also get infected by SARS-CoV-2, characterized inflammatory and vasoactive response in these cells and described an immune-mediate cell death as a consequence of infection in pericytes. Finally, I have developed a mouse model that allows to delineate consequences of cardiomyocyte-restricted infection by SARS-CoV-2 in an animal and describe the role of CCR2⁺ monocyte-derived cells in the establishment of viral infection and injury.

1.7 References

1. LUCKE, B., WIGHT, T. & KIME, E. PATHOLOGIC ANATOMY AND BACTERIOLOGY OF INFLUENZA: EPIDEMIC OF AUTUMN, 1918. *Archives of Internal Medicine* **24**, 154–237 (1919).
2. Martens, C. R. & Accornero, F. Viruses in the Heart: Direct and Indirect Routes to Myocarditis and Heart Failure. *Viruses* **13**, 1924 (2021).
3. Gupta, A. *et al.* Extrapulmonary manifestations of COVID-19. *Nat Med* **26**, 1017–1032 (2020).
4. Akter, A. & Clemente-Casares, X. COVID-19: The Many Ways to Hurt Your Heart. *Viruses* **15**, 416 (2023).

5. Garmaroudi, F. S. *et al.* Coxsackievirus B3 replication and pathogenesis. *Future Microbiology* **10**, 629–653 (2015).
6. Carolyn B. Coyne, M. Steven Oberste, & Mark A. Pallansch. Enteroviruses: Polioviruses, Coxsackieviruses, Echoviruses, and Newer Enteroviruses. in *Fields Virology*.
7. Romero, J. Coxsackieviruses, echoviruses, and numbered enteroviruses (EV-A71, EVD-68, EVD-70). *Mandell, Douglas, and Bennett's Principles and Practice of Infectious Diseases. Philadelphia: Elsevier* 2229–2230 (2020).
8. Tariq, N. & Kyriakopoulos, C. Group B Coxsackie Virus. in *StatPearls* (StatPearls Publishing, 2023).
9. Kaplan, M. H., Klein, S. W., McPhee, J. & Harper, R. G. Group B coxsackievirus infections in infants younger than three months of age: a serious childhood illness. *Rev Infect Dis* **5**, 1019–1032 (1983).
10. Kim, K.-S., Hufnagel, G., Chapman, N. M. & Tracy, S. The group B coxsackieviruses and myocarditis. *Reviews in Medical Virology* **11**, 355–368 (2001).
11. Spanakis, N. *et al.* Coxsackievirus B3 sequences in the myocardium of fatal cases in a cluster of acute myocarditis in Greece. *Journal of Clinical Pathology* **58**, 357–360 (2005).
12. S, K. & K, B. Severe generalized disease (encephalohepatomyocarditis) occurring in the newborn period and due to infection with Coxsackie virus, group B; evidence of intrauterine infection with this agent. *Pediatrics* **22**, (1958).
13. Dancea, A. B. Myocarditis in infants and children: A review for the paediatrician. *Paediatr Child Health* **6**, 543–545 (2001).
14. O'Connell, J. B. The Role of Myocarditis in End-Stage Dilated Cardiomyopathy. *Tex Heart Inst J* **14**, 268–275 (1987).
15. Cetta, F. & Michels, V. V. The Autoimmune Basis of Dilated Cardiomyopathy. *Annals of Medicine* **27**, 169–173 (1995).
16. Błyszczuk, P. Myocarditis in Humans and in Experimental Animal Models. *Frontiers in Cardiovascular Medicine* **6**, 64 (2019).
17. Woodruff, J. F. & Woodruff, J. J. Involvement of T lymphocytes in the pathogenesis of coxsackie virus B3 heart disease. *J Immunol* **113**, 1726–1734 (1974).
18. Nakamura, H., Kunitsugu, I., Fukuda, K., Matsuzaki, M. & Sano, M. Diverse stage-dependent effects of glucocorticoids in a murine model of viral myocarditis. *Journal of Cardiology* **61**, 237–242 (2013).
19. Becher, P. M. *et al.* Cardiac Function Remains Impaired Despite Reversible Cardiac Remodeling after Acute Experimental Viral Myocarditis. *J Immunol Res* **2017**, 6590609 (2017).

20. Cheung, P. K. *et al.* Specific interactions of mouse organ proteins with the 5'untranslated region of coxsackievirus B3: Potential determinants of viral tissue tropism. *Journal of Medical Virology* **77**, 414–424 (2005).
21. Fairweather, D. & Rose, N. R. Coxsackievirus-induced myocarditis in mice: A model of autoimmune disease for studying immunotoxicity. *Methods* **41**, 118–122 (2007).
22. Wessely, R., Henke, A., Zell, R., Kandolf, R. & Knowlton, K. U. Low-Level Expression of a Mutant Coxsackieviral cDNA Induces a Myocytopathic Effect in Culture. *Circulation* **98**, 450–457 (1998).
23. Saraste, A. *et al.* Cardiomyocyte apoptosis in experimental coxsackievirus B3 myocarditis. *Cardiovascular Pathology* **12**, 255–262 (2003).
24. Zhou, F. *et al.* Necroptosis may be a novel mechanism for cardiomyocyte death in acute myocarditis. *Mol Cell Biochem* **442**, 11–18 (2018).
25. Opavsky, M. A. *et al.* Susceptibility to Myocarditis Is Dependent on the Response of $\alpha\beta$ T Lymphocytes to Coxsackieviral Infection. *Circulation Research* **85**, 551–558 (1999).
26. Pappritz, K. *et al.* Immunomodulation by adoptive regulatory T-cell transfer improves Coxsackievirus B3-induced myocarditis. *The FASEB Journal* **32**, 6066–6078 (2018).
27. Latva-Hirvelä, J. *et al.* Development of troponin autoantibodies in experimental coxsackievirus B3 myocarditis. *European Journal of Clinical Investigation* **39**, 457–462 (2009).
28. Takata, S. *et al.* Identification of Autoantibodies With the Corresponding Antigen for Repetitive Coxsackievirus Infection-Induced Cardiomyopathy. *Circulation Journal* **68**, 677–682 (2004).
29. Gangapara, A. *et al.* Coxsackievirus B3 infection leads to the generation of cardiac myosin heavy chain- α -reactive CD4 T cells in A/J mice. *Clinical Immunology* **144**, 237–249 (2012).
30. Fuse, K. *et al.* Myeloid Differentiation Factor-88 Plays a Crucial Role in the Pathogenesis of Coxsackievirus B3-Induced Myocarditis and Influences Type I Interferon Production. *Circulation* **112**, 2276–2285 (2005).
31. Valaperti, A. *et al.* Innate Immune Interleukin-1 Receptor-Associated Kinase 4 Exacerbates Viral Myocarditis by Reducing CCR5+CD11b+ Monocyte Migration and Impairing Interferon Production. *Circulation* **128**, 1542–1554 (2013).
32. Tschöpe, C. *et al.* NOD2 (Nucleotide-Binding Oligomerization Domain 2) Is a Major Pathogenic Mediator of Coxsackievirus B3-Induced Myocarditis. *Circulation: Heart Failure* **10**, e003870 (2017).
33. Flu season. *Centers for Disease Control and Prevention* <https://t.cdc.gov/C03> (2022).
34. Burden of Influenza. *Centers for Disease Control and Prevention* <https://www.cdc.gov/flu/about/burden/index.html> (2022).

35. Saunders-Hastings, P. R. & Krewski, D. Reviewing the History of Pandemic Influenza: Understanding Patterns of Emergence and Transmission. *Pathogens* **5**, 66 (2016).
36. Gabriele Neumann, John J. Treanor, & Yoshihiro Kawaoka. Orthomyxoviruses. in *Fields Virology* vol. 1 650–675 (Ovid Technologies).
37. Mifsud, E. J., Kuba, M. & Barr, I. G. Innate Immune Responses to Influenza Virus Infections in the Upper Respiratory Tract. *Viruses* **13**, 2090 (2021).
38. Steinhauer, D. A., Domingo, E. & Holland, J. J. Lack of evidence for proofreading mechanisms associated with an RNA virus polymerase. *Gene* **122**, 281–288 (1992).
39. Webster, R. G., Laver, W. G., Air, G. M. & Schild, G. C. Molecular mechanisms of variation in influenza viruses. *Nature* **296**, 115–121 (1982).
40. Cox, N. J. & Subbarao, K. Influenza. *The Lancet* **354**, 1277–1282 (1999).
41. Uyeki, T. M. Influenza. *Ann Intern Med* **174**, ITC161–ITC176 (2021).
42. Warren-Gash, C., Smeeth, L. & Hayward, A. C. Influenza as a trigger for acute myocardial infarction or death from cardiovascular disease: a systematic review. *The Lancet Infectious Diseases* **9**, 601–610 (2009).
43. Caldeira, D. & Nogueira-Garcia, B. Myocardial infarction and viral triggers: what do we know by now? *European Heart Journal Supplements* **25**, A12–A16 (2023).
44. Baselga-Moreno, V. *et al.* Influenza epidemiology and influenza vaccine effectiveness during the 2016–2017 season in the Global Influenza Hospital Surveillance Network (GIHSN). *BMC Public Health* **19**, 487 (2019).
45. Martin, S. S., Hollingsworth, C. L., Norfolk, S. G., Wolfe, C. R. & Hollingsworth, J. W. Reversible Cardiac Dysfunction Associated With Pandemic 2009 Influenza A(H1N1). *Chest* **137**, 1195–1197 (2010).
46. Bratincsák, A. *et al.* Fulminant Myocarditis Associated With Pandemic H1N1 Influenza A Virus in Children. *Journal of the American College of Cardiology* **55**, 928–929 (2010).
47. Ammirati, E. *et al.* Clinical Presentation and Outcome in a Contemporary Cohort of Patients With Acute Myocarditis. *Circulation* **138**, 1088–1099 (2018).
48. Ukimura, A., Izumi, T., Matsumori, A. & Society, C. R. C. on M. A. with the 2009 I. A. (H1N1) P. in J. organized by the J. C. A National Survey on Myocarditis Associated With the 2009 Influenza A (H1N1) Pandemic in Japan. *Circulation Journal* **74**, 2193–2199 (2010).
49. Fagnoul, D. *et al.* Myocardial dysfunction during H1N1 influenza infection. *Journal of Critical Care* **28**, 321–327 (2013).
50. Bowles, N. E. *et al.* Detection of viruses in myocardial tissues by polymerase chain reaction: evidence of adenovirus as a common cause of myocarditis in children and adults. *Journal of the American College of Cardiology* **42**, 466–472 (2003).
51. Komai, T., Nakazawa, G., Asai, S. & Ikari, Y. Fatal fulminant myocarditis associated with novel influenza A (H1N1) infection. *European Heart Journal* **32**, 283 (2011).

52. Gdynia, G. *et al.* Sudden death of an immunocompetent young adult caused by novel (swine origin) influenza A/H1N1-associated myocarditis. *Virchows Arch* **458**, 371–376 (2011).
53. Fislová, T. *et al.* Multiorgan distribution of human influenza A virus strains observed in a mouse model. *Arch Virol* **154**, 409–419 (2009).
54. Kotaka, M., Kitaura, Y., Deguchi, H. & Kawamura, K. Experimental influenza A virus myocarditis in mice. Light and electron microscopic, virologic, and hemodynamic study. *Am J Pathol* **136**, 409–419 (1990).
55. Pan, H.-Y. *et al.* Up-regulation of ectopic trypsin in the myocardium by influenza A virus infection triggers acute myocarditis. *Cardiovasc Res* **89**, 595–603 (2011).
56. Pan, H.-Y. *et al.* Ectopic trypsin in the myocardium promotes dilated cardiomyopathy after influenza A virus infection. *American Journal of Physiology-Heart and Circulatory Physiology* **307**, H922–H932 (2014).
57. Lin, K. L., Suzuki, Y., Nakano, H., Ramsburg, E. & Gunn, M. D. CCR2+ Monocyte-Derived Dendritic Cells and Exudate Macrophages Produce Influenza-Induced Pulmonary Immune Pathology and Mortality¹. *The Journal of Immunology* **180**, 2562–2572 (2008).
58. Woods, P. S. *et al.* Lethal H1N1 influenza A virus infection alters the murine alveolar type II cell surfactant lipidome. *American Journal of Physiology-Lung Cellular and Molecular Physiology* **311**, L1160–L1169 (2016).
59. Tschöpe, C. *et al.* Myocarditis and inflammatory cardiomyopathy: current evidence and future directions. *Nat Rev Cardiol* **18**, 169–193 (2021).
60. Filgueiras-Rama, D. *et al.* Human influenza A virus causes myocardial and cardiac-specific conduction system infections associated with early inflammation and premature death. *Cardiovasc Res* **117**, 876–889 (2021).
61. Kenney, A. D. *et al.* Influenza virus replication in cardiomyocytes drives heart dysfunction and fibrosis. *Science Advances* **8**, eabm5371 (2022).
62. Kenney, A. D. *et al.* IFITM3 protects the heart during influenza virus infection. *Proceedings of the National Academy of Sciences* **116**, 18607–18612 (2019).
63. GeurtsvanKessel, C. H. *et al.* Clearance of influenza virus from the lung depends on migratory langerin+CD11b– but not plasmacytoid dendritic cells. *Journal of Experimental Medicine* **205**, 1621–1634 (2008).
64. Nicol, M. Q. & Dutia, B. M. The role of macrophages in influenza A virus infection. *Future Virology* **9**, 847–862 (2014).
65. Zhang, S. *et al.* Epidemiology characteristics of human coronaviruses in patients with respiratory infection symptoms and phylogenetic analysis of HCoV-OC43 during 2010-2015 in Guangzhou. *PLOS ONE* **13**, e0191789 (2018).
66. Madjid, M., Safavi-Naeini, P., Solomon, S. D. & Vardeny, O. Potential Effects of Coronaviruses on the Cardiovascular System: A Review. *JAMA Cardiology* **5**, 831–840 (2020).

67. Ksiazek, T. G. *et al.* A Novel Coronavirus Associated with Severe Acute Respiratory Syndrome. *New England Journal of Medicine* **348**, 1953–1966 (2003).
68. Graham, R. L. & Baric, R. S. Recombination, Reservoirs, and the Modular Spike: Mechanisms of Coronavirus Cross-Species Transmission. *Journal of Virology* **84**, 3134–3146 (2010).
69. SARS | Basics Factsheet | CDC. <https://www.cdc.gov/sars/about/fs-sars.html>.
70. Peiris, J. *et al.* Clinical progression and viral load in a community outbreak of coronavirus-associated SARS pneumonia: a prospective study. *The Lancet* **361**, 1767–1772 (2003).
71. Weiss, S. R. & Leibowitz, J. L. Chapter 4 - Coronavirus Pathogenesis. in *Advances in Virus Research* (eds. Maramorosch, K., Shatkin, A. J. & Murphy, F. A.) vol. 81 85–164 (Academic Press, 2011).
72. Russ, A. *et al.* Nsp16 shields SARS-CoV-2 from efficient MDA5 sensing and IFIT1-mediated restriction. *EMBO reports* **23**, e55648 (2022).
73. Devaraj, S. G. *et al.* Regulation of IRF-3-dependent Innate Immunity by the Papain-like Protease Domain of the Severe Acute Respiratory Syndrome Coronavirus*. *Journal of Biological Chemistry* **282**, 32208–32221 (2007).
74. Hon, K. *et al.* Clinical presentations and outcome of severe acute respiratory syndrome in children. *The Lancet* **361**, 1701–1703 (2003).
75. Severe Acute Respiratory Syndrome (SARS) Epidemiology & Working Group. *Consensus document on the epidemiology of severe acute respiratory syndrome (SARS)*. https://apps.who.int/iris/bitstream/handle/10665/70863/WHO_CDS_CSR_GAR_2003.11_eng.pdf (2003).
76. KWAN, A. C. *et al.* Severe acute respiratory syndrome-related diarrhea. *J Gastroenterol Hepatol* **20**, 606–610 (2005).
77. Hwang, D. M. *et al.* Pulmonary pathology of severe acute respiratory syndrome in Toronto. *Mod Pathol* **18**, 1–10 (2005).
78. Lee, N. *et al.* A Major Outbreak of Severe Acute Respiratory Syndrome in Hong Kong. <https://doi-org.beckerproxy.wustl.edu/10.1056/NEJMoa030685>
<https://www.nejm.org/doi/full/10.1056/nejmoa030685> (2003) doi:10.1056/NEJMoa030685.
79. Tsui, P. T., Kwok, M. L., Yuen, H. & Lai, S. T. Severe Acute Respiratory Syndrome: Clinical Outcome and Prognostic Correlates¹. *Emerg Infect Dis* **9**, 1064–1069 (2003).
80. Donnelly, C. A. *et al.* Epidemiological determinants of spread of causal agent of severe acute respiratory syndrome in Hong Kong. *The Lancet* **361**, 1761–1766 (2003).
81. Chan, K. *et al.* SARS: prognosis, outcome and sequelae. *Respirology* **8**, S36–S40 (2003).
82. Yu, C.-M. *et al.* Cardiovascular complications of severe acute respiratory syndrome. *Postgraduate Medical Journal* **82**, 140–144 (2006).
83. Li, S. S. *et al.* Left Ventricular Performance in Patients With Severe Acute Respiratory Syndrome. *Circulation* **108**, 1798–1803 (2003).

84. Chong, P. Y. *et al.* Analysis of Deaths During the Severe Acute Respiratory Syndrome (SARS) Epidemic in Singapore: Challenges in Determining a SARS Diagnosis. *Archives of Pathology & Laboratory Medicine* **128**, 195–204 (2004).
85. Oudit, G. Y. *et al.* SARS-coronavirus modulation of myocardial ACE2 expression and inflammation in patients with SARS. *European Journal of Clinical Investigation* **39**, 618–625 (2009).
86. Subbarao, K. & Roberts, A. Is there an ideal animal model for SARS? *Trends in Microbiology* **14**, 299–303 (2006).
87. Zhou, P. *et al.* A pneumonia outbreak associated with a new coronavirus of probable bat origin. *Nature* **579**, 270–273 (2020).
88. Lytras, S., Xia, W., Hughes, J., Jiang, X. & Robertson, D. L. The animal origin of SARS-CoV-2. *Science* **373**, 968–970 (2021).
89. Pagani, I., Ghezzi, S., Alberti, S., Poli, G. & Vicenzi, E. Origin and evolution of SARS-CoV-2. *Eur Phys J Plus* **138**, 157 (2023).
90. Tindale, L. C. *et al.* Evidence for transmission of COVID-19 prior to symptom onset. *eLife* **9**, e57149 (2020).
91. Boehmer, T. K. *et al.* Changing Age Distribution of the COVID-19 Pandemic — United States, May–August 2020. *MMWR Morb Mortal Wkly Rep* **69**, 1404–1409 (2020).
92. Kabeerdoss, J. *et al.* Severe COVID-19, multisystem inflammatory syndrome in children, and Kawasaki disease: immunological mechanisms, clinical manifestations and management. *Rheumatol Int* **41**, 19–32 (2021).
93. WHO Coronavirus (COVID-19) Dashboard. <https://covid19.who.int>.
94. Li, M. *et al.* COVID-19 vaccine development: milestones, lessons and prospects. *Sig Transduct Target Ther* **7**, 1–32 (2022).
95. Forchette, L., Sebastian, W. & Liu, T. A Comprehensive Review of COVID-19 Virology, Vaccines, Variants, and Therapeutics. *Curr Med Sci* **41**, 1037–1051 (2021).
96. Chen, Z., Boon, S. S., Wang, M. H., Chan, R. W. Y. & Chan, P. K. S. Genomic and evolutionary comparison between SARS-CoV-2 and other human coronaviruses. *J Virol Methods* **289**, 114032 (2021).
97. Wang, K. *et al.* CD147-spike protein is a novel route for SARS-CoV-2 infection to host cells. *Sig Transduct Target Ther* **5**, 1–10 (2020).
98. Shen, X.-R. *et al.* ACE2-independent infection of T lymphocytes by SARS-CoV-2. *Sig Transduct Target Ther* **7**, 1–11 (2022).
99. Lim, S., Zhang, M. & Chang, T. L. ACE2-Independent Alternative Receptors for SARS-CoV-2. *Viruses* **14**, 2535 (2022).
100. Chen, R. E. *et al.* In vivo monoclonal antibody efficacy against SARS-CoV-2 variant strains. *Nature* **596**, 103–108 (2021).

101. Chen, R. E. *et al.* Resistance of SARS-CoV-2 variants to neutralization by monoclonal and serum-derived polyclonal antibodies. *Nat Med* **27**, 717–726 (2021).
102. Guan, W. *et al.* Clinical Characteristics of Coronavirus Disease 2019 in China. *New England Journal of Medicine* **382**, 1708–1720 (2020).
103. Brandal, L. T. *et al.* Outbreak caused by the SARS-CoV-2 Omicron variant in Norway, November to December 2021. *Euro Surveill* **26**, 2101147 (2021).
104. Menni, C. *et al.* Symptom prevalence, duration, and risk of hospital admission in individuals infected with SARS-CoV-2 during periods of omicron and delta variant dominance: a prospective observational study from the ZOE COVID Study. *The Lancet* **399**, 1618–1624 (2022).
105. Zhou, F. *et al.* Clinical course and risk factors for mortality of adult inpatients with COVID-19 in Wuhan, China: a retrospective cohort study. *The Lancet* **395**, 1054–1062 (2020).
106. Variation in the COVID-19 infection–fatality ratio by age, time, and geography during the pre-vaccine era: a systematic analysis. *The Lancet* **399**, 1469–1488 (2022).
107. Garg, S. *et al.* Clinical Trends Among U.S. Adults Hospitalized With COVID-19, March to December 2020. *Ann Intern Med* **174**, 1409–1419 (2021).
108. Najjar-Debbiny, R. *et al.* Effectiveness of Paxlovid in Reducing Severe Coronavirus Disease 2019 and Mortality in High-Risk Patients. *Clin Infect Dis* ciac443 (2022) doi:10.1093/cid/ciac443.
109. Nalbandian, A. *et al.* Post-acute COVID-19 syndrome. *Nature Medicine* **27**, 601–615 (2021).
110. Carfi, A., Bernabei, R., Landi, F., & for the Gemelli Against COVID-19 Post-Acute Care Study Group. Persistent Symptoms in Patients After Acute COVID-19. *JAMA* **324**, 603–605 (2020).
111. Johansson, M. *et al.* Long-Haul Post–COVID-19 Symptoms Presenting as a Variant of Postural Orthostatic Tachycardia Syndrome: The Swedish Experience. *JACC: Case Reports* **3**, 573–580 (2021).
112. Oronsky, B. *et al.* A Review of Persistent Post-COVID Syndrome (PPCS). *Clinic Rev Allerg Immunol* **64**, 66–74 (2023).
113. Huang, C. *et al.* Clinical features of patients infected with 2019 novel coronavirus in Wuhan, China. *The Lancet* **395**, 497–506 (2020).
114. Goyal, P. *et al.* Clinical Characteristics of Covid-19 in New York City. *N Engl J Med* **382**, 2372–2374 (2020).
115. Arentz, M. *et al.* Characteristics and Outcomes of 21 Critically Ill Patients With COVID-19 in Washington State. *JAMA* **323**, 1612–1614 (2020).

116. Lippi, G., Lavie, C. J. & Sanchis-Gomar, F. Cardiac troponin I in patients with coronavirus disease 2019 (COVID-19): Evidence from a meta-analysis. *Progress in Cardiovascular Diseases* **63**, 390–391 (2020).
117. Shi, S. *et al.* Association of Cardiac Injury With Mortality in Hospitalized Patients With COVID-19 in Wuhan, China. *JAMA Cardiology* **5**, 802–810 (2020).
118. Inciardi, R. M. *et al.* Cardiac Involvement in a Patient With Coronavirus Disease 2019 (COVID-19). *JAMA Cardiology* **5**, 819–824 (2020).
119. Stefanini, G. G. *et al.* ST-Elevation Myocardial Infarction in Patients With COVID-19. *Circulation* **141**, 2113–2116 (2020).
120. Guo, T. *et al.* Cardiovascular Implications of Fatal Outcomes of Patients With Coronavirus Disease 2019 (COVID-19). *JAMA Cardiology* **5**, 811–818 (2020).
121. Fried, J. A. *et al.* The Variety of Cardiovascular Presentations of COVID-19. *Circulation* **141**, 1930–1936 (2020).
122. Spiezia, L. *et al.* COVID-19-Related Severe Hypercoagulability in Patients Admitted to Intensive Care Unit for Acute Respiratory Failure. *Thromb Haemost* **120**, 998–1000 (2020).
123. Chen, T. *et al.* Clinical characteristics of 113 deceased patients with coronavirus disease 2019: retrospective study. *BMJ* **368**, m1091 (2020).
124. Puntmann, V. O. *et al.* Outcomes of Cardiovascular Magnetic Resonance Imaging in Patients Recently Recovered From Coronavirus Disease 2019 (COVID-19). *JAMA Cardiology* (2020) doi:10.1001/jamacardio.2020.3557.
125. Yong, S. J. Long COVID or post-COVID-19 syndrome: putative pathophysiology, risk factors, and treatments. *Infectious Diseases* **53**, 737–754 (2021).
126. Xie, Y., Xu, E., Bowe, B. & Al-Aly, Z. Long-term cardiovascular outcomes of COVID-19. *Nat Med* **28**, 583–590 (2022).
127. Galani, I.-E. *et al.* Untuned antiviral immunity in COVID-19 revealed by temporal type I/III interferon patterns and flu comparison. *Nat Immunol* **22**, 32–40 (2021).
128. Mudd, P. A. *et al.* Distinct inflammatory profiles distinguish COVID-19 from influenza with limited contributions from cytokine storm. *Science Advances* **6**, eabe3024 (2020).
129. Holter, J. C. *et al.* Systemic complement activation is associated with respiratory failure in COVID-19 hospitalized patients. *Proceedings of the National Academy of Sciences* **117**, 25018–25025 (2020).
130. Kruse, J. M. *et al.* Thromboembolic complications in critically ill COVID-19 patients are associated with impaired fibrinolysis. *Critical Care* **24**, 676 (2020).
131. Hottz, E. D. *et al.* Platelet activation and platelet-monocyte aggregate formation trigger tissue factor expression in patients with severe COVID-19. *Blood* **136**, 1330–1341 (2020).
132. Melillo, F. *et al.* Myocardial injury in patients with SARS-CoV-2 pneumonia: Pivotal role of inflammation in COVID-19. *European Journal of Clinical Investigation* **52**, e13703 (2022).

133. Clark, D. E. *et al.* Cardiovascular magnetic resonance evaluation of soldiers after recovery from symptomatic SARS-CoV-2 infection: a case–control study of cardiovascular post-acute sequelae of SARS-CoV-2 infection (CV PASC). *Journal of Cardiovascular Magnetic Resonance* **23**, 106 (2021).
134. Nägele, M. P., Haubner, B., Tanner, F. C., Ruschitzka, F. & Flammer, A. J. Endothelial dysfunction in COVID-19: Current findings and therapeutic implications. *Atherosclerosis* **314**, 58–62 (2020).
135. Bisaccia, G. *et al.* Post-Acute Sequelae of COVID-19 and Cardiovascular Autonomic Dysfunction: What Do We Know? *Journal of Cardiovascular Development and Disease* **8**, 156 (2021).
136. Ståhlberg, M. *et al.* Post-COVID-19 Tachycardia Syndrome: A Distinct Phenotype of Post-Acute COVID-19 Syndrome. *The American Journal of Medicine* **134**, 1451–1456 (2021).
137. Basso, C. *et al.* Pathological features of COVID-19-associated myocardial injury: a multicentre cardiovascular pathology study. *European Heart Journal* **41**, 3827–3835 (2020).
138. Bearnse, M. *et al.* Factors associated with myocardial SARS-CoV-2 infection, myocarditis, and cardiac inflammation in patients with COVID-19. *Modern Pathology* (2021) doi:10.1038/s41379-021-00790-1.
139. Bois, M. C. *et al.* COVID-19–Associated Nonocclusive Fibrin Microthrombi in the Heart. *Circulation* **143**, 230–243 (2021).
140. Pellegrini, D. *et al.* Microthrombi as a Major Cause of Cardiac Injury in COVID-19. *Circulation* **143**, 1031–1042 (2021).
141. Perez-Bermejo, J. A. *et al.* SARS-CoV-2 infection of human iPSC–derived cardiac cells reflects cytopathic features in hearts of patients with COVID-19. *Science Translational Medicine* **13**, eabf7872 (2021).
142. Tavazzi, G. *et al.* Myocardial localization of coronavirus in COVID-19 cardiogenic shock. *European Journal of Heart Failure* **22**, 911–915 (2020).
143. Ackermann, M. *et al.* Pulmonary Vascular Endothelialitis, Thrombosis, and Angiogenesis in Covid-19. *New England Journal of Medicine* **383**, 120–128 (2020).
144. Varga, Z. *et al.* Endothelial cell infection and endotheliitis in COVID-19. *The Lancet* **395**, 1417–1418 (2020).
145. Lamers, M. M. *et al.* SARS-CoV-2 productively infects human gut enterocytes. *Science* **369**, 50–54 (2020).
146. Monteil, V. *et al.* Inhibition of SARS-CoV-2 Infections in Engineered Human Tissues Using Clinical-Grade Soluble Human ACE2. *Cell* **181**, 905-913.e7 (2020).
147. Chen, L., Li, X., Chen, M., Feng, Y. & Xiong, C. The ACE2 expression in human heart indicates new potential mechanism of heart injury among patients infected with SARS-CoV-2. *Cardiovascular Research* **116**, 1097–1100 (2020).

148. Tucker, N. R. *et al.* Myocyte-Specific Upregulation of ACE2 in Cardiovascular Disease. *Circulation* **142**, 708–710 (2020).
149. Yang, L. *et al.* A Human Pluripotent Stem Cell-based Platform to Study SARS-CoV-2 Tropism and Model Virus Infection in Human Cells and Organoids. *Cell Stem Cell* **27**, 125–136.e7 (2020).
150. Choi, S. W. *et al.* Antiviral activity and safety of remdesivir against SARS-CoV-2 infection in human pluripotent stem cell-derived cardiomyocytes. *Antiviral Res* **184**, 104955 (2020).
151. Li, Y. *et al.* SARS-CoV-2 induces double-stranded RNA-mediated innate immune responses in respiratory epithelial-derived cells and cardiomyocytes. *Proceedings of the National Academy of Sciences* **118**, e2022643118 (2021).
152. Marchiano, S. *et al.* SARS-CoV-2 Infects Human Pluripotent Stem Cell-Derived Cardiomyocytes, Impairing Electrical and Mechanical Function. *Stem Cell Reports* **16**, 478–492 (2021).
153. Navaratnarajah, C. K. *et al.* Highly Efficient SARS-CoV-2 Infection of Human Cardiomyocytes: Spike Protein-Mediated Cell Fusion and Its Inhibition. *Journal of Virology* **95**, e01368-21 (2021).
154. Yang, L. *et al.* Cardiomyocytes recruit monocytes upon SARS-CoV-2 infection by secreting CCL2. *Stem Cell Reports* **16**, 2274–2288 (2021).
155. Bojkova, D. *et al.* SARS-CoV-2 infects and induces cytotoxic effects in human cardiomyocytes. *Cardiovascular Research* (2020) doi:10.1093/cvr/cvaa267.
156. Zhang, Z.-S. *et al.* Research advances in pericyte function and their roles in diseases. *Chinese Journal of Traumatology* **23**, 89–95 (2020).
157. Suri, C. *et al.* Requisite Role of Angiopoietin-1, a Ligand for the TIE2 Receptor, during Embryonic Angiogenesis. *Cell* **87**, 1171–1180 (1996).
158. Sato, T. N. *et al.* Distinct roles of the receptor tyrosine kinases Tie-1 and Tie-2 in blood vessel formation. *Nature* **376**, 70–74 (1995).
159. Hellström, M. *et al.* Lack of Pericytes Leads to Endothelial Hyperplasia and Abnormal Vascular Morphogenesis. *Journal of Cell Biology* **153**, 543–554 (2001).
160. Hall, C. N. *et al.* Capillary pericytes regulate cerebral blood flow in health and disease. *Nature* **508**, 55–60 (2014).
161. Almaça, J., Weitz, J., Rodriguez-Diaz, R., Pereira, E. & Caicedo, A. The Pericyte of the Pancreatic Islet Regulates Capillary Diameter and Local Blood Flow. *Cell Metabolism* **27**, 630-644.e4 (2018).
162. Dellavalle, A. *et al.* Pericytes of human skeletal muscle are myogenic precursors distinct from satellite cells. *Nature Cell Biology* **9**, 255–267 (2007).
163. Dore-Duffy, P., Katychew, A., Wang, X. & Van Buren, E. CNS Microvascular Pericytes Exhibit Multipotential Stem Cell Activity. *J Cereb Blood Flow Metab* **26**, 613–624 (2006).

164. Elena Beltramo and Massimo Porta. Pericyte Loss in Diabetic Retinopathy: Mechanisms and Consequences. *Current Medicinal Chemistry* **20**, 3218–3225 (2013).
165. Salmina, A. B., Komleva, Y. K., Lopatina, O. L. & Birbrair, A. Pericytes in Alzheimer's Disease: Novel Clues to Cerebral Amyloid Angiopathy Pathogenesis. in *Pericyte Biology in Disease* (ed. Birbrair, A.) 147–166 (Springer International Publishing, 2019). doi:10.1007/978-3-030-16908-4_7.
166. Chen, J. *et al.* High-resolution 3D imaging uncovers organ-specific vascular control of tissue aging. *Sci Adv* **7**, eabd7819 (2021).
167. Mikawa, T. & Gourdie, R. G. Pericardial Mesoderm Generates a Population of Coronary Smooth Muscle Cells Migrating into the Heart along with Ingrowth of the Epicardial Organ. *Developmental Biology* **174**, 221–232 (1996).
168. Nees, S. *et al.* Isolation, bulk cultivation, and characterization of coronary microvascular pericytes: the second most frequent myocardial cell type in vitro. *American Journal of Physiology-Heart and Circulatory Physiology* **302**, H69–H84 (2011).
169. Tao, Y.-K. *et al.* Notch3 deficiency impairs coronary microvascular maturation and reduces cardiac recovery after myocardial ischemia. *International Journal of Cardiology* **236**, 413–422 (2017).
170. Bengue, M. *et al.* Mayaro Virus Infects Human Brain Cells and Induces a Potent Antiviral Response in Human Astrocytes. *Viruses* **13**, (2021).
171. Chen, W. *et al.* Zika virus NS3 protease induces bone morphogenetic protein-dependent brain calcification in human fetuses. *Nature Microbiology* **6**, 455–466 (2021).
172. Bocci, M. *et al.* Infection of Brain Pericytes Underlying Neuropathology of COVID-19 Patients. *Int J Mol Sci* **22**, 11622 (2021).
173. Cleary, S. J. *et al.* Animal models of mechanisms of SARS-CoV-2 infection and COVID-19 pathology. *British Journal of Pharmacology* **177**, 4851–4865 (2020).
174. Imai, M. *et al.* Syrian hamsters as a small animal model for SARS-CoV-2 infection and countermeasure development. *Proceedings of the National Academy of Sciences* **117**, 16587–16595 (2020).
175. Francis, M. E. *et al.* SARS-CoV-2 infection in the Syrian hamster model causes inflammation as well as type I interferon dysregulation in both respiratory and non-respiratory tissues including the heart and kidney. *PLOS Pathogens* **17**, e1009705 (2021).
176. Rizvi, Z. A. *et al.* Golden Syrian hamster as a model to study cardiovascular complications associated with SARS-CoV-2 infection. *eLife* **11**, e73522 (2022).
177. Winkler, E. S. *et al.* SARS-CoV-2 infection of human ACE2-transgenic mice causes severe lung inflammation and impaired function. *Nat Immunol* **21**, 1327–1335 (2020).

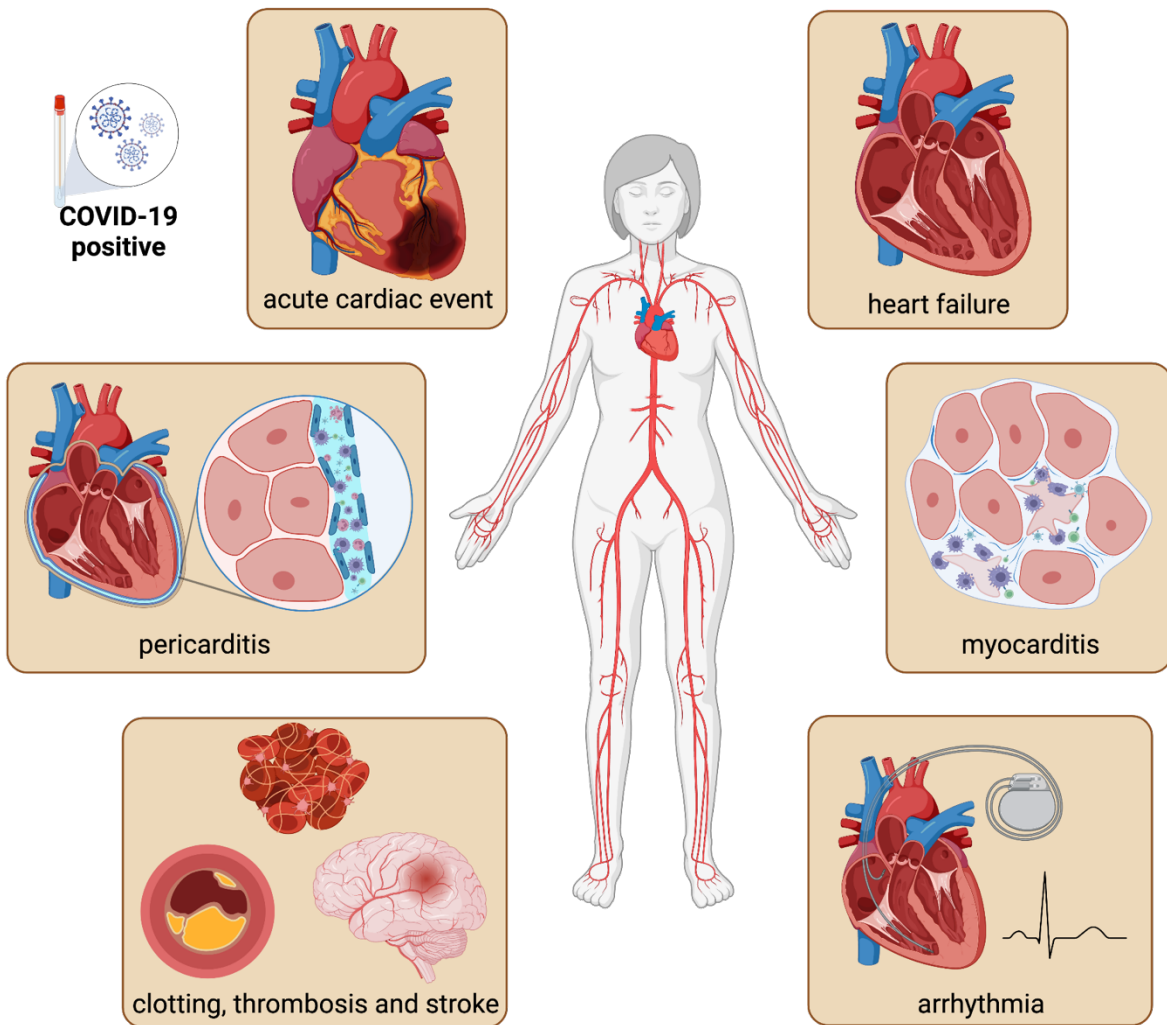


Figure 1.1. Cardiac complications of COVID-19. Cardiac involvement during the clinical course of COVID-19 manifests as acute myocardial injury with elevated troponin, heart failure with decreased ejection fraction, myocarditis, cardiac arrhythmia, thromboembolic events and pericarditis. Evidence of cardiac inflammation can also be present in people who seemingly recover from acute illness.

Chapter 2

SARS-CoV-2 Infects Human Engineered Heart Tissues and Models COVID-19 Myocarditis

This chapter was adapted from an article published in *JACC: Basic to Translational Science*:

Bailey Adam L. *, **Dmytrenko Oleksandr***, Greenberg Lina*, Bredemeyer Andrea L., Ma Pan, Liu Jing, Penna Vinay, Winkler Emma S., Sviben Sanja, Brooks Erin, Nair Ajith P., Heck Kent A., Rali Aniket S., Simpson Leo, Saririan Mehrdad, Hobohm Dan, Stump W. Tom, Fitzpatrick James A., Xie Xuping, Zhang Xianwen, Shi Pei-Yong, Hinson J. Travis, Gi Weng-Tein, Schmidt Constanze, Leuschner Florian, Lin Chieh-Yu, Diamond Michael S., Greenberg Michael J., Lavine Kory J., 2021. SARS-CoV-2 Infects Human Engineered Heart Tissues and Models COVID-19 Myocarditis. *JACC: Basic to Translational Science* 6, 331–345.

*Authors have contributed equally and are co-first authors. AdamLB, KL, MD, MG conceptualized the work; AdamLB and EW performed BSL3 work and virologic studies; OD performed infection analysis, IHC on infected tissue, inflammatory analysis, sorted primary cells; LG and TS generated cardiomyocytes and EHTs; AndreaLB generated macrophages and sorted primary cells; PM, JL, SS, JF, CYL performed human histology and analysis; VP and helped with revisions; EB, AN, KH, AR, LS, MS, DH, TH, WTG, CS, FL provided patient samples; XX, XZ, PYS provided reporter virus; KL, SC, FL performed RNAseq analysis; AdamB, KL, MD, MG, OD wrote and edited manuscript; KL, MD, MG supplied funding

2.1 Summary

There is ongoing debate as to whether cardiac complications of coronavirus disease-2019 (COVID-19) result from myocardial viral infection or are secondary to systemic inflammation and/or thrombosis. We provide evidence that cardiomyocytes are infected in patients with COVID-19 myocarditis and are susceptible to severe acute respiratory syndrome coronavirus 2. We establish an engineered heart tissue model of COVID-19 myocardial pathology, define mechanisms of viral pathogenesis, and demonstrate that cardiomyocyte severe acute respiratory syndrome coronavirus 2 infection results in contractile deficits, cytokine production, sarcomere

disassembly, and cell death. These findings implicate direct infection of cardiomyocytes in the pathogenesis of COVID-19 myocardial pathology and provides a model system to study this emerging disease.

2.2 Introduction

Severe acute respiratory syndrome-coronavirus-2 (SARS-CoV-2) is the cause of the ongoing coronavirus disease-2019 (COVID-19) pandemic. Epidemiological studies have identified pre-existing cardiovascular disease as a risk factor for the development of severe COVID-19 and mortality [reviewed in Madjid et al. ¹]. Cardiovascular manifestations of COVID-19 include elevated troponin, reduced left ventricular (LV) systolic function, and arrhythmias. Cardiac complications occur in 20% to 44% of hospitalized patients, and constitute an independent risk factor for COVID-19 mortality¹⁻⁴. Cardiac magnetic resonance imaging studies have suggested that persistent myocardial injury may be more common than appreciated and occurs in less severe forms of COVID-19⁵⁻⁷. The mechanistic basis by which SARS-CoV-2 results in cardiac dysfunction remains obscure and it is unclear whether these effects are a result of myocardial infection or a systemic inflammatory response to extracardiac infection⁸.

Investigation of the cardiac manifestations of COVID-19 has remained challenging. Rigorous analyses of cardiac tissue obtained from affected patients are lacking. Furthermore, there are few animal models to study cardiovascular complications observed in SARS-CoV-2–infected humans⁹. The most commonly used laboratory animal model, the mouse, is not susceptible to SARS-CoV-2 infection due to poor affinity of the viral spike protein for murine angiotensin converting enzyme 2 (ACE2). Transgenic mice that express human ACE2 under the control of the cytokeratin 18 promotor do not recapitulate ACE2 expression within the human cardiovascular

system¹⁰⁻¹². Therefore, there is a critical need to develop robust model systems that enable the investigation of the cardiovascular complications of COVID-19.

We used human myocardial specimens and devised an engineered heart tissue (EHT) model of COVID-19 myocarditis to test the hypothesis that SARS-CoV-2 promotes cardiac pathology by infecting cardiomyocytes and activating local immune responses. EHT provide unique advantages as model systems for studying COVID-19 cardiac pathology because they generate contractile force, display electrical coupling, promote maturation of human pluripotent stem cell (hPSC)-derived cardiomyocytes, and have cellular organization that mimics myocardial tissue¹²⁻¹⁴. These studies show that cardiomyocytes are a target of SARS-CoV-2, link cardiomyocyte infection to disease pathogenesis, and establish EHT as an experimentally tractable model of COVID-19 myocardial pathology.

2.3 Results

2.3.1 Evidence of Cardiomyocyte Infection in Severe COVID-19 Myocarditis

The pathology of COVID-19 myocarditis remains poorly understood. We obtained autopsy and endomyocardial biopsy specimens from 4 subjects with SARS-CoV-2 infection and clinical diagnoses of myocarditis. Myocardial injury and LV systolic dysfunction were present in each case (**Table 2.1**). Coronary angiography showed no evidence of luminal stenosis or thrombosis. The presence of SARS-CoV-2 RNA from nasopharyngeal samples was confirmed by clinical polymerase chain reaction (PCR) testing.

Postmortem microscopic examination of the LV myocardium showed areas of cardiomyocyte necrosis and degenerative vacuolization of cardiomyocyte cytoplasm accompanied by a mononuclear cell infiltrate (**Figure 2.1A**). These changes were distinct from

postmortem autolytic changes. Examination of the coronary arteries from COVID-19 myocarditis autopsy cases showed nonobstructive mild atherosclerotic changes, consistent with angiogram findings. There was no evidence of microvascular injury or thromboembolic events. Autopsy heart samples from subjects with metastatic carcinoma and an inherited neurodegenerative disease with similar tissue procurement times were included as negative controls.

SARS-CoV-2 spike and nucleocapsid RNA was detected within the myocardium of each COVID-19 myocarditis subject. Viral transcripts were located in cytoplasmic and perinuclear locations within cells that were morphologically consistent with cardiomyocytes (**Figure 2.1B**). Viral transcripts were also present lung airway epithelial cells and rare myocardial adipocytes and pericytes (**Figure 2.2**). Immunostaining for the SARS-CoV-2 nucleocapsid protein showed presence of viral protein in cardiomyocytes (**Figure 2.1C**). The immune cell infiltrate was characterized by accumulation of an admixture of CCR2⁻ and CCR2⁺ macrophages (**Figure 2.1D**). Minimal T-cell infiltration was noted (**Figure 2.1E**). Macrophage abundance was highest in areas of cardiomyocyte injury as depicted by complement deposition (C4d staining, Spearman $r = 0.86$, $p = 0.0005$), a pathological marker of cardiomyocyte cell death¹⁴⁻¹⁶ (**Figure 2.2**). These observations suggest that SARS-CoV-2 can infect the human heart and may contribute to cardiomyocyte cell death and myocardial inflammation.

2.3.2 SARS-CoV-2 Tropism in the Human Heart

ACE2 serves as a cell-surface receptor for SARS-CoV-2 through interactions with the spike protein^{17,18}. Consistent with prior reports, we detected ACE2 mRNA expression in the human heart across the spectrum of age increasing in heart failure^{19,20}. ACE2 mRNA was expressed in cardiomyocytes with significant variation in ACE2 protein expression between individual

cardiomyocytes. hPSC-derived cardiomyocytes and EHTs expressed ACE2 mRNA and protein (**Figure 2.3 and Figure 2.4**).

To determine the susceptibility of different myocardial cell types to SARS-CoV-2 infection, we inoculated combinations of hPSC-derived cardiomyocytes, fibroblasts, and macrophages with wild-type SARS-CoV-2 (USA_WA1/2019). We analyzed tissue culture supernatants for production of infectious virus and measured intracellular viral RNA transcript levels at 3 days post-inoculation. These assays revealed production of infectious virus (**Figure 2.5A**) and viral RNA (**Figure 2.5B**) in cultures that contained hPSC-derived cardiomyocytes. Cultures lacking hPSC-derived cardiomyocytes contained viral loads that were equivalent to media-only controls.

To verify cardiomyocyte selective tropism, we inoculated human cardiac stromal populations with a recombinant SARS-CoV-2 clone containing a NeonGreen fluorescent reporter (SARS-CoV-2-NeonGreen)¹³. NeonGreen is expressed from a viral subgenomic RNA, indicative of active viral replication. Primary human cardiac fibroblasts, endothelial cells, and macrophages were not permissive to SARS-CoV-2 infection (**Figure 2.5, Figure 2.6, Figure 2.7**). hPSC-derived endothelial cells and cardiac fibroblasts were also not susceptible to infection. In contrast, 2 independent lines of hPSC-derived cardiomyocytes were permissive to SARS-CoV-2 infection. Undifferentiated hPSC lines did not show evidence of infection (**Figure 2.7**). hPSC-derived cardiomyocyte infection showed rapid production of infectious virus with peak titers on day 3 post-inoculation (**Figure 2.5C**).

We examined the relationship between viral replication and cell death. NeonGreen-positive cardiomyocytes peaked at day 3 post-inoculation. hPSC-derived cardiomyocyte cell death was

observed beginning 4 to 5 days post-inoculation (**Figure 2.5D**) indicating that viral infection precedes cell death. SARS-CoV-2-infected cardiomyocytes displayed characteristics of cytopathic effect, cellular rounding, clumping, and syncytium formation. Distortion of cellular morphology was evident by day 4 post-inoculation and cultures contained largely dead cells and debris by days 5 to 6 post-inoculation (**Figure 2.5E**).

To examine whether cardiomyocytes are a target of SARS-CoV-2 in a simulated cardiac environment, we infected 2-dimensional tissues assembled with hPSC-derived cardiomyocytes (80%), fibroblasts (10%), and macrophages (10%) with SARS-CoV-2-NeonGreen. Flow cytometry performed 3 days following infection revealed NeonGreen expression only in CD90⁺CD14⁺TNNT2⁺ cardiomyocytes. NeonGreen was not detected in CD90⁺ fibroblasts or CD14⁺ macrophages (**Figures 2.5F, G** and **Figure 2.8**). Transmission electron microscopy of 2-dimensional tissues performed 3 days post-inoculation showed the presence of coronavirus particles within infected hPSC-derived cardiomyocytes. Micrographs revealed structural features of coronaviruses including the presence of a trilaminar envelope and characteristic cross-sections through the nucleocapsid (**Figure 2.5H**)^{21,22}. Virions were identified within perinuclear endosomal-like structures of hPSC-derived cardiomyocytes. We observed various stages of virion assembly including budding from intracellular membranes. Virions were not detected in mock-infected cardiomyocytes.

2.3.3 RNA Sequencing Identified Robust Viral Transcription and Activation of Innate Immune Responses

To examine viral transcription and the host immune response to SARS-CoV-2 infection, we performed RNA sequencing. Cultures containing either hPSC-derived cardiomyocytes,

fibroblasts, or macrophages were either mock-infected or inoculated with SARS-CoV-2. We also examined 2-dimensional tissues assembled with 80% cardiomyocytes, 10% fibroblasts, and 10% macrophages. Cells and tissues were harvested on day 3 post-inoculation. Multidimensionality reduction analysis revealed separation between experimental groups consistent with their distinct cellular composition (**Figure 2.9A**). Infected hPSC-derived cardiomyocytes and 2-dimensional tissues contained abundant viral genomic and subgenomic RNAs identified based on the presence of 5' leader sequences (**Figure 2.9B** and **Figure 2.10**)²³.

Numerous host genes were differentially regulated upon SARS-CoV-2 infection in each of the examined cell types and 2-dimensional tissues (**Figure 2.9C**). Conditions that supported viral replication (hPSC-derived cardiomyocytes and 2-dimensional tissues) displayed the greatest overlap in differentially expressed genes. Cell types that did not support viral replication (fibroblasts and macrophages) also showed differentially expressed host genes (**Figure 2.9D**), suggesting that SARS-CoV-2 virions stimulate host gene expression in the absence of direct viral infection. Pathway analysis revealed that infected hPSC-derived cardiomyocytes and 2-dimensional co-culture tissues showed upregulation of genes associated with immune cell activation, stress-induced transcription, and responses to viral pathogens. Genes associated with muscle contraction, metabolism, oxidative phosphorylation, and mitochondrial function were downregulated (**Figure 2.9E, F**). Host genes differentially expressed in macrophages and fibroblasts were associated with pathways involved in innate immune cell activation, migration, and cytokine responses (**Figure 2.9G, H**).

Specific genes downregulated in infected hPSC-derived cardiomyocytes and 2-dimensional tissues (**Figure 2.9I**) included components of the electron transport chain (adenosine

triphosphate synthase, mitochondrial cytochrome C oxidase, and nicotinamide adenine dinucleotide phosphate dehydrogenase) and metabolic enzymes (glycerol-3-phosphate dehydrogenase, pyruvate dehydrogenase, and succinate dehydrogenase complex). *PDK4*, an inhibitor of pyruvate dehydrogenase, was upregulated in infected hPSC-derived cardiomyocytes and 2-dimensional tissues. Components of the contractile apparatus including cardiac actin, troponins, myosin light and heavy chains, desmin, phospholamban, and calsequestrin were downregulated in infected 2-dimensional tissues. *ACE2* expression was diminished in infected cardiomyocytes and 2-dimensional tissues. Infected hPSC-derived cardiomyocytes and 2-dimensional tissues displayed upregulation of innate immune mediators including *IFNB1* and interferon (IFN)-stimulated genes (*IFIT1*, *IFIT2*, *IFIT3*, *ISG15*, *MX1*, and *OAS1*), early response genes (*FOS*), and cytokines (*TNF*). Consistent with a greater innate immune response in 2-dimensional tissues, several chemokines (*CCL3*, *CCL4*, *CCL7*, *CCL8*, and *CXCL8*) and cytokines (*IL1B*, *IL6*, and *CSF3*) were selectively upregulated in infected 2-dimensional tissues. Macrophages and fibroblasts contributed to enhanced chemokine and cytokine expression in 2-dimensional tissues. *CCL3*, *CCL4*, and *CCL8* were selectively expressed in infected macrophages and *CSF3*, *CXCL8*, *IL1B*, and *IL6* were induced in infected fibroblasts (Figure 2.10).

2.3.4 SARS-CoV-2 Entry Into Cardiomyocytes Is Mediated by ACE2 and Endosomal Cysteine Proteases

A neutralizing human ACE2 (viral receptor) antibody abrogated SARS-CoV-2–NeonGreen infectivity as measured by NeonGreen-positivity and viral RNA extracted from the supernatant of infected cultures. The extent of blockade was comparable to treatment

with remdesivir, a potent inhibitor of the SARS-CoV-2 RNA-dependent RNA polymerase (**Figure 2.11**)²⁴⁻²⁶. After binding to ACE2, the spike protein must undergo proteolytic activation to initiate membrane fusion²⁷. Host proteases located at the plasma membrane (TMPRSS2) or within endosomes (cathepsins) most commonly perform this function. The relative contributions of each of these protease families to SARS-CoV-2 infection varies by cell type^{17,27}. hPSC-derived cardiomyocytes express multiple endosomal proteases including cathepsins and calpains. Low levels of transmembrane protease, serine 2 (TMPRSS2) mRNA were detected in hPSC-derived cardiomyocytes, but not in fibroblasts or macrophages (**Figure 2.11**). To determine whether SARS-CoV-2 enters cardiomyocytes through an endosomal or plasma membrane route, we inoculated hPSC-derived cardiomyocytes with SARS-CoV-2–NeonGreen and administered either the endosomal cysteine protease inhibitor E-64, which blocks cathepsins, or the serine protease inhibitor camostat mesylate, which blocks TMPRSS2 (and possibly TMPRSS4)²⁷. E-64 abolished SARS-CoV-2 infection of hPSC-derived cardiomyocytes as shown by reduced NeonGreen expression and viral RNA within the supernatant. Camostat had no effect on cardiomyocyte infection over a range of doses that significantly affect SARS-CoV-2 infection of lung-derived cell lines where TMPRSS2 mediates viral entry¹⁷. Laboratory cultivated SARS-CoV-2 stocks have acquired a mutation in the furin cleavage site, which alters the preference for proteases (TMPRSS2 vs. cathepsins) that mediate SARS-CoV-2 entry²⁷⁻²⁹. To assess the impact this mutation on cardiomyocyte infectivity and entry, we inoculated hPSC-derived cardiomyocytes with either wild-type SARS-CoV-2 or recombinant SARS-CoV-2 containing the furin cleavage site mutation (Δ PRRA). Both viruses readily infected cardiomyocytes through an endosomal-dependent mechanism (**Figure 2.11**).

2.3.5 EHTs Model COVID-19 Myocarditis

To examine whether SARS-CoV-2 infection of EHTs mimics aspects of COVID-19 myocarditis, we generated EHTs containing hPSC-derived cardiomyocytes, fibroblasts, and macrophages. EHTs were seeded in a collagen-Matrigel matrix between 2 PDMS posts, infected with SARS-CoV-2, and harvested 5 days after inoculation. Hematoxylin and eosin staining revealed increased interstitial cell abundance within the periphery of SARS-CoV-2–infected EHTs (**Figure 2.12A**). Immunostaining for the viral nucleocapsid protein demonstrated evidence of infected cardiomyocytes at the periphery of the tissue, possibly representing limited diffusion of the virus in the EHT environment. CD68 immunostaining showed macrophage accumulation corresponding to sites of viral infection (**Figure 2.12B**, **Figure 2.13**). Infected EHTs accumulated high levels of viral RNA (**Figure 2.12C**). In situ hybridization for viral spike sense and antisense RNA indicated active viral replication within EHTs (**Figure 2.12D**, **Figure 2.10**).

As reduced LV systolic function has been reported in severe cases of COVID-19 myocarditis, we examined the effect of SARS-CoV-2 infection on EHT contractility³⁰. We calculated the average peak displacement and velocity for each spontaneously contracting tissue. EHTs consisting of hPSC-derived cardiomyocytes and fibroblasts were inoculated with SARS-CoV-2, and contractile function analyzed daily. SARS-CoV-2–inoculated tissues showed reduced contraction, speed of contraction, and relaxation relative to the mock-infected tissues (**Figure 2.12E-G**).

To examine whether cardiomyocyte cell death might serve as a mechanism explaining reduced EHT contractility, we performed terminal deoxynucleotidyl transferase dUTP nick end labelling (TUNEL) staining and observed increased numbers of TUNEL-positive cardiomyocytes

in SARS-CoV-2–infected EHTs on day 5 post infection (**Figure 2.14A, B**). Our RNA sequencing data suggested that other mechanisms also may contribute to reduced EHT contractility, including sarcomere structure, metabolism, and/or host immune responses (**Figure 2.9I**). Immunostaining of hPSC-derived cardiomyocytes infected with SARS-CoV-2 revealed evidence of sarcomere loss 3 days following infection (**Figure 2.15C**), a time point that preceded cell death. Immunostaining of EHTs showed reduced troponin T expression in infected cardiomyocytes (**Figure 2.14D, E**).

We then examined the mechanistic relationship between cardiomyocyte infection, inflammatory signaling, sarcomere loss, and cell death. Inhibition of viral entry (ACE2 neutralizing antibody) or viral replication (remdesivir) was sufficient to prevent type I IFN and tumor necrosis factor (TNF) expression following SARS-CoV-2 infection (**Figure 2.14F, G**). Remdesivir similarly reduced inflammatory gene expression in 3-dimensional EHTs (**Figure 2.15**), establishing that viral infection represents the upstream driver of inflammation in our model system.

To examine the impact of cardiomyocyte inflammatory signaling on cell death, sarcomere gene expression, and sarcomere structure, we focused on inhibiting viral nucleic acid sensing in 2-dimensional cultures given their amenability to flow cytometry and high-resolution imaging. TANK-binding kinase 1 (TBK1) is an essential mediator of nucleic acid sensing pathways including RIG-I, MAVS, STING, and TLRs^{31,32}. Inhibition of TBK1 activity reduced type I IFN activity (inflammatory signature in infected cardiomyocytes) (**Figure 2.9I**) without impacting viral load, cardiomyocyte infectivity, or cell death (**Figure 2.14F-I**). While TBK1 inhibition prevented reductions in TNNT2 and MYH7 mRNA expression following SARS-CoV-2 infection,

sarcomere breakdown remained prevalent. In contrast, remdesivir prevented both reductions in TNNT2 and MYH7 mRNA expression and sarcomere loss following SARS-CoV-2 infection (**Figure 2.14J, K**, and **Figure 2.11**). These data indicate that sarcomeric disassembly and cardiomyocyte cell death are the result of cardiomyocyte infection and not inflammation in the EHT system.

2.4 Discussion

Whether cardiac manifestations of COVID-19 are a result of viral infection, systemic inflammation, and/or microvascular thrombosis remains a debated topic. We examined myocardial specimens obtained from individuals with severe COVID-19 myocarditis and revealed evidence of cardiomyocyte infection, cell death, and macrophage infiltration. These findings are consistent with prior reports highlighting infiltration of monocytes, lymphocytes, and plasma cells in an endomyocardial biopsy specimen from a patient with suspected COVID-19 myocarditis and viral RNA within the myocardium of COVID-19 autopsy specimens^{33,34}. The specimens examined in this study differ substantially from published autopsy series, which did not include subjects with cardiac manifestations^{3,35}. Here, we exclusively focused on subjects with COVID-19 infection and severe myocarditis based on echocardiography and clinical presentation.

We further provide evidence that SARS-CoV-2 infects and replicates within human cardiomyocytes. SARS-CoV-2 was unable to replicate in cardiac fibroblasts, endothelial cells, and macrophages. It remains possible that SARS-CoV-2 could also infect other cardiac cell types that are difficult to isolate from the human heart such as pericytes and endocardial cells. Despite these limitations, our findings clearly show that cardiomyocytes are a target of SARS-CoV-2 infection.

To gain insights into the mechanistic basis of cardiomyocyte infection and myocarditis, we developed a human EHT system that recapitulates features of SARS-CoV-2–induced myocarditis. We provide evidence that SARS-CoV-2 infects hPSC-derived cardiomyocytes, resulting in reduced metabolic and contractile apparatus gene expression, sarcomeric disassembly, inflammatory signaling, and cell death. Viral entry was ACE2-dependent and relied on endosomal cysteine protease activity. Our findings are consistent with a recent report suggesting that SARS-CoV-2 infects human cardiac slices, hPSC-derived cardiomyocytes in an ACE2 and cathepsin-dependent manner, and impacts the beating of cardiospheres³⁶. We extend these observations to show that cardiomyocytes supported viral replication, rapidly produced infectious virions, activated type I IFN signaling, and displayed cytopathic features seen with coronavirus infection. Infected EHTs showed reduced contractile force, sarcomere disassembly, and pathological evidence of myocarditis including macrophage activation.

Extrapulmonary cell types are susceptible to SARS-CoV-2 infection^{37–39}. This broader cellular tropism is dictated by ACE2 expression and the ability of the virus to gain access to extrapulmonary tissues. Whether SARS-CoV-2 enters the heart through hematological seeding and/or direct extension from the pleural cavity remains unknown. Among myocardial cell types, cardiomyocytes and pericytes express ACE2 mRNA¹⁹. Cardiac fibroblasts and vascular smooth muscle cells may also express ACE2²⁰. We showed that ACE2 is preferentially expressed in cardiomyocytes and is essential for SARS-CoV-2 to infect cardiomyocytes. It remains to be explored whether cardiomyocyte maturation or remodeling impact vulnerability to viral infection. This possibility is supported by the heterogeneous expression of ACE2 in the human heart and

may explain why pre-existing cardiovascular disease represents a strong risk factor for COVID-19 mortality. Consistent with this idea, ACE2 expression is increased in heart failure^{30,40}.

EHTs provided an opportunity to gain insights into the relationship between cardiomyocyte infection, myocardial inflammation, and contractile dysfunction. Infection of EHTs resulted in inflammatory mediator generation, decreased ACE2 expression, cardiomyocyte cell death, sarcomere breakdown, and reduced sarcomeric and metabolic gene expression. Each of these mechanisms likely contributes to diminished EHT contractility. We showed that cardiomyocyte infection triggers inflammatory gene expression, sarcomere loss, and cell death. Blockade of viral nucleic acid sensing pathways did not prevent sarcomere disassembly or cardiomyocyte cell death. Despite the limitations of the inherent immaturity of hPSC-derived cardiomyocytes and incomplete representation of human myocardial cell types included in EHTs, these findings highlight the central role of cardiomyocyte infection and suggest that targeting viral cell entry, replication, or sarcomere breakdown may improve outcomes in patients with cardiac complications of COVID-19. The relevance of ACE2 downregulation in infected cardiomyocytes will require further clarification as *Ace2*^{-/-} mice display LV systolic dysfunction and heart failure⁴¹.

2.4.1 Study Limitations

While our findings implicate that SARS-CoV-2 cardiomyocyte infection likely contributes to myocardial dysfunction, our findings do not exclude an important role for inflammation or microthrombi in COVID-19 cardiac pathology. Macrophages and fibroblasts likely contribute to the inflammatory response. Despite resistance to SARS-CoV-2 infection, macrophages and fibroblasts generated inflammatory mediators when exposed to SARS-CoV-2. This response could be a result of direct recognition of viral RNAs and proteins or communication with infected

cardiomyocytes through production of soluble mediators or intercellular transfer via gap junctions. Future studies are necessary to dissect the cellular mechanisms and signaling pathways that initiate and convey the adverse impact of myocardial inflammation.

2.5 Conclusions

This study provides evidence that cardiomyocytes are a target of SARS-CoV-2 in the human heart and support the conclusion that SARS-CoV-2 infection of cardiomyocytes and resultant myocardial injury and inflammation contribute to the cardiac manifestations of COVID-19. We show that SARS-CoV-2 infection of 2-dimensional cultures and EHTs results in reductions in cardiac contractility through sarcomere breakdown, disruption of metabolic gene expression, and cardiomyocyte death. Collectively, these findings show that SARS-CoV-2 can productively infect human cardiomyocytes and establish an experimentally tractable platform for mechanistic and therapeutic investigation of COVID-19 myocardial pathology.

2.6 Methods

Biosafety. All aspects of this study were approved by the office of Environmental Health and Safety at Washington University School of Medicine prior to the initiation of this study. Work with SARS-CoV-2 was performed in a BSL-3 laboratory by personnel equipped with powered air purifying respirators (PAPR).

Viruses. The 2019n-CoV/USA_WA1/2019 isolate of SARS-CoV-2 was obtained from the United States Centers for Disease Control (CDC). The NeonGreen SARS-CoV-2 virus was published recently ⁴². The Δ PRRA and accompanying WT SARS-CoV-2 strains were generated from infectious clones by PYS and confirmed by deep sequencing. Infectious stocks were grown

by inoculating Vero cells and collecting supernatant upon observation of cytopathic effect. Debris was removed by centrifugation and passage through a 0.22 μm filter. Supernatant was then aliquoted and stored at -80°C . All infections were performed at a multiplicity of infection (MOI) of 0.1. The NeonGreen SARS-CoV-2 virus stock used in this study was subjected to deep sequencing using ARTIC ⁴³ and found to have a mutation in the furin cleavage site (positions 23606-23608 of NC_045512.2) at a combined frequency of 31%.

Focus forming assay. Vero E6 cells were seeded at a density of 4×10^4 cells per well in flat-bottom 96-well tissue culture plates. The following day, media was removed and replaced with 100 μL of 10-fold serial dilutions of the material to be titered. Two hours later, 135 μL of methylcellulose overlay was added. Plates were incubated for 48 h, then fixed with 4% paraformaldehyde (final concentration) in phosphate-buffered saline for 20 min, followed by permeabilization with saponin-containing buffer. Plates were incubated overnight at 4°C in 100 μL of permeabilization buffer containing 1 $\mu\text{g}/\text{mL}$ of the CR3022 anti-spike monoclonal antibody ⁴⁴. Following washing, 50 μL of goat anti-human secondary antibody conjugated to HRP (Sigma AP504P), diluted 1:1000 in permeabilization buffer, was added for 2 hours at room temperature with shaking. Foci were stained with 50 μL of KPL Trueblue (SeraCare), then scanned and automatically quantitated on a Biospot plate reader (Cellular Technology Limited).

Quantitative RT-PCR. RNA was extracted using the MagMax mirVana Total RNA isolation kit (Thermo Scientific) on the Kingfisher Flex extraction robot (Thermo Scientific). RNA was reverse transcribed and amplified using the TaqMan RNA-to-CT 1-Step Kit (ThermoFisher). Reverse transcription was carried out at 48°C for 15 min followed by 2 min at 95°C . Amplification was accomplished over 50 cycles as follows: 95°C for 15 s and 60°C for 1 min. Copies of SARS-

CoV-2 N gene RNA in samples were determined using a previously published assay⁴⁵. Briefly, a TaqMan assay was designed to target a highly conserved region of the N gene (Forward primer: ATGCTGCAATCGTGCTACAA; Reverse primer: GACTGCCGCCTCTGCTC; Probe: /56-FAM/TCAAGGAAC/ZEN/AACATTGCCAA/3IABkFQ/). This region was included in an RNA standard to allow for copy number determination down to 10 copies per reaction. The reaction mixture contained final concentrations of primers and probe of 500 and 100 nM, respectively. For host genes (ACE2, TMPRSS2, OAS1, MX1, TNF), RNA was reverse-transcribed using the High Capacity cDNA Reverse Transcription Kit (ThermoFisher) and amplified using SYBR Green system (ThermoFisher) with beta2 microglobulin as an internal reference gene.

Quantification of ACE2 expression in RNA-Seq. We performed a differential gene expression analysis using R package DESeq2⁴⁶ on the Care4DCM cohort⁴⁷. The DESeq2 package utilizes negative binomial distribution to model the distribution of RNA-Seq reads, and uses Wald test to calculate p-values⁴⁶. The Care4DCM cohort included 60 DCM patients and 35 controls⁴⁷. Of the 60 DCM patients, 52 received Angiotensin I converting enzyme inhibitors and 8 received Angiotensin II receptor blockers. The myocardial biopsies were extracted from the LV apex by heart catheterization and preserved in liquid nitrogen following standardized protocols. The RNA was extracted from the cardiac tissues using Allprep Kits (Qiagen, Düsseldorf, Germany), then the RNA sequencing was carried out using the TrueSeq RNA Sample Prep Kit (Illumina, San Diego, California, USA)⁴⁷.

Human atrial tissue samples. The study protocol involving human tissue samples was approved by the ethics committees of the Medical Faculty of Heidelberg University (Germany; S-017/2013). Written informed consent was obtained from all patients and the study was conducted

in accordance with the Declaration of Helsinki. Tissue samples of right atrial appendages (RAA) were obtained from patients undergoing open heart surgery for coronary artery bypass grafting or valve repair /replacement in the local heart surgery department.

Atrial and ventricular cardiomyocyte isolation. After excision, tissue samples were immediately placed into preoxygenated transport solution (100 mM NaCl, 10 mM KCl, 1.2 mM KH₂PO₄, 5 mM MgSO₄, 50 mM taurine, 5 mM 3-[N-morpholino] propane sulfonic acid [MOPS], 30 mM 2,3-butanedione monoxime (BDM) and 20 mM glucose, pH 7.0 with NaOH) and subjected to cardiomyocyte isolation within 15 minutes. RAA tissue samples were dissected into small pieces and rinsed 3 times in Ca²⁺-free Tyrode's solution (100 mM NaCl, 10 mM KCl, 1.2 mM KH₂PO₄, 5 mM MgSO₄, 50 mM taurine, 5 mM MOPS, and 20 mM glucose, pH 7.0 with NaOH) supplemented with 2,3-butanedione monoxime (30 mM BDM; Sigma-Aldrich, St. Louis, MO, USA). The solutions were oxygenated with 100% O₂ at 37°C. After digestion with collagenase type I (288 U/ml; Worthington) and protease type XXIV (5 mg/ml; Sigma-Aldrich) for 15 min and agitation in protease-free solution for another 35 min, the cell suspension was filtered through a 200 nm mesh. Subsequently the Ca²⁺ concentration of the cell fraction was increased to 0.2 mM, the cell suspension was centrifuged and calcium tolerant rod-shaped single cardiomyocytes were declared as the cardiomyocyte fraction (CM). Remaining tissue chunks were declared as the non-cardiomyocyte (NM) fraction. Cells were stored in TRIzol-Reagent (ThermoFisher) at -20°C. Isolation of total RNA was performed, using TRIzol-Reagent (ThermoFisher) and frozen tissue samples were processed according to the manufacturer's protocol. Synthesis of single-stranded cDNA was carried out with the Maxima First Strand cDNA Synthesis Kit (ThermoFisher), using 3 µg of total RNA per 20 µl reaction. For quantitative real-time PCR (qPCR) 10 µl reactions,

consisting of 0.5 μ l cDNA, 5 μ l TaqMan Fast Universal Master Mix (ThermoFisher), and 0.5 μ l 6-carboxyfluorescein (FAM)-labeled TaqMan probes and primers (TaqMan Gene Expression Assays; ThermoFisher) were analyzed using the StepOnePlus (Applied Biosystems, Foster City, CA, USA) PCR system. hACE2 primers and probes (Hs01085333_m1) were purchased from ThermoFisher. The glyceraldehyde 3-phosphate dehydrogenase housekeeping gene (GAPDH: Hs99999905_m1) was used for normalization. All RT-qPCR reactions were performed as triplicates and control experiments in the absence of cDNA were included. Means of triplicates were used for the $2^{-\Delta\text{Ct}}$ calculation, where $2^{-\Delta\text{Ct}}$ corresponds to the ratio of mRNA expression versus GAPDH.

Flow cytometry. Cells were dissociated to single-cell suspension with 0.25% trypsin (Gibco), then washed and incubated with Zombie-violet viability stain (Biolegend) at a dilution of 1:500 in 100 μ L of PBS at room temperature. In some assays, antibodies against surface proteins were incubated with the cells. Fibroblasts were identified using anti-CD90 PE (Biolegend, catalog number 328110) and macrophages were identified using anti-CD14 APC (Biolegend, catalog number 367118). Cells then were fixed with 4% paraformaldehyde (final concentration) in phosphate-buffered saline for 20 min and analyzed on the MACSQuant 10 (Miltenyi Biotec) or the LSRFortessa X20 (Becton Dickinson Biosciences). Analysis was performed using FlowJo 10.6.1 (Becton Dickinson & Co).

hPSC culture and cardiomyocyte differentiation. The parent stem cell line, BJFF.6, was generated from the human BJ fibroblast line (ATCC, catalog number: CRL-2522) by the Genome Engineering and iPSC Center at Washington University in St. Louis. This parent cell line has no known mutations associated with heart disease and the stem cells are pluripotent as assessed by

immunofluorescence staining⁴⁸. Differentiation to hPSC-derived cardiomyocytes was performed as previously described⁴⁸. Briefly, stem cells were maintained in feeder-free culture and differentiation was initiated by temporal manipulation of WNT signaling^{49,50}. hPSC-derived CMs were enriched using metabolic selection⁵¹, yielding >90% cardiomyocytes⁴⁸. All experiments were conducted at least 30 days after the initiation of differentiation.

Differentiation (and validation) of stem cell derived cardiac fibroblasts. hPSC derived cardiac fibroblasts were differentiated using the method of Zhang et al.⁵². Briefly, differentiation was initiated by directing the BJFF stem cell line towards a mesoderm/cardiac progenitor lineage by the activation and subsequent inhibition of WNT signaling using CHIR-99021 and IWP2 respectively. These cells were then directed to become proepicardial cells by the addition of retinoic acid and WNT CHIR 99021 followed by TGF β inhibition (SB431542, Tocris Bioscience 1614). Finally, the pro-epicardial cells were directed to become quiescent cardiac fibroblasts by the addition of FGF2 and higher levels of TGF β inhibition. Derivation of hPSC-cardiac fibroblasts was validated by measuring gene expression using RT-PCR. They showed high levels of both cardiac specific genes, GATA4 and TCF21 as well as general fibroblast genes COL1A1 and DDR2 (Fig. S1c).

Fibroblast culture. BJ fibroblasts (ATCC, catalog number: CRL-2522) were cultured in Eagle's Minimum Essential Medium with 10% FBS and 1% Pen-Strep (Gibco, catalog number: 15140122). Human ventricular cardiac fibroblasts that were harvested from normal adult ventricular tissue were obtained from Lonza, maintained at low passage number (<12), and cultured according to the manufacturer's recommendations in FGM-3 growth media.

Macrophage culture. CD34⁺ cells isolated from human cord blood were cultured in Iscove's Modified Dulbecco's Medium with 10% FBS, 1% Pen-Strep, and 10 ng/mL of human macrophage colony stimulating factor (M-CSF, R&D Systems, catalog number 216-MC) for at least 10 days to generate mature macrophages before use in experiments.

Endothelial cell culture. H1 hPSCs were differentiated into vascular endothelial cells following the published protocol⁵³. Arterial endothelium was identified as CD34⁺CD184⁺CD73⁺ cells using appropriate antibodies (BD Biosciences, anti-CD34 PE-Cy7 [cat # 560710], anti-CD184 APC [cat #560936], anti-CD73 PE [cat #550257]) and isolated by flow cytometric cell sorting on a BD FACSAriaII. These cells were cultured in StemPro-34 serum free media (ThermoFisher, cat# 10639011).

Isolation of primary human cardiac endothelial cells and macrophages. Human myocardium was dissected into ~200 mg pieces and digested in 3mL DMEM containing 250U/mL collagenase IV, 60 U/mL hyaluronidase and 60 U/mL DNaseI for 45 minutes at 37°C. Following digest and red blood cell lysis, the resultant single cell suspension was incubated with anti-CD14 PE (cat #301806), anti-CD64 PE-Cy7 (cat #305022), anti-CD45 FITC (cat #304006), and anti-CD31 BV421 (cat #303124) (all antibodies from Biolegend). Macrophages were identified as CD14⁺CD64⁺CD45⁺ cells and endothelial cells were identified as CD31⁺CD64⁻CD45⁻ cells. Cells were isolated by flow cytometric cell sorting on a BD FACSMelody and cultured in StemPro-34 supplemented with either M-CSF or VEGF (R&D Systems, cat #293-VE).

Two-dimensional cell cultures and tissues. hPSC-derived cardiomyocytes, fibroblasts, and/or macrophages were dissociated from two-dimensional cultures using 0.25% Trypsin-EDTA, resuspended in media containing RPMI-1640 with 20% FBS and 10 μM Y-27632 and plated on

gelatin coated tissue culture dishes. After 48 hours, the media was changed to DMEM High glucose (4 mg/mL), 10% FBS, 1% non-essential amino acids, 1% GlutaMAX Supplement, and 1% Pen-Strep. All drug compounds were purchased from Selleckchem (ruxolitinib, catalog number S8932; MRT67307, catalog number S7948; E-64, catalog number S7379; camostat, catalog number S2874) and resuspended to a stock concentration of 10 μ M in PBS or DMSO (depending on the solubility profile), then diluted to working concentration in culture media (described above) and sterile-filtered.

Immunostaining of hPSC-derived cardiomyocytes and confocal fluorescence microscopy. Immunostaining was performed as previously described with a few modifications⁴⁸. Briefly, cardiomyocytes were fixed for 20 minutes in 4% formaldehyde in phosphate buffered saline (PBS). Cells were then permeabilized with 0.4% Triton X-100 for 20 minutes at room temperature. The cells were blocked for 1 hour using a blocking solution containing 3% bovine serum albumin, 5% donkey serum, 0.1% Triton X-100, and 0.02% sodium azide in PBS. Primary antibodies (rabbit anti Troponin T, 1:400, Abcam, ab45932) were added for 1-2 hours at room temperature or overnight at 4°C. Cells were then washed with PBS before incubating for 1 hour in secondary antibody (Cy3 donkey anti-rabbit, Jackson Immunoresearch, 711165152). 4',6-diamidino-2-phenylindole (DAPI) was used at a 1:50000 dilution to stain for nuclei. Cells were visualized using a Nikon A1Rsi confocal microscope (Washington University Center for Cellular Imaging). Z-stacks of cells with 40x magnification were recorded in sequential scanning mode. Images were processed in ImageJ and Z-stacks were converted to standard deviation projections

⁵⁴.

Engineered heart tissues (EHTs). EHTs were prepared according to a published protocol⁵⁵ with modifications. Casting molds for tissue formation were prepared using PDMS at a 1:25 ratio. 1 mL of PDMS was poured into each well of a 24-well plate and a Teflon spacer (EHT Technologies GmbH; Hamburg, Germany) was placed inside to generate a well. The PDMS was degassed under high vacuum and baked overnight at 65°C. The Teflon spacers were removed using ethanol.

Prior to use, the casting molds were sterilized with ethanol, dried with nitrogen gas, and placed under UV light for 10-15 min. 1% pluronic-F127 in PBS was added to the molds for 20 min to block the surface from adhering to the seeded tissues. The pluronic was removed, the casting molds were rinsed twice with PBS, and then dried. Silicone racks consisting of two pairs of PDMS posts (EHT Technologies GmbH, Hamburg, Germany) were positioned such that each pair of PDMS posts fit within one casting mold.

The procedure for seeding of tissues was modified from⁵⁵. Working on ice, rat collagen-I (1 mg/mL final concentration) was combined with equal parts 2x DMEM containing FBS and neutralized with sodium hydroxide. Growth factor reduced Matrigel (Corning, catalog number: 354230) was added to a final concentration of 0.77 g/mL. hPSC-derived CMs, fibroblasts, and/or macrophages were dissociated from two-dimensional cultures with 0.25% Trypsin-EDTA and the Trypsin was quenched in RPMI-1640 with 20% FBS media containing 10 g/mL of DNaseI. Cells were then centrifuged, resuspended in media containing RPMI-1640 with 20% FBS and 10 μ M Y-27632, and combined with the collagen/Matrigel mixture. Each tissue contained 10⁶ hPSC-derived CMs, 5% fibroblasts, and 10% macrophages. Tissues were seeded in the casting molds with the silicone racks in a 100 μ L volume. After polymerizing around the silicone racks for 2 h at 37°C,

the tissues were covered overnight with RPMI-1640 containing 20% FBS. The tissues, attached to the posts of the silicone racks, then were moved out of the casting molds and transferred into media containing DMEM High glucose (4 mg/mL), 10% FBS, 1% non-essential amino acids, 1% GlutaMAX Supplement, and 1% Pen-Strep. Consistent with previous reports, engineered heart tissue contraction was observed ~2-5 days after seeding, and the displacement increased over time as the tissues organize and mature⁵⁵. By day 7 post seeding, all tissues generated at least 0.025 mm of displacement (see details below). EHTs were inoculated with SARS-CoV-2 at least 7 days after tissue seeding, and EHT contraction and morphology were measured daily throughout the course of the experiment.

Analysis of engineered heart tissue contractility. EHTs between two PDMS posts were visualized on an EVOS microscope and videos of spontaneously contracting posts were recorded at 30 frames per second using an iPhone with built-in camera (**Videos 1 and 2**). We used the 2 mm diameter of the caps on the posts to calibrate the pixels per mm for each video. We wrote a custom script in MATLAB to calculate the displacement of the posts as a function of time. Automated tracking was done using the computer vision toolbox and the displacement was calculated as a function of time. A second order polynomial spline fit was applied to remove any drift in the camera position. Traces were smoothed using a Savitsky-Golay filter and peaks in the displacement were identified using the findpeaks algorithm. The average and standard deviation of the displacement was then calculated for each ~60 sec video. The time for force development was defined as the time required to achieve 75% activation and the time for relaxation was defined as the time to relax to 75% of the peak activation.

Histology of autopsy and engineered heart tissues. Tissues were fixed with 10% NBF for 7 days, embedded in 1% agar, mounted in cassettes, and embedded in paraffin. Target markers were visualized using Opal 4-Color Manual IHC Kit (Perkin-Elmer) with the following changes: 1) 10% NBF fixation step was substituted for treatment with 10% MeOH + 10% hydrogen peroxide in water for 20 min; 2) during antigen retrieval, the vessel with AR6 was brought to boiling and slides were immediately transferred into deionized water; 3) blocking buffer was substituted for 10% FBS in TBST. Primary antibodies against human sarcomeric actin (Sigma A2127), human Troponin T (ThermoFisher MS-295-P1), human CD68 (BioRad MCA5709), human ACE2 (Abcam ab15348), human Ki67 (Abcam ab16667), human CCR2 (Abcam ab176390), SARS-CoV-2-N (Sino Biological 40143-R001) were used. Cell death was assessed using TUNEL staining from *In Situ* Cell Death Detection Kit (Roche) with Opal-based costain for sarcomeric actin as described above. Viral RNA was directly visualized with RNAscope Multiplex Fluorescent Reagent Kit v2 Assay (Advanced Cell Diagnostics) and RNAscope 2.5 HD Detection Reagent - RED (Advanced Cell Diagnostics) using positive-strand and negative strand probes for ORF1ab. Images were collected on a confocal microscope (Zeiss LSM 700 Laser Scanning Confocal) and processed using ZenBlack (Zeiss) and ImageJ (NCBI). Troponin staining was quantified using manual cell tracing in ImageJ (NCBI) from at least three areas and 30 cells analyzed per tissue.

Electron microscopy. Cells grown on aclar coverslips were briefly rinsed in 0.15 M cacodylate buffer that was warmed to 37°C followed by the addition of 2.5% glutaraldehyde, 2% paraformaldehyde, 0.2% tannic acid in 0.15 M cacodylate buffer with 2 mM CaCl₂, pH 7.4 at 37°C. Once added, the coverslips were returned to a 37°C incubator for 15 min followed by

overnight fixation at room temperature. Post fixation, samples were rinsed in 0.15 M cacodylate buffer 4 times for 15 min each followed by a secondary fixation in 1% OsO₄/1.5% K₃Fe(CN)₆ in 0.15 M cacodylate buffer for 1.5 h in the dark. The coverslips were then rinsed 4 times in ultrapure water for 15 min each followed by *en bloc* staining with 2% aqueous uranyl acetate overnight at 4°C in the dark. After another 4 water washes, the samples were dehydrated in a graded ethanol series (30%, 50%, 70%, 90%, 100% x4) for 10 min for each step. Once dehydrated, cells were infiltrated with LX112 resin over a period of 2 days. The coverslips then were flat embedded and polymerized at 60°C for 48 h. Once polymerized, the aclar coverslips were peeled away from the resin, and small areas were excised and mounted perpendicularly on a blank epoxy stub for cross sectioning. 70 nm sections were then cut and imaged on a TEM (JEOL JEM-1400 Plus) at 120 KeV.

RNA sequencing and analysis. Samples were prepared according to library kit manufacturer's protocol, indexed, pooled, and sequenced on an Illumina NovaSeq 6000. Basecalls and demultiplexing were performed with Illumina's bcl2fastq software and a custom python demultiplexing program with a maximum of one mismatch in the indexing read. RNA-seq reads were then aligned to the Human Ensembl GRCh38.76 primary assembly and SARS-CoV-2 NCBI NC_045512 Wuhan-Hu-1 genome with STAR version 2.5.1a⁵⁶. Gene counts were derived from the number of uniquely aligned unambiguous reads by Subread:featureCount version 1.4.6-p5⁵⁷. Isoform expression of known Ensembl transcripts were estimated with Salmon version 0.8.2⁵⁸. Sequencing performance was assessed for the total number of aligned reads, total number of uniquely aligned reads, and features detected. The ribosomal fraction, known junction saturation, and read distribution over known gene models were quantified with RSeQC version 2.6.2⁵⁹.

All gene counts were imported into the R/Bioconductor package EdgeR ⁶⁰ and TMM normalization size factors were calculated to adjust for samples for differences in library size. Ribosomal genes and genes not expressed in at least four samples greater than one count-per-million were excluded from further analysis. The TMM size factors and the matrix of counts were then imported into the R/Bioconductor package Limma ⁶¹. Weighted likelihoods based on the observed mean-variance relationship of every gene and sample were then calculated for all samples with the `voomWithQualityWeights` ⁶². The performance of all genes was assessed with plots of the residual standard deviation of every gene to their average log-count with a robustly fitted trend line of the residuals. Differential expression analysis was then performed to analyze for differences between conditions and the results were filtered for only those genes with Benjamini-Hochberg false-discovery rate adjusted p-values less than or equal to 0.05.

For each contrast extracted with Limma, global perturbations in known Gene Ontology (GO) terms, MSigDb, and KEGG pathways were detected using the R/Bioconductor package GAGE ⁶³ to test for changes in expression of the reported log 2 fold-changes reported by Limma in each term versus the background log 2 fold-changes of all genes found outside the respective term. The R/Bioconductor package heatmap3 ⁶⁴ was used to display heatmaps across groups of samples for each GO or MSigDb term with a Benjamini-Hochberg false-discovery rate adjusted p-value less than or equal to 0.05. Perturbed KEGG pathways where the observed log 2 fold-changes of genes within the term were significantly perturbed in a single-direction versus background or in any direction compared to other genes within a given term with p-values less than or equal to 0.05 were rendered as annotated KEGG graphs with the R/Bioconductor package Pathview ⁶⁵.

To find the most critical genes, the raw counts were variance stabilized with the R/Bioconductor package DESeq2 ⁴⁶ and then analyzed via weighted gene correlation network analysis with the R/Bioconductor package WGCNA ⁶⁶. Briefly, all genes were correlated across each other by Pearson correlations and clustered by expression similarity into unsigned modules using a power threshold empirically determined from the data. An eigengene was created for each *de novo* cluster and its expression profile was then correlated across all coefficients of the model matrix. Because these clusters of genes were created by expression profile rather than known functional similarity, the clustered modules were given the names of random colors where grey is the only module that has any pre-existing definition of containing genes that do not cluster well with others. These *de novo* clustered genes were then tested for functional enrichment of known GO terms with hypergeometric tests available in the R/Bioconductor package clusterProfiler ⁶⁷. Significant terms with Benjamini-Hochberg adjusted p-values less than 0.05 were then collapsed by similarity into clusterProfiler category network plots to display the most significant terms for each module of hub genes in order to interpolate the function of each significant module. The information for all clustered genes for each module were combined with their respective statistical significance results from Limma to identify differentially expressed genes.

Statistical analysis. Statistical tests were chosen based on accepted standards. The Kolmogorov-Smirnov test was used to test for normality. Parametric (t-test) and non-parametric (Mann-Whitney test) statistical methods were used when appropriate. Statistical significance was assigned when *P* values were < 0.05 using Prism Version 8 (GraphPad). Specific tests are indicated in the figure legends. Mean values and median values are displayed for parametric tests and nonparametric tests, respectively.

2.7 References

1. Madjid, M., Safavi-Naeini, P., Solomon, S. D. & Vardeny, O. Potential Effects of Coronaviruses on the Cardiovascular System: A Review. *JAMA Cardiology* **5**, 831–840 (2020).
2. Zhou, F. *et al.* Clinical course and risk factors for mortality of adult inpatients with COVID-19 in Wuhan, China: a retrospective cohort study. *The Lancet* **395**, 1054–1062 (2020).
3. Lindner, D. *et al.* Association of Cardiac Infection With SARS-CoV-2 in Confirmed COVID-19 Autopsy Cases. *JAMA Cardiology* (2020) doi:10.1001/jamacardio.2020.3551.
4. Bhatla, A. *et al.* COVID-19 and cardiac arrhythmias. *Heart Rhythm* **17**, 1439–1444 (2020).
5. Huang, L. *et al.* Cardiac Involvement in Patients Recovered From COVID-2019 Identified Using Magnetic Resonance Imaging. *JACC: Cardiovascular Imaging* **13**, 2330–2339 (2020).
6. Puntmann, V. O. *et al.* Outcomes of Cardiovascular Magnetic Resonance Imaging in Patients Recently Recovered From Coronavirus Disease 2019 (COVID-19). *JAMA Cardiology* (2020) doi:10.1001/jamacardio.2020.3557.
7. Daniels, C. J. *et al.* Prevalence of Clinical and Subclinical Myocarditis in Competitive Athletes With Recent SARS-CoV-2 Infection: Results From the Big Ten COVID-19 Cardiac Registry. *JAMA Cardiology* **6**, 1078–1087 (2021).
8. Tersalvi, G. *et al.* Elevated Troponin in Patients With Coronavirus Disease 2019: Possible Mechanisms. *Journal of Cardiac Failure* **26**, 470–475 (2020).
9. Cleary, S. J. *et al.* Animal models of mechanisms of SARS-CoV-2 infection and COVID-19 pathology. *British Journal of Pharmacology* **177**, 4851–4865 (2020).
10. Letko, M., Marzi, A. & Munster, V. Functional assessment of cell entry and receptor usage for SARS-CoV-2 and other lineage B betacoronaviruses. *Nature Microbiology* **5**, 562–569 (2020).
11. Wan, Y., Shang, J., Graham, R., Baric, R. S. & Li, F. Receptor recognition by the novel coronavirus from Wuhan: an analysis based on decade-long structural studies of SARS coronavirus. *Journal of virology* **94**, e00127-20 (2020).
12. Abe, M. & Oshima, R. G. A single human keratin 18 gene is expressed in diverse epithelial cells of transgenic mice. *The Journal of cell biology* **111**, 1197–1206 (1990).
13. Xie, X. *et al.* An Infectious cDNA Clone of SARS-CoV-2. *Cell Host & Microbe* **27**, 841–848.e3 (2020).
14. Michaud, K. *et al.* Diagnosis of myocardial infarction at autopsy: AECVP reappraisal in the light of the current clinical classification. *Virchows Arch* **476**, 179–194 (2020).
15. Sabatasso, S. *et al.* Early markers for myocardial ischemia and sudden cardiac death. *Int J Legal Med* **130**, 1265–1280 (2016).

16. Multiplex quantitative imaging of human myocardial infarction by mass spectrometry-immunohistochemistry | SpringerLink. <https://link-springer-com.beckerproxy.wustl.edu/article/10.1007/s00414-018-1813-9>.
17. Hoffmann, M. *et al.* SARS-CoV-2 Cell Entry Depends on ACE2 and TMPRSS2 and Is Blocked by a Clinically Proven Protease Inhibitor. *Cell* **181**, 271-280.e8 (2020).
18. Bao, L. *et al.* The pathogenicity of SARS-CoV-2 in hACE2 transgenic mice. *Nature* **583**, 830–833 (2020).
19. Chen, L., Li, X., Chen, M., Feng, Y. & Xiong, C. The ACE2 expression in human heart indicates new potential mechanism of heart injury among patients infected with SARS-CoV-2. *Cardiovascular Research* **116**, 1097–1100 (2020).
20. Tucker, N. R. *et al.* Myocyte-Specific Upregulation of ACE2 in Cardiovascular Disease. *Circulation* **142**, 708–710 (2020).
21. Goldsmith, C. S. *et al.* Ultrastructural Characterization of SARS Coronavirus. *Emerg Infect Dis* **10**, 320–326 (2004).
22. Goldsmith, C. S., Miller, S. E., Martines, R. B., Bullock, H. A. & Zaki, S. R. Electron microscopy of SARS-CoV-2: a challenging task. *The Lancet* **395**, e99 (2020).
23. Kim, D. *et al.* The Architecture of SARS-CoV-2 Transcriptome. *Cell* **181**, 914-921.e10 (2020).
24. Gordon, C. J. *et al.* Remdesivir is a direct-acting antiviral that inhibits RNA-dependent RNA polymerase from severe acute respiratory syndrome coronavirus 2 with high potency. *Journal of Biological Chemistry* **295**, 6785–6797 (2020).
25. Yin, W. *et al.* Structural basis for inhibition of the RNA-dependent RNA polymerase from SARS-CoV-2 by remdesivir. *Science* **368**, 1499–1504 (2020).
26. Agostini, M. L. *et al.* Coronavirus susceptibility to the antiviral remdesivir (GS-5734) is mediated by the viral polymerase and the proofreading exoribonuclease. *MBio* **9**, e00221-18 (2018).
27. Simmons, G., Zmora, P., Gierer, S., Heurich, A. & Pöhlmann, S. Proteolytic activation of the SARS-coronavirus spike protein: Cutting enzymes at the cutting edge of antiviral research. *Antiviral Research* **100**, 605–614 (2013).
28. Hoffmann, M., Kleine-Weber, H. & Pöhlmann, S. A Multibasic Cleavage Site in the Spike Protein of SARS-CoV-2 Is Essential for Infection of Human Lung Cells. *Molecular Cell* **78**, 779-784.e5 (2020).
29. Johnson, B. A. *et al.* Loss of furin cleavage site attenuates SARS-CoV-2 pathogenesis. *Nature* **591**, 293–299 (2021).
30. Hu, H. & Fang, F. M. X. W. Y. Coronavirus fulminant myocarditis saved with glucocorticoid and human immunoglobulin ;European Heart Journal ;Oxford Academic.
31. Zhou, R., Zhang, Q. & Xu, P. TBK1, a central kinase in innate immune sensing of nucleic acids and beyond. *Acta Biochimica et Biophysica Sinica* **52**, 757–767 (2020).

32. Bartok, E. & Hartmann, G. Immune Sensing Mechanisms that Discriminate Self from Altered Self and Foreign Nucleic Acids. *Immunity* **53**, 54–77 (2020).
33. Tavazzi, G. *et al.* Myocardial localization of coronavirus in COVID-19 cardiogenic shock. *European Journal of Heart Failure* **22**, 911–915 (2020).
34. Puelles, V. G. *et al.* Multiorgan and Renal Tropism of SARS-CoV-2. *New England Journal of Medicine* **383**, 590–592 (2020).
35. Basso, C. *et al.* Pathological features of COVID-19-associated myocardial injury: a multicentre cardiovascular pathology study. *European Heart Journal* **41**, 3827–3835 (2020).
36. Bojkova, D. *et al.* SARS-CoV-2 infects and induces cytotoxic effects in human cardiomyocytes. *Cardiovascular Research* (2020) doi:10.1093/cvr/cvaa267.
37. Lamers, M. M. *et al.* SARS-CoV-2 productively infects human gut enterocytes. *Science* **369**, 50–54 (2020).
38. Monteil, V. *et al.* Inhibition of SARS-CoV-2 Infections in Engineered Human Tissues Using Clinical-Grade Soluble Human ACE2. *Cell* **181**, 905-913.e7 (2020).
39. Yang, L. *et al.* A Human Pluripotent Stem Cell-based Platform to Study SARS-CoV-2 Tropism and Model Virus Infection in Human Cells and Organoids. *Cell Stem Cell* **27**, 125-136.e7 (2020).
40. Bos, J. M. *et al.* Marked Up-Regulation of ACE2 in Hearts of Patients With Obstructive Hypertrophic Cardiomyopathy: Implications for SARS-CoV-2–Mediated COVID-19. *Mayo Clinic Proceedings* **95**, 1354–1368 (2020).
41. Crackower, M. A. *et al.* Angiotensin-converting enzyme 2 is an essential regulator of heart function. *Nature* **417**, 822–828 (2002).
42. Xie, X. *et al.* An Infectious cDNA Clone of SARS-CoV-2. *Cell Host Microbe* **27**, 841-848.e3 (2020).
43. Pipelines, D. *et al.* COVID-19 ARTIC v3 Illumina library construction and sequencing protocol v4 (protocols.io.bgxjxxkn). doi:10.17504/protocols.io.bgxjxxkn.
44. ter Meulen, J. *et al.* Human monoclonal antibody combination against SARS coronavirus: synergy and coverage of escape mutants. *PLoS Med.* **3**, e237 (2006).
45. Case, J. B., Bailey, A. L., Kim, A. S., Chen, R. E. & Diamond, M. S. Growth, detection, quantification, and inactivation of SARS-CoV-2. *Virology* **548**, 39–48 (2020).
46. Love, M. I., Huber, W. & Anders, S. Moderated estimation of fold change and dispersion for RNA-seq data with DESeq2. *Genome Biol.* **15**, 550 (2014).
47. Meder, B. *et al.* Epigenome-Wide Association Study Identifies Cardiac Gene Patterning and a Novel Class of Biomarkers for Heart Failure. *Circulation* **136**, 1528–1544 (2017).
48. Clippinger, S. R. *et al.* Disrupted mechanobiology links the molecular and cellular phenotypes in familial dilated cardiomyopathy. *Proc. Natl. Acad. Sci. U.S.A.* **116**, 17831–17840 (2019).

49. Lian, X. *et al.* Robust cardiomyocyte differentiation from human pluripotent stem cells via temporal modulation of canonical Wnt signaling. *Proc. Natl. Acad. Sci. U.S.A.* **109**, E1848–1857 (2012).
50. Lian, X. *et al.* Directed cardiomyocyte differentiation from human pluripotent stem cells by modulating Wnt/ β -catenin signaling under fully defined conditions. *Nat Protoc* **8**, 162–175 (2013).
51. Sharma, A. *et al.* Derivation of highly purified cardiomyocytes from human induced pluripotent stem cells using small molecule-modulated differentiation and subsequent glucose starvation. *J Vis Exp* (2015) doi:10.3791/52628.
52. Zhang, H. *et al.* Generation of Quiescent Cardiac Fibroblasts From Human Induced Pluripotent Stem Cells for In Vitro Modeling of Cardiac Fibrosis. *Circ. Res.* **125**, 552–566 (2019).
53. Dege, C. & Sturgeon, C. M. Directed Differentiation of Primitive and Definitive Hematopoietic Progenitors from Human Pluripotent Stem Cells. *J Vis Exp* (2017) doi:10.3791/55196.
54. Schindelin, J. *et al.* Fiji: an open-source platform for biological-image analysis. *Nat. Methods* **9**, 676–682 (2012).
55. Breckwoldt, K. *et al.* Differentiation of cardiomyocytes and generation of human engineered heart tissue. *Nat Protoc* **12**, 1177–1197 (2017).
56. Dobin, A. *et al.* STAR: ultrafast universal RNA-seq aligner. *Bioinformatics* **29**, 15–21 (2013).
57. Liao, Y., Smyth, G. K. & Shi, W. featureCounts: an efficient general purpose program for assigning sequence reads to genomic features. *Bioinformatics* **30**, 923–930 (2014).
58. Patro, R., Duggal, G., Love, M. I., Irizarry, R. A. & Kingsford, C. Salmon provides fast and bias-aware quantification of transcript expression. *Nat. Methods* **14**, 417–419 (2017).
59. Wang, L., Wang, S. & Li, W. RSeQC: quality control of RNA-seq experiments. *Bioinformatics* **28**, 2184–2185 (2012).
60. Robinson, M. D., McCarthy, D. J. & Smyth, G. K. edgeR: a Bioconductor package for differential expression analysis of digital gene expression data. *Bioinformatics* **26**, 139–140 (2010).
61. Ritchie, M. E. *et al.* limma powers differential expression analyses for RNA-sequencing and microarray studies. *Nucleic Acids Res.* **43**, e47 (2015).
62. Liu, R. *et al.* Why weight? Modelling sample and observational level variability improves power in RNA-seq analyses. *Nucleic Acids Res.* **43**, e97 (2015).
63. Luo, W., Friedman, M. S., Shedden, K., Hankenson, K. D. & Woolf, P. J. GAGE: generally applicable gene set enrichment for pathway analysis. *BMC Bioinformatics* **10**, 161 (2009).
64. Zhao, S., Guo, Y., Sheng, Q. & Shyr, Y. Advanced heat map and clustering analysis using heatmap3. *Biomed Res Int* **2014**, 986048 (2014).

65. Luo, W. & Brouwer, C. Pathview: an R/Bioconductor package for pathway-based data integration and visualization. *Bioinformatics* **29**, 1830–1831 (2013).
66. Langfelder, P. & Horvath, S. WGCNA: an R package for weighted correlation network analysis. *BMC Bioinformatics* **9**, 559 (2008).
67. Yu, G., Wang, L.-G., Han, Y. & He, Q.-Y. clusterProfiler: an R package for comparing biological themes among gene clusters. *OMICS* **16**, 284–287 (2012).

Table 2.1. Control and COVID-19 myocarditis patient demographic data

	Age (yrs)	Sex	Race	ARDS	Co-morbidities	ECG findings	Coronary angiography	Trop I (ng/ml)	Echo findings	Cause of death
Control 1 autopsy	59	F	C	-	-	NSR			EF 65%	ovarian cancer
Control 2 autopsy	19	M	C	-	-	NSR			EF 55%	genetic neurologic disorder
Case 1 Autopsy Hosp day 4	61	M	H	yes	-	ST-segment elevation	no obstructive disease	7.457	global EF<30%	cardiac arrest
Case 2 Autopsy Hosp day 8	54	M	C	yes	-	bradycardia AV block	not performed	10.94	global EF 45%	cardiac arrest
Case 3 EMBx Hosp day 3	62	F	H	yes	-	ST-segment elevation	no obstructive disease	37.77	global EF 30%	cardiac arrest
Case 4 EMBx Hosp day 1	22	F	H	yes	postpartum obesity	ST-segment elevation	no obstructive disease	6.49	global EF 40-45%	survived

AV: atrioventricular, C: Caucasian, EF: ejection fraction, EMBx: endomyocardial biopsy, F: female, H: Hispanic, LV: left ventricular, M: male. All subjects were diagnosed with COVID-19 by nasopharyngeal swab PCR. Day of autopsy or EMBx relative to COVID-19 diagnosis is provided in column 1. Case 2: postmortem coronary evaluation revealed no evidence of thrombosis or atherosclerotic coronary artery disease.

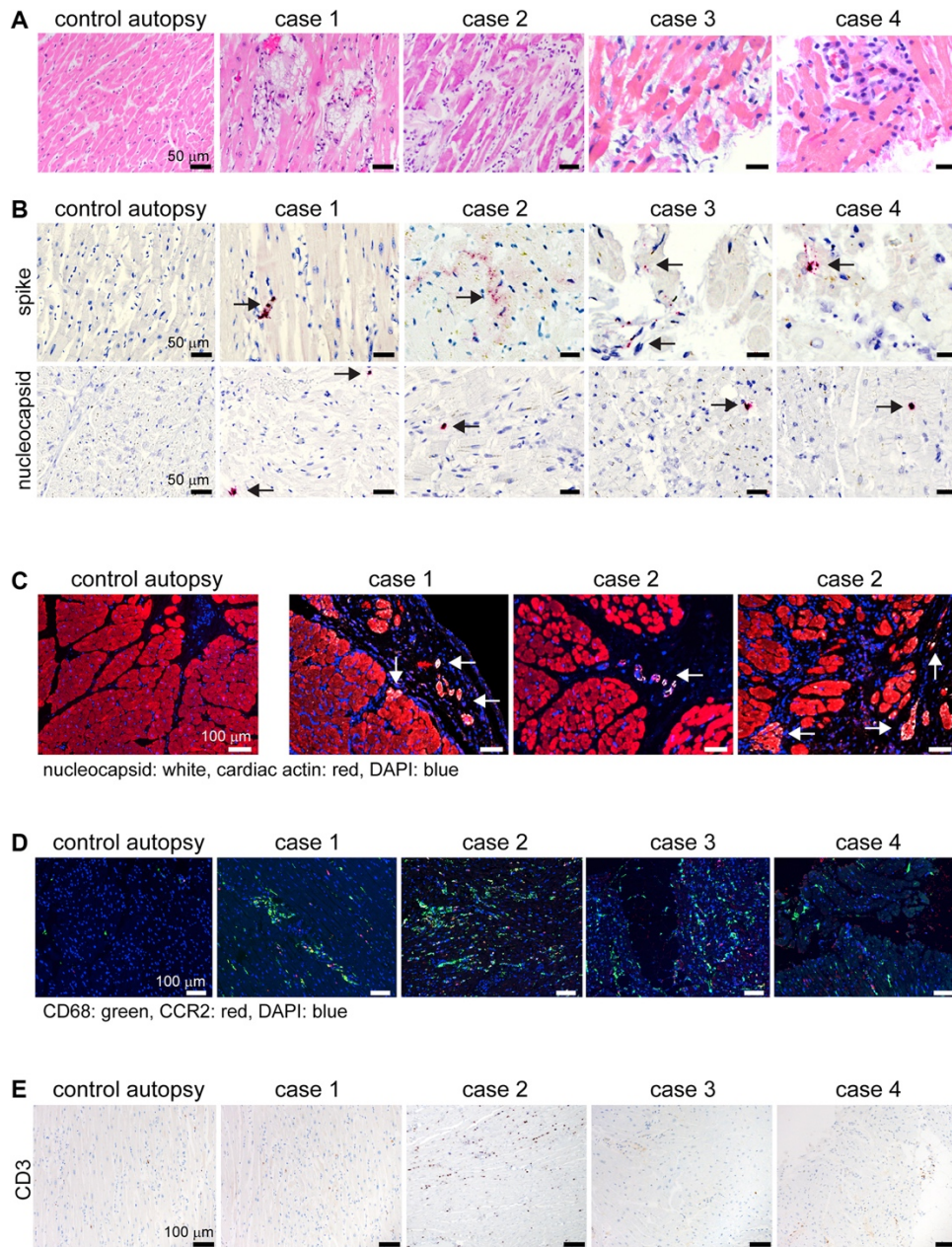


Figure 2.1. Specimens From Patients With Severe COVID-19 Myocarditis Show Evidence of SARS-CoV-2 Cardiomyocyte Infection (A) Hematoxylin and eosin staining of cardiac autopsy (anterior left ventricular wall) and biopsy samples (right ventricular septum) from subjects without coronavirus disease-2019 (COVID-19) (control case) and patients with severe COVID-19 myocarditis (case 1-4). (B) In situ hybridization for severe acute respiratory syndrome-coronavirus-2 (SARS-CoV-2) spike and nucleocapsid RNA (red). Hematoxylin: blue. The arrows denote viral RNA staining in cells with cardiomyocyte morphology. (C) Immunostaining of control and COVID-19 myocarditis cardiac autopsy tissue for SARS-CoV-2 nucleocapsid (white) and cardiac actin (red). DAPI: blue. The arrows denote nucleocapsid staining in cardiomyocytes. (D) Immunostaining of control and COVID-19 myocarditis specimens for CD68 (green) and CCR2 (red). DAPI: blue. (E) Immunostaining of control and COVID-19 myocarditis tissue for CD3 (brown). Hematoxylin: blue. DAPI = 4',6-diamidino-2-phenylindole.

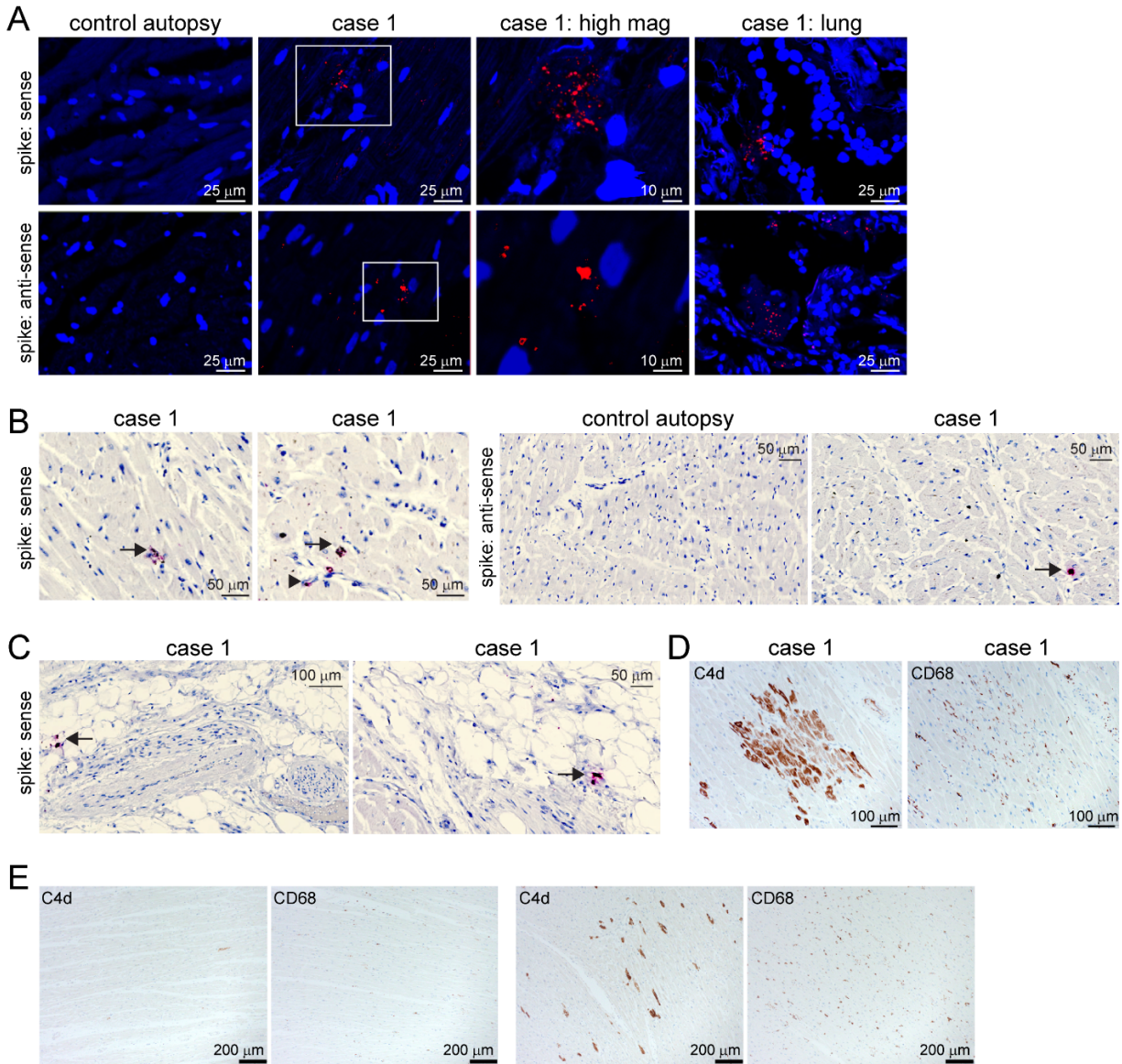


Figure 2.2. *In situ* hybridization for SARS-CoV-2 RNA in cardiac autopsy specimens. **A**, *in situ* hybridization of cardiac autopsy and lung autopsy tissue for SARS-CoV-2 spike RNA showing evidence of viral infection. Red: spike RNA probes, Blue: DAPI. **B**, *In situ* hybridization of cardiac autopsy for SARS-CoV-2 (red) in control and COVID-19 myocarditis autopsy tissue. Staining is present within cardiomyocytes found in the COVID-19 myocarditis specimen (arrow). Arrowhead indicates spike staining in perivascular cells. No staining was evident in the control cases. Blue: hematoxylin. **C**, Spike sense probe staining (red) in epicardial adipose tissue. Staining (arrows) is present in perivascular adipocyte tissue. Blue: hematoxylin. **D-E**, Immunostaining of COVID-19 myocarditis cardiac autopsy tissue for C4d (brown) and CD68 (brown). Corresponding areas from serial sections are shown.

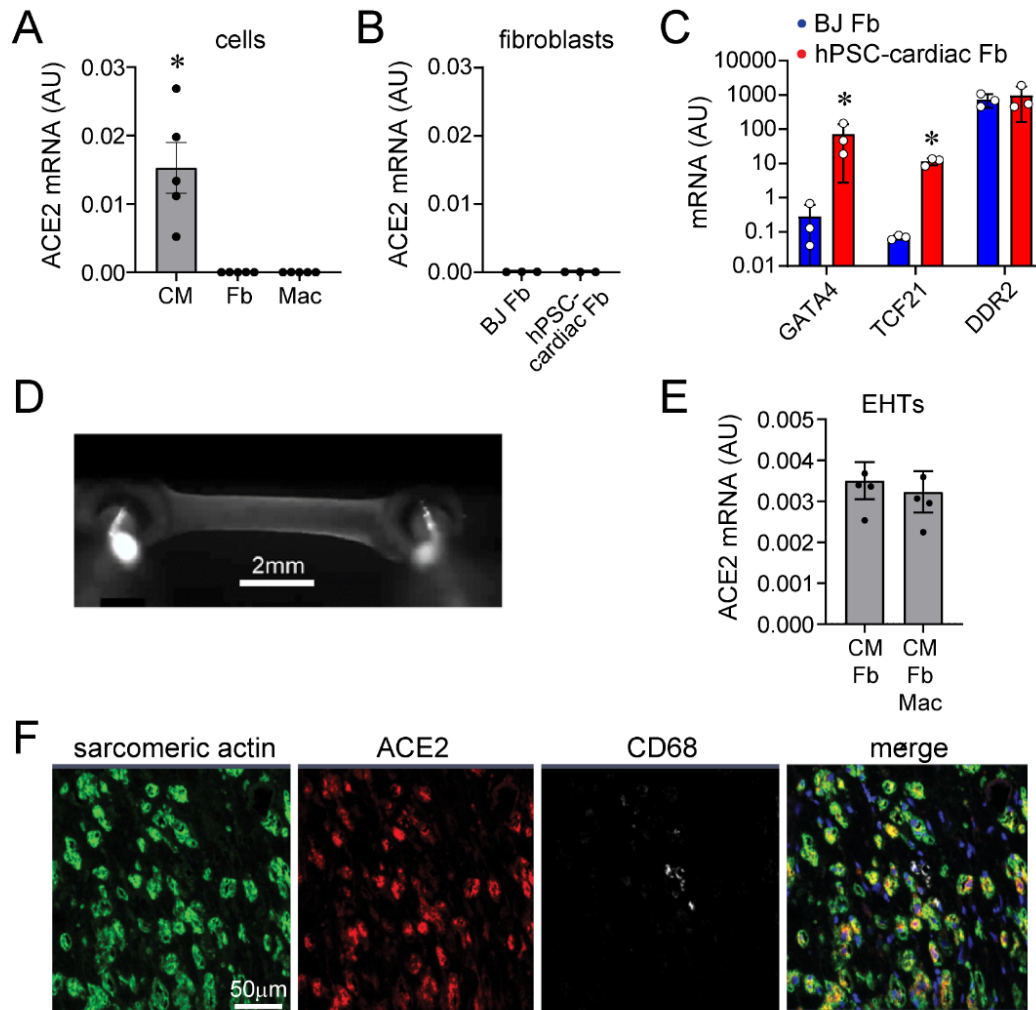


Figure 2.3. ACE2 expression and infectivity of hPSC-derived cells in human engineered heart tissues. **A**, Quantitative RT-PCR measurements showing *ACE2* mRNA expression in hPSC-derived cardiomyocytes (CM). *ACE2* was not detected in human fetal cord blood-derived macrophages (Mac) or dermal fibroblasts (Fb). Each data point represents an independent experiment (n=5) and error bars denote standard error of the mean. **B**, *ACE2* was not detectable in hPSC-derived cardiac fibroblasts or BJ dermal fibroblasts. Each data point represents an independent experiment (n=3). **C**, Quantitative RT-PCR showing marked enrichment of *GATA4* and *TCF21* mRNA expression in hPSC-derived cardiac fibroblasts compared to BJ fibroblasts. Both fibroblast populations express *DDR2*. Data is presented on a log₁₀ scale. Each data point represents an independent experiment (n=5), bar height corresponds to the mean value, and error bars denote standard deviation. * denotes p<0.05 compared to BJ fibroblasts (t-test). **D**, Human engineered heart tissue formed between two deformable PDMS posts. When the tissue contracts, it displaces the posts. **E**, Quantitative RT-PCR measurements of *ACE2* mRNA expression in engineered heart tissues (EHTs). Data points indicate individual samples (n=4). Bars denote the mean value and error bars reflect standard error of the mean. **F**, Immunohistochemistry of EHTs demonstrating *ACE2* expression (red) in hPSC-derived cardiomyocytes (green, sarcomeric actin). Macrophages (white, CD68). DAPI: blue. Representative image from 7 analyzed specimens.

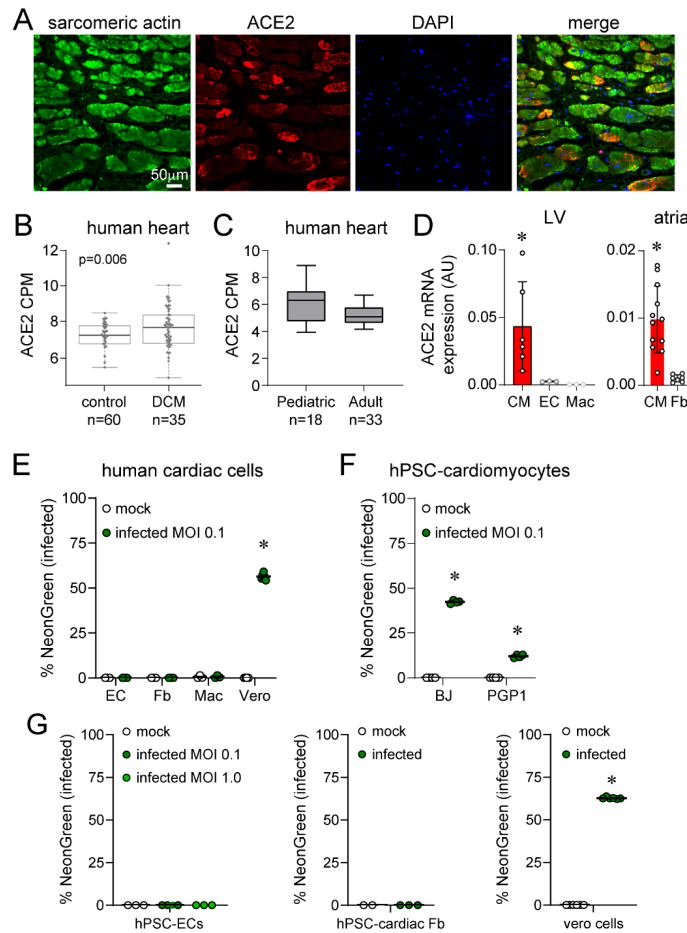


Figure 2.4: ACE2 is expressed in the human heart and in stem cell derived cardiomyocytes. **A**, Immunohistochemistry of human heart tissue showing ACE2 (red) expression in cardiomyocytes (green, sarcomeric actin). Representative images from 5 analyzed specimens. **B**, RNA sequencing demonstrating ACE2 mRNA expression in myocardial biopsies obtained from adult controls and heart failure patients. Data is displayed as counts per million (CPM). Box and whisker plot, p-value represents t-test. **C**, RNA sequencing demonstrating ACE2 mRNA expression in adult and pediatric heart tissue. Data are displayed as counts per million (CPM). Box and whisker plot. **D**, Quantitative RT-PCR measurements showing ACE2 mRNA expression in human primary left ventricular (LV) cardiomyocytes (CM), endothelial cell (EC), macrophages (Mac), atrial cardiomyocytes, and atrial fibroblasts (Fb). Error bars denote standard error of the mean. * $p < 0.05$ compared to atrial fibroblasts (t-test). **E**, Inoculation of primary human endothelial cells (EC), fibroblasts (Fb), and macrophages (Mac) with mock (black) or SARS2-CoV-2-NeonGreen (green, MOI 0.1). Vero cells are included as a positive control. Data is presented as the percent of live cells that express NeonGreen indicating infection. Each data point represents cells isolated from an individual patient sample. * $p < 0.05$ compared to mock infection (t-test). **F**, Inoculation of 2 different hPSC-derived cardiomyocyte lines (BJ, PGP1) with mock (black) or SARS2-CoV-2-NeonGreen (green, MOI 0.1). * $p < 0.05$ compared to mock infection (t-test). **G**, Inoculation of hPSC-derived endothelial cells (EC) and hPSC-derived cardiac fibroblasts with mock (black) or SARS2-CoV-2-NeonGreen (green, MOI 0.1, 1.0). Vero cells are included as a positive control. Each data point represents biological replicates and bars denote mean values. * $p < 0.05$ compared to mock infection (t-test).

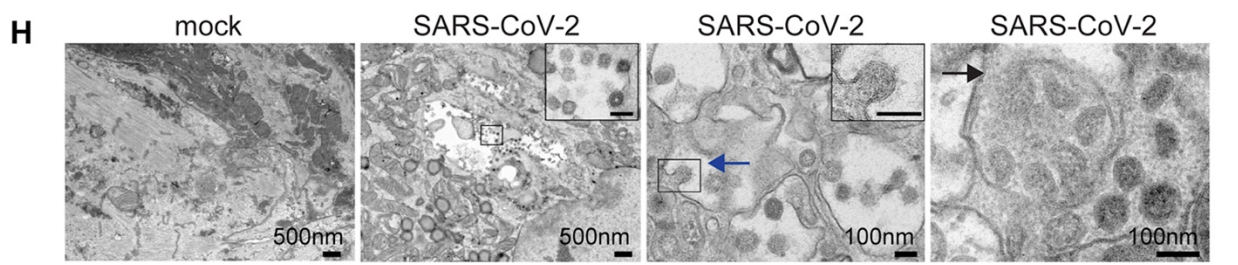
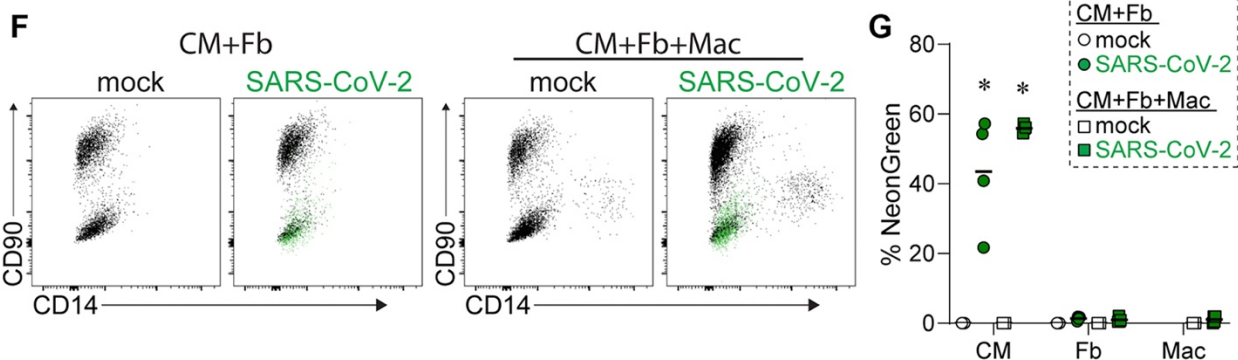
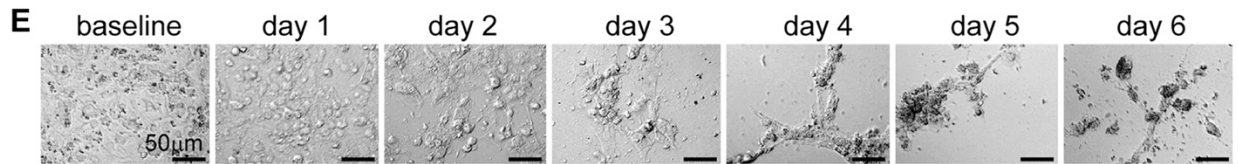
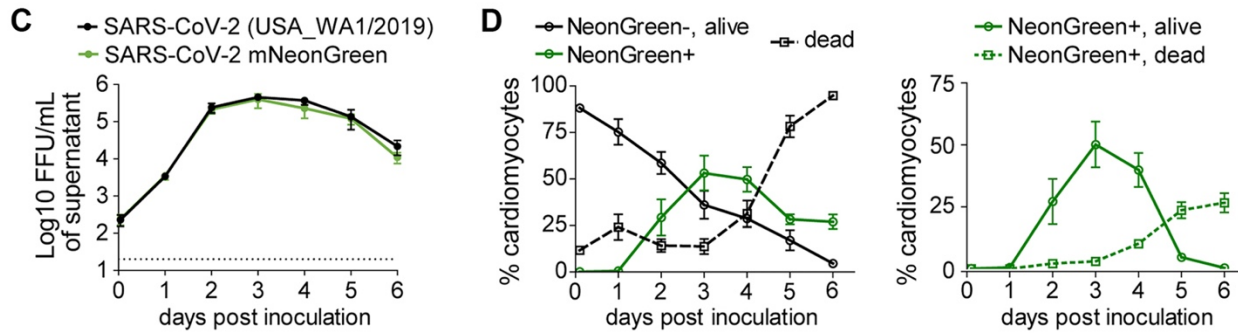
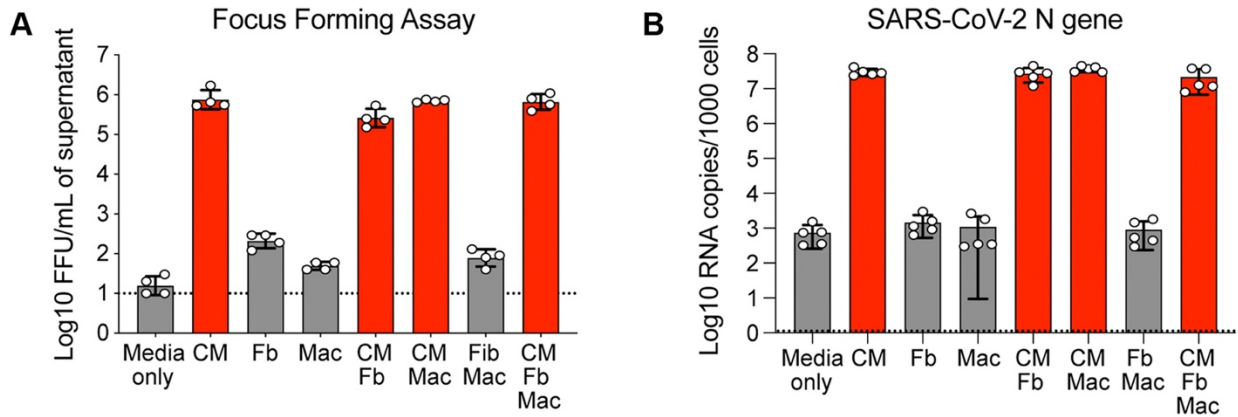


Figure 2.5. SARS-CoV-2 Infects Cardiomyocytes (A) Focus-forming assay measuring production of infectious virus from human pluripotent stem cell (hPSC)-derived cardiomyocytes (CM), fibroblasts (Fb), and macrophages (Mac) inoculated with SARS-CoV-2 (multiplicity of infection [MOI], 0.1). Media only denotes wells that contain no cells. Assays were performed 3 days following inoculation. **Dashed line** indicates limit of assay detection. (B) Quantitative real-time polymerase chain reaction (RT-PCR) showing viral N-gene copies in cultures containing CM, Fb, and Macs inoculated with SARS-CoV-2 (MOI 0.1). RNA was collected 3 days post-inoculation (n = 5 per group). (C) Focus-forming assay measuring infectious SARS-CoV-2 (**black line** indicates wild-type; **green line** indicates NeonGreen) in supernatant of hPSC-derived cardiomyocytes over time following inoculation (MOI 0.1). A **dashed line** indicates the limit of detection (n = 4 per group). (D) Two-dimensional cultures of hPSC-derived cardiomyocytes were inoculated with SARS-CoV-2 (MOI 0.1) and analyzed for viability (Zombie-Violet) and infection (NeonGreen) as a function of time by flow cytometry. **Right plot** shows viability of NeonGreen-positive cells (n = 4 per group). (A–D) Mean values are plotted and error bars denote standard error of the mean. (E) Brightfield microscopy showing cytopathic effect in hPSC-derived cardiomyocytes infected with SARS-CoV-2 (MOI 0.1). Representative images from 5 individual samples. (F) Flow cytometry of 2-dimensional tissues containing CM and Fb (**left**) or CM, Fb, and Mac (**right**) harvested on day 3 following mock infection or inoculation with SARS-CoV-2 (MOI 0.1). Representative plot from 4 independent samples. Cardiomyocytes (CD90-CD14-) showed prominent NeonGreen fluorescence (**green overlay**). NeonGreen signal was not detected in fibroblasts (CD90+CD14-) or macrophages (CD90-CD14+). (G) Quantification of NeonGreen-positive cells from 2-dimensional tissues containing hPSC-cardiomyocytes and fibroblasts or hPSC-cardiomyocytes, fibroblasts, and macrophages (n = 4 per group). Bars denotes median value. *p < 0.05 compared to mock infection (Mann-Whitney test). (H) Transmission electron microscopy micrographs of cardiomyocytes in 2-dimensional tissues infected with either mock or SARS-CoV-2 (MOI 0.1). Tissues were harvested on day 3 post-inoculation. Viral budding (**blue arrow**) and endosomal compartments filled with virions (**black arrow**) are denoted. Scale bars in insets are 100 nm. Representative image from 4 independent samples. FFU = focus forming units; other abbreviation as in **Figure 2.1**.

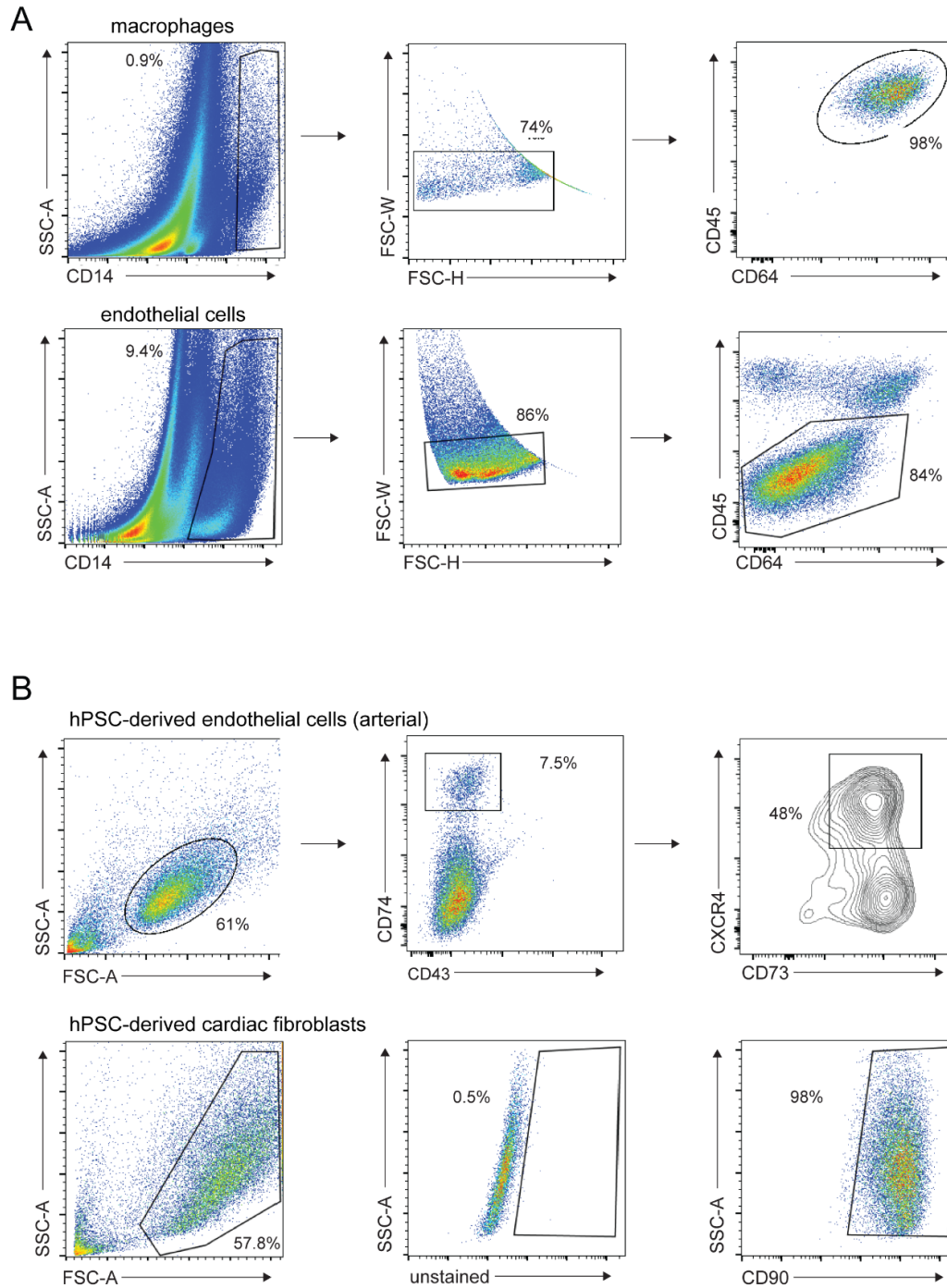


Figure 2.6. Flow cytometry gating strategies for primary human cardiac cell types and hPSC-derived endothelial cells and cardiac fibroblasts. A, Flow cytometry gating scheme for primary cardiac macrophages and endothelial cells. B, Flow cytometry gating strategies for hPSC-derived endothelial cells and cardiac fibroblasts. Representative plots and percentages are shown.

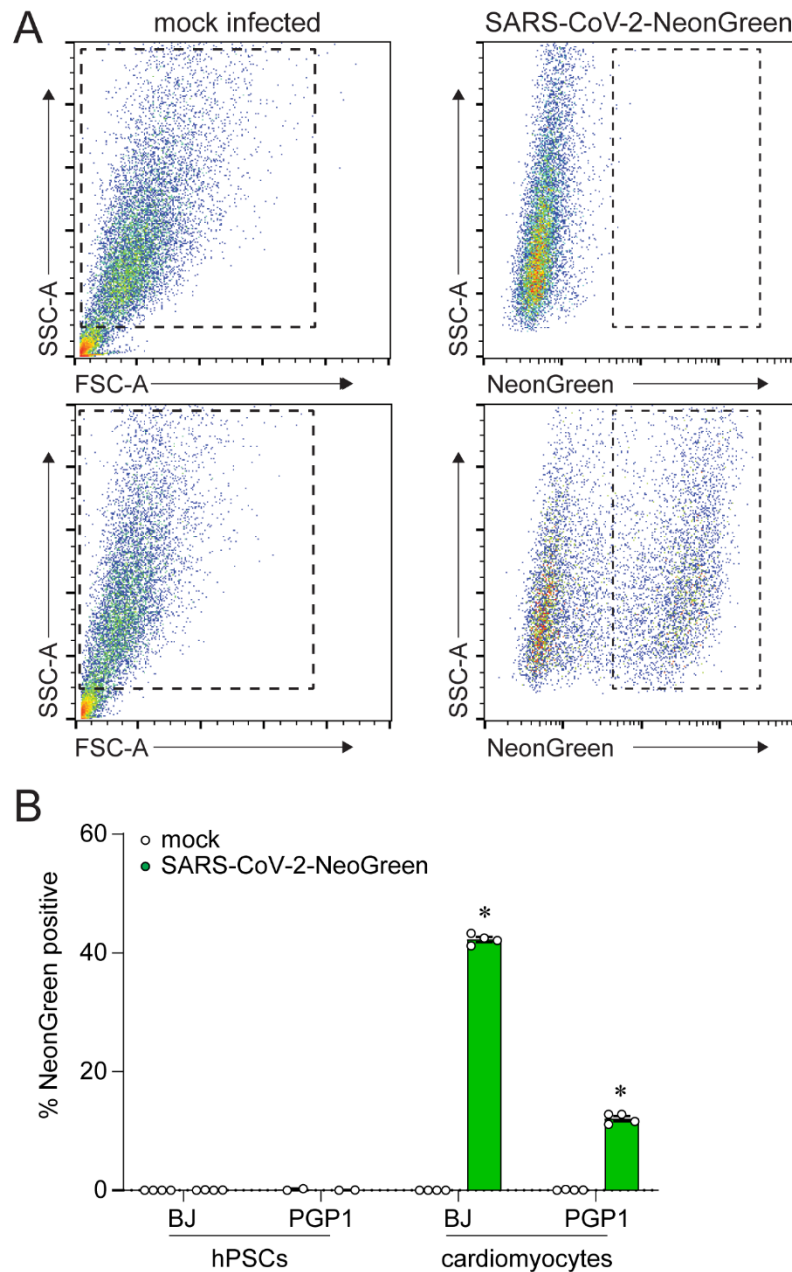


Figure 2.7. SARS-CoV-2 infects hPSC-derived cardiomyocytes but not undifferentiated hPSC lines.

A, Flow cytometry gating scheme. hPSC-derived cardiomyocytes were either mock infected or inoculated with SARS-CoV-2-mNeonGreen (MOI 0.1) and harvested 3 days later. NeonGreen expression was measured using flow cytometry. **B**, Two independent undifferentiated hPSCs (BJ and PGP1 cell lines) or hPSC-derived cardiomyocytes were mock-infected or inoculated with SARS-CoV-2-mNeonGreen (MOI 0.1) and harvested 3 days later. The percentage of NeonGreen positive cells was quantified by flow cytometry. Data points indicate individual samples. Error bars denote standard error of the mean and bars correspond to the mean value. * $p < 0.05$ compared to mock infection (t-test).

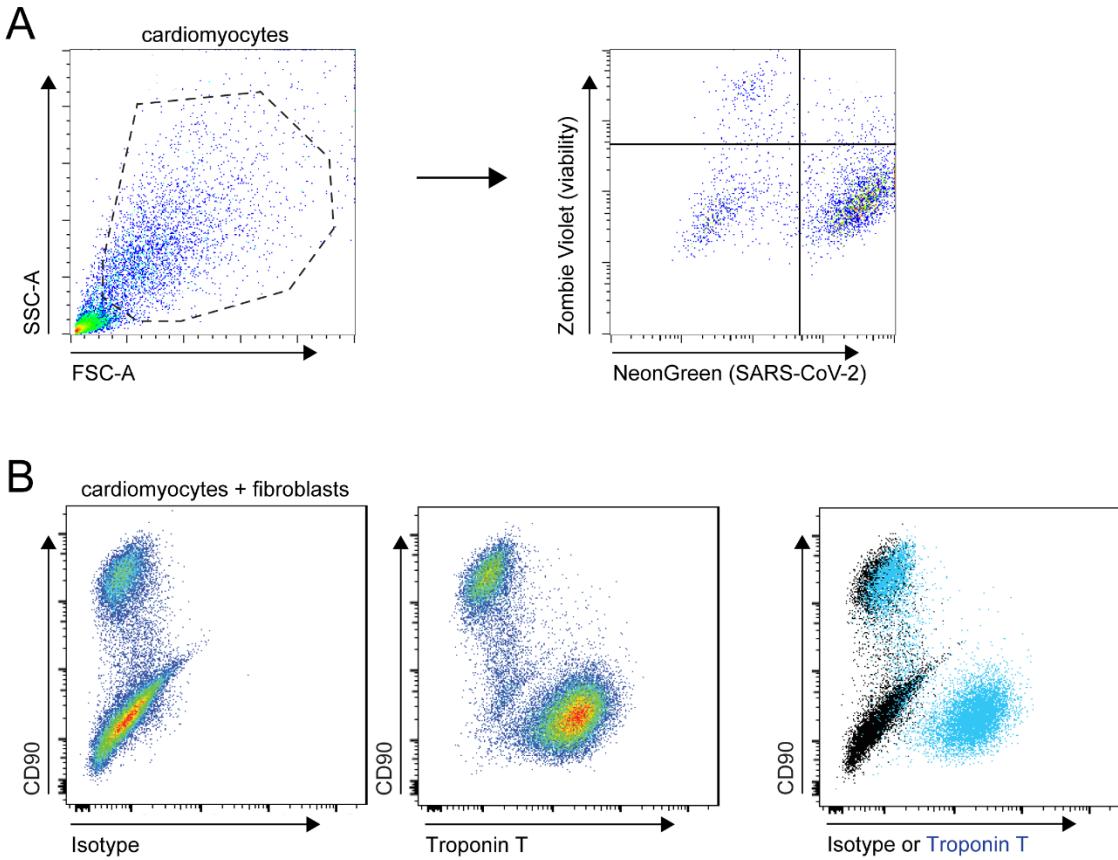


Figure 2.8. Flow cytometry gating schemes. **A**, hPSC-derived cardiomyocytes were infected with SARS-CoV-2-NeonGreen (MOI 0.1) and harvested 4 days after inoculation. Cells were stained with Zombie-Violet viability dye. Representative plot from 4 independent experiments. **B**, Mixed two-dimensional cultures of hPSC-derived cardiomyocytes and fibroblasts were permeabilized and stained with anti-CD90 and anti-Troponin T (TNNT2) antibodies to confirm that the CD90⁻ cells in **Fig. 2** are cardiomyocytes (CD90⁻TNNT2⁺).

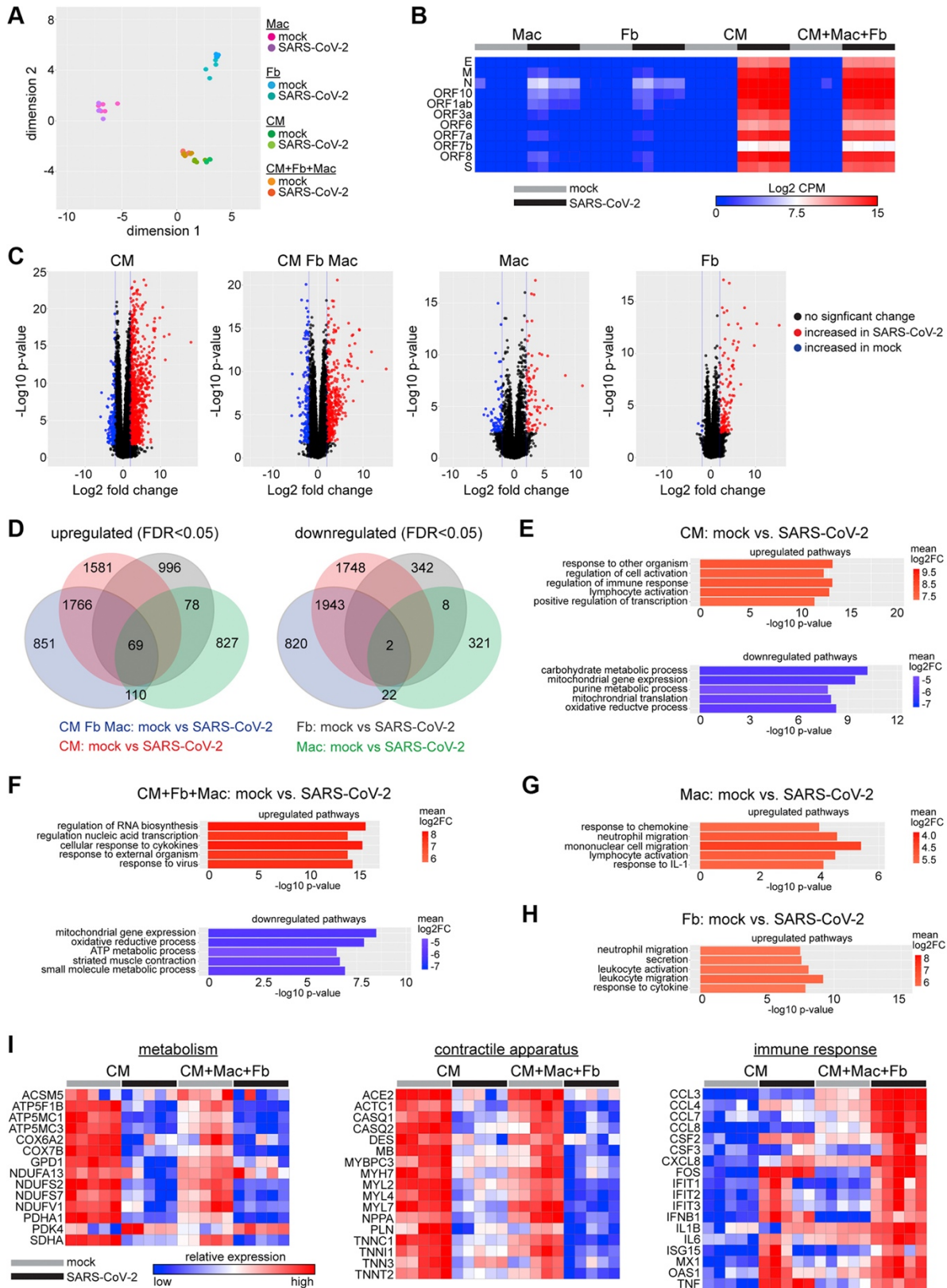


Figure 2.9. RNA Sequencing Identified Viral Transcription and Activation of Innate Immune Response in hPSC-Derived Cardiomyocytes and Tissues (A) MDS plot of RNA sequencing data obtained from mock and SARS-CoV-2–infected (MOI 0.1) hPSC-derived CMs, Fbs, Macs, and 2-dimensional tissues (CM + Fb + Mac). Cells and tissues were harvested on day 3 post-inoculation (n = 5 per group). (B) Heatmap of SARS-CoV-2 viral gene expression. Color scale denotes absolute expression as log₂ counts per million reads (CPM) (scale: **blue** = 0, **red** = 15). (C) Volcano plots showing differentially expressed genes between mock and SARS-CoV-2–infected conditions. **Black dots** indicate no significant change, **red dots** indicate upregulated during infection (log₂ fold change > 2, FDR p < 0.05), and **blue dots** indicate downregulated during infection (log₂ fold change < -2, FDR p < 0.05). Data points correspond to individual transcripts. (D) Venn diagram of genes upregulated and downregulated in each cell type and tissues. Differential expression is based on change relative to corresponding uninfected (mock) samples. (E to H) Gene ontology (GO) pathway analysis of CM (E), CM + Fb + Mac (F), Mac (G) and Fib (H) showing top 5 upregulated (**red**) and downregulated (**blue**) pathways in SARS-CoV-2–infected samples compared to mock. Color indicates log₂ fold change (log₂FC). (I) Heat maps of selected differentially expressed genes implicated in metabolism (**left**), contractile apparatus (**center**), and immune response (**right**). CM and tissues (CM + Mac + Fb) are displayed. Color scale denotes relative gene expression (high **red**, low **blue**) across cell types and conditions. ATP = adenosine triphosphate; FDR = false discovery rate; IL = interleukin. other abbreviations as in **Figures 2.1 and 2.5**

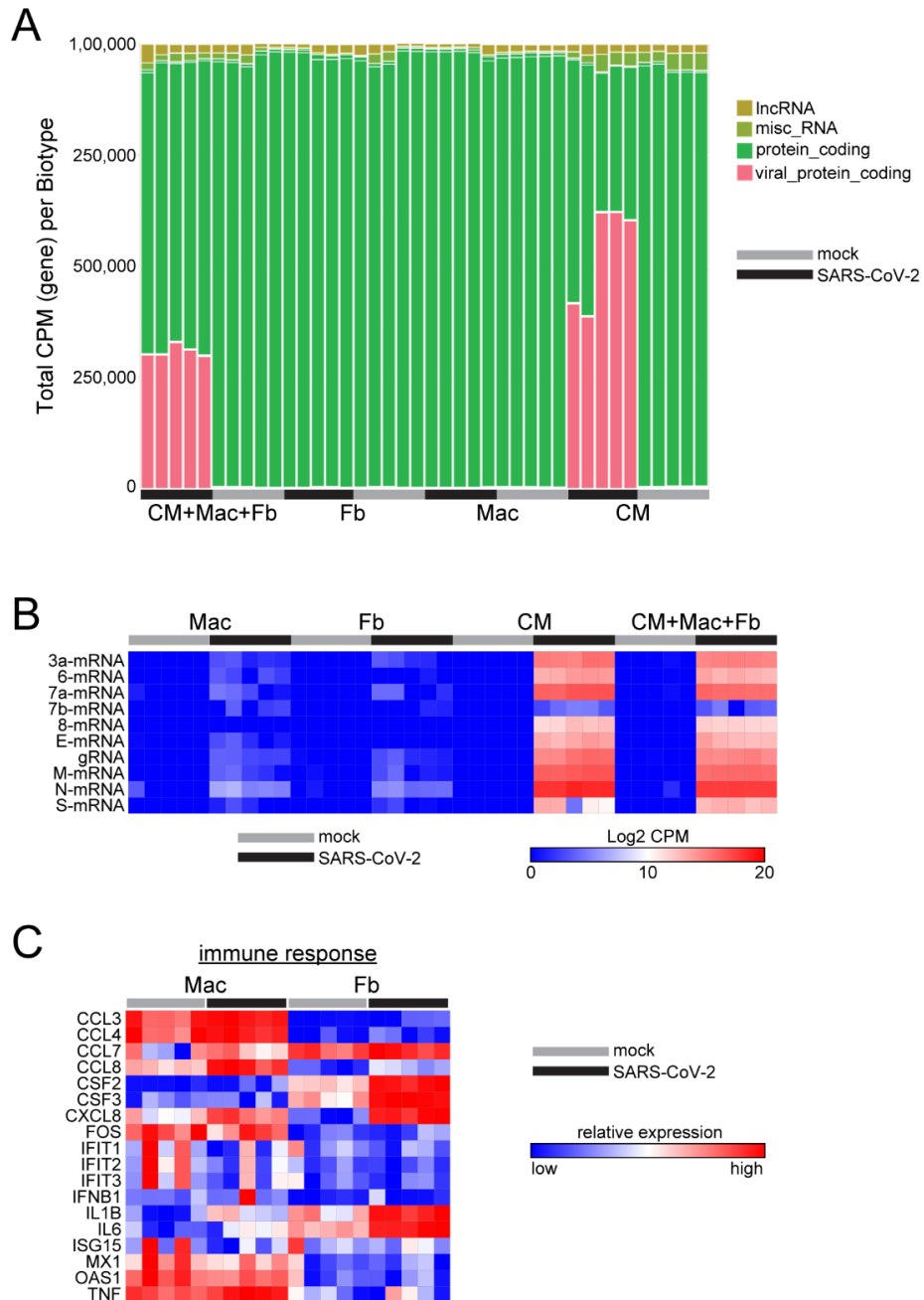


Figure 2.10. RNA sequencing of mock and SARS-CoV-2 infected hPSC-derived cardiomyocytes, fibroblasts, macrophages, and two-dimensional tissues. **A**, Biotype plot showing different classes of RNAs identified in RNA sequencing of mock (grey) and SARS-CoV-2 (black) infected cells. CPM: counts per million. **B**, Heat map showing the absolute expression of viral subgenomic RNAs. **C**, Heat map showing relative expression of chemokines, cytokines, and interferon stimulated transcripts in mock and SARS-CoV-2 infected macrophages and fibroblasts. Colors correspond to the relative expression of each transcript across cell types and experimental conditions. CM: hPSC-derived cardiomyocyte, Fb: fibroblast, Mac: macrophage.

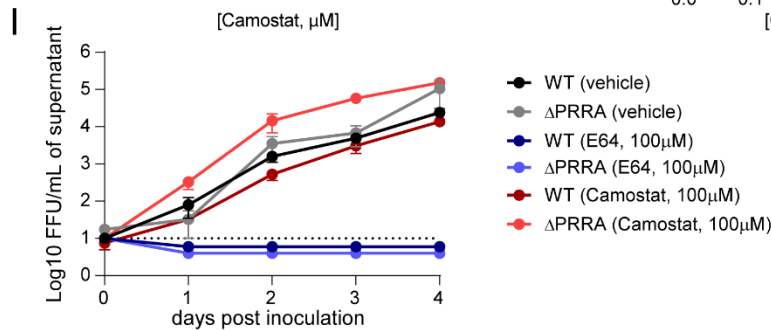
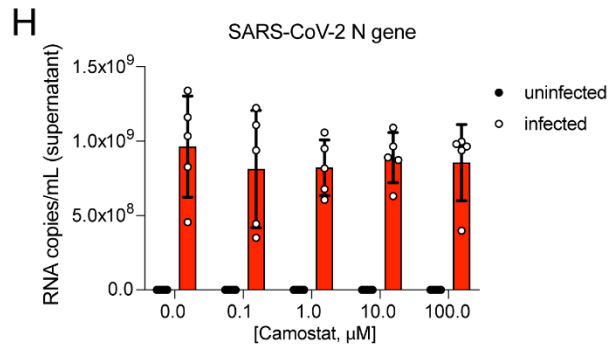
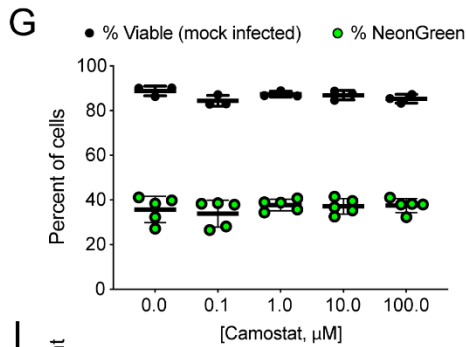
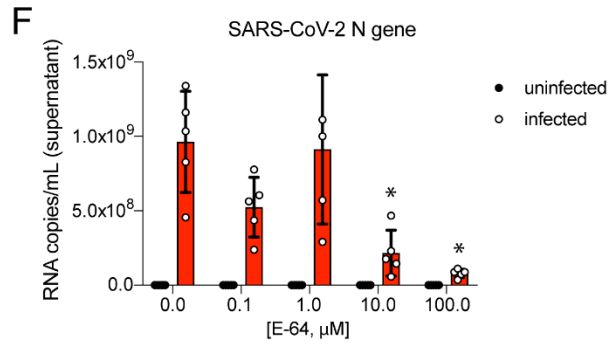
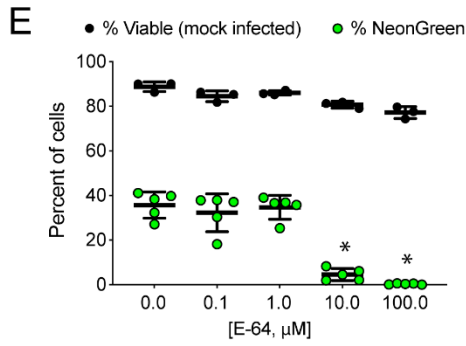
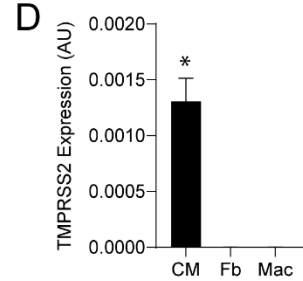
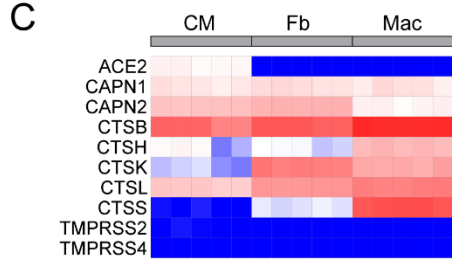
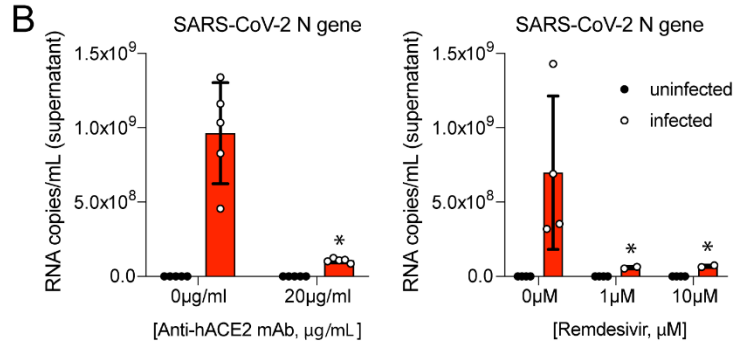
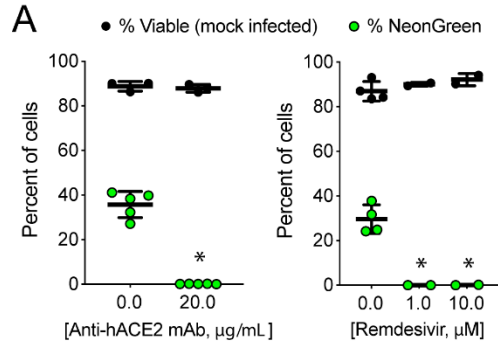


Figure 2.11. SARS-CoV-2 entry of hPSC-derived cardiomyocytes is mediated by ACE2 and endosomal cysteine proteases. **A-B**, hPSC-derived cardiomyocytes were infected with mock or inoculated with SARS-CoV-2-mNeonGreen (MOI 0.1). Cells were treated with either vehicle control, anti-human ACE2 neutralizing antibody (Anti-hACE2 mAb, left), or remdesivir (inhibitor of RNA-dependent RNA polymerase, right) at the indicated concentrations. Cells were analyzed by flow cytometry on day 3 post-inoculation for viral infection (NeonGreen, green circles) and viability (Zombie-Violet, black circles) (**A**). The presence of viral RNA in the tissue culture supernatant was also quantified by RT-PCR (**B**). Each data point corresponds to an individual sample/experiment, bar denotes the median value, error bars denote 25th and 75th percentile, * $p < 0.05$ compared to infected cells treated with vehicle control (Mann-Whitney test). **C**, Heatmap of host genes implicated in SARS-CoV-2 cell entry in uninfected hPSC-derived cardiomyocytes (CM), fibroblasts (Fb), and macrophages (Mac). Color scale indicates absolute gene expression levels. **D**, Quantitative RT-PCR for TMPRSS2 in uninfected hPSC-derived cardiomyocytes (CM), fibroblasts (Fb), and macrophages (Mac). $n=5$ for each cell type, bar denotes the mean value, error bars denote standard error of the mean, * $p < 0.05$ compared to other cell populations (t-test). **E-H**, hPSC-derived cardiomyocytes were mock infected or inoculated with SARS-CoV-2-NeonGreen (MOI 0.1). Cells were treated with either vehicle control, endosomal cysteine protease inhibitor E-64 (**E-F**), or serine protease inhibitor camostat (**G-H**) at the indicated concentrations. Cells were analyzed by flow cytometry on day 3 post-inoculation for viral infection (NeonGreen, green circles) and viability (Zombie-Violet, black circles) (**E,G**). Viral RNA in the tissue culture supernatant was quantified by RT-PCR (**F,H**). Each data point corresponds to an individual sample/experiment, bar denotes the median value, error bars denote 25th and 75th percentile, * $p < 0.05$ compared to infected cells treated with vehicle control (Mann-Whitney test). **I**, hPSC-derived cardiomyocytes were mock infected or inoculated with WT SARS-CoV-2 or \square PRRA SARS-CoV-2 (furin cleavage site mutation). Cells were treated with either vehicle, E64, or camostat at the indicated concentrations, beginning 1 hour prior to infection and continuing for the duration of the experiment. Focus forming assays were performed using cell culture supernatant at 1, 2, 3, and 4 days after inoculation. $n=4$ per experimental group.

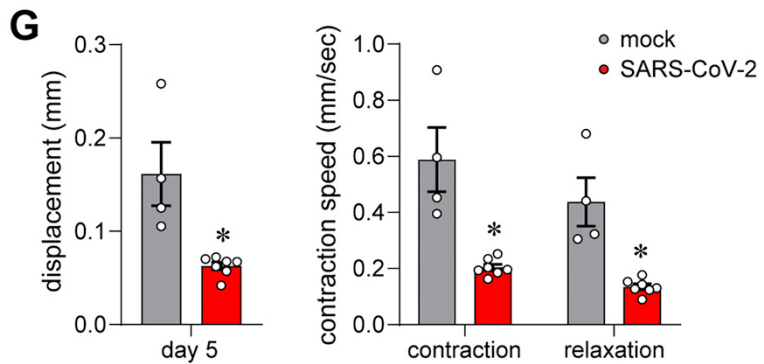
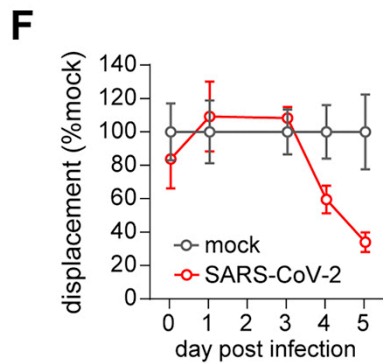
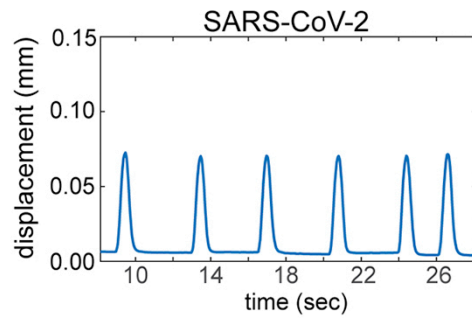
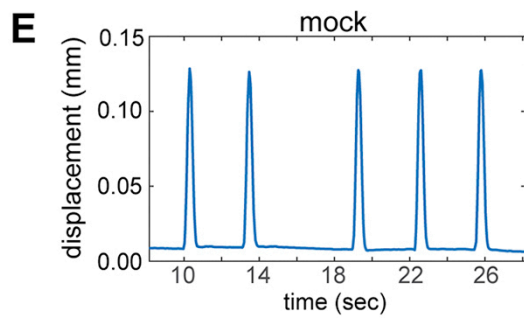
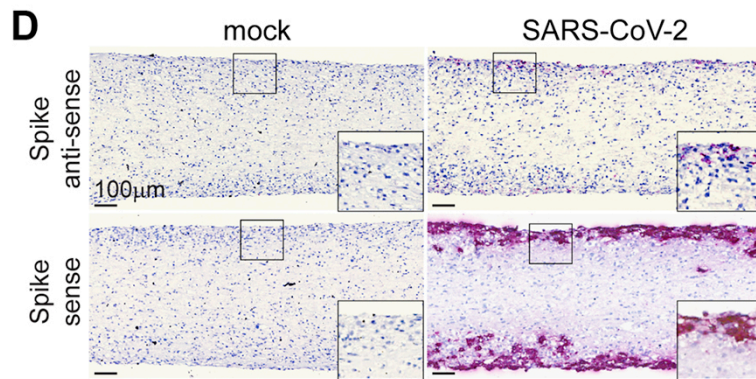
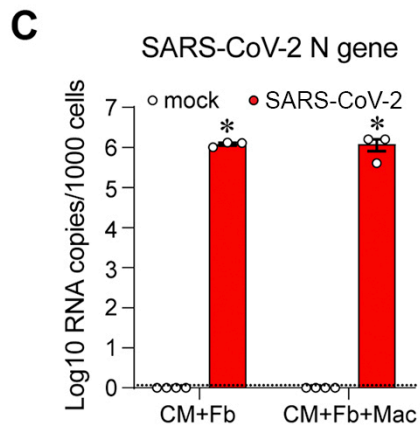
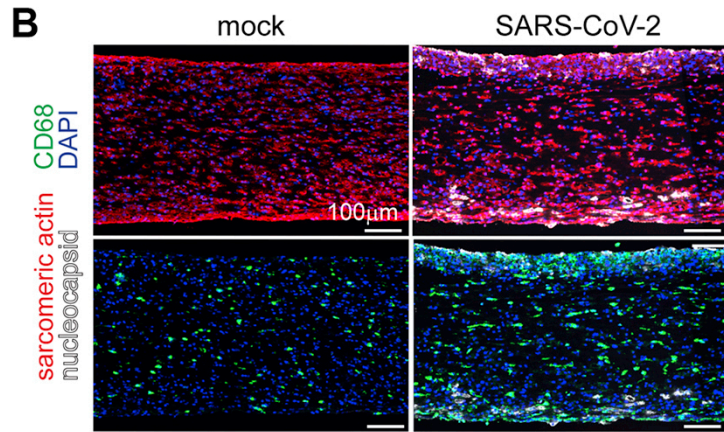
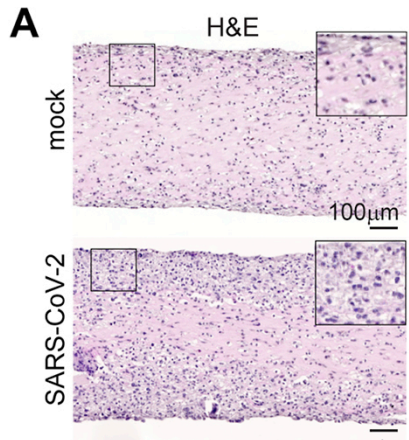


Figure 2.12. EHTs Recapitulate Aspects of COVID-19 Myocarditis (A) Hematoxylin and eosin (H&E)–stained sections of 3-dimensional engineered heart tissue (EHT) consisting of hPSC-derived CM, Fbs, and Macs 5 days following mock infection or inoculation with SARS-CoV-2 (MOI 0.1). Insets are high-magnification images of the boxed areas. Representative images from 4 independent samples. (B) Immunostaining of mock or SARS-CoV-2–infected 3-dimensional EHTs for sarcomeric actin (cardiomyocytes, **red**), CD68 (macrophages, **green**), and nucleocapsid protein (**white**). EHTs were harvested 5 days post-inoculation. **Blue**: DAPI. Representative images from 4 independent samples. (C) Quantitative RT-PCR of SARS-CoV-2 N-gene expression in EHTs consisting of hPSC-derived CM, Fb, and/or Macs. EHTs were either mock infected or inoculated with SARS-CoV-2 (MOI 0.1) and harvested 5 days post-inoculation. **Error bars** denote SE of the mean. **Dotted line**: limit of detection. * $p < 0.05$ compared to uninfected control (mock, Student *t* test test). (D) In situ hybridization for SARS-CoV-2 spike RNA sense and antisense strands (**red**) in EHTs 5 days after mock or SARS-CoV-2 infection (MOI 0.1). **Blue**: hematoxylin. Representative images from 4 independent specimens. Insets are high magnification images of the boxed areas. (E) Spontaneous beating displacement traces for infected and uninfected EHTs on day 5 post-infection. (F) Displacement (relative to uninfected mock condition) generated by spontaneous beating of EHTs as a function of time following inoculation with SARS-CoV-2 (MOI 0.1). Each data point represents a mean value from 4 to 7 independent samples, **error bars** denote SE of the mean. (G) Quantification of absolute displacement (**left**) and contraction speed (**right**) generated by spontaneous beating of EHTs 5 days following mock or SARS-CoV-2 infection (MOI 0.1). **Error bars** represent SE of the mean; * $p < 0.05$ compared to mock (Student’s *t*-test test). Abbreviations as in **Figures 2.1** and **2.5**.

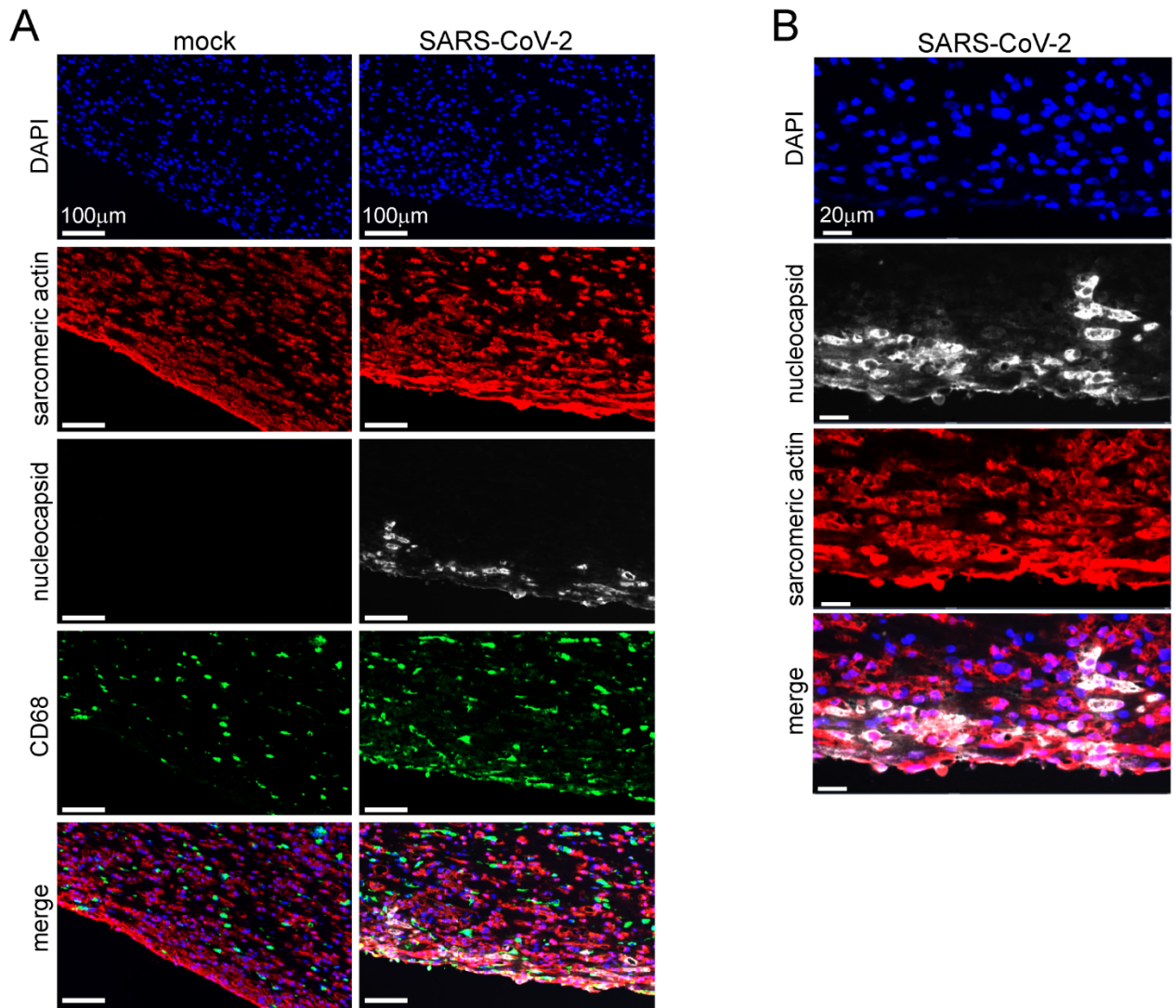


Figure 2.13. Confocal microscopy of mock and SARS-CoV-2 infected three-dimensional EHTs. **A**, Images of mock and SARS-CoV-2 infected three-dimensional EHTs stained with sarcomeric actin (cardiomyocytes, red), nucleocapsid protein (white), and CD68 (macrophages, green). **B**, High magnification images of SARS-CoV-2 infected three-dimensional EHTs demonstrating co-localization of nucleocapsid (white) and sarcomeric actin (red) staining. EHTs were harvested 5 days after infection. Images are representative of 4 independent experiments.

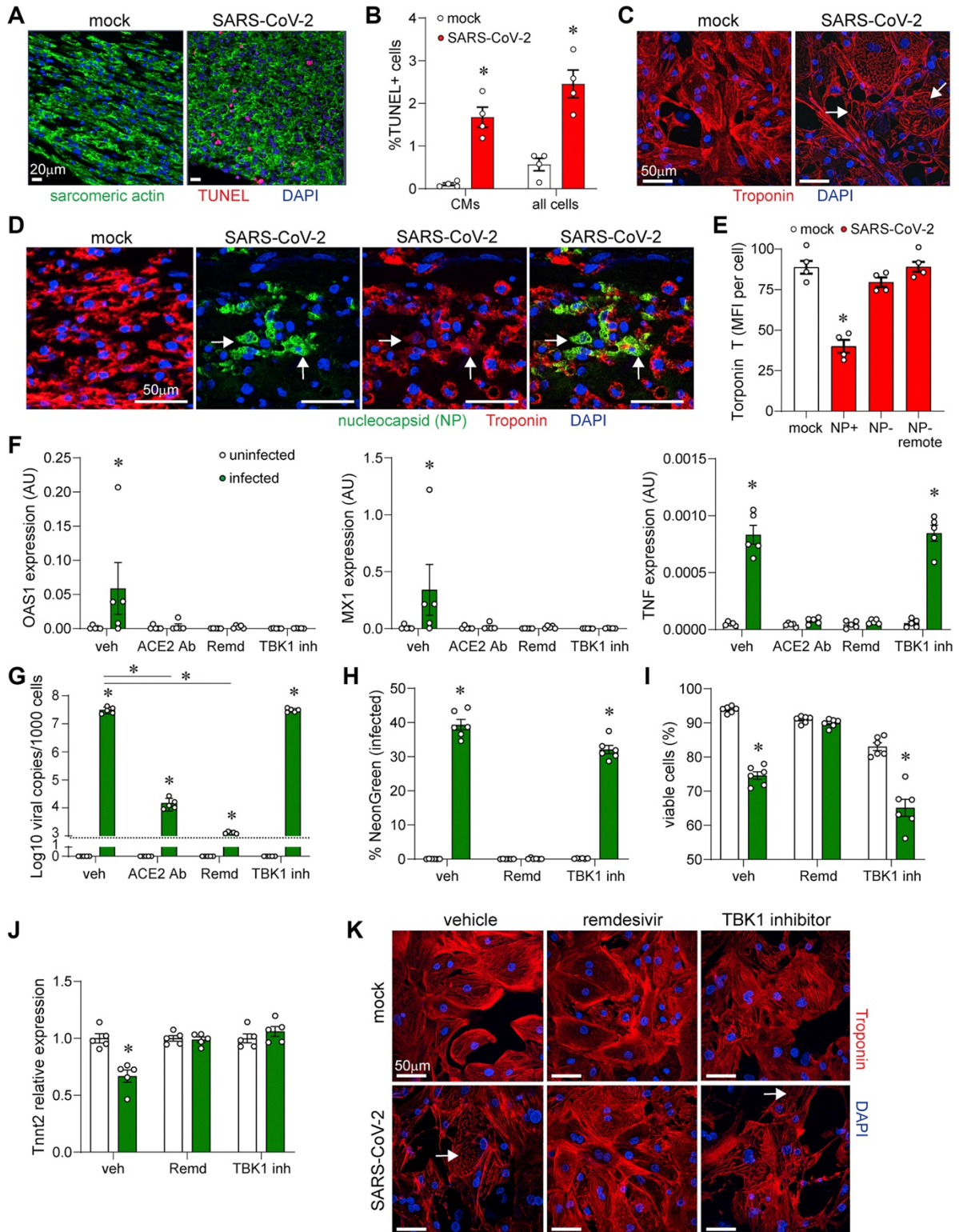


Figure 2.14. Mechanisms of Reduced EHT Contractility (A) Terminal deoxynucleotidyl transferase dUTP nick end labelling (TUNEL) stain (**red**) and cardiac actin (**green**) immunostaining of EHTs (CM +Fb + Mac) 5 days after mock or SARS-CoV-2 infection (MOI 0.1). **Blue**: DAPI. Representative images from 4 independent experiments. (B) Quantification of TUNEL-positive cells in areas of viral infection. **Error bars** represent SE of the mean, * $p < 0.05$ compared to mock (Student *t* test). (C) Immunostaining of hPSC-derived cardiomyocytes for troponin T (red) 3 days after inoculation with mock control or SARS-CoV-2–NeonGreen (MOI 0.1). **Blue**: DAPI. Arrows denote areas of sarcomere disassembly. (D) Immunostaining of EHTs for troponin T (**red**) and SARS-CoV-2 nucleocapsid (**green**) 5 days after inoculation with mock control or SARS-CoV-2–NeonGreen (MOI 0.1). **Blue**: DAPI. Arrows denote SARS-CoV-2 nucleocapsid–positive cells with reduced troponin T staining. (E) Quantification of troponin T staining in mock (**white**) and SARS-CoV-2 infected (**red**) EHTs. Data is presented as mean fluorescence intensity (MFI). MFI was measured in infected (nucleocapsid-positive [NP+]) cardiomyocytes and uninfected (NP-) cardiomyocytes located proximal or remote to areas of infection. **Error bars** represent SE of the mean, * $p < 0.05$ compared to mock (Student *t* test). (F) Quantitative RT-PCR measuring OAS1, MX1, and tumor necrosis factor (TNF) mRNA expression in hPSC-derived cardiomyocytes 3 days post-inoculation with mock control (**white**) or SARS-CoV-2 (**green**, MOI 0.1). Cells were treated with vehicle, angiotensin-converting enzyme 2 antibody (ACE2 Ab) (20 $\mu\text{g/ml}$), remdesivir (10 μM), or TBK inhibitor (MRT67307, 10 μM). **Error bars** indicate SE of the mean. * $p < 0.05$ compared to mock control (Student *t* test). (G) Quantitative RT-PCR of SARS-CoV-2 N gene expression in hPSC-derived cardiomyocytes that were either mock infected (**white**) or inoculated with SARS-CoV-2 (**green**, MOI 0.1) and harvested 3 days post-inoculation. **Error bars** denote SE of the mean. **Dotted line**: limit of detection. * $p < 0.05$ compared to uninfected control (analysis of variance [ANOVA]) or vehicle infected as indicated by the bar (ANOVA). (H,I) Flow cytometry measuring the percent of infected (H) and viable (I) cardiomyocytes following either mock infection (**white**) or inoculation with SARS-CoV-2 (**green**, MOI 0.1). Cells were harvested and analyzed 3 days post-inoculation. **Error bars** denote SE of the mean. * $p < 0.05$ compared to uninfected control (ANOVA). (J) Quantitative RT-PCR measuring TNNT2 mRNA expression 3 days post-inoculation with mock control (**white**) or SARS-CoV-2 (**green**, MOI 0.1). **Error bars** indicate SE of the mean. * $p < 0.05$ compared to mock control (ANOVA). (K) Immunostaining for troponin T (**red**) 3 days post-inoculation with mock control or SARS-CoV-2–NeonGreen (MOI 0.1). **Blue**: DAPI. **Arrows** denote areas of sarcomere disassembly. Abbreviations as in **Figures 2.1** and **2.5**

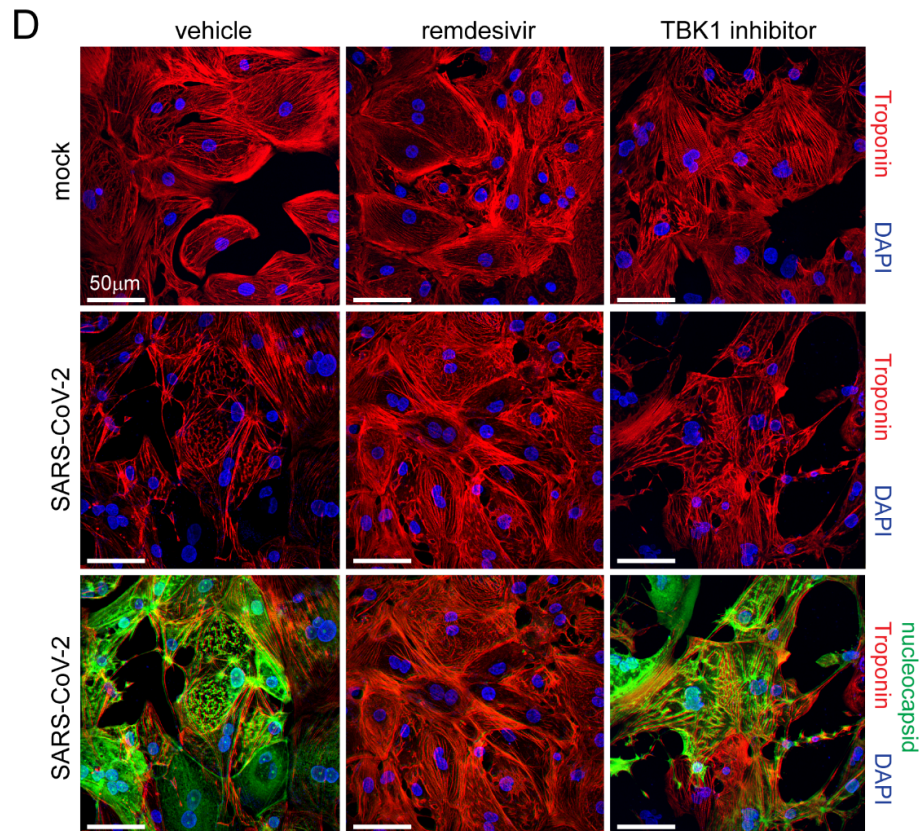
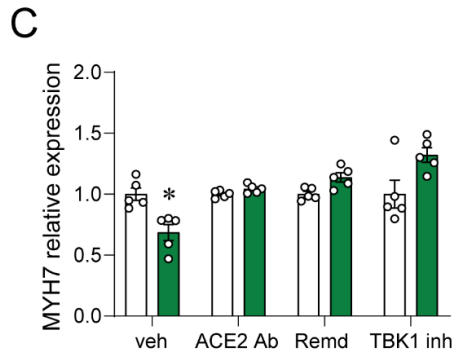
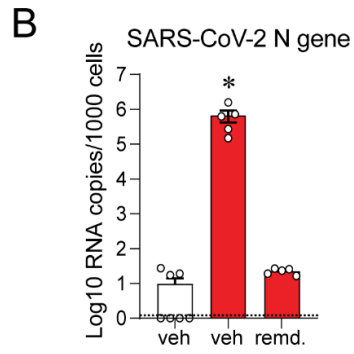
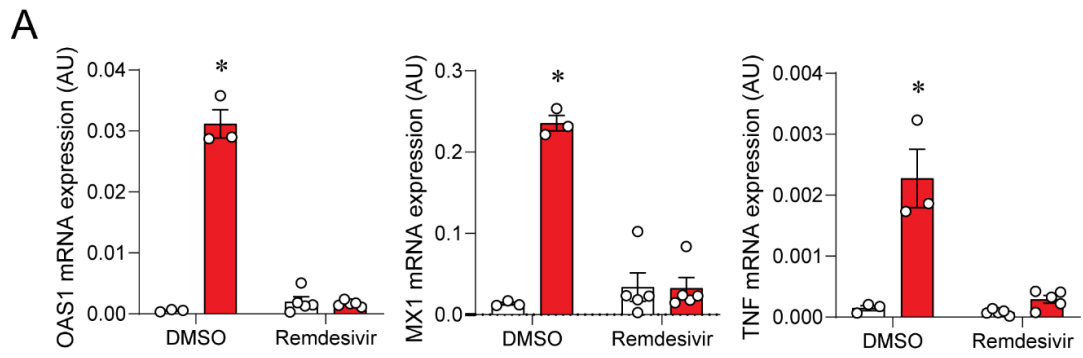


Figure 2.15. SARS-CoV-2 infection drives type I interferon signaling and sarcomere breakdown in hPSC-derived cardiomyocytes. **A**, Quantitative RT-PCR measuring OAS1, MX1, and TNF mRNA expression in 3D EHTs 5 days after inoculation with mock control (white) or SARS-CoV-2 (red, MOI 0.1). EHTs were treated with vehicle (DMSO) or remdesivir (10 μ M). Each data point denotes a biologically unique sample, bar height corresponds to the mean, and error bars indicate standard error of the mean. * $p < 0.05$ compared to vehicle control (t-test). **B**, EHTs were either mock infected (white) or inoculated with SARS-CoV-2 (red, MOI 0.1). EHTs were treated with either vehicle control, 10 μ M or 10 μ M of remdesivir (Remd.). Five days post-infection EHTs were homogenized and SARS-CoV-2 N gene RNA was measured by quantitative RT-PCR. Each data point denotes an individual EHT, bar height corresponds to the mean, error bars represent standard error of the mean, dotted line denotes lower limit of detection, * $p < 0.05$ compared to mock vehicle (t-test). **C**, Quantitative RT-PCR measuring MYH7 mRNA expression in hPSC-derived cardiomyocytes 3 days after inoculation with mock control (white) or SARS-CoV-2 (green, MOI 0.1). Cells were treated with vehicle, ACE2 Ab (20 μ g/ml), remdesivir (10 μ M), or TBK inhibitor (MRT67307, 10 μ M). Each data point denotes a biologically unique sample, bar height corresponds to the mean, and error bars indicate standard error of the mean. * $p < 0.05$ compared to mock control (ANOVA). **D**, Immunostaining of hPSC-derived cardiomyocytes for Troponin T (red) 3 days after inoculation with mock control or SARS-CoV-2-NeonGreen (MOI 0.1). hPSC-derived cardiomyocytes were treated with vehicle, remdesivir (10 μ M) or TBK inhibitor (MRT67307, 10 μ M). Endogenous NeonGreen fluorescence is shown (nucleocapsid, green). Blue: DAPI.

Chapter 3

Human Cardiac Pericytes are Susceptible to SARS-CoV-2 Infection

This chapter was adapted from an article published in *JACC: Basic to Translational Science*:

Brumback, B.D. *, **Dmytrenko, O.** *, Robinson, A.N., Bailey, A.L., Ma, P., Liu, J., Hicks, S.C., Ng, S., Li, G., Zhang, D.M., Lipovsky, C.E., Lin, C.-Y., Diamond, M.S., Lavine, K.J., Rentschler, S.L., 2023. Human Cardiac Pericytes Are Susceptible to SARS-CoV-2 Infection. *JACC: Basic to Translational Science* 8, 109–120. <https://doi.org/10.1016/j.jacbts.2022.09.001>

*BB and OD contributed equally to this work and are joint first authors. KL and SR contributed equally to this work and are joint senior authors. BB procured cardiac slices, performed histology and analysis, designed experiments, wrote and edited the manuscript; OD performed infection of cultures in BSL3, all virologic assays and analysis, designed experiments, wrote and edited the manuscript; AB infected cardiac slices; AR, PM, JL, SH performed isolation and culture of primary cells; SN, GL, DZ, CL performed cardiac slice preparation; CYL analyzed human histology; MD, KL, SR conceptualized, funded, and supervised the study, edited the manuscript.

3.1 Summary

COVID-19 is associated with serious cardiovascular complications, with incompletely understood mechanism(s). Pericytes have key functions in supporting endothelial cells and maintaining vascular integrity. We demonstrate that human cardiac pericytes are permissive to SARS-CoV-2 infection in organotypic slice and primary cell cultures. Viral entry into pericytes is mediated by endosomal proteases, and infection leads to up-regulation of inflammatory markers, vasoactive mediators, and nuclear factor kappa-B–dependent cell death. Furthermore, we present evidence of cardiac pericyte infection in COVID-19 myocarditis patients. These data demonstrate

that human cardiac pericytes are susceptible to SARS-CoV-2 infection and suggest a role for pericyte infection in COVID-19.

3.2 Introduction

SARS-CoV-2 infection leads to a constellation of serious cardiovascular manifestations in subsets of patients, including myocardial damage, myocarditis, arrhythmias, heart failure, acute coronary syndromes, thrombosis, and hemodynamic dysregulation¹. A recent population-based study demonstrated an increased risk of serious vascular complications, including acute myocardial infarction and ischemic stroke, in COVID-19 patients². COVID-19 also is associated with endothelial inflammation and dysfunction³, marked by up-regulation of proinflammatory mediators and endothelial damage⁴. Postmortem analyses of hearts from 41 COVID-19 patients revealed capillary, arteriole, and small artery microthrombi in 20% of cases⁵.

The mechanisms underlying cardiovascular complications of COVID-19 are incompletely understood. Evaluation of infection in the heart has suggested that cardiomyocytes and cardiac interstitial cells may be targets of SARS-CoV-2 infection⁶⁻⁹. In contrast, several studies have reported that SARS-CoV-2 is unable to infect cultured endothelial cells^{6,10}. Intriguingly, cardiac pericytes express angiotensin-converting enzyme 2 (ACE2), a host receptor for SARS-CoV-2, at high levels¹¹. Pericytes have a critical role in maintaining endothelial integrity and vascular homeostasis. Conceptually, SARS-CoV-2 infection of pericytes could contribute to the vascular manifestations of COVID-19 including thrombosis, inflammation, and hemodynamic derangements¹². Recent work has shown that pericyte-like cells generated from human pluripotent stem cell-derived neural crest stem cells can be productively infected by SARS-CoV-2¹³. To date, no studies have evaluated whether cardiac pericytes, which are thought to be derived from

epicardium¹⁴, are targets of SARS-CoV-2 infection. Here, we demonstrate that human cardiac pericytes are susceptible to SARS-CoV-2 infection, reveal that the production of inflammatory and vasoactive mediators and cell death are consequences of pericyte SARS-CoV-2 infection, and show evidence of pericyte infection in cardiac tissue from COVID-19 patients.

3.3 Results

3.3.1 ACE2 is Expressed in Human Cardiac Pericytes *In Situ*

Single-cell RNA sequencing of the human heart established that *ACE2* mRNA is expressed in cardiac pericytes¹⁵. To confirm ACE2 protein expression in pericytes, we performed immunohistochemistry on human ventricular tissue from nonfailing donor hearts rejected from transplantation (**Table 3.1**). In vascular regions, we observed ACE2 staining surrounding CD31⁺ endothelial cells (**Figure 3.1A**). Costaining for platelet-derived growth factor receptor beta (PDGFR β) (pericyte marker) showed that pericytes express ACE2 (**Figure 3.2A**, **Figure 3.1B**). We also observed ACE2 expression in some cardiomyocytes, as previously reported (**Figure 3.1C**)^{6,8}. These data demonstrate that cardiac pericytes and cardiomyocytes both express ACE2.

3.3.2 Human Cardiac Pericytes are Permissive to SARS-CoV-2 Infection

To evaluate SARS-CoV-2 tropism in human heart tissue, we utilized an ex vivo organotypic slice culture system¹⁶. Briefly, 400- μ m slices of left ventricular myocardium from nonfailing donor hearts were cultured at a liquid-air interface on transwell inserts. Slices were inoculated with 5×10^5 focus forming units of SARS-CoV-2 (USA_WA1/2020 strain). Slices then were cultured for 24 or 48 hours. In situ hybridization revealed the presence of SARS-CoV-2 *S* RNA (**Figure 3.2B**) with increased signal over time (**Figure 3.3A, B**). We identified the presence of the replication intermediate (antisense RNA) for both *ORF1ab* and *S* genes in cells

where genomic *S* gene RNA was present 48 hours after inoculation (**Figure 3.2B, Figure 3.3C**). SARS-CoV-2 RNAs colocalized with *PDGFRB* mRNA in perivasculature regions (**Figure 3.2C**). Immunostaining for SARS-CoV-2 nucleocapsid protein (NP) revealed viral protein in PDGFR β ⁺ cells surrounding CD31⁺ endothelial cells, suggesting that SARS-CoV-2 can infect cardiac pericytes productively in a native tissue environment (**Figure 3.2D, Figure 3.4**). We further demonstrated that PDGFR β colocalizes with another pericyte marker NG2 (**Figure 3.5A**) and found colocalization of NG2 with NP in infected cardiac slices (**Figure 3.5B**). We also observed SARS-CoV-2 RNA within the myocardium, consistent with previous studies demonstrating cardiomyocyte infection (**Figure 3.4**)^{7,8}.

3.3.3 SARS-CoV-2 Infects Human Primary Cardiac Pericytes

To elucidate mechanisms of viral entry and explore consequences of cardiac pericyte infection, we isolated cardiac pericytes (CD146⁺CD45⁻CD56⁻CD34⁻CD117⁻ cells) from nonfailing and failing human left ventricular tissue using fluorescence-activated cell sorting and established primary cultures by modifying a published protocol¹⁷ (**Figure 3.6A, B, Table 3.1**). Cultured cardiac pericytes displayed a morphology consistent with pericytes *in vivo*¹⁸ and expressed pericyte-specific markers (PDGFR β , NG2, and NOTCH3) (**Figure 3.6 D, E**). Primary cardiac pericytes retained PDGFR β and ACE2 protein expression in culture (**Figures 2A, B**).

Pericytes isolated from 3 independent donors were inoculated with SARS-CoV-2 WA1/2020 or SARS-CoV-2 mNeonGreen (WA1/2020 background)¹⁹ at a multiplicity of infection (MOI) of 1 and cultured for up to 7 days. Measurement of infectious virus by focus-forming assay revealed robust viral replication, which peaked at 2 to 3 days postinoculation (**Figure 3.7C**). Similar kinetics were observed for the Alpha (B.1.1.7), Beta (B.1.351), or Delta (B.1.617.2)

SARS-CoV-2 variants (**Figure 3.7D**). SARS-CoV-2 infection of cultured cardiac pericytes was corroborated by immunostaining (**Figure 3.7E**) and flow cytometry (**Figure 3.7F**). Approximately 40% of cells were mNeonGreen⁺ on day 1 postinoculation (**Figure 3.7F**). We observed virus-induced pericyte cell death beginning after day 4 postinoculation (**Figure 3.7G**).

To determine whether SARS-CoV-2 could infect human endothelial cells or pericytes from other organs, we inoculated primary cardiac microvascular endothelial cells, brain pericytes, and placental pericytes under the same conditions but did not detect productive infection (**Figure 3.8A**). Each of these cell types expressed lower levels of *ACE2* mRNA compared with cardiac pericytes (**Figure 3.8B**). These data suggest that not all pericytes are permissive to SARS-CoV-2 infection (**Figure 3.8A, B**). To assess if coculture of pericytes and endothelial cells made endothelial cells susceptible to infection, we inoculated primary cardiac pericytes, endothelial cells, or a 1:1 mixture of pericytes and endothelial cells with reporter mNeonGreen virus. Pericytes remained the only cell type with detectable viral replication, suggesting that coculture does not alter the permissiveness of at least some endothelial cells to SARS-CoV-2 infection (**Figure 3.8C**).

3.3.4 SARS-CoV-2 Enters Cardiac Pericytes Through an Endosomal Pathway

After binding to ACE2, the SARS-CoV-2 spike protein undergoes a proteolytic event that is necessary for fusion of the viral and host membranes and entry into the cell. Activation of spike by TMPRSS proteases mediates entry at the plasma membrane. Alternatively, spike activation via endosomal cathepsins enables cell entry through fusion with endo-lysosomal membranes^{20,21}. Human cardiac pericytes express ACE2, as well as genes encoding cathepsin B (*CTSB*) and L (*CTSL*) and furin (*FURIN*) proteins, but have undetectable levels of *TMPRSS2* or *TMPRSS4* (**Figure 3.9A**). To define the mechanism of viral cell entry, we treated

cardiac pericytes with anti-ACE2 neutralizing antibody, camostat mesylate (TMPRSS2 and TMPRSS4 inhibitor), and/or E-64 (endosomal cysteine protease inhibitor). We then inoculated cells with SARS-CoV-2 mNeonGreen at a high MOI of 20 to ensure that a high percentage of cells was infected in culture, which allowed us to focus on cell entry rather than other parts of the replication cycle and avoid prolonged exposure to inhibitors. After 20 hours, we used flow cytometry to assess the percentage of cardiac pericytes that expressed mNeonGreen (mNeonGreen⁺; PDGFR β ⁺) as an indicator of viral infection¹⁵ (**Figure 3.9B, C**). Neutralizing anti-ACE2 antibody and E-64 treatment significantly reduced the number of infected pericytes (**Figure 3.7H**). However, camostat treatment did not suppress pericyte infection (**Figure 3.7H**). Next-generation sequencing confirmed that the polybasic furin cleavage motif, which enhances spike cleavage by TMPRSS2 and TMPRSS4 proteases, was intact and present at 100% of SARS-CoV-2 mNeonGreen and USA_WA1/2020 viral stocks (see Methods section). Combining E-64 and camostat did not further reduce pericyte infection (**Figure 3.7H**). In all drug treatment conditions, cardiac pericytes maintained their identity as evidenced by PDGFR β ⁺ expression (**Figure 3.7I**), and minimal cell death was observed indicating that cell viability was not affected by either inhibitor (**Figure 3.7J**). Inhibition of entry was dose-dependent for E-64 (**Figure 3.9D**), and drug toxicity was not detected at the doses used (**Figure 3.9E and S7F**). We observed similar responses to anti-ACE2 antibody, E64, and camostat treatment when cardiac pericytes were infected at an MOI of 1 (**Figure 3.10**).

To further test the requirement for endosomal proteases in viral entry, we used bafilomycin-A1, a potent H⁺-ATPase inhibitor that prevents endosomal acidification required for the activity of cysteine proteases. Similar to previous entry inhibitor experiments, pericytes were

pretreated with bafilomycin for 2 hours, inoculated with high MOI 20 of SARS-CoV-2 mNeonGreen, and collected for flow cytometry 20 hours later. Bafilomycin decreased infection at and above 10 nmol/L (**Figure 3.11A**) and did not cause loss of pericyte identity (**Figure 3.11B**) or cell death (**Figure 3.11C**) at tested concentrations. To focus on early stages of viral entry, we treated pericytes with an anti-SARS-CoV-2 neutralizing monoclonal antibody (mAb SARS2-38, 20 $\mu\text{g}/\text{mL}$)²² after initial infection. This method allowed us to isolate entry from subsequent rounds of infection and spread in the culture. Primary cardiac pericytes were pretreated with 10 nmol/L bafilomycin for 2 hours, infected with SARS-CoV-2 mNeonGreen, and then treated with anti-SARS-CoV-2 neutralizing mAb or vehicle 4 hours later. Cells were harvested for flow cytometry 8 hours after initial virus exposure (**Figure 3.11D**). Pericyte infection was diminished in the presence of bafilomycin but not by treatment with the neutralizing antibody (**Figure 3.11E, F**). Together, these results demonstrate that SARS-CoV-2 entry into cardiac pericytes is at least partially dependent on ACE2 and endosomal proteases.

3.3.5 Cardiac Pericyte Infection Elicits Inflammatory and Vasoactive Responses and Alters Endothelial Cell Transcription

To examine the transcriptomic changes induced by SARS-CoV-2 infection, we inoculated cardiac pericytes from all 3 donors with SARS-CoV-2 mNeonGreen (MOI of 1) and performed RNA sequencing 4 days postinoculation. We observed high levels of infection (**Figure 3.7C**) and minimal cell death (**Figure 3.7G, Figure 3.11**) at this time point. Principal component analysis demonstrated independent clustering of mock and SARS-CoV-2-infected cardiac pericytes (**Figure 3.12 A, B**). Gene ontology pathway analysis revealed increases in the innate immune response to pathogens, type I interferon (IFN) signaling, and leukocyte degranulation (**Figure**

3.12C). We observed expression of SARS-CoV-2 viral genes in infected samples from all 3 donors (**Figure 3.12D**), along with several inflammatory chemokines and cytokines (**Figure 3.12E**). Similar findings have been reported in other cell types infected with SARS-CoV-2²³. Of note, chemokine genes, such as *CXCL1*, *CXCL5*, *CXCL6*, *CCL7*, and *CCL8*, were down-regulated in infected cardiac pericytes, suggesting a distinct pattern of immune activation in these cells (**Figure 3.12E**). Type I IFNs and interferon-stimulated genes (ISGs) showed uniform up-regulation after infection (**Figure 3.12F**). We also observed up-regulation of vasoactive genes (*EDN1*, *EDN2*) and down-regulation of *ACE2*, a hallmark of SARS-CoV-2 infection²⁴. Differential expression of key genes was validated by reverse transcription quantitative polymerase chain reaction (RT-qPCR) (**Figure 3.12H, J**). Given that interleukin (IL)-6 and -8 are elevated in COVID-19 patients²⁵, we performed targeted RT-qPCR for the genes encoding these cytokines and demonstrated up-regulation of *IL6* in all 3 donors, whereas *IL8* was only significantly up-regulated in one of the 3 donors (**Figure 3.13**).

Given that robust up-regulation of IFN signaling and cytokines can lead to cell death, we examined whether inhibiting the inflammatory response in infected pericytes would reduce death of infected cells (**Figure 3.7G**). TPCA-1, a potent and selective inhibitor of I- κ B kinase signaling, has been shown to blunt IFN signaling pathway and reduce production of pro-inflammatory cytokines^{26,27}. TPCA-1 treatment led to dose-dependent inhibition of type I IFN response genes and cytokine expression (**Figure 3.14A**) in infected pericytes and caused no significant cell death in uninfected cells (**Figure 3.14B**). Nuclear factor kappa-B (NF- κ B) inhibition did not inhibit pericyte infection or influence death of infected cells within the first 2 days (**Figure 3.14C**). However, NF- κ B inhibition resulted in a dose-dependent increase in survival and abundance of

infected cells 6 days after virus inoculation (**Figure 3.14D**). These data suggest that NF- κ B signaling contributes to the death of infected cardiac pericytes possibly through the generation of inflammatory mediators.

Because pericytes reside in proximity to endothelial cells and are crucial for vascular homeostasis, we next tested the effects of pericyte infection on endothelial cell activation. Pericyte conditioned medium was collected from mock-infected pericytes (Mock Cond Media) or SARS-CoV-2 infected pericytes (CoV2 Cond Media). Fresh pericyte culture medium with supernatant from uninfected Vero-TMPRSS cells was introduced to control for effects of pericyte culture media and cellular components of Vero-TMPRSS cells, which are used to propagate virus (Mock). Fresh pericyte culture medium spiked with the same amount of virus as in infected conditioned medium (6.5×10^4 focus forming units/mL) was used to control for effects of SARS-CoV-2 virus on endothelial cells (CoV2). Human umbilical vein endothelial cells were treated with a mix of endothelial cell medium and 1 of the 4 experimental conditions (Mock, CoV2, Mock Cond Media, CoV2 Cond Media) for 24 hours, at which point RNA was harvested for RT-qPCR. We observed an increase in type I IFN response (**Figure 3.15A**) and chemokine expression (CXCL2 and CCL5) in endothelial cells exposed to CoV2 conditioned media (**Figure 3.15B**), suggesting that infected pericytes produce soluble mediators that trigger inflammatory responses in cultured endothelial cells. Thrombomodulin (*THBD*) was down-regulated following exposure to CoV2 and CoV2 conditioned media (**Figure 3.15C**), highlighting that viral exposure may elicit changes in endothelial cell biology in the absence of productive infection. THBD protein expression also appeared to be reduced in infected cardiac slices (**Figure 3.15E**). These results demonstrate that infection of cardiac pericytes leads to inflammatory and vasoactive responses in infected pericytes

and uninfected endothelial cells that might be relevant to the clinical manifestations and pathology of COVID-19.

3.3.6 SARS-CoV-2 Infection in COVID-19 Patients

We obtained autopsy specimens from 2 myocarditis subjects with confirmed SARS-CoV-2 infection and 1 autopsy heart sample from a subject who did not have COVID-19 as a negative control, which underwent similar time to procurement and preservation procedures (**Table 3.1**). In situ hybridization targeting the SARS-CoV-2 *S* gene revealed evidence of viral RNA within perivascular regions of both COVID-19 cases that colocalized with *PDGFRB* mRNA (**Figure 3.16A**). Immunostaining for the SARS-CoV-2 nucleocapsid protein also revealed evidence of viral protein expression in PDGFR β ⁺ cells (**Figure 3.16B**), suggesting that cardiac pericytes are targets of SARS-CoV-2 infection in humans.

3.4 Discussion

We provide multiple lines of evidence that cardiac pericytes are targets of SARS-CoV-2 infection. Infected cardiac pericytes remain viable for several days in culture, suggesting they may indeed serve as a previously hypothesized site of replication and reservoir of virus¹⁵. Infected pericytes display an inflammatory signature and express vasoactive mediators that could affect vascular function and vasoreactivity and release soluble mediators capable of activating endothelial cells in vitro. Cardiac pericyte cell death at later stages of infection combined with an inflammatory response in endothelial cells could lead to loss of endothelial integrity, endothelial cell dysfunction, basement membrane exposure, and thrombosis. Although pericyte-like cells derived from human neural crest stem cells have been shown to be productively infected by SARS-CoV-2¹³, commercially available pericytes from the brain and placenta were not productively

infected by SARS-CoV-2 in this study. It remains unknown whether pericytes from other organs, such as the lungs and kidneys, can be infected and elicit a similar response. Although human autopsy specimens suggest that cardiac pericyte infection can occur in human disease, these studies represent the tissue state at the time of collection, typically late in disease progression, which precludes insights into in vivo viral kinetics and downstream sequelae. Future studies are needed to elucidate the pathophysiological consequences of pericyte infection in vivo and their collective contribution to cardiovascular manifestations of COVID-19.

3.4.1 Study Limitations

While the use of primary human cardiac pericytes allowed us to mechanistically dissect consequences of pericyte infection by SARS-CoV-2 in a relevant human model, in vivo studies are required to address how pericyte infection relates to the systemic, cardiac, and vascular manifestations of COVID-19. Further animal studies are also necessary to define relevant signaling mechanisms between infected pericytes and endothelial cells, including the role of contact-mediated signaling.

3.5 Conclusions

This study identifies human cardiac pericytes as a novel target of SARS-CoV-2. We demonstrate that pericyte infection leads to innate inflammatory response, NF- κ B-dependent pericyte cell death, and production of soluble factors that activate endothelial cells. These findings position mural cell infection as a new mechanism contributing to the cardiovascular manifestations of COVID-19.

3.6 Methods

Biosafety. All aspects of this study were approved by the Office of Environmental Health and Safety at Washington University School of Medicine before the initiation of this study. Work with SARS-CoV-2 was performed in a BSL-3 laboratory by personnel equipped with powered air-purifying respirators (PAPR).

Human Tissue Acquisition. Non-failing human hearts were obtained from Mid-America Transplant Services (MTS) in St. Louis, MO, USA. Failing human failure tissue (anterior wall of the left ventricle) was obtained through the Translational Cardiovascular Biobank and Repository (TCBR) at Washington University. Hearts were perfused and transported with Belzer UW Cold Storage Solution (Bridge to Life). Human organotypic cardiac slices were made from fresh tissue from non-failing heart sources, and cardiac pericytes were isolated from fresh tissue from both failing and non-failing heart sources, as described in detail in subsequent Detailed Methods subsections. Control and COVID-19 myocarditis autopsy specimens were obtained from Barnes Jewish Hospital in St. Louis, MO. Detailed subject information is available in **Table S1**. Experimental protocols were approved by the Washington University in St. Louis Institutional Review Board (IRB). Non-failing human heart tissue and autopsy specimens were exempt from IRB and failing human heart tissue was procured under the TCBR IRB Protocol #201104172. Informed consent was obtained for all tissue used in this study, and all experiments were performed in accordance with all human research guidelines.

Preparation and culture of human organotypic cardiac slices. Organotypic cardiac slices were made from the left ventricle of explanted human hearts as previously described¹⁶. Briefly, an approximately 1 cm by 1 cm cube of left ventricular tissue was cut in the University of Wisconsin

(UW) cold storage solution from a region near the left anterior descending artery and the circumflex artery. Premade 4% agarose gel was glued to the tissue stage of a vibrating microtome (7000 smz-2, Campden Instruments) and the tissue cube was mounted endocardium up using Histoacryl glue (B. Braun). 400 μ m thickness slices were cut tangential to the endocardium, in a 4°C bath of oxygenated (100% O₂) modified Tyrode's solution with excitation-contraction uncoupler 2,3-butanedione (NaCl 140 mM, KCl 6 mM, glucose 10 mM, HEPES 10 mM, MgCl₂ 1 mM, CaCl₂ 1.8 mM, BDM 10 mM, pH 7.4). Slices were cultured on porous transwell inserts (PICM0RG50, Millipore) in 6-well culture plates with 1.1 ml of culturing medium (medium 199 (M4530, Sigma) supplemented with 1% penicillin-streptomycin, 1X ITS supplement, and 10 mM 2,3-butanedione). Culture plates were placed in a 37°C incubator with humidified air and 5% CO₂ for 24 or 48 hrs before slices were harvested for experiments. The medium was changed every 24 hrs until harvest.

Primary human cardiac pericyte isolation and culture. Human myocardium was dissected into ~200 mg pieces and digested in 3 mL of DMEM containing 250 U/mL collagenase IV (Sigma C5138), 60 U/mL hyaluronidase type 1-s (Sigma H3506), and 60 U/mL DNase I (Sigma D4527) for 45 min at 37°C as adapted from previously published work²⁸. Following digestion and red blood cell lysis, the resultant single-cell suspension was incubated with anti-CD146 APC (Biolegend cat#361315), anti-CD56 APC-Cy7 (Biolegend cat#362511), anti-CD34 PE-Cy7 (Biolegend cat#343615), anti-CD45 BV421 (Biolegend cat#368521), and anti-CD117 PE (Biolegend cat#375206). Pericytes were identified as CD146⁺/CD34⁻/CD56⁻/CD117⁻/CD45⁻ cells as previously published²⁹. Cells were isolated by flow cytometric cell sorting on a BD FACSMelody and cultured in Pericyte Medium (Sciencell cat#1201). For infection experiments,

cells were plated at 8×10^3 cells/cm² in flat-bottomed 24-well plates 2-4 days before the start of an experiment.

Placental pericyte culture. Proliferating human pericytes from the placenta (hPC-PL) (Promocell, C-12981, Lot: 463Z019.1; ZenBio, PER-F, Lot: ZB00822) were cultured with 4,000 cells per cm² seeding density in Pericyte Growth Medium 2 (Promocell, C28041) or Pericyte Growth Medium (Neuromics, PER-1) according to published company protocols. The medium was changed every 2-3 days, and cells were passaged when >70% confluency was reached. Cells were detached with Accutase (STEMCELL Technologies) and harvested via centrifugation. RT-qPCR was performed on hPC-PL cell pellets in RNAlater (PromoCell, C-14095, Lots: 434Z033) and cultured hPC-PL cells (Promocell, C-12980, Lot: 463Z019.1; ZenBio, PER-F, Lot: ZB00822).

Brain pericyte culture. Human brain microvascular pericytes (HBMVP) (Neuromics, HMP104, Lots: 2870, 2871, and 2872) were cultured with 4,000 cells per cm² seeding density in Pericyte Growth Medium (Neuromics, PGB001) according to published company protocol. The medium was changed every 2-3 days, and cells were passaged when >70% confluency was reached. Cells were detached with a Detach Kit (PromoCell) and harvested via centrifugation. RT-qPCR was performed on cultured HCMEC cells.

Endothelial cell culture. Human cardiac microvascular endothelial cells (HCMEC) (PromoCell, C-12285, Lot: 446Z001.1) were cultured with 15,000 cells per cm² seeding density in Endothelial Cell Growth Medium MV (Promocell, C22120) according to published company protocol. The medium was changed every 2-3 days, and cells were passaged when >70% confluency was reached. Cells were detached with a Detach Kit (PromoCell) and harvested via centrifugation. RT-qPCR was performed on HCMEC cell pellets in RNAlater (PromoCell, C-

14029, Lots: 439Z034.6 and 446Z026.3) and cultured HCMEC cells (PromoCell, C-12285, Lot: 446Z001.1).

Human umbilical vein endothelial cells (HUVEC) were cultured at 10,000 cells per cm² seeding density in vascular basal medium (ATCC PSC-100-030) with Endothelial Cell Growth Kit-VEGF supplement (ATCC PSC-100-041) on rat tail collagen coated plates (Sigma) according to company published protocol. The medium was changed every 3-4 days and cells were passaged at 80-90% confluency with 0.05% Trypsin (Sigma).

Endothelial cell - pericyte co-culture. Co-culture wells were coated with rat collagen and HUVEC and primary cardiac pericyte suspension was mixed and plated at 7,500 cells per cm² of each cell type (15,000 cells per cm² total). 50:50 mix of pericyte and endothelial cell media was used for culture. Cells were cultured for 4 days to allow attachment and equilibration and then infected at MOI 1 with SARS-CoV-2 mNeonGreen (see details in “Virus and infection” section below).

Small molecule inhibitors. Small molecule inhibitors TPCA-1 (IkB IKK inhibitor, Tocris 2559), camostat mesylate (serine protease inhibitor, Selleckem S2874), E-64 (cysteine protease inhibitor, Selleckem S7379), Bafilomycin-A1 (H⁺-ATPase inhibitor, Sigma SML 1661) were diluted in DMSO at 10mM and stored in -20C. Working dilutions were made fresh prior to every experiment in pericyte medium.

Virus and infection. The USA_WA1/2020 isolate of SARS-CoV-2 (WA1/2020) was obtained from the United States Centers for Disease Control (CDC). The NeonGreen SARS-CoV-2 virus stock was obtained from P-Y. Shi (University of Texas Medical Branch, Galveston, TX)¹⁹. B.1.1.7 (Alpha), B.1.351 (Beta), and B.1.617.2 (Delta) strains of SARS-CoV-2 were obtained from

infected individuals. All viral stocks were propagated on Vero-TMPRSS2 cells (a gift of S. Ding Washington University), deep-sequenced with the ARTIC protocol for Illumina sequencing³⁰, and found to have no mutations in the S gene furin cleavage site (positions 23606-23608 of NC_045512.2).

Inoculations of cardiac slices were performed at a multiplicity of infection (MOI) of ~1. This was performed by inoculating each slice with 500 μ L of virus stock containing $\sim 5 \times 10^5$ focus forming units (FFU) of SARS-CoV-2, with half of the inoculum delivered directly onto the tissue and half added to the media below the transwell insert.

Inoculations of primary cells were performed at an MOI of 1 unless stated otherwise. Cells were replated for the experiments and allowed to settle for at least 2 days before the infection. The viral stock was diluted by the appropriate cell culture medium and added onto cells instead of the growth medium for 3 hours to allow viral entry. After incubation, cells were washed with 1 mL of warm PBS three times and replaced with fresh culture medium (unless stated otherwise). Supernatant from Vero-TMPRSS2 cells not infected with the virus and processed identically to the viral stock preparation procedures was used as a mock at the largest volume of viral stock used for the experiment. All stock propagation and infection of cell cultures were performed at an approved Biosafety Level 3 facility.

Focus-Forming Assay. Vero-TMPRSS2-hACE2 cells²² (a gift from A. Creanga and B. Graham, National Institutes of Health) were seeded at a density of 5×10^4 cells per well in flat-bottom 96-well tissue culture plates with DMEM supplemented with 10% FBS. The next day, media was replaced with 100 μ L of 10-fold serial dilutions of the material to be titered (diluted in

DMEM 5% FBS). After a one-hour incubation period, 135 μ L of methylcellulose overlay was added. Plates were incubated for 24 hrs, then fixed with 4% paraformaldehyde (PFA) in phosphate-buffered saline for 20 min, followed by permeabilization with saponin-containing buffer. Plates were incubated overnight at 4°C in 50 μ L of permeabilization buffer containing 1:3000 dilution of supernatant collected from the murine IgG1 hybridoma SARS2-16.C6³¹ anti-spike monoclonal antibody. Following washing, 50 μ L of goat anti-human secondary antibody conjugated to HRP (Sigma AP504P), diluted 1:500 in permeabilization buffer, was added for 3 hours at room temperature with shaking. The assay was developed with 50 μ L of KPL Trueblue (SeraCare), wells with foci were imaged and automatically quantified on a Biospot plate reader (Cellular Technology Limited).

Pericyte conditioned medium. To obtain primary cardiac pericyte conditioned medium, cardiac pericytes were plated and allowed to reach 90% confluence. Following 3-hour inoculation with SARS-CoV-2 WA1/2020 at MOI1 or Vero-TMPRSS2 mock control, the infectious media was replaced as described above with fresh pericyte medium. After 4 days of infection, conditioned pericyte medium was collected, centrifuged at 5000xg to remove cellular debris, and stored at -80C for further use. Media was assessed for live virus by focus-forming assay (see details in “Focus-Forming Assay” section above).

Quantitative RT-PCR. For primary cell lines, RNA was isolated using the RNeasy Plus Mini Kit (Qiagen) or RNeasy Micro Kit (Qiagen) with gDNA removal. RNA concentration was determined with NanoDrop One (ThermoFisher) and reverse-transcribed using the High-Capacity cDNA Reverse Transcription Kit (ThermoFisher) or iScript Reverse Transcription Supermix (BioRad). Gene expression was assayed using the PowerSYBR Green PCR MasterMix (Applied

Biosystems) using primers listed below and quantified using the QuantStudio Flex 6 Real-Time PCR system (Applied Biosystems). Relative fold changes were calculated using the comparative C_T method, with glyceraldehyde 3-phosphate dehydrogenase (GAPDH) as an internal reference gene.

Table 3.2. Human RT-qPCR oligonucleotide sequences

Source	Target	Forward (5'-3')	Reverse (5'-3')
IDT	<i>GAPDH</i>	GAACATCATCCCTGCCTCTAC	CAGTGAGCTTCCCCTTCAG
	<i>NOTCH3</i>	CGAGAGCTGCAGTCAGAATATC	GGCAGGCACAGTAGAAAGAA
	<i>NG2</i>	AACCAGGGTAACCTCCTACA	TCCTTCTCCTTGCCCTCTTA
	<i>TCF21</i>	CAGATCCTGGCTAACGACAAA	CCACTTCTTTTCAGGTCACTCTC
	<i>DCN</i>	CAGTTGAGGTGGGTTTCCATAG	CCCAGCATAACGTCTTGGATTT
	<i>PECAM</i>	AGGATGACGTGCTGTTTTAC	CACTCCTTCCACCAACACCT
	<i>TNNT2</i>	ACAGAGCGGAAAAGTGGGAAG	CTCATATTTCTGCTGCTTGAAC
	<i>ACE2</i>	TCCATTGGTCTTCTGTCACCCG	AGACCATCCACCTCCACTTCTC
	<i>TMPRSS2</i>	CCTCTAACTGGTGTGATGGCGT	TGCCAGGACTTCCTCTGAGATG
	<i>TMPRSS4</i>	GCAGTTCCCACTCACTTTCT	CCCTCCATTCTGCTTCGTAAA
	<i>CTSB</i>	GCTTCGATGCACGGGAACAATG	CATTGGTGTGGATGCAGATCCG
	<i>CTSL</i>	GGAGACATGACCAGTGAAGAAT	CGTAGCCTTTCTCTCTCCAATC
	<i>FURIN</i>	CTACTCCGCAGATGGGTTTAAT	GTCAGCGTCCCATAGTTGTT
	<i>CXCL2</i>	CTGCTCCTGCTCCTGGTG	AGGGTCTGCAAGCACTGG
Sigma-Aldrich	<i>OAS1</i>	ATTGTAAGAAGAAGCTTGGG	CAGAGTTGCTGGTAGTTTATG
	<i>MX1</i>	CAGGCTTTGTGAATTACAGG	TCTTCAATTTTGGACTTGGC
	<i>IFNB1</i>	ATTCTAACTGCAACCTTTTCG	GTTGTAGCTCATGGAAAGAG
	<i>TNF</i>	AGGCAGTCAGATCATCTTC	TTATCTCTCAGCTCCACG
	<i>IL1B</i>	CTAAACAGATGAAGTGCTCC	GGTCATTCTCCTGGAAGG
	<i>IL1A</i>	AGAGGAAGAAATCATCAAGC	TTATACTTTGATTGAGGGCG
	<i>IL6</i>	GCAGAAAAAGGCAAAGAATC	CTACATTTGCCGAAGAGC

<i>IL8</i>	GTTTTGAAGAGGGCTGAG	TTTGCTTGAAGTTTCACTGG
<i>EDN1</i>	CAAGCAGGAAAAGAACTCAG	CTGGTTTGTCTTAGGTGTTT
<i>EDN2</i>	TGAGGGACATTTCCACAG	GCTTCCTTCCCAATGTTC
<i>ANGPT1</i>	ATGTTAACAGGAGGATGGTG	GAAGTAGTGCCACTTTATCC
<i>PDGFRB</i>	GGGAAGAGAAGTTTGAGATTC	TTCTTTTTGTAACCTTCGCC
<i>PROCR</i>	TTCTCTTTCCCTAGACTGC	CATATGAAGTCTTTGGAGGC
<i>VWF</i>	TGTATCTAGAACTGAGGCTG	CCTTCTGGGTCATAAAGTC
<i>THBD</i>	AAATGCTATGAGATGCATGG	TTGAAAATCAGAGATGGTGC
<i>PECAMI</i>	AGATACTCTAGAACGGAAGG	CAGAGGTCTTGAAATACAGG

Fluorescent In situ hybridization. Autopsy cardiac specimens were formalin-fixed and paraffin-embedded. Human organotypic cardiac slices were fixed in 10% neutral buffered formalin for 7 days to ensure viral inactivation, dehydrated via an ethanol gradient, and then embedded in paraffin blocks. RNA-ISH was performed on 5 µm tissue sections using the RNAScope® Multiplex Fluorescent V2 Assay (Advanced Cell Diagnostics) according to the manufacturer's protocol. Briefly, slides were deparaffinized with xylene (5 min, twice), washed in 100% ethanol (2 min, twice), and incubated with RNAScope® Hydrogen Peroxide for 10 min to quench endogenous peroxidases. Target retrieval was performed with RNAScope® Target Retrieval Buffer at 99-100°C for 30 min followed by treatment with RNAScope® Protease Plus for 30 min at 37°C. Slides were then hybridized with cataloged target probes at 40°C for 2 hrs, and signals for each channel were then amplified according to the manufacturer's instructions. OPAL fluorophores (520, 570, and 690) were used at 1:750 dilution in TSA buffer to visualize targets. Slides were treated with TrueBlack Lipofuscin Autofluorescence Quencher (Biotium) for 5 min, stained with Spectral Dapi (Advanced Cell Diagnostics) for 30 sec, and mounted in Vectashield PLUS mounting medium (Vector Labs). Samples were imaged on an LSM700 confocal

microscope using ZEN software (Zeiss). Quantification of viral targets was performed with the open-source Color Pixel Counter plugin for ImageJ (National Institutes of Health).

Table 3.3. Human ISH Target Probes

Target	Probe	Product Number
<i>SARS-CoV-2 S (sense)</i>	V-nCoV2019-S-C2, V-nCoV2019-S-C3	848561-C2, C3
<i>SARS-CoV-2 S (antisense)</i>	V-nCoV2019-S-sense-C2	845701-C2
<i>SARS-CoV-2 ORF1ab (antisense)</i>	V-nCoV2019-orf1ab-sense	859151
<i>PDGFRβ</i>	Hs-PDGFRB-C4	548991-C4

Immunostaining. Cardiac Tissue: Slices were fixed in 10% neutral buffered formalin for 7+ days, dehydrated via an ethanol gradient, and then embedded in paraffin blocks. 5 μ m thick sections were placed on slides and baked at 60°C for at least 1 hour. Slides were deparaffinized with Xylenes and rehydrated in an ethanol gradient. Immunohistochemistry was performed using the OPAL™ 4-Color Manual Kit (Akoya Biosciences). Briefly, antigen retrieval was performed with AR6 buffer at 99-100°C for 30 min, followed by washing in TBS-Tween 0.5% and blocking for 10 min in Ms + Rb Blocking Solution (Akoya Biosciences). Sections were incubated with primary antibodies overnight at 4°C in blocking solution, washed, and then incubated with Opal Polymer HRP Ms + Rb solution for 10 min. Slides were then washed and incubated with the desired reactive fluorophore (Opal 520, Opal 570, or Opal 690) for 10 min followed by washing. For multiplexing, the slides were then stripped in AR6 buffer at 99-100°C for 15 min and then cooled and washed. Slides were then subjected to the next cycle of blocking through fluorophore incubations until all targets had been processed. Slides were treated with TrueBlack Lipofuscin Autofluorescence Quencher (Biotium) for 5 min, stained with Opal Spectral Dapi for 5 min, and mounted in Vectashield PLUS mounting medium (Vector Labs). Viral nucleocapsid protein was

stained with anti-Coronavirus Nucleocapsid Antibody (1:2000, SinoBiological, 40143-R001). The following antibodies were used for identifying cell types: anti-PDGFR β [Y92] - C-terminal (1:1000, Abcam, ab32570), Neural/Glial Antigen 2 (NG2) monoclonal antibody (9.2.27) (1:1000, Invitrogen, 14-6504-82), anti-CD31/PECAM-1 (1:1000, Novus Biologicals, NB100-2284), and Anti-Cardiac Troponin I (1:3000, Abcam, ab47003). Thrombomodulin was stained with Anti-Thrombomodulin antibody [EPR4051] (1:1000, Abcam, ab109189). Samples were imaged on an LSM700 confocal microscope using ZEN software (Zeiss).

Cardiac Pericytes: Cell culture samples for microscopy were seeded in chamber slides at 3500 cells/cm² and fixed in 4% PFA for 20 min at room temperature, followed by washing in TBS-Tween 0.5%. Immunohistochemistry was performed using the OPAL™ 4-Color Manual Kit (Akoya Biosciences). Cells were incubated in Ms + Rb Blocking Solution for 10 min and then incubated with primary antibodies for 3 hr at room temperature. Cells were then washed and incubated with Opal Polymer HRP Ms + Rb solution for 10 min. Cells were then washed and incubated with the desired reactive fluorophore (Opal 520, Opal 570, or Opal 690) for 10 min followed by washing. For multiplexing, the slides were then stripped in AR6 buffer at 99-100°C for 15 min, cooled, and washed. Slides were then subjected to the next cycle of blocking through fluorophore incubations until all targets had been processed. Pericyte markers were stained using the following antibodies: anti-PDGFR beta [Y92] - C-terminal (1:1000, Abcam, ab32570) and Neural/Glial Antigen 2 (NG2) monoclonal antibody (9.2.27) (1:1000, Invitrogen, 14-6504-82). Viral nucleocapsid protein was stained with anti-Coronavirus Nucleocapsid antibody (1:2000, SinoBiological, 40143-R001). Samples were imaged on an LSM700 confocal microscope using ZEN software (Zeiss).

TUNEL Staining. Click-iT™ TUNEL Alexa Fluor™ 594 Imaging Assay (ThermoFisher, C10246) was performed to detect the presence of DNA strand breaks as described in the manufacturer's protocol. Briefly, cells were fixed with 4% paraformaldehyde for 15 min and then permeabilized with 0.25% Triton X-100 for 20 min at room temperature. For positive control, cells were incubated with 1 unit of DNase I (ThermoFisher, 18068015) diluted into 1X DNase I Reaction Buffer for 30 min at room temperature. The TdT reaction and Click-iT Plus reaction were then performed according to the protocol without modification. Following the completion of these reactions, immunohistochemistry was performed using the OPAL™ 4-Color Manual Kit (Akoya Biosciences) followed by DNA staining with DAPI as described above.

RNA Sequencing. RNA was extracted using the 5X MagMax Pathogen RNA/DNA isolation kit (Thermo Scientific cat# 4462359) on the Kingfisher Flex extraction robot (Thermo Scientific). Total RNA integrity was determined using a TapeStation, and library preparation was performed with 10 ng of total RNA for samples with a Bioanalyzer RIN score greater than 8.0. ds-cDNA was prepared using the SMARTer Ultra Low RNA Kit for Illumina Sequencing (Takara-Clontech) per the manufacturer's protocol. cDNA was then fragmented using a Covaris E220 sonicator using peak incident power 18, duty factor 20%, cycles per burst 50 for 120 seconds. The cDNA was blunt-ended, had an A base added to the 3' ends, and then had Illumina sequencing adapters ligated to the ends. Ligated fragments were then amplified for 12-15 cycles using primers incorporating unique dual index tags. The fragments for each sample were then pooled in an equimolar ratio and sequenced on an Illumina NovaSeq-6000 using paired-end reads extending 150 bases. Basecalls and demultiplexing were performed with Illumina's Real-Time Analysis version 1.9 and the reads for each sample were then aligned to the Homo sapiens Ensembl release

76 primary assembly and SARS-CoV-2 Wuhan-Hu-1 strain with STAR version 2.5.1a³². Gene counts were derived from the number of uniquely aligned unambiguous reads by Subread:featureCount version 1.4.6-p5³³. Isoform expression of known Ensembl transcripts was estimated with Salmon version 0.8.2³⁴. Sequencing performance was assessed for the total number of aligned reads, the total number of uniquely aligned reads, and features detected. The ribosomal fraction, known junction saturation, and read distribution over known gene models were quantified with RSeQC version 2.6.2³⁵.

All gene counts were then imported into the R/Bioconductor package EdgeR³⁶ and TMM normalization size factors were calculated to adjust for samples for differences in library size. Ribosomal genes and genes not expressed in the smallest group size minus one sample greater than one count-per-million were excluded from further analysis. The TMM size factors and the matrix of counts were then imported into the R/Bioconductor package Limma³⁷. Weighted likelihoods based on the observed mean-variance relationship of every gene and sample were then calculated for all samples and the count matrix was transformed to moderated log₂ counts-per-million with Limma's voomWithQualityWeights³⁸. The performance of all genes was assessed with plots of the residual standard deviation of every gene to their average log-count with a robustly fitted trend line of the residuals. Differential expression analysis was then performed to analyze for differences between conditions and the results were filtered for only those genes with Benjamini-Hochberg false-discovery rate adjusted p-values less than or equal to 0.05.

For each contrast extracted with Limma, global perturbations in known Gene Ontology (GO) terms, MSigDb, and KEGG pathways were detected using the R/Bioconductor package GAGE³⁹ to test for changes in expression of the reported log₂ fold-changes reported by Limma

in each term versus the background log 2 fold-changes of all genes found outside the respective term. The R/Bioconductor package heatmap3⁴⁰ was used to display heatmaps across groups of samples for each GO or MSigDb term with a Benjamini-Hochberg false-discovery rate adjusted p-value less than or equal to 0.05. Perturbed KEGG pathways where the observed log 2 fold-changes of genes within the term were significantly perturbed in a single-direction versus background or any direction compared to other genes within a given term with p-values less than or equal to 0.05 were rendered as annotated KEGG graphs with the R/Bioconductor package Pathview⁴¹.

To find the most critical genes, the Limma voomWithQualityWeights transformed log 2 counts-per-million expression data was then analyzed via weighted gene correlation network analysis with the R/Bioconductor package WGCNA⁴². Briefly, all genes were correlated across each other by Pearson correlations and clustered by expression similarity into unsigned modules using a power threshold empirically determined from the data. An eigengene was then created for each *de novo* cluster and its expression profile was then correlated across all coefficients of the model matrix. Because these clusters of genes were created by expression profile rather than known functional similarity, the clustered modules were given the names of random colors where grey is the only module that has any pre-existing definition of containing genes that do not cluster well with others. These *de novo* clustered genes were then tested for functional enrichment of known GO terms with hypergeometric tests available in the R/Bioconductor package clusterProfiler⁴³. Significant terms with Benjamini-Hochberg adjusted p-values less than 0.05 were then collapsed by similarity into clusterProfiler category network plots to display the most significant terms for each module of hub genes to interpolate the function of each significant

module. The information for all clustered genes for each module was then combined with their respective statistical significance results from Limma to determine whether or not those features were also found to be significantly differentially expressed.

Flow cytometry. Cells were dissociated to single-cell suspension with 0.25% trypsin (Gibco). Pericytes were identified using anti-human PDGFR β APC (Biolegend cat# 323608) and endothelial cells were identified using anti-human CD31 PE (Biolegend cat# 303106) stained at 1:200 at 4°C for 20 min. Viability was determined by Zombie-violet amine-reactive dye (Biolegend cat# 423113) at a dilution of 1:500 in 100 μ L of PBS at 4°C for 20 min. Infection was assessed by intracellular mNeonGreen levels. After fixation with 4% PFA in PBS for 20 min, cells were analyzed on the FACS Melody (Becton Dickinson Biosciences). Analysis was performed using FlowJo 10.7.1 (Becton Dickinson & Co).

Statistical analysis. All data are expressed as means \pm standard error of the mean (SEM). For comparison of more than two experimental groups, the statistical significance of observed differences in mean was evaluated using a one-way or two-way analysis of variance (ANOVA), followed by a post hoc Tukey's, Dunnett's, or Sidak's multiple comparison test. For comparison of two experimental groups, an equal or unequal variance Student's t-test, as determined by an F test for equality of two variances, was used and a two-tailed p-value of <0.05 was considered statistically significant. In comparing correlated samples, repeated-measures ANOVA was used. All data were analyzed with parametric tests, given the small sample sizes for each experiment with insufficient power to reject the null hypothesis of distribution normality. All analyses were performed using Prism Version 9 (GraphPad, San Diego, California).

3.7 References

1. Gupta, A. *et al.* Extrapulmonary manifestations of COVID-19. *Nat Med* **26**, 1017–1032 (2020).
2. Katsoularis, I., Fonseca-Rodríguez, O., Farrington, P., Lindmark, K. & Connolly, A.-M. F. Risk of acute myocardial infarction and ischaemic stroke following COVID-19 in Sweden: a self-controlled case series and matched cohort study. *The Lancet* **398**, 599–607 (2021).
3. Nägele, M. P., Haubner, B., Tanner, F. C., Ruschitzka, F. & Flammer, A. J. Endothelial dysfunction in COVID-19: Current findings and therapeutic implications. *Atherosclerosis* **314**, 58–62 (2020).
4. Sims, J. T. *et al.* Characterization of the cytokine storm reflects hyperinflammatory endothelial dysfunction in COVID-19. *Journal of Allergy and Clinical Immunology* **147**, 107–111 (2021).
5. Pellegrini, D. *et al.* Microthrombi as a Major Cause of Cardiac Injury in COVID-19. *Circulation* **143**, 1031–1042 (2021).
6. Bailey Adam L. *et al.* SARS-CoV-2 Infects Human Engineered Heart Tissues and Models COVID-19 Myocarditis. *JACC: Basic to Translational Science* **6**, 331–345 (2021).
7. Bearnse, M. *et al.* Factors associated with myocardial SARS-CoV-2 infection, myocarditis, and cardiac inflammation in patients with COVID-19. *Modern Pathology* (2021) doi:10.1038/s41379-021-00790-1.
8. Bojkova, D. *et al.* SARS-CoV-2 infects and induces cytotoxic effects in human cardiomyocytes. *Cardiovascular Research* (2020) doi:10.1093/cvr/cvaa267.
9. Lindner, D. *et al.* Association of Cardiac Infection With SARS-CoV-2 in Confirmed COVID-19 Autopsy Cases. *JAMA Cardiology* **5**, 1281–1285 (2020).
10. McCracken, I. R. *et al.* Lack of Evidence of Angiotensin-Converting Enzyme 2 Expression and Replicative Infection by SARS-CoV-2 in Human Endothelial Cells. *Circulation* **143**, 865–868 (2021).
11. Chung, M. K. *et al.* COVID-19 and Cardiovascular Disease. *Circ Res* **128**, 1214–1236 (2021).
12. Robinson, F. A. *et al.* Role of angiotensin-converting enzyme 2 and pericytes in cardiac complications of COVID-19 infection. *American Journal of Physiology-Heart and Circulatory Physiology* **319**, H1059–H1068 (2020).
13. Wang, L. *et al.* A human three-dimensional neural-perivascular ‘assembloid’ promotes astrocytic development and enables modeling of SARS-CoV-2 neuropathology. *Nat Med* **27**, 1600–1606 (2021).
14. Murray, I. R. *et al.* Skeletal and cardiac muscle pericytes: Functions and therapeutic potential. *Pharmacology & Therapeutics* **171**, 65–74 (2017).
15. Chen, L., Li, X., Chen, M., Feng, Y. & Xiong, C. The ACE2 expression in human heart indicates new potential mechanism of heart injury among patients infected with SARS-CoV-2. *Cardiovascular Research* **116**, 1097–1100 (2020).

16. Kang, C. *et al.* Human Organotypic Cultured Cardiac Slices: New Platform For High Throughput Preclinical Human Trials. *Sci Rep* **6**, 28798 (2016).
17. Chen, W. C. W. *et al.* Human Myocardial Pericytes: Multipotent Mesodermal Precursors Exhibiting Cardiac Specificity. *STEM CELLS* **33**, 557–573 (2015).
18. Dore-Duffy, P. & Cleary, K. Morphology and Properties of Pericytes. in *The Blood-Brain and Other Neural Barriers: Reviews and Protocols* (ed. Nag, S.) 49–68 (Humana Press, 2011). doi:10.1007/978-1-60761-938-3_2.
19. Xie, X. *et al.* An Infectious cDNA Clone of SARS-CoV-2. *Cell Host & Microbe* **27**, 841–848.e3 (2020).
20. Hoffmann, M. *et al.* SARS-CoV-2 Cell Entry Depends on ACE2 and TMPRSS2 and Is Blocked by a Clinically Proven Protease Inhibitor. *Cell* **181**, 271–280.e8 (2020).
21. Simmons, G., Zmora, P., Gierer, S., Heurich, A. & Pöhlmann, S. Proteolytic activation of the SARS-coronavirus spike protein: Cutting enzymes at the cutting edge of antiviral research. *Antiviral Research* **100**, 605–614 (2013).
22. VanBlargan, L. A. *et al.* A potently neutralizing SARS-CoV-2 antibody inhibits variants of concern by utilizing unique binding residues in a highly conserved epitope. *Immunity* **54**, 2399–2416.e6 (2021).
23. Deinhardt-Emmer, S. *et al.* SARS-CoV-2 Causes Severe Epithelial Inflammation and Barrier Dysfunction. *Journal of Virology* **95**, e00110-21 (2021).
24. Ni, W. *et al.* Role of angiotensin-converting enzyme 2 (ACE2) in COVID-19. *Critical Care* **24**, 422 (2020).
25. Del Valle, D. M. *et al.* An inflammatory cytokine signature predicts COVID-19 severity and survival. *Nat Med* **26**, 1636–1643 (2020).
26. Du, Z. *et al.* Inhibition of Type I Interferon-Mediated Antiviral Action in Human Glioma Cells by the IKK Inhibitors BMS-345541 and TPCA-1. *Journal of Interferon & Cytokine Research* **32**, 368–377 (2012).
27. Nan, J. *et al.* TPCA-1 Is a Direct Dual Inhibitor of STAT3 and NF- κ B and Regresses Mutant EGFR-Associated Human Non-Small Cell Lung Cancers. *Molecular Cancer Therapeutics* **13**, 617–629 (2014).
28. AU - Bajpai, G. & AU - Lavine, K. J. Isolation of Macrophage Subsets and Stromal Cells from Human and Mouse Myocardial Specimens. *JoVE* e60015 (2019) doi:10.3791/60015.
29. Chen, W. C. W. *et al.* Human Myocardial Pericytes: Multipotent Mesodermal Precursors Exhibiting Cardiac Specificity. *Stem Cells* **33**, 557–573 (2015).
30. R&d, D. P. *et al.* COVID-19 ARTIC v3 Illumina library construction and sequencing protocol. (2020).

31. VanBlargan, L. A. *et al.* A potentially neutralizing SARS-CoV-2 antibody inhibits variants of concern by utilizing unique binding residues in a highly conserved epitope. *Immunity* S1074-7613(21)00348-4 (2021) doi:10.1016/j.immuni.2021.08.016.
32. Dobin, A. *et al.* STAR: ultrafast universal RNA-seq aligner. *Bioinformatics* **29**, 15–21 (2013).
33. Liao, Y., Smyth, G. K. & Shi, W. featureCounts: an efficient general purpose program for assigning sequence reads to genomic features. *Bioinformatics* **30**, 923–930 (2014).
34. Patro, R., Duggal, G., Love, M. I., Irizarry, R. A. & Kingsford, C. Salmon provides fast and bias-aware quantification of transcript expression. *Nat Methods* **14**, 417–419 (2017).
35. Wang, L., Wang, S. & Li, W. RSeQC: quality control of RNA-seq experiments. *Bioinformatics* **28**, 2184–2185 (2012).
36. Robinson, M. D., McCarthy, D. J. & Smyth, G. K. edgeR: a Bioconductor package for differential expression analysis of digital gene expression data. *Bioinformatics* **26**, 139–140 (2010).
37. Ritchie, M. E. *et al.* limma powers differential expression analyses for RNA-sequencing and microarray studies. *Nucleic Acids Research* **43**, e47–e47 (2015).
38. Liu, R. *et al.* Why weight? Modelling sample and observational level variability improves power in RNA-seq analyses. *Nucleic Acids Research* **43**, e97–e97 (2015).
39. Luo, W., Friedman, M. S., Shedden, K., Hankenson, K. D. & Woolf, P. J. GAGE: generally applicable gene set enrichment for pathway analysis. *BMC Bioinformatics* **10**, 161 (2009).
40. Zhao, S., Guo, Y., Sheng, Q. & Shyr, Y. Advanced Heat Map and Clustering Analysis Using Heatmap3. *BioMed Research International* **2014**, 986048 (2014).
41. Luo, W. & Brouwer, C. Pathview: an R/Bioconductor package for pathway-based data integration and visualization. *Bioinformatics* **29**, 1830–1831 (2013).
42. Langfelder, P. & Horvath, S. WGCNA: an R package for weighted correlation network analysis. *BMC Bioinformatics* **9**, 559 (2008).
43. Yu, G., Wang, L.-G., Han, Y. & He, Q.-Y. clusterProfiler: an R Package for Comparing Biological Themes Among Gene Clusters. *OMICS* **16**, 284–287 (2012).

Table 3.1 Patient and donor Demographics

ID	Use of Tissue	Sex	Age (yrs)	Cause of Death/ Procurement	Comorbidities					
					HF Etiology	HTN	CAD	DM	BMI	Smoker (>20 packs/yr)
1	COVID Case 1	M	54	Cardiac Arrest	None	N	N	N	-	N
2	COVID Case 2	M	61	Cardiac Arrest	None	N	N	N	-	N
3	Autopsy Control	M	68	Respiratory Failure	None	N	N	N	27.4	N
4	Organotypic Slices Donor 1	F	36	Anoxia	None	Y	N	N	21.0	Y
5	Organotypic Slices Donor 2	M	49	Anoxia	None	N	N	N	27.4	Y
6	Organotypic Slices Donor 3	F	34	Anoxia/ Cardiac Arrest	None	N	N	N	34.5	N
7	Pericyte Donor 1	M	63	Explant	ICM	Y	Y	Y	35.0	Y
8	Pericyte Donor 2	M	45	Explant	NICM (chemo induced)	Y	N	Y	23.2	Y
9	Pericyte Donor 3	F	38	Anoxia	None	N	N	N	29.2	Y

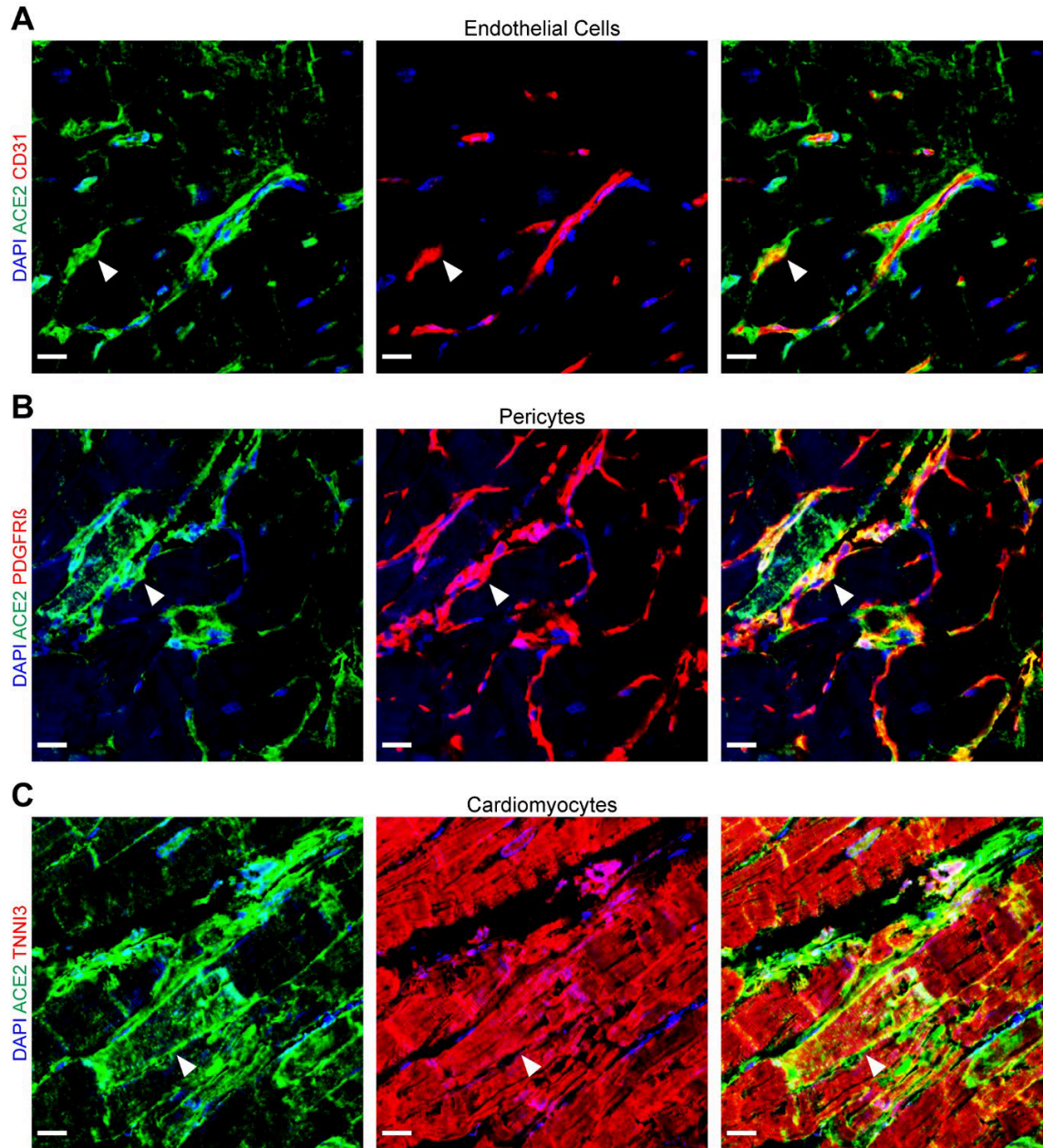


Figure 3.1. ACE2 protein is expressed on cardiac pericytes and cardiomyocytes. (A-C) Immunostaining was performed on human left ventricular tissue to determine cell types expressing ACE2 in the heart (n=3 donors). (A) Representative immunostaining for ACE2 (green) and endothelial cell marker CD31 (red) demonstrates that ACE2 is expressed in cells in close contact with endothelial cells. (B) Representative immunostaining for ACE2 (green) and pericyte marker PDGFR β (red) demonstrates that pericytes express ACE2 as indicated by the overlay (arrowhead). (C) Representative immunostaining for the ACE2 (green) and the cardiomyocyte marker TNNI3 (red) reveals that cardiomyocytes can express ACE2 as indicated by the overlay (arrowhead). All scale bars 10 μ m

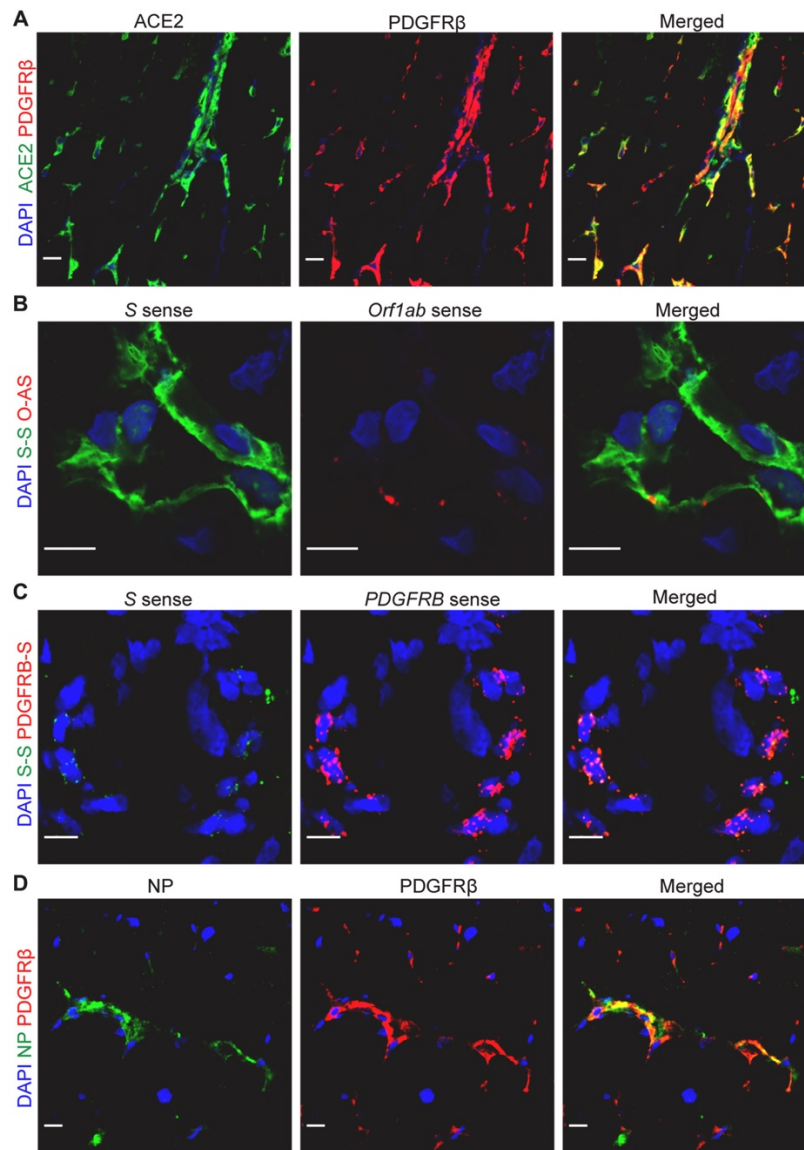


Figure 3.2 Detection of SARS-CoV-2 in Pericytes of Inoculated Ventricular Organotypic Slices (A) Representative immunostaining for angiotensin-converting enzyme 2 (ACE2) (green) and platelet-derived growth factor receptor beta (PDGFRβ) (red) in human left ventricular tissue (n = 3 independent donor hearts). (B to D) Cardiac slices were inoculated with 5×10^5 focus forming units of SARS-CoV-2 WA1/2020 (approximately MOI of 1) and harvested 48 hours later (n = 3). (B) Representative RNA in situ hybridization of SARS-CoV-2 *S* sense (S-S) (green) and SARS-CoV-2 *ORF1ab* antisense (O-AS) (red) at 48 hours postinoculation. (C) Representative RNA in situ hybridization of SARS-CoV-2 *S* sense (S-S) (green) and pericyte marker *PDGFRB* sense (red), and (D) immunostaining for the SARS-CoV-2 NP (green) with pericyte marker PDGFRβ (red). All scale bars: 10 μm. All images representative from 3 technical slice replicates from each of the 3 independent donor hearts. DAPI = 4',6-diamidino-2-phenylindole.

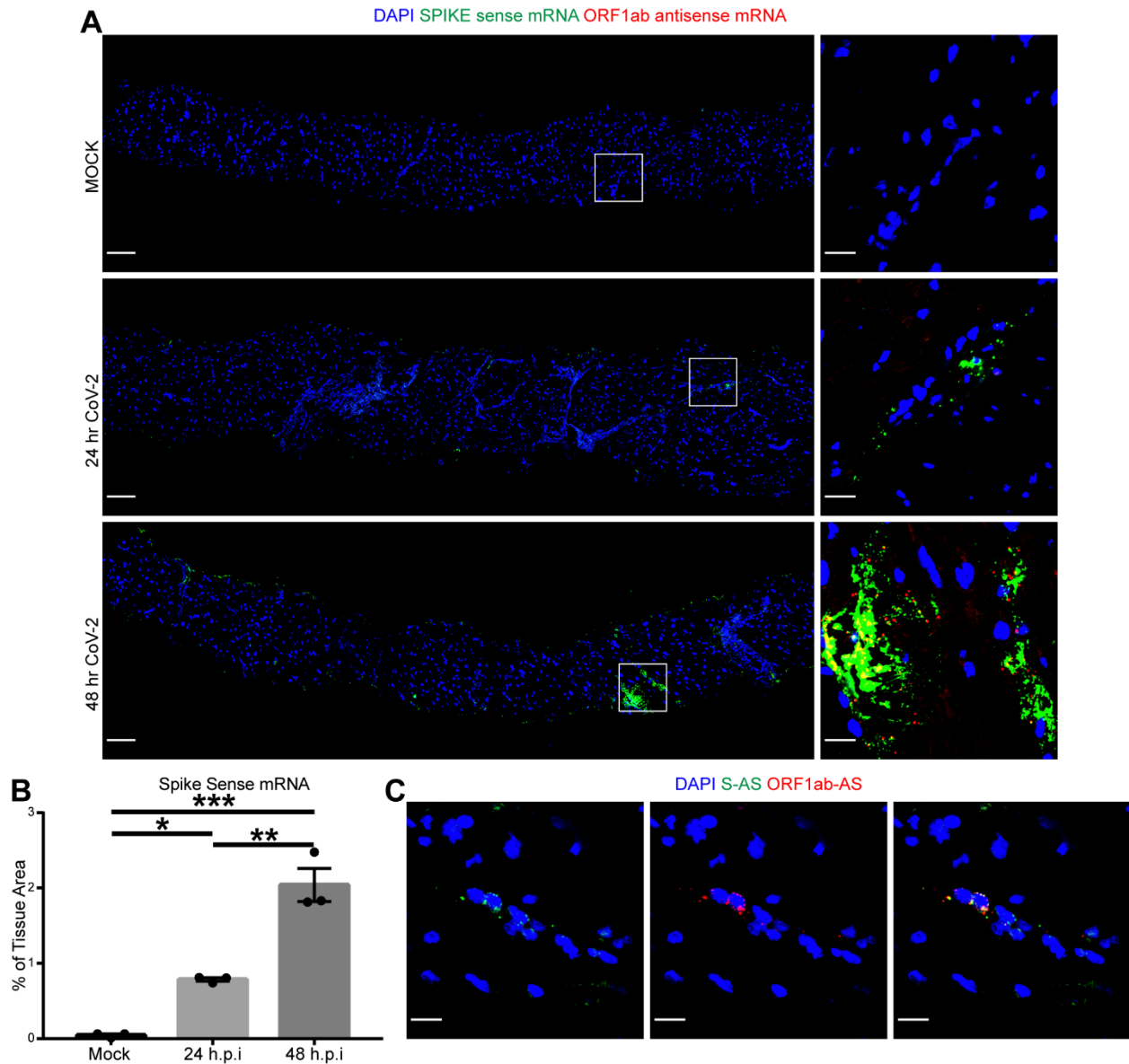


Figure 3.3. Detection of SARS-CoV-2 genomic and replication intermediate RNAs in cultured cardiac slides. (A-B) Cardiac slices were inoculated with 5×10^5 focus forming units (FFU) of SARS-CoV-2 WA1/2020 strain (approximately MOI of 1) and harvested at indicated time points (n=3 donors). (A) Representative RNA-ISH of SARS-CoV-2 S sense (green) and SARS-CoV-2 ORF1ab antisense (red) demonstrates the presence of SARS-CoV-2 genomic RNA by 24 hrs post-inoculation and appreciable subgenomic (replicating intermediate) RNA at 48 hrs post-inoculation, with little background of either channel in the mock condition. Scale bar on whole slice image: 100 μ m. Scale bar on zoom panels: 20 μ m. (B) Quantification of the Spike sense RNA-ISH demonstrates a significant increase of viral RNA between 24 and 48 hr time points, both of which are greater than the background detected in the mock condition (n=3). (C) Representative RNA-ISH of SARS-CoV-2 S antisense (S-AS, green) and ORF1ab antisense (O-AS, red) demonstrates the presence of SARS-CoV-2 subgenomic (replicating intermediate) RNA at 48 hrs post-inoculation. Scale bar: 20 μ m. One-way ANOVA with Tukey's post-test p-value < 0.05 (*), p < 0.01 (**), p < 0.001 (***).

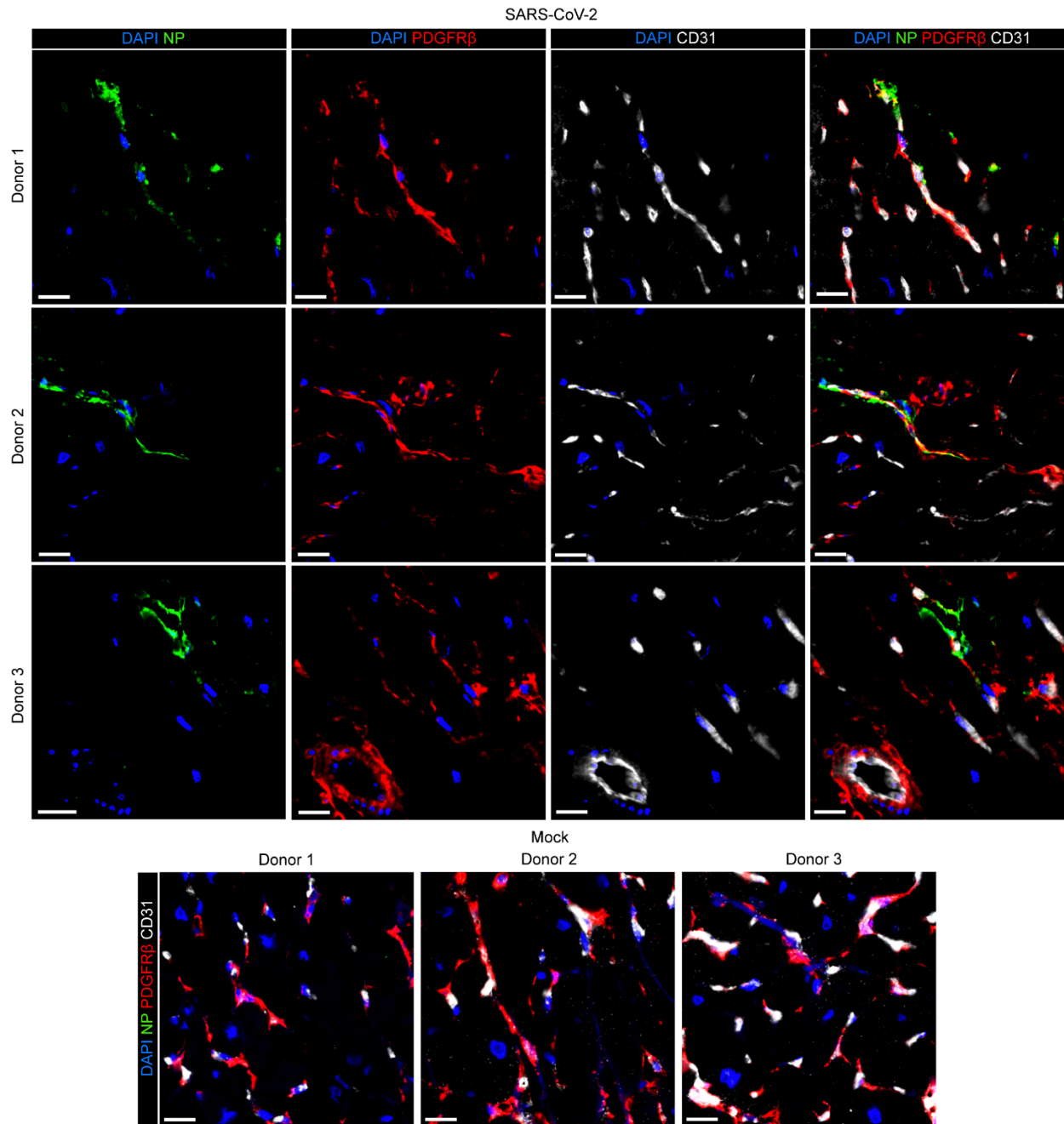


Figure 3.4. Detection of SARS-CoV-2 nucleocapsid protein within pericytes of cardiac slices. Cardiac slices were inoculated with 5×10^5 focus forming units (FFU) of SARS-CoV-2 WA1/2020 (approximately MOI of 1) and harvested at 48 hrs post-inoculation (n=3). Immunostaining for the SARS-CoV-2 nucleocapsid protein (NP, green) with pericyte marker PDGFR β (red) and endothelial cell marker CD31 (white) identifies the presence of SARS-CoV-2 within cardiac pericytes surrounding endothelium in three separate donor hearts and no evidence of viral protein in the mock condition. All scale bars: 10 μ m.

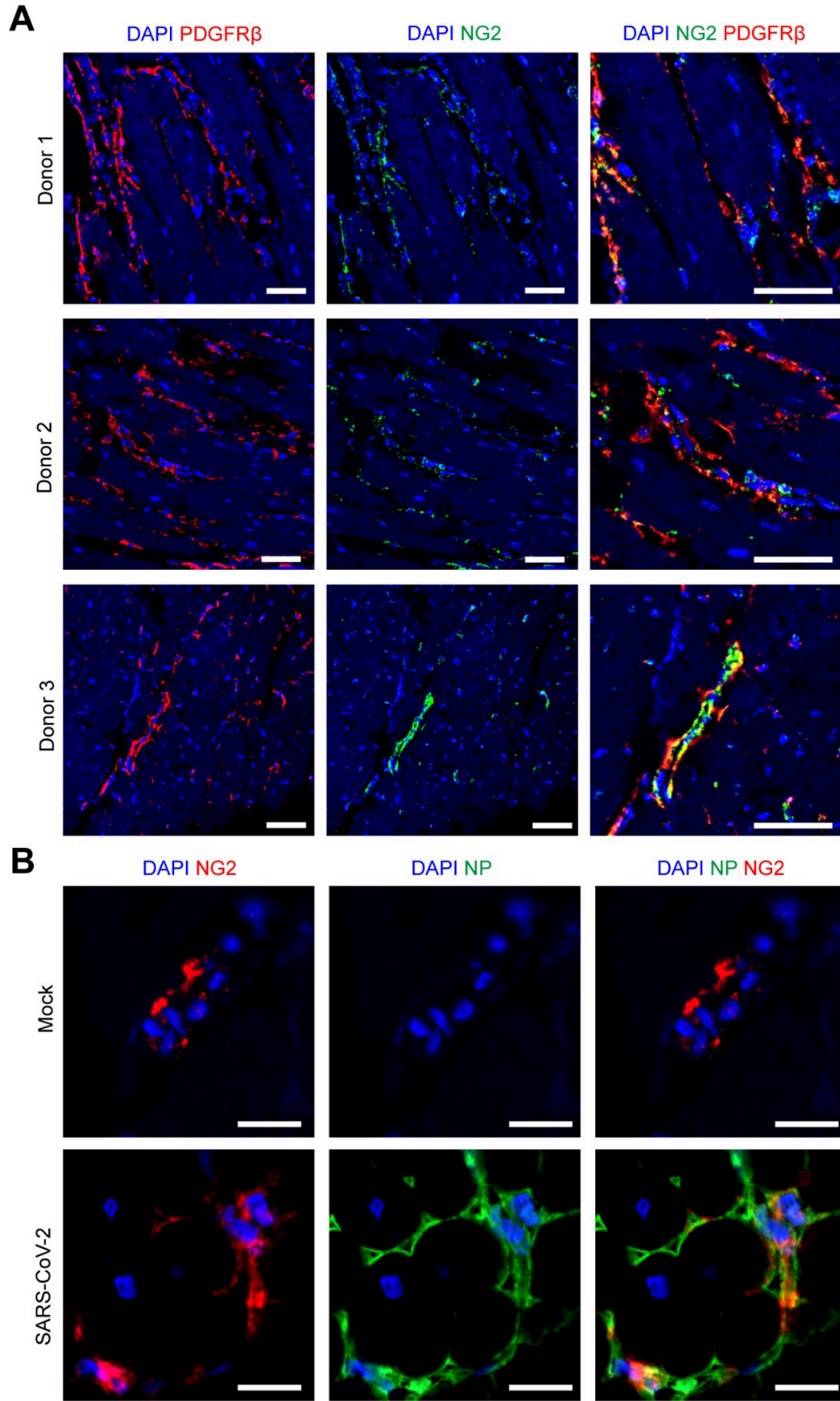


Figure 3.5. Detection of SARS-CoV-2 nucleocapsid protein within NG2-positive pericytes of human cardiac tissue. (A) Immunostaining for two pericyte markers NG2 (green) and PDGFR β (red) on human left ventricular tissue demonstrates colocalization of the proteins (n=3 donors). Scale bars: 50 μ m. (B) Cardiac slices from human left ventricular tissue were inoculated with 5×10^5 focus forming units (FFU) of SARS-CoV-2 WA1/2020 (approximately MOI of 1) and harvested at 48 hrs post-inoculation (n=3). Representative immunostaining for the SARS-CoV-2 nucleocapsid protein (NP, green) with pericyte marker NG2 (red) identifies the presence of SARS-CoV-2 within cardiac pericytes surrounding endothelium in three separate donor hearts and no evidence of viral protein in the mock condition (representative of n=3 donors). All scale bars: 20 μ m.

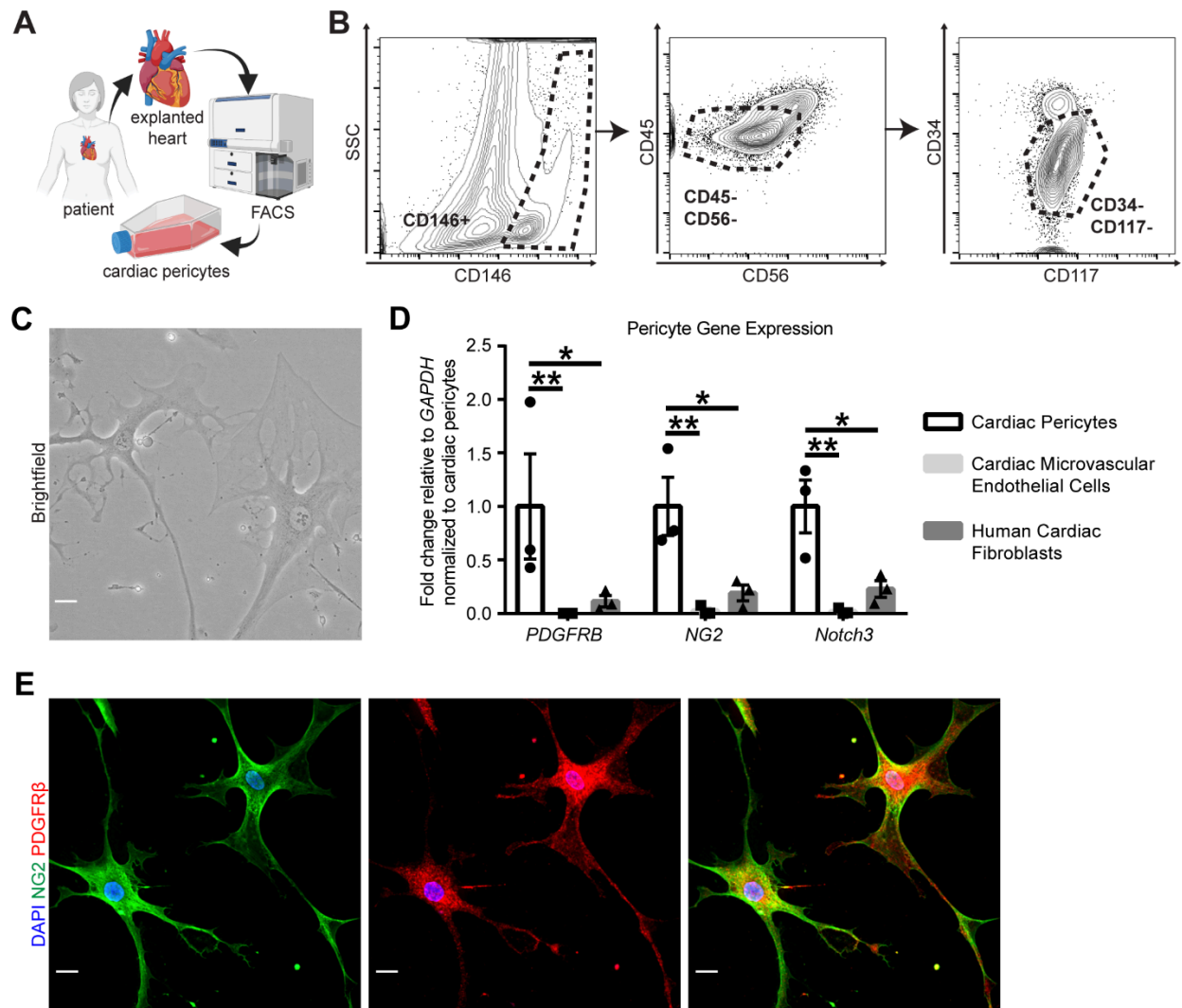


Figure 3.6. Isolation of cardiac pericytes from human hearts. (A) Scheme summarizing the process of cardiac pericyte isolation from explanted donor hearts (n=3). (B) Fluorescence-activated cell sorting (FACS) plots showing gating strategy used to sort for pericytes (CD146+, CD45-, CD56-, CD34-, and CD117-). (C) Representative brightfield image showing the morphology of sorted pericytes in culture (n=3). (D) Real-time quantitative PCR demonstrates that isolated human cardiac pericytes (HCP) have significant enrichment of characteristic pericyte cell marker genes including *PDGFRB*, *NG2*, and *Notch3* compared to primary human cardiac microvascular endothelial cells and human cardiac fibroblasts (n=3). Statistical comparison to cardiac pericyte group for each gene; two-way ANOVA with Dunnet's post-test, p-value <0.05 (*), p<0.01 (**). (E) Representative immunostaining demonstrates that cultured pericytes co-express both NG2 (green) and PDGFR β (red) protein (n=3). All scale bars: 10 μ m

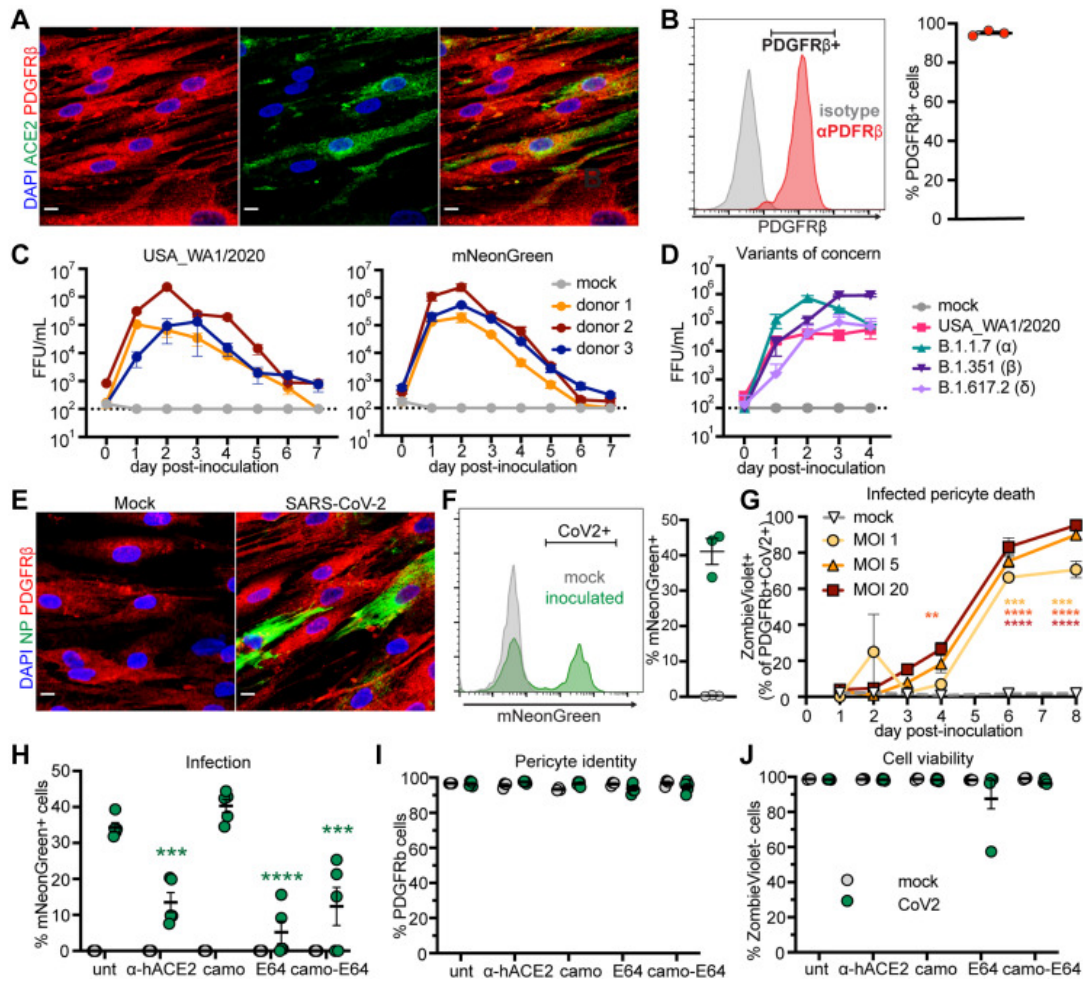


Figure 3.7. SARS-CoV-2 Productively Infects Human Primary Cardiac Pericytes. (A) Immunostaining for ACE2 (green) and PDGFR β (red) of cardiac pericytes isolated from left ventricle (n = 3 donors). (B) Representative flow cytometry histogram and quantification of PDGFR β in pericytes (n = 3). (C and D) Focus-forming assay time course of pericyte infection with SARS-CoV-2 WA1/2020 and SARS-CoV-2 mNeonGreen (n = 3) (C) and Alpha (B.1.1.7), Beta (B.1.351), and Delta (B.1.617.2) SARS-CoV-2 variants (representative of n = 2) (D); **dotted line** indicates limit of detection. (E) Immunostaining for the SARS-CoV-2 nucleocapsid protein (NP) (green) and PDGFR β (red) (n = 3). (F) Representative flow cytometry histogram and quantification of cardiac pericyte infection (mNeonGreen) at day 1 postinoculation with multiplicity of infection (MOI) of 20 (n = 3). (G) Flow cytometry-based cell viability (ZombieViolet+ = dead) time course of inoculated pericytes. Statistical comparison to mock at corresponding time point. (H to J) Pericytes were pretreated with vehicle (unt), 10 μ g/mL of human anti-ACE2 antibody (α -hACE2), 100 μ mol/L of serine protease inhibitor camostat methylate (camo), 100 μ mol/L of cysteine protease inhibitor E-64 (E64), or a combination of camostat methylate and E-64 (camo-E64) for 1 hour, inoculated with mock or SARS-CoV-2 mNeonGreen at MOI of 20 for 20 hours (n = 2). Quantification of infection (mNeonGreen+) (D), pericyte identity (PDGFR β +) (E), and cell viability (Zombie-Violet-) (F). (D to F) **Points** represent separate wells; statistical comparison to untreated inoculated group. Repeated in 2 donors. 2-way analysis of variance with Dunnet's post-test: ** P < 0.01; *** P < 0.001. Scale bars: 20 μ m. Abbreviations as in [Figure 3.2](#).

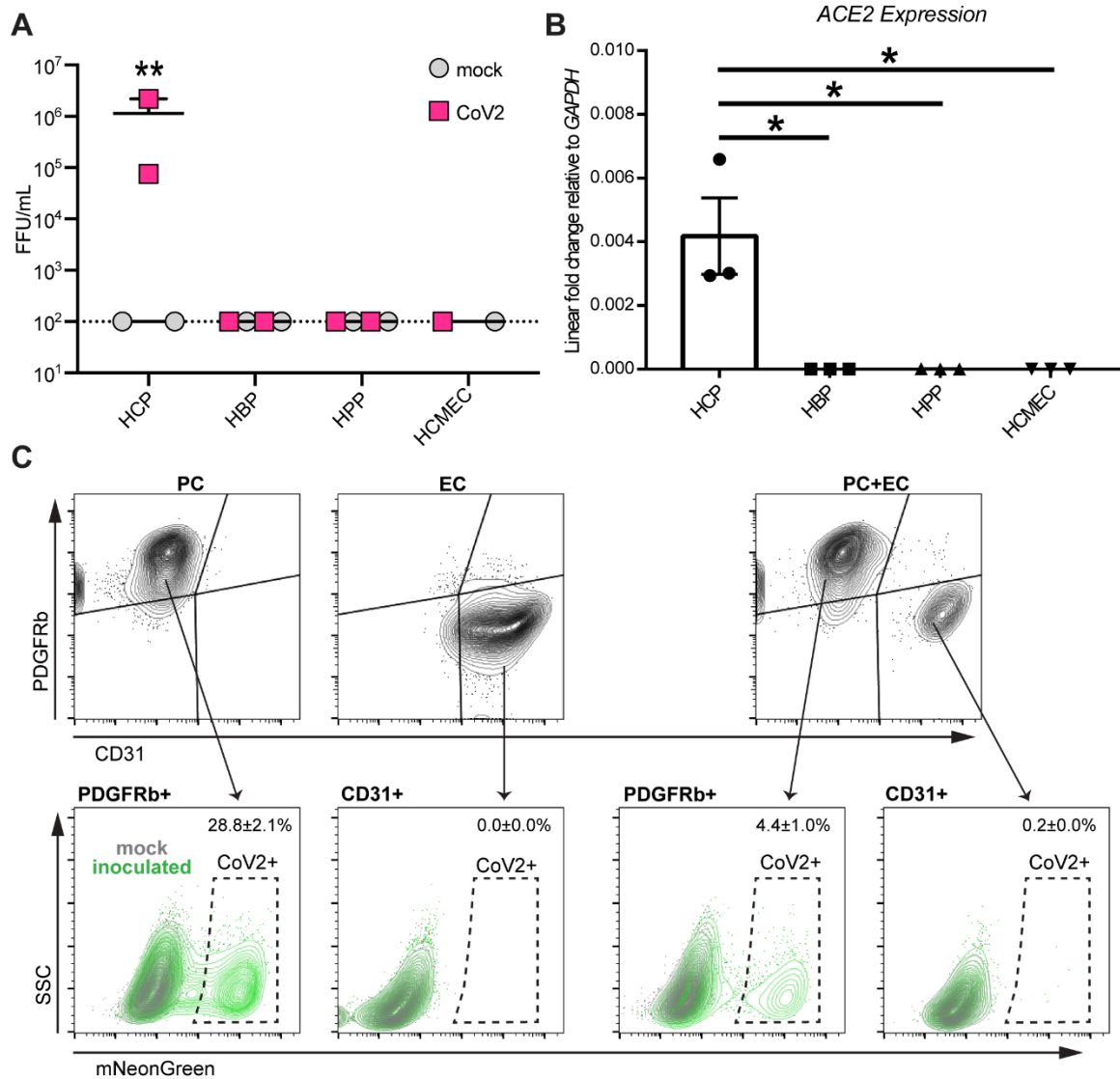


Figure 3.8. Selective susceptibility of human cardiac pericytes to SARS-CoV-2 infection. (A) Human primary cardiac pericytes (HCP, n=2), brain pericytes (HBP, n=2), placental pericytes (HPP, n=2), and cardiac microvascular endothelial cells (HCMEC, n=1) were inoculated with SARS-CoV-2 WA1/2020 at an MOI of 1 and did not support infection over a 4-day time course by focus-forming assays. (B) Analysis of *ACE2* expression via real-time quantitative PCR demonstrates significantly greater *ACE2* expression in human cardiac pericytes (HCP) compared to brain pericytes (HBP), placental pericytes (HPP), and cardiac microvascular endothelial cells (HCMEC), which all express much lower levels of *ACE2* (n=3 donors per cell type). Statistical comparison to cardiac pericyte (HCP) group; two-way ANOVA with Dunnet's post-test correction, p-value <0.05 (*), p<0.01 (**). (C) Human primary cardiac pericytes were co-cultured with HUVECs, infected with SARS-CoV-2 mNeonGreen (MOI 1) and assessed for infection by flow cytometry at day 4. Conditions are pericytes only (PC), HUVEC only (EC) and mix of pericytes and HUVEC (PC+EC). Pericytes and endothelial cells are distinguished by PDGFRb (pericyte marker) and CD31 (endothelial cell marker) in the top panel. Histograms of mNeonGreen (SARS-CoV-2 infection) of each cell type in the bottom demonstrate that only cardiac pericytes support viral replication in co-culture.

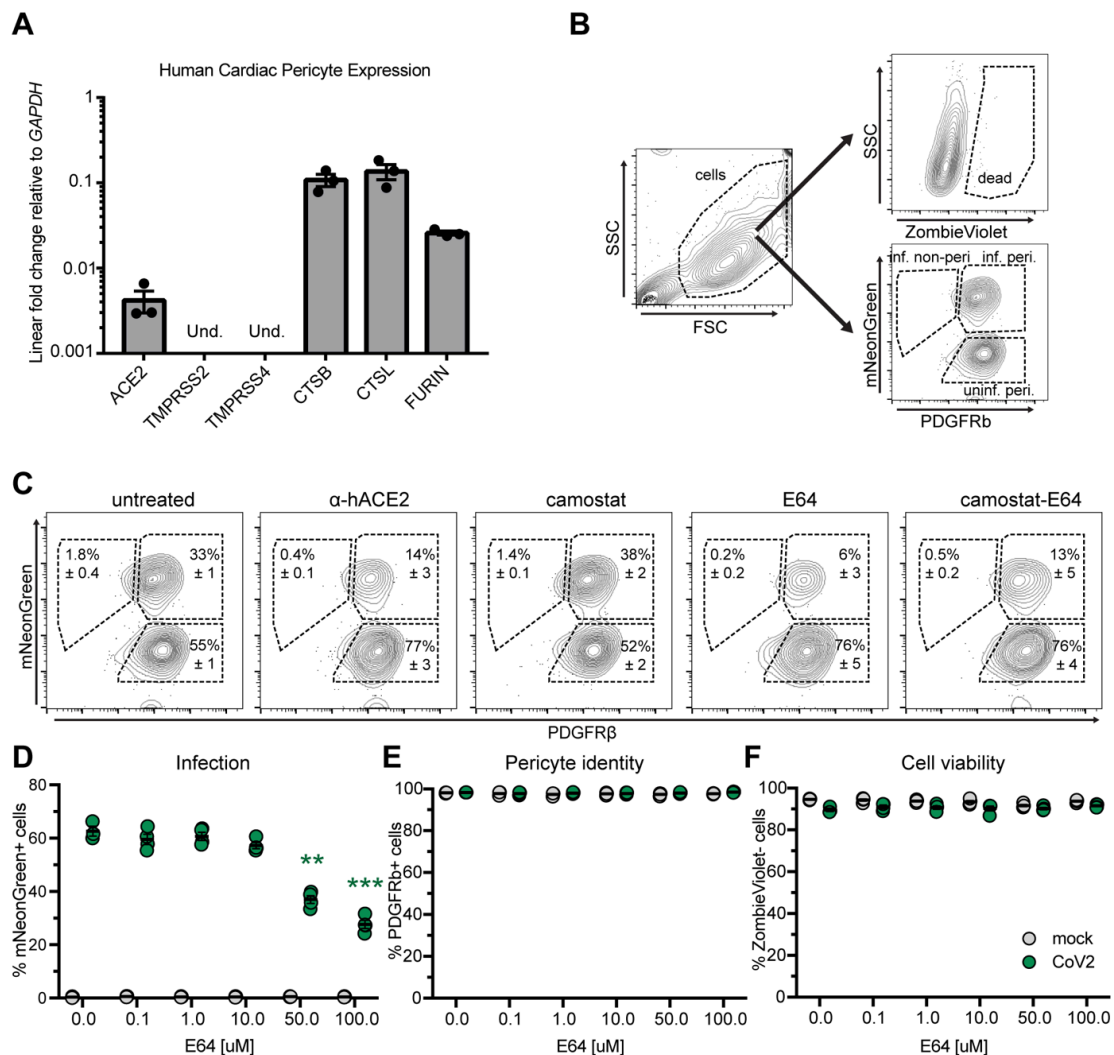


Figure 3.9. SARS-CoV-2 enters human cardiac pericytes in ACE2- and cysteine protease-dependent manner. (A) Real-time quantitative PCR showing expression of ACE2, cysteine proteases CTSB and CTSL, and FURIN and undetectable (Und.) levels of TMPRSS2 or TMPRSS4; each data point denotes cardiac pericytes from separate donors (n=3). (B-F) Primary cardiac pericytes were pretreated with vehicle (unt), 10 μg/mL of anti-human ACE2 antibody (α-hACE2), 100 μM of serine protease inhibitor camostat methylate (camo), 100 μM of cysteine protease inhibitor E-64 (E64) or a combination (camo-E64) for 1 hour, inoculated with mock or SARS-CoV-2 mNeonGreen at MOI of 20 for 20 hrs and analyzed by flow cytometry (n=2). (B) Gating strategy. Gates correspond to dead cells (ZombieViolet+), infected non-pericytes (mNeonGreen+; PDGFRb-), infected pericytes (mNeonGreen+; PDGFRb+), and uninfected pericytes (mNeonGreen-; PDGFRb+). (C) Representative flow plots from infected treatment groups with gate quantification (average ± standard error of the mean). (D-F) Pericytes were treated with a concentration gradient of E-64 in pericyte media prior to infection. Same gating strategy as in C was used. Quantification of infection (mNeonGreen) (D), pericyte identity (PDGFRβ+) (E) and cell viability (Zombie-Violet-) (F) show dose-response of infection levels to E-64 and no effect of the inhibitor on cell state or viability; two-way ANOVA with Dunnet's post-test compared to 0 μM E64 condition: p-value <0.01 (**), p <0.001 (***), nonsignificant not shown.

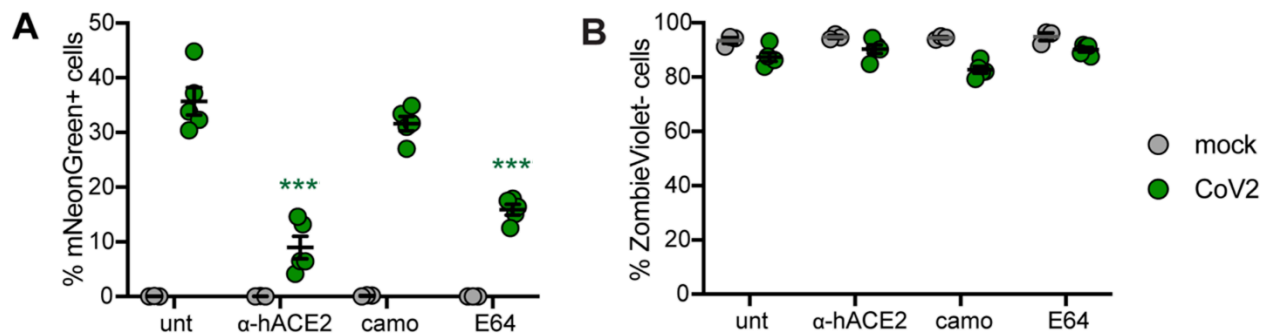


Figure 3.10. Inhibition of cysteine proteases and ACE2 decreases pericyte infection with SARS-CoV-2 for an extended period. Primary cardiac pericytes were pretreated with vehicle (unt), 10 $\mu\text{g}/\text{mL}$ anti-human ACE2 antibody ($\alpha\text{-hACE2}$), 100 μM serine protease inhibitor camostat methylate (camo) or 100 μM cysteine protease inhibitor E-64 (E64) for 1 hour, inoculated with mock or SARS-CoV-2 mNeonGreen at MOI of 1 and harvested for flow cytometry after 4 days ($n=1$). **(A)** Quantification of infection (as percent mNeonGreen+ cells of total cells) and **(B)** cell viability (ZombieViolet+). Experiments were performed on cardiac pericytes isolated from one donor. Individual points represent separate infected wells; statistical comparison of each infected and uninfected condition to untreated infected and uninfected groups respectively; two-way ANOVA with Dunnet's post-test: $p\text{-value} < 0.001$ (***), nonsignificant not shown.

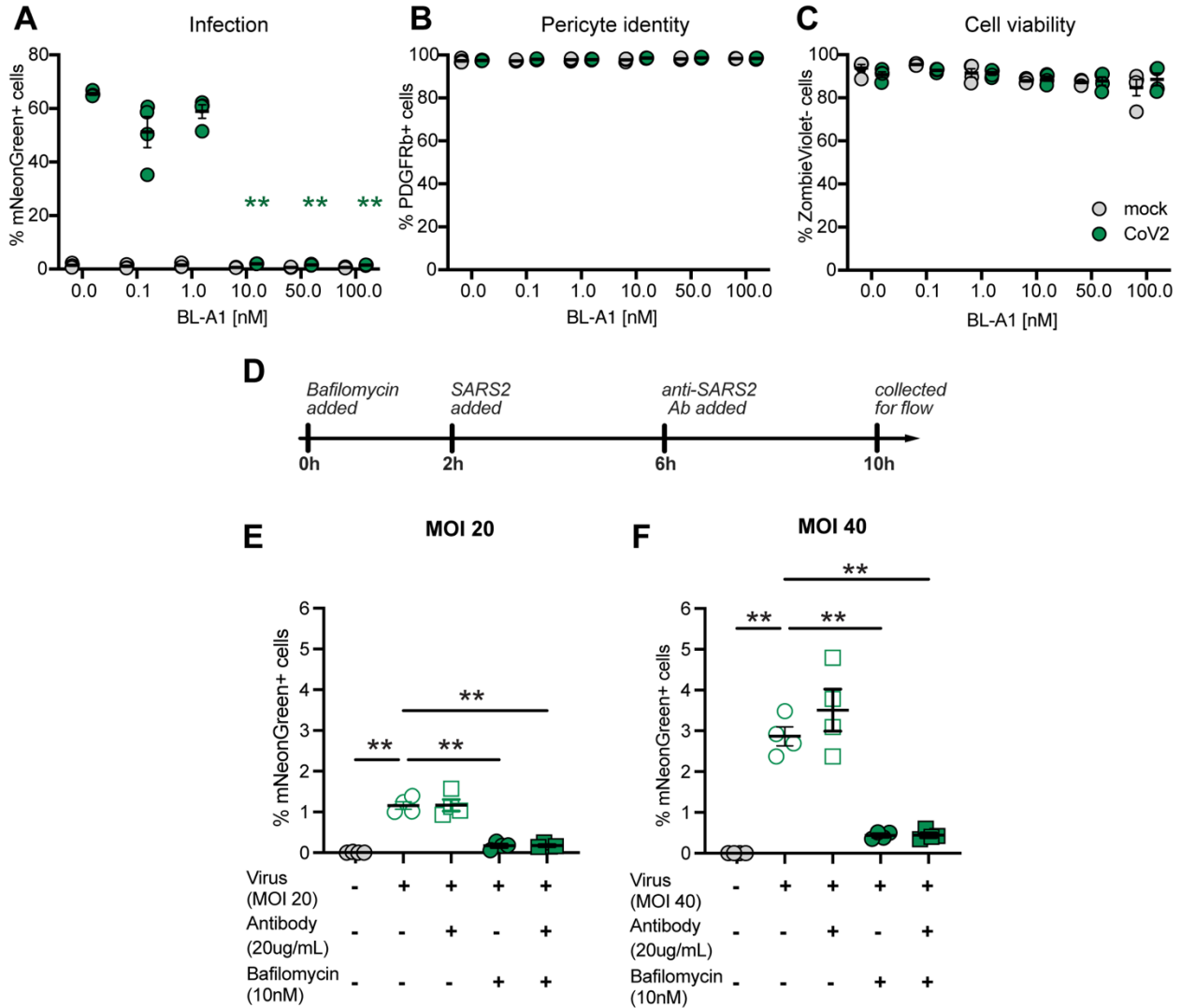


Figure 3.11. Inhibition of endosomal acidification decreases pericyte infection early in replication cycle independent of cell-to-cell spread.(A-C) To block endosomal acidification required for cathepsin function, primary cardiac pericytes were pretreated for 2 hours with a concentration gradient of H-ATPase inhibitor bafilomycin-A1 (BL-A1), inoculated with mock or SARS-CoV-2 mNeonGreen at MOI of 20 and harvested for flow cytometry after 20 hours (n=2). Quantification of (A) infection (as % mNeonGreen+ cells of total cells), (B) pericyte identity (as % PDGFRb+ cells of total cells) and (C) cell viability (ZombieViolet- cells of total cells). (D-E) To further focus on entry, earlier collection was performed. (D) Experimental outline. Primary cardiac pericytes were pretreated with 10nM BL-A1 for 2 hours, then infected with MOI 20 or MOI 40 of SARS-CoV-2 mNeonGreen or mock, and treated with SARS-CoV-2 neutralizing antibody or vehicle 4 hours after infection. Cells were harvested for flow cytometry 8 hours after infection. (E) Quantification of infection (as % mNeonGreen+ cells of all cells) with MOI 20 (left) and MOI 40 (right) shows that viral entry is inhibited by BL-A1 treatment. Experiments were performed on cardiac pericytes isolated from two donors and representative experiments shown. Individual points represent separate infected wells; statistical comparison of each infected and uninfected condition to untreated infected and uninfected groups respectively; two-way ANOVA with Dunnet's post-test: p-value <0.01 (**), nonsignificant not shown.

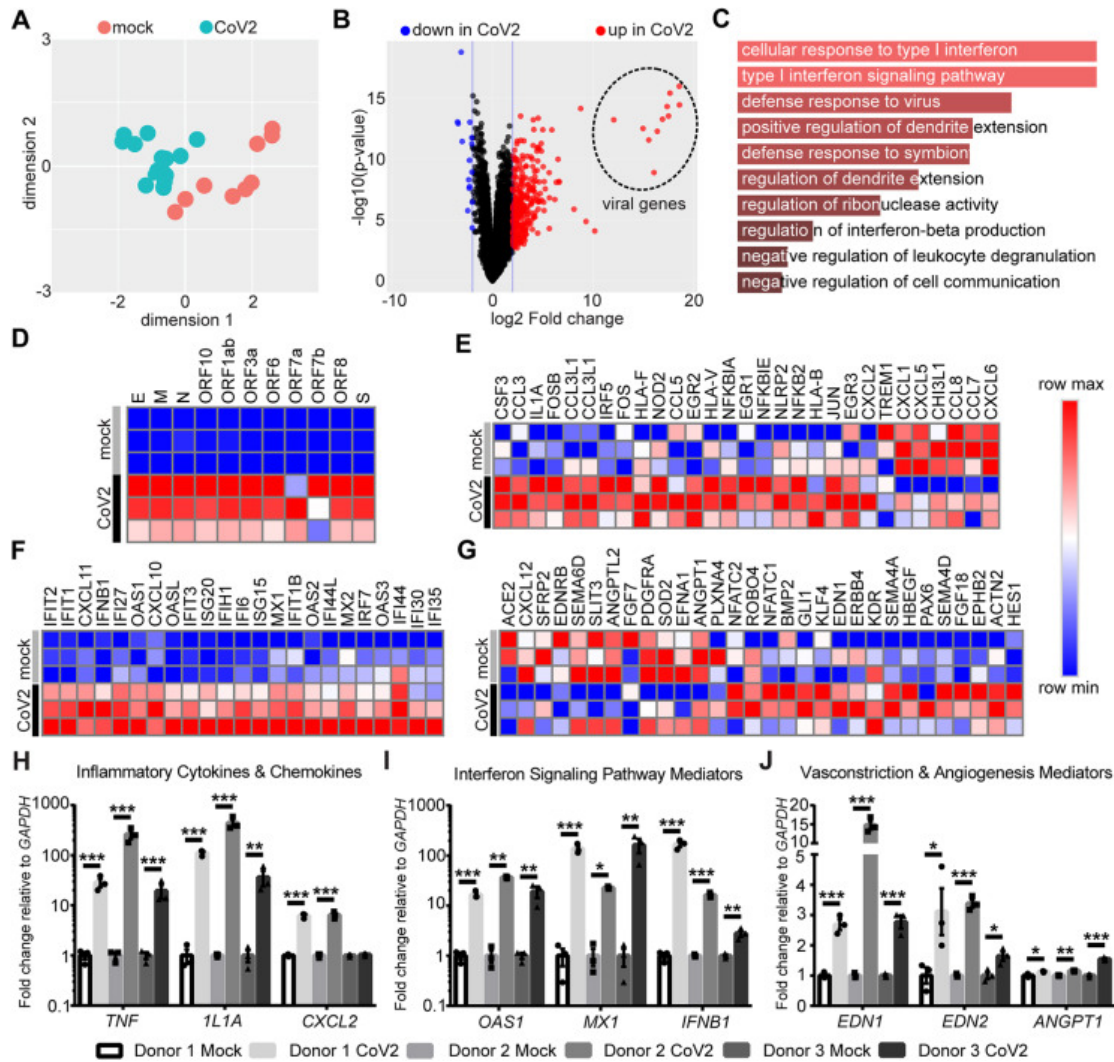


Figure 3.12. SARS-CoV-2 Infection Upregulates Type I IFN Signaling, Inflammatory Pathways, and Vasoactive Genes in Cardiac Pericytes (A to G) RNA sequencing of pericytes at 4 dpi. Cardiac pericytes from 3 donors were inoculated with SARS-CoV-2 mNeonGreen (5 technical replicates/donor) or mock (3 technical replicates/donor). (A) Multidimensional scaling plot with mock (red) and SARS-CoV-2 infected (CoV2) (green) samples; dots represent technical replicates. (B) Volcano plot showing differentially expressed genes between mock and infected samples. Each dot represents a gene, with blue denoting down-regulated genes, black denoting genes nonsignificant changes, and red denoting up-regulated genes. (C) Gene ontology pathway analysis with top 10 up-regulated pathways in infected pericytes. (D to G) Heat maps of selected differentially expressed genes of viral origin (D), pericyte genes involved in inflammatory response (E); response to IFN signaling (F); and vascular development, homeostasis, and function (G). (H to J) Reverse transcription quantitative polymerase chain reaction analyses of genes encoding inflammatory cytokines and chemokines (H), type I interferon signaling pathway components (I), and vasoconstriction and angiogenesis mediators (J); data points denote separate wells (3 technical replicates/donor) with statistical comparison to mock group for each donor; an equal or unequal variance Student's t-test, as determined by an F test for equality of 2 variances: * $P < 0.05$; ** $P < 0.01$; *** $P < 0.001$, nonsignificant comparisons not shown. GAPDH = glyceraldehyde 3-phosphate dehydrogenase; other abbreviations as in Figure 3.2.

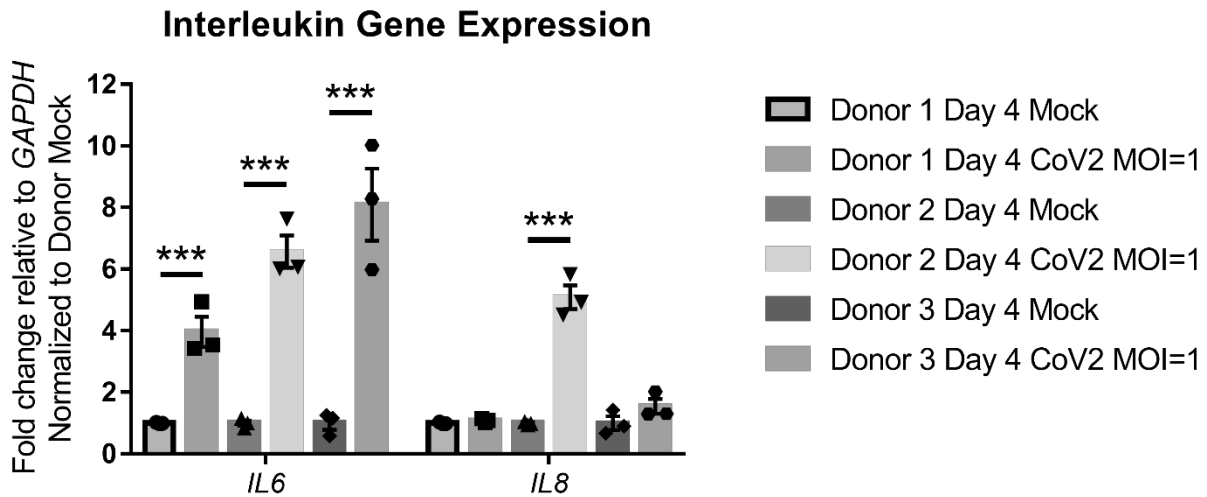


Figure 3.13. SARS-CoV-2 infection reproducibly upregulates IL6 and can upregulate IL8 in cardiac pericytes. Cardiac pericytes from 3 donors (3 technical replicates/donor) were inoculated with SARS-CoV-2 mNeonGreen or mock and harvested 4 days post-inoculation. Real-time quantitative PCR analyses of genes encoding inflammatory cytokines IL-6 and IL-8 demonstrate upregulation of IL6 in all three donors and upregulation of IL8 in one donor. Data points denote separate wells (3 technical replicates/donor) with statistical comparison to mock group for each donor; equal variance, Student's t-test p-value <0.001 (***), nonsignificant not shown.

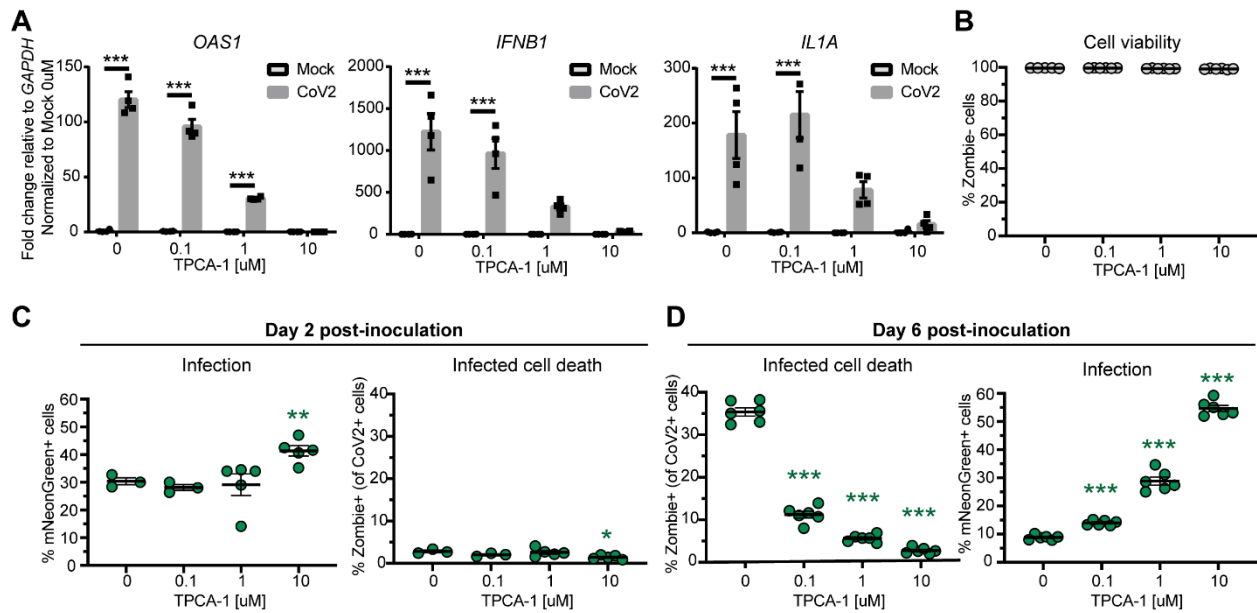


Figure 3.14. Inhibition of NFκB signaling decreases cell death in infected pericytes. Primary cardiac pericytes were pretreated with vehicle (0.0), 0.1, 1, or 10 μM I-kappa B kinase inhibitor TPCA-1 for 4 hours, inoculated with mock or SARS-CoV-2 mNeonGreen at MOI of 1 and harvested for RNA or flow cytometry at specified times (representative data from n=1, experiment repeated twice). **(A)** Real-time quantitative PCR for OAS1, IFNB1, and IL1A at day 4 post-inoculation (dpi 4) demonstrates TPCA-1 dose-dependent downregulation of inflammatory gene expression, with levels comparable to DMSO vehicle control at 10 μM of TPCA-1. **(B)** Quantification of cell death (as % Zombie- cells of total cells) in uninfected inhibitor-treated pericytes at dpi 6 demonstrates no significant TPCA-1 toxicity. **(C)** Quantification of infection (as % mNeonGreen+ cells of total cells) and death of infected pericytes (as % Zombie+ cells of mNeonGreen+ cells) at dpi 2. **(D)** Quantification of infected pericyte cell death (as % Zombie+ cells of mNeonGreen+ cells) and abundance of infected pericytes (as % mNeonGreen+ cells of total cells) shows dose-dependent protection from cell death and increased abundance of infected cells with TPCA-1 treatment at dpi 6. **(A-D)** Experiments were performed on cardiac pericytes isolated from one donor. Individual points represent separate infected wells (n=4) for each condition; experiment was repeated two times (representative experiment shown). Statistical comparison of each infected and uninfected condition to untreated infected and uninfected groups, respectively; two-way ANOVA with Sidak's post-test p-value <0.05 (*), p<0.01 (**), p<0.001 (***), nonsignificant not shown.

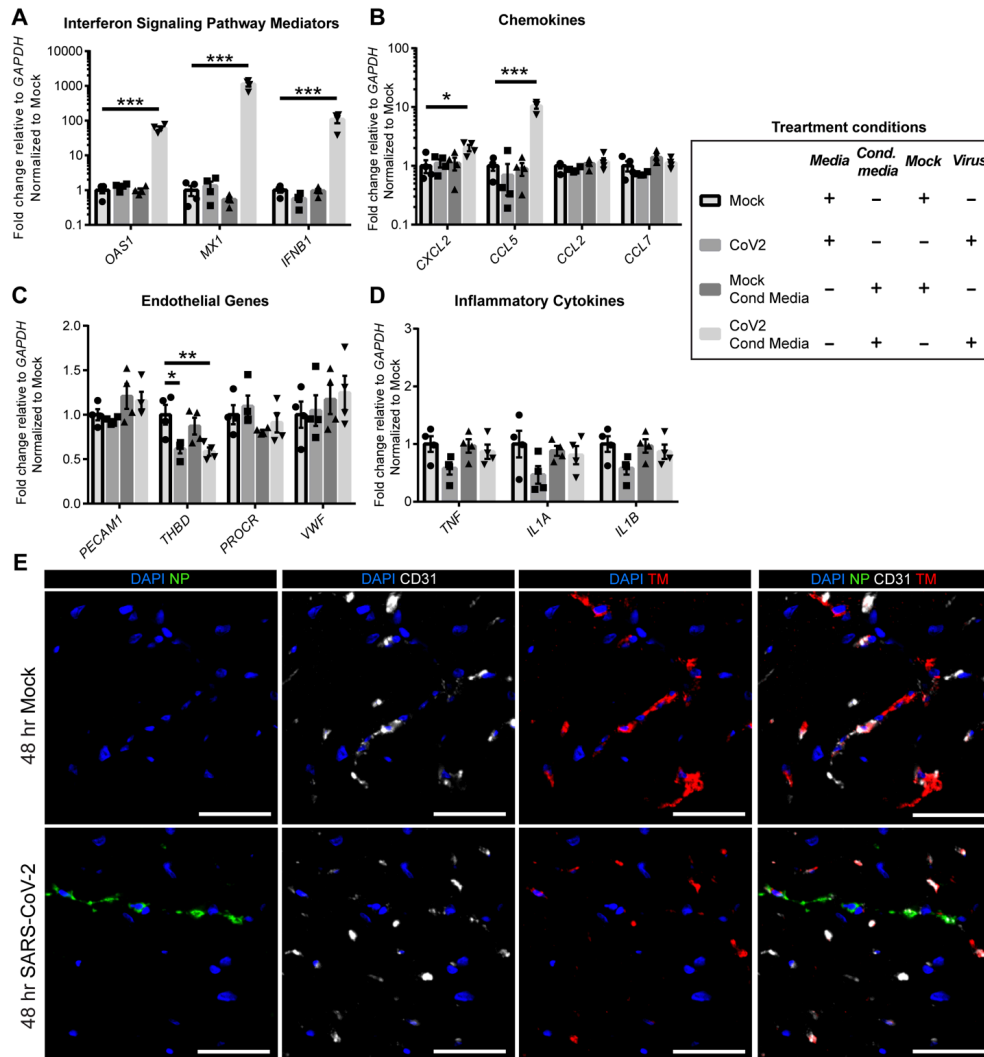


Figure 3.15. Infected cardiac pericyte-conditioned medium leads to upregulation of type I interferon signaling and downregulation of thrombomodulin. (A-D) HUVEC cells were cultured in endothelial cell media supplemented with one of four conditions: 1) Fresh pericyte culture medium with supernatant from uninfected Vero-TMPRSS cells (Mock), 2) Fresh pericyte culture medium with SARS-CoV-2 (CoV2, 6.5×10^4 FFU/mL), 3) Conditioned pericyte medium from Vero-TMPRSS2 mock-treated pericytes (Mock Cond Media), and 4) Conditioned pericyte medium from SARS-CoV-2-treated pericytes (MOI=1) (CoV2 Cond Media). Real-time quantitative PCR demonstrates (A) upregulation of type I interferon signaling pathway mediators with CoV2 Cond Media (B) upregulation of CXCL2 and CCL5 with CoV2 Cond Media, (C) downregulation of THBD in the CoV2 and CoV2 Cond Media, and (D) no changes in IL-1A, IL-1B and TNF cytokine expression. Individual points represent separate infected wells ($n=4$) for each condition. Statistical comparison of each condition to mock, respectively; one-way ANOVA, p -value <0.05 (*), $p < 0.01$ (**), $p < 0.001$ (***), nonsignificant not shown. (E) Cardiac slices from human left ventricular tissue were inoculated with 5×10^5 focus forming units (FFU) of SARS-CoV-2 WA1/2020 (approximately MOI of 1) and harvested at 48 hrs post-inoculation ($n=3$). Representative immunostaining for thrombomodulin (TM, red) with endothelial cell marker CD31 (white) and the SARS-CoV-2 nucleocapsid protein (NP, green) demonstrates lower levels of thrombomodulin in the endothelial cells near the presence of virus (representative of $n=3$ donors). All scale bars: 50 μ m.

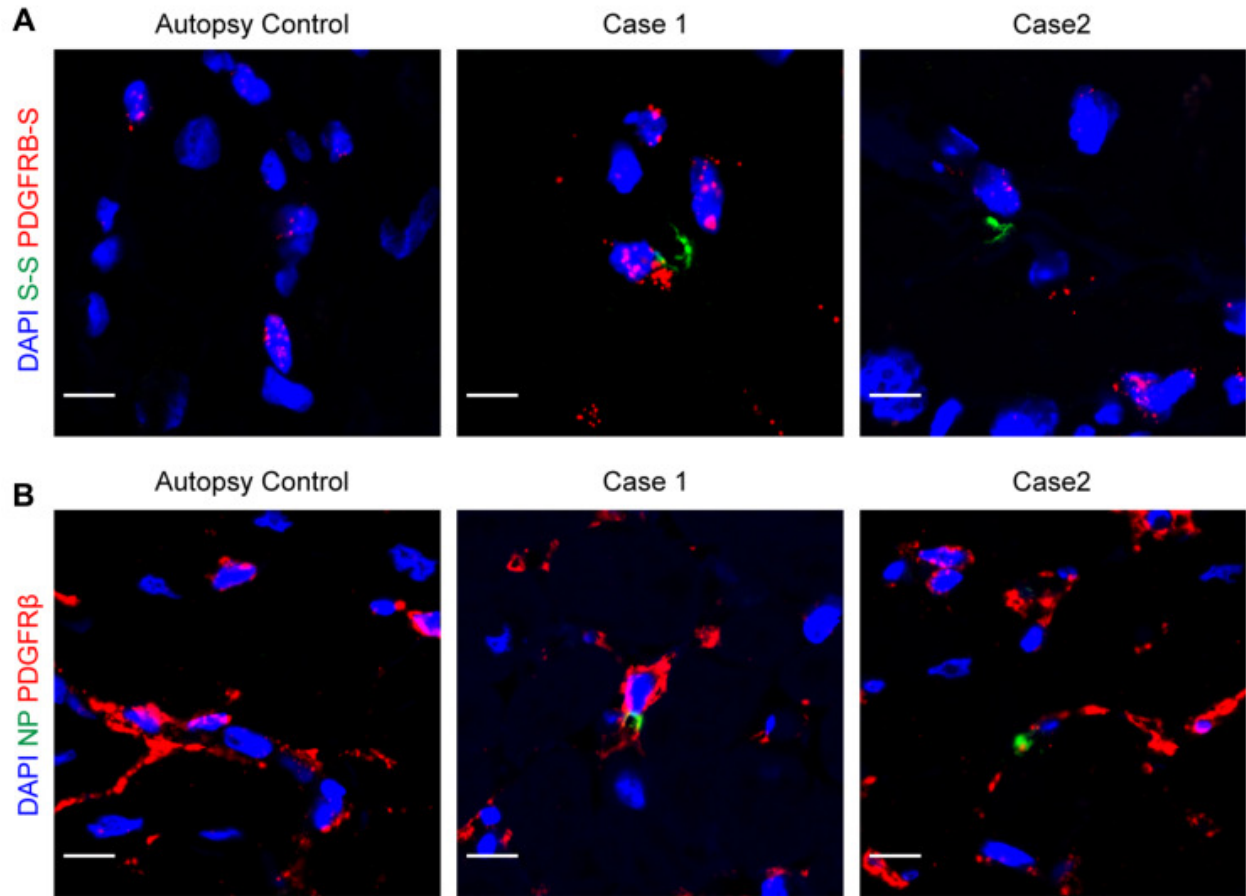


Figure 3.16. Detection of SARS-CoV-2 in Pericytes of COVID-19 Cardiac Autopsy Specimens (A) RNA in situ hybridization of SARS-CoV-2 S sense (S-S) (green) with pericyte marker PDGFRB sense (PDGFRB-S) (red) in the perivascular region of autopsy control (n = 1) and COVID-19-positive formalin-fixed paraffin-embedded specimens (n = 2). (B) Immunostaining for the SARS-CoV-2 NP (green) and pericyte marker PDGFR β (red) within the perivascular region of autopsy control (n = 1) and COVID-19-positive formalin-fixed paraffin-embedded specimens (n = 2). Abbreviations as in **Figure 3.2**.

Chapter 4

Mouse Model of Cardiomyocyte-Restricted SARS-CoV-2 Infection

4.1 Summary

Cardiovascular manifestations of COVID-19 are common among the patients and vary in severity and presentation. Human cardiomyocytes are susceptible to SARS-CoV-2 and have been proposed as a potential target for the virus in this disease. However, the contribution of viral infection to clinical course of COVID-19 remains unknown and robust small animal models of cardiac disease are lacking. Here we offer a novel Cre-LoxP based mouse model of cardiac-restricted infection with SARS-CoV-2. These mice show transient cardiac infection that leads to mild injury on histology, increased macrophage accumulation in cardiac tissue and moderate cardiac dysfunction. Inhibition of CCR2 signaling rescues the functional phenotype and leads to lower viral burden in the heart by facilitating viral clearance. These data demonstrate that the cardiac-restricted mouse model of SARS-CoV-2 infection recapitulates key aspects of human COVID-19-associated cardiac disease and can be used to gain insight into its molecular mechanisms as well as to test tissue-specific countermeasures.

4.2 Introduction

Severe Acute Respiratory Syndrome Coronavirus 2 (SARS-CoV-2) is a member of beta-coronavirus family which causes Coronavirus Disease 2019 (COVID-19). While respiratory tract involvement and severe pneumonia are hallmarks of the disease, other affected organs involve kidneys, brain, gastrointestinal system, vasculature and heart¹⁻⁴. In acute cases, patients experience

cardiac symptoms such as shortness of breath, chest pain, and palpitations during the course of COVID-19. They also show evidence of cardiac damage by ECG, elevated CRP and troponin, echocardiographic evidence of decreased left ventricular (LV) systolic function, magnetic resonance imaging signs of inflammation, and fibrosis on histology⁵⁻¹². Furthermore, uncontrolled tachycardia, chest pain and palpitations are components of post-acute COVID-19 syndrome (PACS)¹³, commonly known as “long COVID-19”, suggesting that heart damage is a potential lasting feature of this disease.

While cardiac involvement in the disease became obvious early during the pandemic, the exact mechanism of cardiac injury remained poorly understood. Multiple studies have detected viral proteins and RNA in cardiac tissue of patients with COVID-19 as well as histologic evidence of cardiac injury such as myocardial fibrosis and macrophage-predominant immune infiltration^{5,14-16}. In vitro models demonstrate that human stem cell-derived cardiomyocytes are one of the two main cell types in the heart that are susceptible to SARS-CoV-2 infection^{15,17}. This infection is dependent on viral receptor ACE2^{15,18}, involves endosomal route of viral entry that is distinct from that of lung cells^{14,18,19}. Infected cells have been reported to form syncytia, have decreased electric and contractile functions, and ultimately die^{14,20,21}. However, these studies offer limited perspective on functional changes in the whole organ as well as the roles of immune response in pathogenesis of cardiac COVID-19 due to the in vitro nature of the models used.

Most current animal models of SARS-CoV-2 infection either develop mild disease without appreciable heart involvement or are focused on pulmonary disease^{22,23}. Hamsters are naturally susceptible to SARS-CoV-2 and have been shown to develop heart disease after infection²⁴⁻²⁶. However, mechanistic interrogation of infection in this model is restricted by the lack of reagents

and genetic tools for hamsters that are readily available in mice. Murine models have been limited at the start of the pandemic due to natural resistance of wild-type mice to early strains of SARS-CoV-2 as a result of poor binding of spike protein of the virus to mouse ACE2 receptor²⁷. Therefore, a modification of either the virus or the host was required. Transgenic mice expressing human ACE2 (hACE2) have been successfully used to study pulmonary disease and its response to vaccination and therapeutics²⁸⁻³⁰. Since a replacement strategy in which hACE2 being driven by murine ACE2 promoter did not produce robust disease³¹, these studies utilized animals with hACE2 expression driven by pulmonary tissue-associated promoters or vectors such as keratin 18 (K18) promoter or adenoviral vector^{27,32}. However, these approaches led to hACE2 expression in non-physiologic locations and limited the viral spread to the areas of promoter activity, which did not allow for interrogation of cardiac infection. Alternatively, naturally occurring and artificially mutated strains of SARS-CoV-2 that harbor N501Y mutation in the spike protein can infect wild type mice have been successfully utilized³³. However, pulmonary disease in these animals can confound interpretation of any cardiac findings.

In this study, we demonstrate the natural spread of infection from lung to heart in wild type mouse infected with SARS-CoV-2. We further offer a novel Cre-LoxP-based conditional knock-in animal model in which the expression of hACE2 is restricted to cardiomyocytes. In these mice, Cre enzyme is driven by cardiac-specific myosin heavy chain (MYH6) promoter and excises a stop codon in Rosa26-loxP-STOP-loxP-hACE2 construct. These animals show cardiac-restricted infection with SARS-CoV-2, accumulation of macrophages in the heart, and experience transient cardiac dysfunction, which is dependent on CCR2⁺ monocyte recruitment. This model allows to interrogate effects of cardiomyocyte infection with SARS-CoV-2 on pathogenesis of COVID-19

without being confounded by the cardiac dysfunction caused by pulmonary disease. Furthermore, it offers a powerful in vivo platform for testing of novel therapeutics for cardiac disease associated with COVID-19.

4.3 Results

4.3.1 SARS-CoV-2 Infects Cardiac Tissue in Unrestricted and Cardiac-Restricted Murine Models of Infection

Multiple studies have shown evidence of cardiac tissue infection by SARS-CoV-2 in patients with COVID-19^{5,8,14,34}. To elucidate if cardiac infection can occur in mice during primary pulmonary disease caused SARS-CoV-2, we intranasally infected wild type 129 mice with B.1.351 strain of SARS-CoV-2 at 1×10^6 FFU as previously described^{29,31}. B.1.351 strain of SARS-CoV-2 used in these experiments harbors an N501Y mutation in spike that makes it capable of binding mouse ACE2 receptor and infecting wild type animals (**Figure 4.1A**)³³. Infected animals had high copy numbers of viral RNA in lungs and heart as well as detectable RNA in the serum (**Figure 4.1B**). Infected mice also lost weight as a result of infection (**Figure 4.1C**), consistent with previously published observations³¹. These data suggest that when given intranasally and unrestricted by receptor expression, SARS-CoV-2 can spread from its primary infection site in the lungs to the heart in the mouse.

Cardiomyocytes are one of the cell types that is susceptible to SARS-CoV-2 infection in human cardiac tissue^{5,14}. In order to study the effects of direct infection of SARS-CoV-2 on cardiovascular system, we developed a mouse in which infection with SARS-CoV-2 is restricted to cardiomyocytes. Such approach allowed us to ensure that any observed cardiac pathology is not confounded by the pulmonary disease that develops in other models. We crossed mice expressing

Cre driven by a cardiomyocyte-specific myosin heavy chain 6 promoter (MYH6-Cre) with animals that carry a human *ACE2* sequence under exogenous CAG promoter in the Rosa locus preceded by a floxed STOP codon (Rosa-loxP-STOP-loxP-hACE2). Cre-mediated excision of STOP codon in the progeny animals (MYH6-hACE2) ensured cardiomyocyte-restricted expression of hACE2 (**Figure 4.1D**). Cre-expressing animals have specific expression of *hACE2* RNA (**Figure 4.1E**) and hACE2 protein (**Figure 4.1F**) in cardiac tissue. Cre-negative control (ctrl) and Cre-positive experimental animals (hACE2-KI) got intravenously inoculated with 10^6 FFU of WA1/2020 strain of SARS-CoV-2. This strain does not harbor N501Y mutation and is restricted to human rather than mouse version of ACE2 receptor for entry. Intravenous route of infection was chosen to bypass the lung and deliver SARS-CoV-2 into the heart tissue. This approach also models hematogenous spread that is suggested by viral RNA titers in serum of 129 mice (**Figure 4.1B**). Three days post-inoculation (dpi) viral RNA was detected at high levels only in hearts of hACE2-KI animals and spleen of both control and hACE2-KI animals, while lung, brain, kidney, liver, small intestine, skeletal muscle and serum remained negative for viral RNA (**Figure 4.1G**). This viral RNA was no longer present in the heart at dpi 9 (**Figure 4.1H**). To assess replication ability of the detected virus, we used primers that are specific to the subgenomic region of N gene expressed only during active viral replication. Subgenomic viral RNA was only detected in the hearts of hACE2-KI animals, suggesting that the signal seen in the spleen is due to non-replicating virus, most likely some of the original input sequestered from circulation (**Figure 4.1I**). Collectively, these data suggest that transgenic MYH6-hACE2 mice express human ACE2 selectively in cardiac tissue and that the heart of these animals is the only site of substantial SARS-CoV-2 replication.

4.3.2 Cardiac Infection with SARS-CoV-2 Leads to Left Ventricular Dysfunction and Macrophage Accumulation in the Heart.

Cardiac function of MYH6-hACE2 mice was evaluated by echocardiography, after which animals Cre-positive (hACE2-KI) and Cre-negative (control) were inoculated with SARS-CoV-2 and assessed at 1 and 4 weeks (**Figure 4.2A**). Left ventricular ejection fraction and fractional shortening were both moderately decreased in hACE2-KI group compared to control animals 1 week after viral inoculation (**Figure 4.2B-C**). The groups did not differ in ejection fraction at baseline and hACE2-KI animals recovered heart function by 4 weeks after viral inoculation (**Figure 4.2D**). Animals also did not lose weight throughout the duration of experiment, suggesting the lack of severe systemic disease. Focal areas of injury and mononuclear cell accumulation were seen on histology of cardiac tissue collected from these animals at 1 week post infection (**Figure 4.2E**).

Macrophages are the most abundant immune cell type in the heart and are implicated in multiple forms of cardiac pathology³⁵. We used histology to characterize immune composition in infected tissues and found that there was an increase in total CD45⁺ immune cells (**Figure 4.2F**) and CD68⁺ macrophages (**Figure 4.2G**) in hACE2-KI animals at 1 week after inoculation. Flow cytometry of cardiac tissue was used for in-depth characterization of the immune cell types and has shown an increase in myeloid cells, total macrophages and CCR2⁺ macrophages in hACE2-KI animals compared to Cre-negative controls (**Figure 4.2H-I**). No change was observed in relative numbers of these cells (**Figure 4.3A**) as well as in absolute and relative numbers of CCR2⁻ macrophages, neutrophils, CD8 T cells, and B cells (**Figure 4.3B-D**). A statistically significant increase of relative number of CD4 T cells was seen but was not accompanied by increase in

absolute numbers of these cells and was of low magnitude (**Figure 4.3 C-D**). Together these data show that SARS-CoV-2 infection in the heart leads to mild transient cardiac dysfunction and is accompanied by accumulation of CCR2⁺ macrophages.

4.3.3 SARS-CoV-2 Causes Downregulation of Sarcomere and Metabolism Genes.

To evaluate transcriptional changes associated with viral infection of cardiac tissue, RNAseq was performed on heart homogenates from animals at dpi 3. Three age-matched animal groups were sequenced: naïve (Cre-negative animals that have not been injected with the virus), control (Cre-negative animals that were intravenously injected with SARS-CoV-2) and hACE2-KI (Cre-positive animals that were intravenously injected with SARS-CoV-2).

Gene expression was different between 3 groups as evident by PCA plot clustering (**Figure 4.4A**). Differential expression analysis between hACE2-KI and naïve groups revealed a 213 of upregulated and a 247 of significantly downregulated genes (**Figure 4.4B**). Only 21 of those were associated with viral replication as seen from the differential expression analysis between hACE2-KI and control groups (**Figure 4.4C**). Among the host genes highly upregulated during productive viral infection were Hoxc8 (homeobox transcription factor responsible for cartilage formation³⁶), Cltn (chaperone of amino acid transporters^{37,38}), Cidec (lipid deposition regulator³⁹), Cdh15 (growth factor increased in response to cardiac injury⁴⁰), Atp2a1 (SERCA1 Ca⁺⁺ sarcoplasmic transporter⁴¹) (**Figure 4.4D**). Viral genes were only expressed in hACE2-KI group, with N, Orflab and S gene expression being the highest (**Figure 4.4E**). Viral presence, regardless of replication capacity, lead to a significant downregulation of genes encoding sarcomere elements and channels important in muscle physiology (**Figure 4.4F**) and metabolism (**Figure 4.4G**). This finding was

similar to our previous observation of sarcomere element downregulation of infected cardiomyocytes in vitro¹⁴. Interestingly, neither viral replication nor non-replicating circulating virus have not led to an increased Type I, II or III interferon response (**Figure 4.4H**).

Together these data suggest that while viral replication did not lead to a drastic change in gene expression profile in the heart, circulation of viral particles could contribute to decrease in metabolic and sarcomere gene levels.

4.3.4 CCR2 Blockade Rescues Cardiac Dysfunction and Increases Viral Clearance During Cardiac Infection with SARS-CoV-2.

CCR2⁺ macrophages in the heart are primarily monocyte-derived cells recruited into the heart during injury⁴². They are implicated in adverse remodeling during sterile inflammatory processes such as myocardial infarction and volume overload injury^{43,44}. To investigate the role of CCR2⁺ cells in the pathophysiology of cardiac SARS-CoV-2 infection, we utilized previously published blockade strategy using anti-CCR2 antibody⁴⁵. This treatment prevents CCR2-dependent monocyte egress from bone marrow and recruitment of cells to the sites of injury⁴⁵. Cre-negative controls and Cre-positive hACE2-KI animals were pretreated with either anti-CCR2 or isotype control antibody 1 day prior to viral inoculation and then treated every 2 days throughout the duration of the experiment (**Figure 4.5A**). Successful blockade of monocyte egress was confirmed by flow cytometry analysis of CD45⁺/CD11b⁺/Ly6G⁻/Ly6C-high/CCR2⁺ cells in the blood at dpi 2 (**Figure 4.5A**). To evaluate functional changes associated with CCR2 blockade, transthoracic echocardiography was performed at one week after viral inoculation. Isotype-treated hACE2-KI animals showed decrease in both ejection fraction and fractional shortening after infection when compared to the isotype-treated control group, consistent with the findings

presented above. However, CCR2 blockade restored ejection fraction in hACE2-KI animals back to the baseline (**Figure 4.5B**). Furthermore, anti-CCR2 treated hACE2-KI animals had less macrophages in cardiac tissue compared to the isotype-treated hACE2-KI group (**Figure 4.5C**).

To assess the effects of CCR2 blockade on viral burden, we harvested heart tissue from the same four groups of animals at dpi 3 (72 hours post-inoculation), a timepoint when robust viral titers have been seen previously. Viral RNA load was decreased about 10-fold with anti-CCR2 treatment of hACE2-KI mice compared to isotype treated animals (**Figure 4.5D**). The effect of CCR2 blockade on replicating virus was even more profound as seen by qPCR for subgenomic region of N (**Figure 4.5D**). In order to test whether CCR2⁺ cell recruitment is necessary for establishment of viral infection or its clearance, we collected cardiac tissue from the same four groups of animals at an earlier timepoint (36 hours post-inoculation). At this early timepoint, the cardiac tissues of hACE2-KI animals showed similar levels of SARS-CoV-2 RNA regardless of antibody treatment, suggesting that CCR2 blockade aids with viral clearance rather than prevents early establishment of infection in the heart (**Figure 4.5E**).

Together these data demonstrate that recruitment of CCR2⁺ cells to the heart during cardiac SARS-CoV-2 infection drives cardiac dysfunction and prevents early viral clearance.

4.4 Discussion

In this study, we describe a novel MYH6-hACE transgenic mouse that expresses human ACE2 exclusively in cardiomyocytes and can be used to model in vivo cardiomyocytes-restricted infection of SARS-CoV-2. We found that viral RNA was detected in mouse hearts at dpi 3 and was cleared by 1 week after intravenous inoculation. Viral infection in these animals leads to a macrophage-predominant immune cell accumulation at 1 week post-inoculation and is

accompanied with a decrease in left ventricular ejection fraction and fractional shortening detected by transthoracic echocardiography. This functional change is dependent on CCR2+ cell recruitment to the heart and CCR2 signaling blockade improves viral clearance from the heart.

Cardiac involvement during the course of SARS-CoV-2 is common but is mild in most human cases¹⁰. Clinically significant cardiac changes are associated with more severe disease requiring hospitalization^{11,12,14}. The dysfunction we observed in MYH6-hACE2 mouse model was characterized by a 10% decrease in left ventricular ejection fraction and fractional shortening following the infection. This moderate decrease allows us to model changes that are physiologically relevant to most patients rather than focusing on severe disease confined to the hospitalized subgroup. Furthermore, the animals have recovered cardiac function several weeks after the infection, which further corresponds to the recovery seen in most people affected with cardiovascular COVID-19^{11,46,47}.

Another unique strength of the model is its ability to isolate functional effects of cardiac disease caused by SARS-CoV-2 infection from those of other systems. Since the heart is physically linked with the other organs in the body via blood vessels, changes to their function can affect cardiac physiology independent of a direct cardiac insult in a form of viral infection. These are especially likely since severe pulmonary disease has been reported in the mouse models⁴⁸. In addition to direct vascular and hemodynamic strain that such infection can cause, pulmonary disease is accompanied with robust systemic inflammatory response that can alter cardiac function. MYH6-hACE2 mouse model offers a chance to control for these factors and instead focus on the cardiac phenotypes caused by infection of the heart with SARS-CoV-2 and intrinsic response of

cardiac cells to the virus. While interplay between multiple infected organs and systemic inflammation may play key roles in cardiac injury and dysfunction during clinical course of COVID-19, knowledge of their individual contributions facilitated by our model can further our understanding of pathophysiology and be crucial for development of organ-specific therapies.

The nature of immune response in SARS-COV-2 infection has been closely studied since the beginning of the pandemic due to interests in application of novel and existing immunotherapies for the disease. Unlike other viral myocarditis models where a lymphocytic immune infiltrate is common, we observed macrophage accumulation in hearts of MYH6-hACE2 animals⁴⁹. This finding mimics immune response in COVID-19 associated cardiovascular disease, in which patients presented primarily with monocyte and macrophage-rich infiltrate in the cardiac tissue^{5,11,14,50}. Our study further shows a role of CCR2+ cells in establishing the cardiac dysfunction in this model and delaying viral clearance from the heart. Monocytes and macrophages have been previously implicated in pathogenesis of COVID-19 in patients, but their role in disease establishment has been associated with FcγR- or hACE2-mediated abortive infection of these cells^{51,52}. However, in our model macrophages lack hACE2 and circulating IgG antibodies are not expected to develop this early in infection (at dpi 3). Moreover, the blockade of monocyte-derived macrophages at an earlier time point (36 hours post-inoculation) does not change viral loads in the heart and implicates these cells in impeding clearance rather than establishment of infection. The exact mechanism of such clearance remains to be further explored.

MYH6-hACE2 mouse model of cardiac infection with SARS-COV-2 can be further used for characterization of long-term effects of SARS-COV-2. Post-acute COVID-19 Syndrome (PACS) is fairly common in patients and recent large studies show that cardiovascular

complication are frequent even 1 year from acute infection⁵³. However, the mechanisms behind such persistent change are not understood. MYH6-hACE2 mouse offers a great opportunity to assess long-term consequences of cardiomyocyte infection by subjecting animals to secondary insult such as hypertensive injury (phenylephrine - angiotensin I injury), vigorous exercise (treadmill challenge), metabolic stress (high-fat diet). Alternatively, the model also allows for interrogation of prior cardiovascular insults on later cardiac SARS-CoV-2 infection. Obesity, diabetes, cardiac events are known risk factors for severe COVID-19 in humans but their role is not known in cardiac disease associated with COVID-19. As such, cardiovascular insults can be administered prior to infection and thus can be expanded to those performed outside of BSL-3 level barrier, including ischemia-reperfusion injury. Finally, utilization of a mouse-adapted strain of SARS-CoV-2 can be used to model systemic infection with a potential exacerbated cardiac disease.

While SARS-CoV-2 infection of MYH6-hACE2 mice provides a robust model for study of cardiovascular component of COVID-19 pathophysiology, we acknowledge several limitations. These animals have non-physiologic levels of ACE2 since it is driven by exogenous synthetic promoter (CAG)⁵⁴. This expression is further independent of the natural ACE2 regulation⁵⁵. Furthermore, this model excludes non-cardiomyocyte cells which can play a role in cardiac dysfunction caused by viral infection. Finally, the model excludes potentially important effects of systemic disease on the heart, which is why it should be used in combination with other approaches to elucidate a more complete picture of cardiac disease seen in COVID-19 patients.

In summary, we show that infection of MYH6-hACE2 transgenic mice with SARS-CoV-2 leads to robust transient viral replication in the heart and macrophage-heavy immune infiltrate

that mediates decreased cardiac function in these animals. MYH6-hACE2 mouse is an attractive model for cardiac-restricted infection with SARS-CoV-2 and can be useful for understanding cardiac pathogenesis of this agent as well as designing organ-specific therapeutics for COVID-19.

4.5 Methods

Biosafety All parts of this project were reviewed and approved by the Environmental Health and Safety Office at Washington University School of Medicine. Work with SARS-CoV-2 strains was carried out in laminar flow cabinets inside a BSL-3 laboratory by trained personnel equipped with powered air purifying respirators (PAPR).

Viruses. The WA1/2020 isolate of SARS-CoV-2 was obtained from the United States Centers for Disease Control (CDC). The B.1.351 isolate was obtained from a nasopharyngeal swab. Infectious stocks were grown by passaging virus twice on Vero-TMPRSS2 cells and collecting supernatant upon observation of cytopathic effect. Debris was removed by centrifugation and passage through a 0.22 µm filter, supernatant was stored at -80 °C. Stocks were sequenced for mutational burden and no additional mutations in furin cleavage site were found. The site was previously reported to confer changes in virulence of SARS-CoV-2 *in vitro* and *in vivo*⁵⁶.

Animals. Animal studies were carried out in accordance with the recommendations in the Guide for the Care and Use of Laboratory Animals of the National Institutes of Health. Study protocols were reviewed and approved by the Institutional Animal Care and Use Committee at the Washington University School of Medicine (assurance number A3381-01). Intranasal inoculation with virus were performed under anesthetic effect of ketamine hydrochloride and xylazine.

Intravenous inoculation with virus was performed via retroorbital injection under anesthetic effects of isoflurane. All efforts were made to minimize animal suffering.

129 mice (strain: 129S2/SvPasCr1) were obtained from Charles River Laboratories. Animals were housed in groups and fed standard chow diet. Male and female mice 17-20 weeks of age were intranasally inoculated with 1.0×10^6 FFU of B.1.351 strain of SARS-CoV-2. Mock infection (supernatant collected from Vero-TMPRSS2 cells used for viral propagation but uninfected with virus) was used as control.

MYH6-Cre (Tg(Myh6-cre)1Jmk/J) was graciously donated by Dr. Abhinav Diwan at Washington University in St. Louis. Rosa-LoxP-STOP-LoxP-hACE2 mice were obtained from Cyagen. Rosa-LoxP-STOP-LoxP-hACE2 mice were engineered to harbor a human sequence of ACE2 (hACE2) introduced into Rosa locus under exogenous CAG promoter and preceded with a stop codon surrounded by LoxP sites. MYH6-Cre-Rosa-LoxP-STOP-LoxP-hACE2 (MYH6-hACE2) animals were bred at Washington University School of medicine animal facilities. Animals were housed in groups and fed standard chow diet. All animal used for the study were heterozygous for hACE2, Cre-negative animals were used as controls while Cre-positive animals comprised experimental group. Male and female mice 10-14-weeks of age were intravenously inoculated with 1.0×10^6 PFU of WA1/2020 strain of SARS-CoV-2.

Antibody treatment was performed with anti-CCR2 antibody (clone MC-21) obtained from Dr. Matthias Mack at Universitat Regensburg. Mice received a loading dose of $50 \mu\text{g}$ via intraperitoneal (IP) injection one day prior to viral inoculation. Inhibition of CCR2 was maintained for the duration of the experiment with $25 \mu\text{g}$ of antibody administered IP every other day. Rat

IgG2a isotype (Leinco Technologies, clone 1-1, cat# I11) was used at the same injection regiment and dose for isotype control group.

Quantitative RT-PCR Tissues were harvested after perfusion of circulatory system with 7mL of PBS. Tissues were homogenized in Trizol reagent (Invitrogen). Chloroform was added, homogenates vortexed and separated by centrifugation. Aqueous layer was transferred to PureLink Mini RNA columns (Thermo Fisher Scientific) and RNA was extracted per manufacturer's protocol and treated with DNase (Qiagen).

Genomic and subgenomic copies of SARS-CoV-2 N gene RNA were quantified using previously published assay⁵⁷. Briefly, TaqMan RNA-to-CT 1-Step Kit (ThermoFisher) was used with reverse transcription step at 48°C for 15 min and amplification over 50 cycles of 95°C for 15 s and 60°C for 1 min. Genomic copies of SARS-CoV-2 N gene RNA were detected using the following primers and probes: Forward primer: ATGCTGCAATCGTGCTACAA; Reverse primer: GACTGCCGCCTCTGCTC; Probe: /56-FAM/TCAAGGAAC/ZEN/AACATTGCCAA/3IABkFQ/. Subgenomic copies of SARS-CoV-2 N gene RNA were detected using the following primers and probes: forward primer: ACCAACCAACTTTCGATCTCTT'; Reverse primer: GCGTTCTCCATTCTGGTTACT; Probe: /56-FAM/ACGTTTGGT/ZEN/GGACCCTCAGATTCA/ 3IABkFQ/. A separate standard was designed for each of the primer sets to allow for copy number determination down to 10 copies per reaction. The reaction mixture contained final concentrations of primers and probe of 500 and 100 nM, respectively.

For hACE2 detection, reverse-transcription was carried out using the High Capacity cDNA Reverse Transcription Kit (ThermoFisher) and amplification performed with SYBR Green system (ThermoFisher) with 36B4 as an internal reference gene.

Cardiac histology For CD68 and hACE2 staining, cardiac tissues were fixed with 4% PFA for 24 hours, embedded in O.C.T. compound (Fisher HealthCare) and sectioned on cryostat at 10um thick. Slides were permeabilized with 0.25% tritonX (Sigma), blocked with 10% FBS in PBS, incubated with primary antibodies overnight, secondary antibodies for 1 hour, and mounted with Vectashield mounting medium with DAPI (Sigma). Primary antibodies against mouse CD68 (Biolegend 137002, 1:400) and human ACE2 (Abcam ab15348, 1:250) were used. Secondary fluorophore-conjugated antibodies used included AlexaFluor555 anti-Rat IgG (Invitrogen A21434) and AlexaFluor555 anti-Rabbit IgG (Invitrogen A21428).

For CD45 staining, cardiac tissues were fixed with 10% NBF for 7 days, embedded in paraffin and sectioned on microtome into 10um thick sections. Mouse CD45 was visualized using Opal 4-Color Manual IHC Kit (Perkin-Elmer) with the following changes: 1) 10% NBF fixation step was substituted for treatment with 10% MeOH + 10% hydrogen peroxide in water for 20 min; 2) blocking buffer was substituted for 10% FBS in TBST. Images were collected on a confocal microscope (Zeiss LSM 700 Laser Scanning Confocal Microscope) and analyzed in ZenBlue and ZenBlack software (Zeiss). For CD68 and CD45 stains, at least 3 different images of most affected of each heart areas were taken and manually quantified. For human ACE2, representative images were taken without quantification.

Echocardiography Transthoracic echocardiography of mice was performed inside sterile laminar flow hood of BSL3 facility using Vevo3100 echocardiographer (FujiFilm VisualSonics).

Animals were lightly sedated with 2% avertin (Sigma) administered as needed to keep the mouse unrestrained in the left lateral recumbent position. Heat pad was used to prevent heat loss. Animal heart rate was monitored to assess proper depth of anesthesia with the target range of 550-650 beats per minute. B-mode of left ventricle in long axis projection and M-mode of short axis projection were recorded. Ejection fraction and fractional shortening of the left ventricle were measured on B-mode videos in long axis view in Vevo LAB software (FujiFilm VisioalSonics, version 5.7.1) using speckle tracing algorithm Vevo Strain for 2 consecutive heartbeats in representative clips.

Flow cytometry Animal hearts were processed using a modification of the previously published protocol⁵⁸. Briefly, hearts were perfused with PBS, major vessels and atria removed and ½ of the organ used for flow cytometry. Tissue was minced with a razor blade and digested in DMEM with collagenase IV (250U/mL, Sigma), DNase I (60U/mL, Sigma) and hyaluronidase I (60U/mL, Sigma) at 37°C with agitation. Digest was inactivated with HBB and resulting suspension was passed through a 40um filter. Red blood cell lysis was performed with ACK buffer (Gibco). Single cell suspension was stained with 1:200 dilution of antibodies. Myeloid heart panel included mouse CD45-PerCP/Cy5.5 (Biolegend 103132), CD11b-PE/Cy7 (Biolegend 101215), Ly6G-FITC (Biolegend 127606), Ly6C-BV510 (Biolegend 128033), CD64-APC (Biolegend 139305), MHCII-APC/Cy7 (Biolegend 107628), CCR2-BV421 (Biolegend 150605). Lymphoid heart panel included CD45-PerCP/Cy5.5 (Biolegend 103132), CD11b-BV785 (Biolegend 101243), CD8b-PE/Cy7 (Biolegend 126615), CD4-PE (Biolegend 116005), CD19-BV510 (Biolegend 115546). Blood panel included CD45-PerCP/Cy5.5 (Biolegend 103132), CD11b-BV785 (Biolegend 101243), Ly6G-FITC (Biolegend 127606), Ly6C-BV605 (Biolegend 128036),

CD19-BV510 (Biolegend 115546), CD8b-PE/Cy7 (Biolegend 126615), CD4-PE (Biolegend 116005). Cells were fixed in 4% PFA for 20 min. Myeloid heart panel was processed on FACS Melody (Becton, Dickinson and Company). Blood and lymphoid heart panels were processed on Aurora (Cytex).

All flow cytometry analysis was performed in FlowJo (Becton, Dickinson and Company, version 10.8.1)

RNA sequencing. Bulk RNA sequencing was performed by GTAC@MGI at Washington University in St. Louis. RNA samples from heart homogenates were prepared according to library kit manufacturer's protocol, indexed, pooled, and sequenced on an Illumina NovaSeq 6000. Basecalls and demultiplexing were performed with Illumina's bcl2fastq software and a custom python demultiplexing program with a maximum of one mismatch in the indexing read. RNA-seq reads were then aligned to the Ensembl release 101 primary assembly with STAR version 2.7.9a⁵⁹. Gene counts were derived from the number of uniquely aligned unambiguous reads by Subread:featureCount version 2.0.3⁶⁰. Isoform expression of known Ensembl transcripts were quantified with Salmon version 1.5.2⁶¹. Sequencing performance was assessed for the total number of aligned reads, total number of uniquely aligned reads, and features detected. The ribosomal fraction, known junction saturation, and read distribution over known gene models were quantified with RSeQC version 4.0⁶².

All gene counts were then imported into the R/Bioconductor package EdgeR5 and TMM normalization size factors were calculated to adjust for samples for differences in library size. Ribosomal genes and genes not expressed in the smallest group size minus one samples greater than one count-per-million were excluded from further analysis. The TMM size factors and the

matrix of counts were then imported into the R/Bioconductor package Limma⁶³. Weighted likelihoods based on the observed mean-variance relationship of every gene and sample were then calculated for all samples with the `voomWithQualityWeights`⁶⁴ function and were fitted using a Limma generalized linear model with additional unknown latent effects as determined by surrogate variable analysis (SVA)⁶⁵. The performance of all genes was assessed with plots of the residual standard deviation of every gene to their average log-count with a robustly fitted trend line of the residuals. Differential expression analysis was then performed to analyze for differences between conditions and the results were filtered for only those genes with Benjamini-Hochberg false-discovery rate adjusted p-values less than or equal to 0.05.

For each contrast extracted with Limma, global perturbations in known Gene Ontology (GO) terms, MSigDb, and KEGG pathways were detected using the R/Bioconductor package GAGE⁶⁶ to test for changes in expression of the reported log 2 fold-changes reported by Limma in each term versus the background log 2 fold-changes of all genes found outside the respective term. The R/Bioconductor package heatmap3⁶⁷ was used to display heatmaps across groups of samples for each GO or MSigDb term with a Benjamini-Hochberg false-discovery rate adjusted p-value less than or equal to 0.05. Perturbed KEGG pathways where the observed log 2 fold-changes of genes within the term were significantly perturbed in a single-direction versus background or in any direction compared to other genes within a given term with p-values less than or equal to 0.05 were rendered as annotated KEGG graphs with the R/Bioconductor package Pathview⁶⁸.

To find the most critical genes, the Limma `voomWithQualityWeights` transformed log 2 counts-per-million expression data was then analyzed via weighted gene correlation network

analysis with the R/Bioconductor package WGCNA⁶⁹. Briefly, all genes were correlated across each other by Pearson correlations and clustered by expression similarity into unsigned modules using a power threshold empirically determined from the data. An eigengene was then created for each de novo cluster and its expression profile was then correlated across all coefficients of the model matrix. Because these clusters of genes were created by expression profile rather than known functional similarity, the clustered modules were given the names of random colors where grey is the only module that has any pre-existing definition of containing genes that do not cluster well with others. These de-novo clustered genes were then tested for functional enrichment of known GO terms with hypergeometric tests available in the R/Bioconductor package clusterProfiler⁷⁰. Significant terms with Benjamini-Hochberg adjusted p-values less than 0.05 were then collapsed by similarity into clusterProfiler category network plots to display the most significant terms for each module of hub genes in order to interpolate the function of each significant module. The information for all clustered genes for each module were then combined with their respective statistical significance results from Limma to determine whether or not those features were also found to be significantly differentially expressed.

Statistics Statistical tests that were used are specified in individual figures. Statistical analysis was performed in Prism (GraphPad, version 9.4.1).

4.6 References

1. Hu, B., Guo, H., Zhou, P. & Shi, Z.-L. Characteristics of SARS-CoV-2 and COVID-19. *Nature Reviews Microbiology* (2020) doi:10.1038/s41579-020-00459-7.
2. Lai, C.-C., Ko, W.-C., Lee, P.-I., Jean, S.-S. & Hsueh, P.-R. Extra-respiratory manifestations of COVID-19. *International Journal of Antimicrobial Agents* **56**, 106024 (2020).
3. Szekely Yishay *et al.* Spectrum of Cardiac Manifestations in COVID-19. *Circulation* **142**, 342–353 (2020).

4. Wadman, M., Couzin-Frankel, J., Kaiser, J. & Maticic, C. A rampage through the body. *Science* **368**, 356–360 (2020).
5. Basso, C. *et al.* Pathological features of COVID-19-associated myocardial injury: a multicentre cardiovascular pathology study. *European Heart Journal* **41**, 3827–3835 (2020).
6. Bearnse, M. *et al.* Factors associated with myocardial SARS-CoV-2 infection, myocarditis, and cardiac inflammation in patients with COVID-19. *Modern Pathology* (2021) doi:10.1038/s41379-021-00790-1.
7. Mueller, C. *et al.* Cardiovascular biomarkers in patients with COVID-19. *European Heart Journal. Acute Cardiovascular Care* (2021) doi:10.1093/ehjacc/zuab009.
8. Lindner, D. *et al.* Association of Cardiac Infection With SARS-CoV-2 in Confirmed COVID-19 Autopsy Cases. *JAMA Cardiology* (2020) doi:10.1001/jamacardio.2020.3551.
9. Madjid, M., Safavi-Naeini, P., Solomon, S. D. & Vardeny, O. Potential Effects of Coronaviruses on the Cardiovascular System: A Review. *JAMA Cardiology* **5**, 831–840 (2020).
10. Puntmann, V. O. *et al.* Outcomes of Cardiovascular Magnetic Resonance Imaging in Patients Recently Recovered From Coronavirus Disease 2019 (COVID-19). *JAMA Cardiology* (2020) doi:10.1001/jamacardio.2020.3557.
11. Zeng, J.-H. *et al.* First case of COVID-19 complicated with fulminant myocarditis: a case report and insights. *Infection* **48**, 773–777 (2020).
12. Doyen, D., Mocerri, P., Ducreux, D. & Dellamonica, J. Myocarditis in a patient with COVID-19: a cause of raised troponin and ECG changes. *The Lancet* **395**, 1516 (2020).
13. Nalbandian, A. *et al.* Post-acute COVID-19 syndrome. *Nature Medicine* **27**, 601–615 (2021).
14. Bailey Adam L. *et al.* SARS-CoV-2 Infects Human Engineered Heart Tissues and Models COVID-19 Myocarditis. *JACC: Basic to Translational Science* **6**, 331–345 (2021).
15. Sharma, A. *et al.* Human iPSC-Derived Cardiomyocytes Are Susceptible to SARS-CoV-2 Infection. *Cell Reports Medicine* **1**, 100052 (2020).
16. Bojkova, D. *et al.* SARS-CoV-2 infects and induces cytotoxic effects in human cardiomyocytes. *Cardiovascular Research* (2020) doi:10.1093/cvr/cvaa267.
17. Williams, T. L. *et al.* Human embryonic stem cell-derived cardiomyocyte platform screens inhibitors of SARS-CoV-2 infection. *Commun Biol* **4**, 1–8 (2021).
18. Rudraraju, R. *et al.* Parallel use of pluripotent human stem cell lung and heart models provide new insights for treatment of SARS-CoV-2. 2022.09.20.508614 Preprint at <https://doi.org/10.1101/2022.09.20.508614> (2022).
19. Hoffmann, M. *et al.* SARS-CoV-2 Cell Entry Depends on ACE2 and TMPRSS2 and Is Blocked by a Clinically Proven Protease Inhibitor. *Cell* **181**, 271-280.e8 (2020).

20. Navaratnarajah, C. K. *et al.* Highly Efficient SARS-CoV-2 Infection of Human Cardiomyocytes: Spike Protein-Mediated Cell Fusion and Its Inhibition. *Journal of Virology* **95**, e01368-21 (2021).
21. Marchiano, S. *et al.* SARS-CoV-2 Infects Human Pluripotent Stem Cell-Derived Cardiomyocytes, Impairing Electrical and Mechanical Function. *Stem Cell Reports* **16**, 478–492 (2021).
22. Cleary, S. J. *et al.* Animal models of mechanisms of SARS-CoV-2 infection and COVID-19 pathology. *British Journal of Pharmacology* **177**, 4851–4865 (2020).
23. Johansen, M. D. *et al.* Animal and translational models of SARS-CoV-2 infection and COVID-19. *Mucosal Immunology* **13**, 877–891 (2020).
24. Imai, M. *et al.* Syrian hamsters as a small animal model for SARS-CoV-2 infection and countermeasure development. *Proceedings of the National Academy of Sciences* **117**, 16587–16595 (2020).
25. Sia, S. F. *et al.* Pathogenesis and transmission of SARS-CoV-2 in golden hamsters. *Nature* **583**, 834–838 (2020).
26. Rizvi, Z. A. *et al.* Golden Syrian hamster as a model to study cardiovascular complications associated with SARS-CoV-2 infection. *eLife* **11**, e73522 (2022).
27. Hassan, A. O. *et al.* A SARS-CoV-2 Infection Model in Mice Demonstrates Protection by Neutralizing Antibodies. *Cell* **182**, 744-753.e4 (2020).
28. Hassan, A. O. *et al.* A Single-Dose Intranasal ChAd Vaccine Protects Upper and Lower Respiratory Tracts against SARS-CoV-2. *Cell* **183**, 169-184.e13 (2020).
29. Chen, R. E. *et al.* In vivo monoclonal antibody efficacy against SARS-CoV-2 variant strains. *Nature* **596**, 103–108 (2021).
30. Ying, B. *et al.* Boosting with variant-matched or historical mRNA vaccines protects against Omicron infection in mice. *Cell* **185**, 1572-1587.e11 (2022).
31. Winkler, E. S. *et al.* SARS-CoV-2 Causes Lung Infection without Severe Disease in Human ACE2 Knock-In Mice. *Journal of Virology* **96**, e01511-21 (2022).
32. Jiang, R.-D. *et al.* Pathogenesis of SARS-CoV-2 in Transgenic Mice Expressing Human Angiotensin-Converting Enzyme 2. *Cell* **182**, 50-58.e8 (2020).
33. Niu, Z. *et al.* N501Y mutation imparts cross-species transmission of SARS-CoV-2 to mice by enhancing receptor binding. *Sig Transduct Target Ther* **6**, 1–3 (2021).
34. Bräuninger, H. *et al.* Cardiac SARS-CoV-2 infection is associated with pro-inflammatory transcriptomic alterations within the heart. *Cardiovascular Research* **118**, 542–555 (2022).
35. Lavine, K. J. *et al.* The Macrophage in Cardiac Homeostasis and Disease: JACC Macrophage in CVD Series (Part 4). *Journal of the American College of Cardiology* **72**, 2213–2230 (2018).
36. Seifert, A., Werheid, D. F., Knapp, S. M. & Tobiasch, E. Role of Hox genes in stem cell differentiation. *World J Stem Cells* **7**, 583–595 (2015).

37. Danilczyk, U. *et al.* Essential role for collectrin in renal amino acid transport. *Nature* **444**, 1088–1091 (2006).
38. Malakauskas, S. M. *et al.* Aminoaciduria and altered renal expression of luminal amino acid transporters in mice lacking novel gene collectrin. *American Journal of Physiology-Renal Physiology* **292**, F533–F544 (2007).
39. Li, Y. *et al.* Cidec differentially regulates lipid deposition and secretion through two tissue-specific isoforms. *Gene* **641**, 265–271 (2018).
40. Rochette, L., Dogon, G., Zeller, M., Cottin, Y. & Vergely, C. GDF15 and Cardiac Cells: Current Concepts and New Insights. *International Journal of Molecular Sciences* **22**, 8889 (2021).
41. Guglielmi, V. *et al.* Characterization of sarcoplasmic reticulum Ca²⁺ ATPase pumps in muscle of patients with myotonic dystrophy and with hypothyroid myopathy. *Neuromuscular Disorders* **26**, 378–385 (2016).
42. Epelman, S. *et al.* Embryonic and Adult-Derived Resident Cardiac Macrophages Are Maintained through Distinct Mechanisms at Steady State and during Inflammation. *Immunity* **40**, 91–104 (2014).
43. Bajpai, G. *et al.* The human heart contains distinct macrophage subsets with divergent origins and functions. *Nature Medicine* **24**, 1234–1245 (2018).
44. Bajpai, Geetika *et al.* Tissue Resident CCR2[−] and CCR2⁺ Cardiac Macrophages Differentially Orchestrate Monocyte Recruitment and Fate Specification Following Myocardial Injury. *Circulation Research* **124**, 263–278 (2019).
45. Mack, M. *et al.* Expression and Characterization of the Chemokine Receptors CCR2 and CCR5 in Mice1. *The Journal of Immunology* **166**, 4697–4704 (2001).
46. Hu, H., Ma, F., Wei, X. & Fang, Y. Coronavirus fulminant myocarditis treated with glucocorticoid and human immunoglobulin. *Eur Heart J* **42**, 206 (2020).
47. Daniels, C. J. *et al.* Prevalence of Clinical and Subclinical Myocarditis in Competitive Athletes With Recent SARS-CoV-2 Infection: Results From the Big Ten COVID-19 Cardiac Registry. *JAMA Cardiology* **6**, 1078–1087 (2021).
48. Winkler, E. S. *et al.* SARS-CoV-2 infection of human ACE2-transgenic mice causes severe lung inflammation and impaired function. *Nature Immunology* **21**, 1327–1335 (2020).
49. Tam, P. E. Coxsackievirus Myocarditis: Interplay between Virus and Host in the Pathogenesis of Heart Disease. *Viral Immunology* **19**, 133–146 (2006).
50. Fox, S. E., Falgout, L. & Vander Heide, R. S. COVID-19 myocarditis: quantitative analysis of the inflammatory infiltrate and a proposed mechanism. *Cardiovasc Pathol* **54**, 107361 (2021).
51. Sefik, E. *et al.* Inflammasome activation in infected macrophages drives COVID-19 pathology. *Nature* **606**, 585–593 (2022).

52. Junqueira, C. *et al.* FcγR-mediated SARS-CoV-2 infection of monocytes activates inflammation. *Nature* **606**, 576–584 (2022).
53. Xie, Y., Xu, E., Bowe, B. & Al-Aly, Z. Long-term cardiovascular outcomes of COVID-19. *Nat Med* **28**, 583–590 (2022).
54. Jun-ichi, M. *et al.* Expression vector system based on the chicken β-actin promoter directs efficient production of interleukin-5. *Gene* **79**, 269–277 (1989).
55. Turner, A. J. ACE2 Cell Biology, Regulation, and Physiological Functions. *The Protective Arm of the Renin Angiotensin System (RAS)* 185–189 (2015) doi:10.1016/B978-0-12-801364-9.00025-0.
56. Johnson, B. A. *et al.* Loss of furin cleavage site attenuates SARS-CoV-2 pathogenesis. *Nature* **591**, 293–299 (2021).
57. Case, J. B., Bailey, A. L., Kim, A. S., Chen, R. E. & Diamond, M. S. Growth, detection, quantification, and inactivation of SARS-CoV-2. *Virology* **548**, 39–48 (2020).
58. AU - Bajpai, G. & AU - Lavine, K. J. Isolation of Macrophage Subsets and Stromal Cells from Human and Mouse Myocardial Specimens. *JoVE* e60015 (2019) doi:10.3791/60015.
59. Dobin, A. *et al.* STAR: ultrafast universal RNA-seq aligner. *Bioinformatics* **29**, 15–21 (2013).
60. Liao, Y., Smyth, G. K. & Shi, W. featureCounts: an efficient general purpose program for assigning sequence reads to genomic features. *Bioinformatics* **30**, 923–930 (2014).
61. Patro, R., Duggal, G., Love, M. I., Irizarry, R. A. & Kingsford, C. Salmon provides fast and bias-aware quantification of transcript expression. *Nat Methods* **14**, 417–419 (2017).
62. Wang, L., Wang, S. & Li, W. RSeQC: quality control of RNA-seq experiments. *Bioinformatics* **28**, 2184–2185 (2012).
63. Ritchie, M. E. *et al.* limma powers differential expression analyses for RNA-sequencing and microarray studies. *Nucleic Acids Research* **43**, e47–e47 (2015).
64. Liu, R. *et al.* Why weight? Modelling sample and observational level variability improves power in RNA-seq analyses. *Nucleic Acids Research* **43**, e97–e97 (2015).
65. Leek, J. T. & Storey, J. D. Capturing Heterogeneity in Gene Expression Studies by Surrogate Variable Analysis. *PLOS Genetics* **3**, e161 (2007).
66. Luo, W., Friedman, M. S., Shedden, K., Hankenson, K. D. & Woolf, P. J. GAGE: generally applicable gene set enrichment for pathway analysis. *BMC Bioinformatics* **10**, 161 (2009).
67. Zhao, S., Guo, Y., Sheng, Q. & Shyr, Y. Advanced Heat Map and Clustering Analysis Using Heatmap3. *BioMed Research International* **2014**, 986048 (2014).
68. Luo, W. & Brouwer, C. Pathview: an R/Bioconductor package for pathway-based data integration and visualization. *Bioinformatics* **29**, 1830–1831 (2013).
69. Langfelder, P. & Horvath, S. WGCNA: an R package for weighted correlation network analysis. *BMC Bioinformatics* **9**, 559 (2008).

70. Yu, G., Wang, L.-G., Han, Y. & He, Q.-Y. clusterProfiler: an R Package for Comparing Biological Themes Among Gene Clusters. *OMICS* **16**, 284–287 (2012).

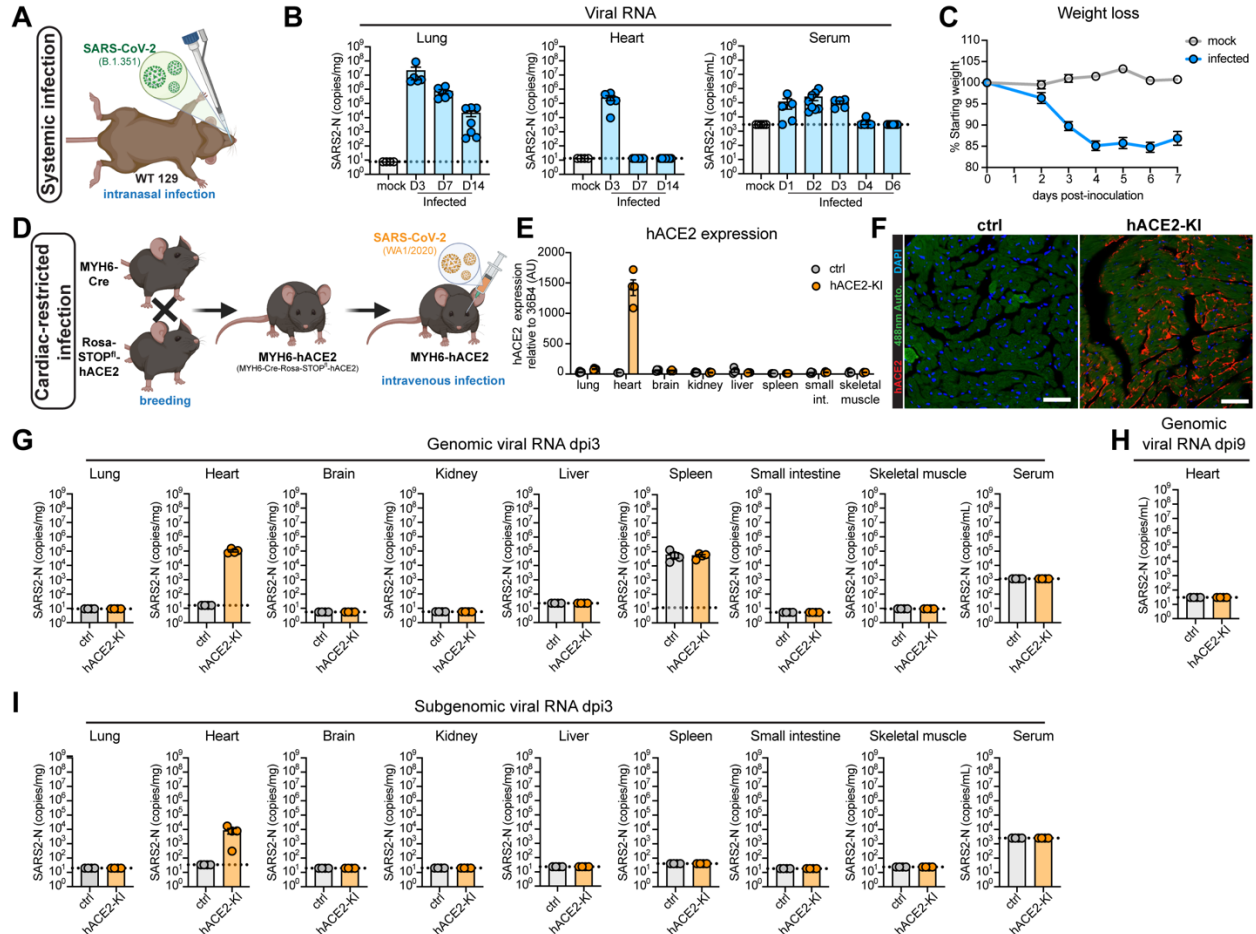


Figure 4.1. Systemic and cardiac-restricted murine models of SARS-CoV-2 infection. (A) Schematic of intranasal mouse infection with SARS-CoV-2: 129 mice were inoculated with B.1.351 (beta) strain of SARS-CoV-2. (B) qPCR for viral *N* gene in lung (left), heart (center) and serum (right); D on X-axis for days post inoculation; dotted line – limit of detection. (C) Mouse weight as percent of starting weight over time. Points represent mean weight (n=4 mock, n=7 infected), error bars for standard error of mean. (D) Schematic of cardiac-restricted mouse infection with SARS-CoV-2: MYH6-Cre-Rosa-STOP^{fl}-hACE2 (MYH6-hACE2) mice with cardiac-specific expression of hACE2 were intravenously infected with hACE2-restricted strain of SARS-CoV-2 (WA1/2020). (E) qPCR for human *ACE2* from Cre- (ctrl) and Cre+ (hACE2-KI) MYH6-hACE2 animals in tissues; in reference to murine *36B4*. (F) Immunofluorescence for human *ACE2* in Cre- (ctrl) and Cre+ (hACE2-KI) animals; DAPI (nuclei) - blue, 488nm autofluorescence (tissue) – green, hACE2 – red. (G) qPCR for SARS-CoV-2 *N* genomic RNA at day 3 post-inoculation in tissues; dotted line – limit of detection. (H) qPCR for SARS-CoV-2 *N* genomic RNA at day 9 post-inoculation in heart; dotted line – limit of detection. (I) qPCR for SARS-CoV-2 *N* subgenomic RNA at day 3 post-inoculation in tissues; dotted line – limit of detection. Unless specified otherwise, points represent measurements for individual mice, bars represent mean and error bars – standard error of mean.

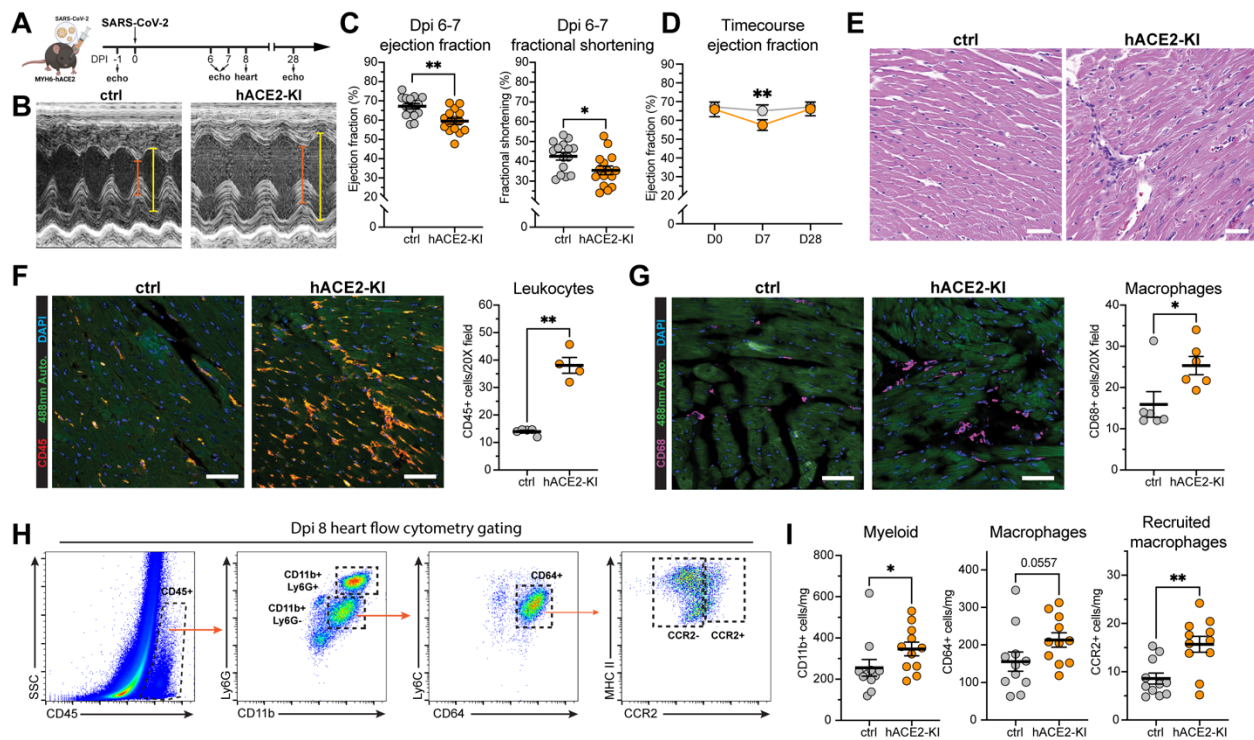


Figure 4.2. Infection with SARS-CoV-2 leads to cardiac dysfunction and macrophage accumulation. (A) MYH6-hACE2 mice (Cre- ctrl and Cre+ hACE2-KI) underwent intranasal inoculation with SARS-CoV-2, serial transthoracic echocardiography and heart collection at dpi 8-9. (B) Representative M-mode images of left ventricle in control (ctrl) and hACE2-KI mice at dpi7; orange line denotes systolic dimension, yellow line – diastolic. (C) Quantification of left ventricular ejection fraction (left) and left ventricular fractional shortening (right) at dpi 6-7. (D) Time course of LV ejection fraction; grey – ctrl, orange – hACE2-KI, D – dpi; points represent mean in group, 2-way ANOVA with Dunnett’s multiple comparisons (compared to D0 of each group). (E) Representative hematoxylin-eosin stained image of cardiac tissue at dpi8. (F, G) Representative immunofluorescence images of cardiac tissue with quantification; DAPI (nuclei) – blue, 488nm fluorescence (tissue) – green, CD45 (immune cells) – red, CD68 (macrophages) – magenta; (H) Gating strategy for myeloid immune cells in the heart. (I) Absolute event number quantification of key myeloid populations by flow cytometry. Unless stated otherwise, points represent measurements for individual mice, error bars – standard error of mean and statistics is Mann-Whitney non-parametric test, * $p < 0.05$, ** $p < 0.01$

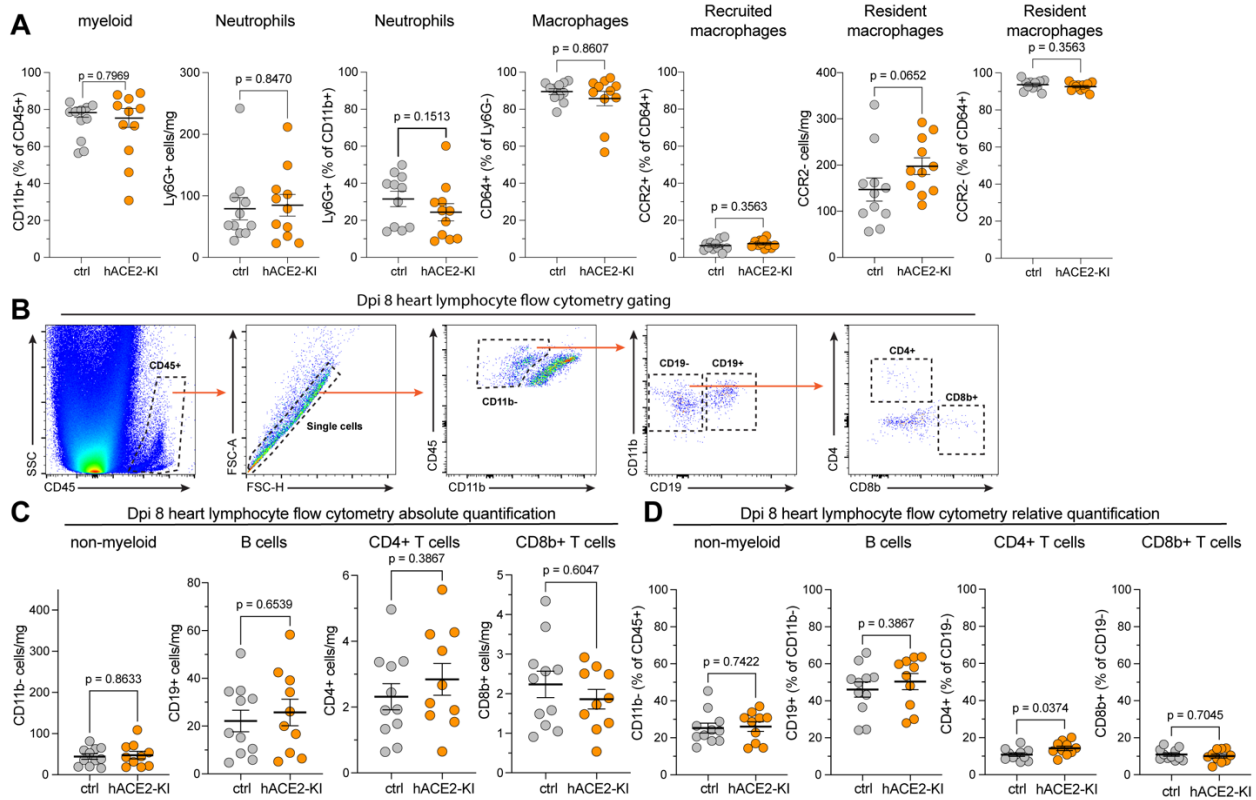


Figure 4.3. Flow cytometry of cardiac immune cells from infected MYH6-hACE2 mice at dpi 8. (A) Quantification of flow cytometry of myeloid cells in the heart at dpi 8. Absolute and relative quantifications of gates according to Figure 4.2. **(B)** Gating scheme of flow cytometry of lymphoid cells in the heart at dpi 8. **(C)** Quantification of cardiac flow cytometry at dpi 8 (number of cells per mg tissue). **(D)** Quantification of cardiac flow cytometry at dpi 8 (percent of parent gate). Points represent measurements for individual mice, bars represent mean and error bars – standard error of mean. Statistical test: Mann-Whitney nonparametric test with p-values listed on graph comparing Cre-negative control (ctrl) and Cre-positive hACE expressing animals (hACE2-KI)

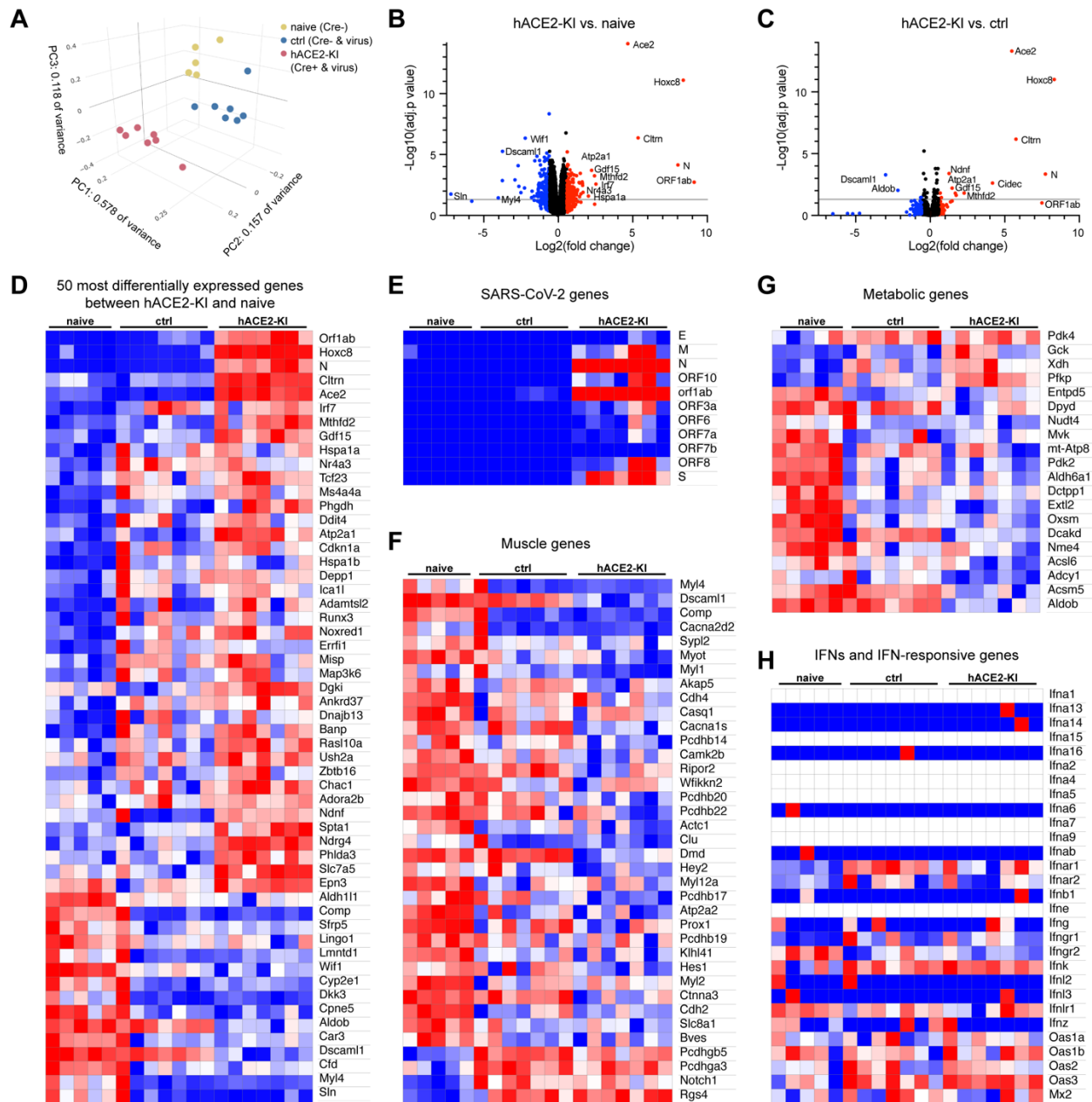


Figure 4.4. SARS-CoV-2 causes downregulation of sarcomere and metabolism genes. RNAseq at dpi3 of bulk heart homogenate from naïve (Cre-negative, not treated with virus), ctrl (Cre-negative, injected with virus) and hACE2-KI (Cre+ injected with virus). **(A)** 3-dimensional principal component plot; points represent individual mice, color-coded by group. **(B-C)** Volcano plots showing differentially expressed genes between hACE2-KI and naïve groups **(B)** and hACE2-KI and ctrl groups **(C)**. Points represent individual genes. Grey line - significance cutoff at adjusted $p = 0.05$. Blue for downregulated ($FC < -1.4$), red for upregulated ($FC > 1.4$). Most differentially expressed genes are labeled. **(D-H)** Heat maps for 50 most differentially expressed genes between hACE2-KI and naïve groups **(D)**, viral genes **(E)**, genes involved in muscle physiology and development **(F)**, metabolic genes **(G)**, Interferon and interferon-responsive genes **(H)**. Normalized expression used in D, F, G; $\log_2(\text{CPM})$ values used in E and H.

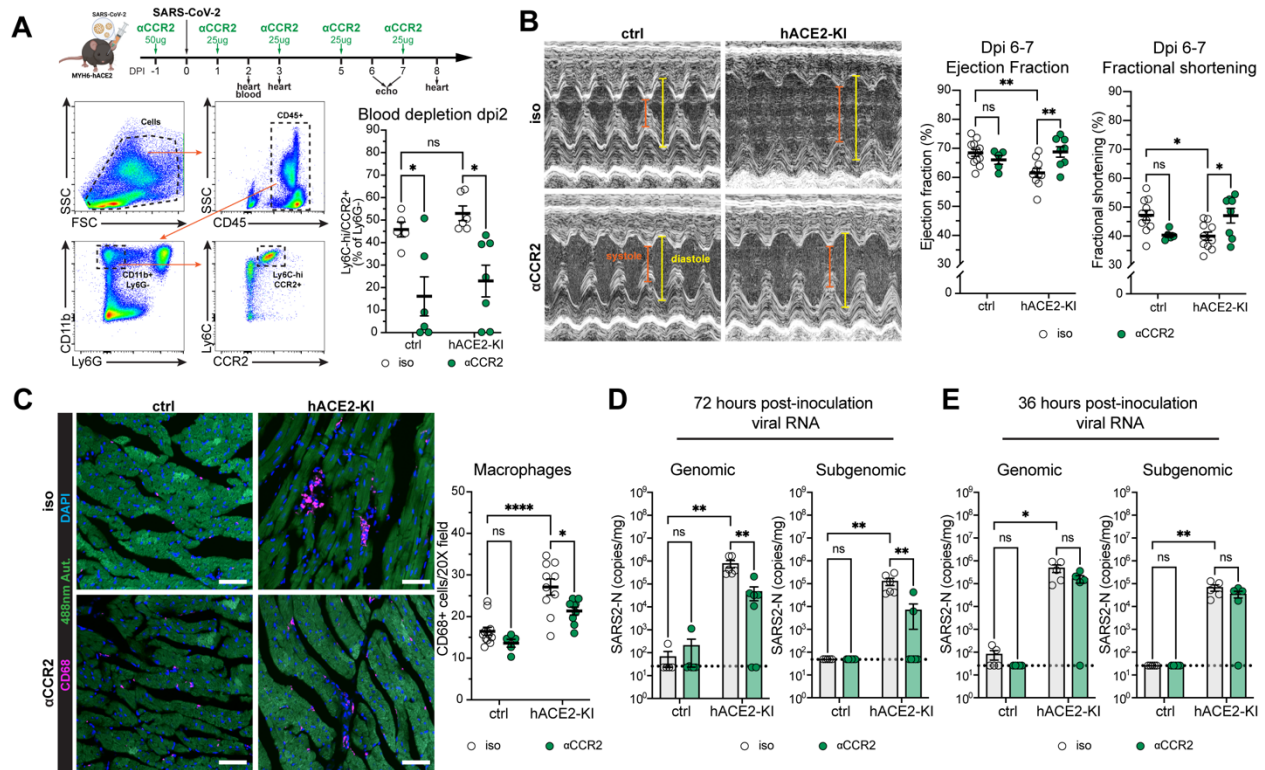


Figure 4.5. CCR2 blockade rescues cardiac dysfunction and decreases viral burden in MYH6-hACE2 model. (A) MYH6-hACE2 mice (Cre- ctrl and Cre⁺ hACE2-KI) were pre-treated with α CCR2 antibody, underwent intranasal inoculation with SARS-CoV-2, serial bleeding, transthoracic echocardiography and heart collection. (Bottom) Flow cytometry myeloid gating scheme on blood at dpi3 with quantification of Ly6C^{hi}/CCR2⁺ gate (B) Representative M-mode images of left ventricle at dpi6-7; orange line denotes systolic dimension, yellow line – diastolic. Quantification of left ventricular ejection fraction and left ventricular fractional shortening at dpi 6-7. (C) Representative immunofluorescence images of macrophages in cardiac tissue with quantification; DAPI (nuclei) – blue, 488nm fluorescence (tissue) – green, CD68 (macrophages) – magenta; qPCR for viral *N* gene genomic (left) and subgenomic (right) RNA in the heart at 72 hours post-inoculation (D) and 36 hours post-inoculation (E); dashed line – limit of detection. Points represent measurements of individual mice, error bars – standard error of mean and statistics is 2-way ANOVA with Dunnett’s multiple comparisons. ns – not significant, * $p < 0.05$, ** $p < 0.01$, *** $p < 0.001$, **** $p < 0.0001$

Chapter 5

Conclusions and Future Directions

Parts of this chapter were adapted from a review published in *Viruses*:

Dmytrenko, O., Lavine, K.J., 2022. Cardiovascular Tropism and Sequelae of SARS-CoV-2 Infection. *Viruses* 14, 1137.

5.1 Cardiomyocytes in SARS-CoV-2 Infection

Human cardiomyocytes have been shown to be targeted by viruses that cause cardiac dysfunction in patients, such as influenza and coxsackie virus B3¹⁻³. These specialized contractile cells of the heart have been identified as targets of SARS-CoV-2 in human pluripotent stem-cell (hPSC) derived tissue culture models, 3D contractile organoids and cardiac tissue slices⁴⁻¹¹. Infection of these cells by SARS-CoV-2 *in vitro* is dependent on ACE2 for viral entry and leads to aberrant electrical activity and cell death. However, the effect infected cardiomyocytes exhibit on other cardiac cells has been less understood. Additionally, the role such infection plays in contractile dysfunction observed in some patients remained unclear. Engineered heart tissues (EHTs) offer a tractable, medium-throughput organoid model of cardiac tissue composed of hPSC-derived cardiomyocytes, fibroblasts and macrophages embedded in a collagen matrix¹². The system is suspended in media on two posts rather than attached to the surface of the plate, allowing for modeling of contractile force and assessment of 3D organization of cellular components, their alignment and interactions. Here, we describe further evidence of cardiomyocyte infection with SARS-CoV-2 in humans, as well as the impact of infection on EHTs and 2D co-culture models.

After binding to ACE2, Coronavirus spike proteins must undergo proteolytic activation to initiate membrane fusion¹³. Host proteases located at the plasma membrane (i.e., TMPRSS2) or within endosomes (i.e., cathepsins, calpains) typically perform this function. The relative contributions of each of these protease families to SARS-CoV-2 cell entry varies by cell-type^{13,14}. hPSC-derived cardiomyocytes robustly express numerous endosomal proteases and low levels of TMPRSS2. Application of the endosomal cysteine protease inhibitor E-64, which blocks cathepsin and calpain activity, abolished SARS-CoV-2 cardiomyocyte infection. Blockade of TMPRSS2 activity using the serine protease inhibitor camostat mesylate had no effect on the ability of SARS-CoV-2 to infect cardiomyocytes. Collectively these studies demonstrate that SARS-CoV-2 infects cardiomyocytes and achieves entry into the cell through an endosomal pathway.

Consequences of SARS-CoV-2 cardiomyocyte infection *in vitro* include activation of innate immune pathways, reduced contractility and conduction velocity, and cell death. Infected hPSC-derived cardiomyocytes and human adult cardiomyocytes express pro-inflammatory chemokines (*CCL2*, *CCL7*, *CCL5*, *CCL8*, *CCL11*, *CXCL1*, *CXCL6*, *CXCL12*) and elicit type I (IFN- α , - β) and type III (IFN- λ) interferon responses^{4,8,10,11}. Production of CCL2 by infected cardiomyocytes can potentially mediate monocyte chemotaxis. While IFN- α and IFN- λ pre-treatment protects cardiomyocytes from infection, the endogenous role of IFN signaling following infection is yet to be defined⁴.

SARS-CoV-2 infection also leads to marked reductions in cardiomyocyte contractility. Engineered heart tissues comprised on hPSC-derived cardiomyocytes and cardiac fibroblasts display reduced force production following infection. Cardiomyocyte infection leads to reductions in expression of genes important for sarcomere function, excitation contraction coupling, and

metabolism^{4,8,10,11}. Immunostaining studies have further revealed evidence of sarcomere breakdown and fragmentation, which were both evident in autopsy and biopsy samples collected from patients with COVID-19 myocarditis. The mechanistic basis of sarcomere breakdown is of considerable interest and remains under investigation.

Electrophysiological alterations and cardiomyocyte cell death represent late sequelae of cardiomyocyte infection⁴⁻¹⁰. Cardiomyocyte cell death has been observed across cardiomyocyte preparations. Inhibition of viral replication was sufficient to prevent cell death and innate immune responses. Conversely, innate immune responses triggered by sensing of viral nucleic acids failed to impact the extent of cardiomyocyte cell death or sarcomere breakdown. Further studies are necessary to clarify the cell death pathways activated by infection and define mechanistic links between infection, innate immune responses, sarcomere maintenance, and metabolism.

5.2 Cardiac Pericytes in SARS-CoV-2 Infection

Cardiac pericytes are vascular support cells that govern angiogenesis of small and intermediate vessels, preserve endothelial cell integrity and directly regulate blood flow through vasculature¹⁵. Their high level of ACE2 expression made them a proposed target for SARS-CoV-2 infection early in the pandemic of COVID-19¹⁶. Pericytes from the brain support infection with SARS-CoV-2, but it remained unclear if their cardiac counterparts can be infected with the virus and if such infection contributes to the pathophysiology of COVID-19¹⁷. Here, we described the first evidence of primary human cardiac pericytes being susceptible to SARS-CoV-2 infection. We further investigated the mechanism of viral entry into these cells, the consequences of infection on pericytes themselves and on other vascular cells which pericytes normally interact with.

Conceptually, infection of pericytes could contribute to the observed vascular manifestations of SARS-CoV-2 infection including thrombosis, inflammation, and hemodynamic derangements¹⁸⁻²⁰. The close proximity between pericytes and vascular endothelial cells may explain why vascular structures within the myocardium contained SARS-CoV-2 RNA^{4,21-23}. Indeed, *in situ* hybridization and immunostaining for pericyte markers and SARS-CoV-2 RNAs and proteins in autopsy samples confirmed that pericytes are a target for SARS-CoV-2.

SARS-CoV-2 readily infects cardiac pericytes within primary cultures and organotypic heart slice preparations. It is not yet clear if pericytes in other tissues and organ systems are all permissive to SARS-CoV-2 infection. It should be noted that cardiac pericytes are unique from an embryologic standpoint as they are derived from the epicardium²⁴ and may have properties distinct from pericytes found in other locations. Cardiac pericyte infection occurs across variants of concern, is dependent on cell surface ACE2 expression, and proceeds through the endosomal route of entry. The role of syncytia formation in viral spread and pathology of infection remains to be addressed.

Consequences of SARS-CoV-2 pericyte infection include cytokine production, generation of vasoactive mediators, and cell death. RNA sequencing of infected pericytes revealed marked differential expression of genes associated with in the innate immune response to pathogens, type I interferon signaling, leukocyte chemotaxis, and degranulation. Upregulation of vasoactive genes including endothelin 1 and 2 (EDN1, EDN2) and downregulation of ACE2, a hallmark of SARS-CoV-2 infection²⁵ were also observed. Infected cardiac pericytes remain viable for several days in culture, suggesting they may serve as a previously unrecognized site of replication and reservoir of virus. Cells in culture produced soluble mediators that caused a robust antiviral interferon

response in endothelial cultured cells. However, a non-cardiac endothelial cell line was used in the study. As the biology of endothelial cells can differ vastly between organs, and cell lines do not always recapitulate *in vivo* phenotypes, additional research with more physiologic endothelial cell lines and primary cultures is needed to assess the effects of infected cardiac pericytes on cardiac vasculature. Further investigation is also required to address the effect of soluble mediators produced by pericytes on endothelial barrier permeability, its susceptibility to viral infection and propensity to attract immune cells. All of these changes can mechanistically contribute to vascular manifestations of COVID-19. Additionally, the role of contact-mediated signaling between infected pericytes and endothelial cells remains unknown. Such interactions are vital for homeostatic maintenance of endothelial barriers, and their role in pericyte infection remains to be uncovered²⁶.

Cardiac pericytes cell did undergo cell death at later stages of infection. Loss of endothelial integrity, endothelial cell dysfunction, basement membrane exposure, and microvascular thrombosis may represent sequelae of cardiac pericyte cell death. Future studies are required to elucidate the pathophysiological consequences of pericyte infection *in vivo* and their collective contribution to cardiovascular manifestations of COVID-19.

5.3 Cardiomyocyte-Restricted Mouse Model of SARS-CoV-2 infection

Animal models of SARS-CoV-2 infection include wild type and transgenic mice, hamsters, ferrets, and non-human primates²⁷. Most models have focused on recapitulating elements of human pulmonary disease, which excluded significant extrapulmonary manifestations of SARS-CoV-2 infection from rigorous scientific evaluation. Here, we described a novel transgenic murine model

of SARS-CoV-2 infection in the heart, a MYH6-hACE2 mouse. These animals express hACE2 exclusively in cardiomyocytes utilizing a Cre driven by cardiomyocyte-specific promoter for myosin heavy chain 6 (MYH6). In cardiomyocytes, Cre enzyme excises a stop codon in a Rosa26 locus, allowing for expression of human ACE2 (hACE2) under exogenous CAG promoter. High levels of hACE2 expression are observed in these mice and restricted to cardiac tissue. Intravenous inoculation of these animals with SARS-CoV-2 (WA1/2020 strain) leads to heart-restricted viral replication, mild injury, infiltration of monocyte-derived macrophages and mild cardiac dysfunction by 1 week of infection. This dysfunction is dependent on CCR2 signaling and spontaneously resolves at 4 weeks post-infection.

No animal model of SARS-COV-2 infection includes all aspects of human COVID-19. To specifically study the effects of COVID-19 on the heart, however, our approach to overexpression of human ACE2 in cardiomyocytes offers considerable advantages. Although not physiologic, restricted high hACE2 expression in the heart offers a unique opportunity to dissect the role of cardiac infection in pathogenesis of COVID-19 outside of pulmonary or other extrapulmonary disease. Another big advantage is reliance on the human form of the receptor rather than the native animal one. This ensures that the spike-ACE2 interactions that might be important for binding, entry and spread are recapitulated in a species-appropriate manner. However, such overexpression largely shifts the focus away from the natural function of the receptor. ACE2 participates in blood pressure modulation of renin-angiotensin-aldosterone system (RAAS). It converts angiotensin I and angiotensin II into angiotensin 1-9 and angiotensin 1-7 respectively. The resulting peptides act in vasodilatory manner, counteracting vasopressive actions of angiotensin I and angiotensin II²⁸. While in our studies hACE2 overexpression by itself did not lead to significant pathology or

functional changes, this model is not suitable for evaluation of phenotypes that rely on endogenous ACE2 function or natural regulation.

The importance of SARS-CoV-2 strain selection for the MYH6-hACE2 model of cardiac restricted infection is worth discussing. To achieve cardiomyocyte restriction, a strain must rely on human ACE2 for entry into the host. Thus, its spike cannot harbor N501Y mutation which has been previously described to confer mouse tropism to the virus²⁹. As such, early strains (such as WA1/2020) and delta are the only ones that can be utilized in the model. MYH6-hACE2 model cannot be used for a head-to-head comparison of isolated cardiac disease caused by most variants of concern, including currently circulating omicron strains³⁰. However, utilizing a mouse-adapted strain in MYH6-hACE2 mice allows for study of exacerbated cardiac disease in the background of systemic infection. While not the original purpose behind the model development, systemic infection of these animals can shed light on crosstalk between lung and heart during the course of SARS-CoV-2 infection.

The macrophage-predominant immune infiltrate observed in MYH6-hACE2 mouse model of cardiac infection with SARS-COV-2 is unique and recapitulates findings from human disease^{31,32}. We provide evidence for the deleterious effect of CCR2⁺ monocytes and monocyte-derived macrophages on cardiac function and their importance for viral replication at day 3 of infection in MYH6-hACE2 model. Furthermore, the level of viral RNA does not depend on CCR2 signaling at 36 hours post-infection, suggesting that CCR2⁺ cells influence viral burden between 36 and 72 hours, or later. However, the exact role of these cells in infection establishment and pathology is not understood.

Macrophages and monocytes have been implicated in pathogenesis of multiple viruses and support replication of at least 35 different species³³. Viral infection of CCR2+ cells and their role as a reservoir and delivery vehicle during cardiac SARS-COV-2 infection must be considered. Multiple studies have identified protein and RNA elements of SARS-CoV-2 in human primary and cultured monocytes and macrophages³⁴⁻³⁷. As professional phagocytes, it is not surprising that these cells will harbor fragments of engulfed pathogens and exhibit activation. However, new evidence emerged suggesting abortive replication of SARS-CoV-2 rather than pure phagocytosis occurs in human monocytes. This study also demonstrates a CD16-mediated hACE2-independent mechanism of viral entry. If CCR2+ cells were to serve a reservoir role in our model, a hACE2-independent mechanism of infection would be required since the SARS-CoV-2 strain used is hACE2-restricted and hACE2 expression is not expected on monocytes and macrophages³⁷. However, CD16-mediated route of entry requires presence of anti-viral IgG antibodies, which normally take over 1 week to develop and are not expected at dpi 3 when we observe the effect on viral titers³⁸. Thus, a CD16-mediated monocyte infection is unlikely. However, a possibility of alternate receptor for CCR2+ cells cannot be completely discounted and has to be further investigated.

An alternative explanation for the functional improvements and reduced viral levels with CCR2 depletion is that CCR2+ cells prevent effective viral clearance at the later stages of the infection. There is also a possibility that viral titers and cardiac function are not intrinsically tied in this model and that CCR2+ cells elicit direct damage to cardiac tissue. Macrophages and specifically CCR2+ monocyte-derived macrophages have been previously implicated in multiple non-infectious cardiac diseases^{39,40}. Moreover, CCR2+ cells have been shown to drive mortality

in lethal influenza model through inducible nitric oxide synthase activation, providing an example of a detrimental effect of these cells in a viral setting⁴¹. Although we did not observe severe cardiac injury on histology in this model, histologically undetectable changes that impair contractility are nevertheless possible. Thus, the role of direct injury from CCR2+ cells on tissue has to be further addressed. Finally, the contribution of resident macrophages to heart dysfunction during cardiac infection with SARS-CoV-2 needs to be evaluated. The contribution of this cell population can be assessed in the future using available an antibody-based or genetic depletion strategy for these cells^{42,43}.

One of the most intriguing avenues for further investigation is the use of MYH6-hACE2 mice to model long-term cardiac consequences of SARS-CoV-2 infection as well as study comorbidities of this disease. Most patients with post-acute COVID-19 syndrome suffer from severe fatigue and exercise intolerance⁴⁴. Effects of COVID-19-associated mild cardiac disease on long-term health are not understood. After recovery from acute viral disease, mice can be challenged with exercise and cardiovascular insults such as hypertension or atherogenic diet to model long-term consequences of cardiac infection with SARS-CoV-2. Conversely, allowing the insults to occur prior to viral infection one can investigate the role of comorbidities and preexisting conditions on cardiac course of SARS-CoV-2 infection.

Overall, MYH6-hACE2 mouse model provides a unique opportunity for mechanistic investigation of cardiovascular disease during SARS-CoV-2 infection.

5.4 Concluding Remarks

Cardiovascular manifestations of SARS-CoV-2 infection are common among the patients with COVID-19. Cardiac complications during viral illness are not unique features of SARS-CoV-

2, but their importance in the disease course and long-term prognosis are poorly understood. This dissertation focused on direct infection of cardiac tissue as a potential mechanism for SARS-CoV-2-associated cardiovascular disease. I identified cardiomyocytes and cardiac pericytes as the cell types susceptible to infection in the heart. Cardiomyocyte infection *in vitro* leads to a robust inflammatory response, activation of neighboring cells, reduced contractility and ultimate cell death. *In vivo* isolated infection of cardiomyocytes leads to decreased cardiac function that is dependent on CCR2+ cell response. Cardiac pericytes also robustly respond to SARS-CoV-2 infection by upregulating type I interferons, producing vasoactive substances and ultimately dying in an NFkB-dependent fashion. These findings improve our understanding of the cell-specific response to the virus outside of the primary site of infection and will help with design of better therapies and preventative measures. Further studies focusing on cardiovascular and other extrapulmonary features of COVID-19 will be required for management of current pandemic and associated chronic diseases as well as future pandemics.

5.5 References

1. Filgueiras-Rama, D. *et al.* Human influenza A virus causes myocardial and cardiac-specific conduction system infections associated with early inflammation and premature death. *Cardiovasc Res* **117**, 876–889 (2021).
2. Wessely, R., Henke, A., Zell, R., Kandolf, R. & Knowlton, K. U. Low-Level Expression of a Mutant Coxsackieviral cDNA Induces a Myocytopathic Effect in Culture. *Circulation* **98**, 450–457 (1998).
3. Zhou, F. *et al.* Necroptosis may be a novel mechanism for cardiomyocyte death in acute myocarditis. *Mol Cell Biochem* **442**, 11–18 (2018).
4. Perez-Bermejo, J. A. *et al.* SARS-CoV-2 infection of human iPSC-derived cardiac cells reflects cytopathic features in hearts of patients with COVID-19. *Science Translational Medicine* **13**, eabf7872 (2021).
5. Yang, L. *et al.* A Human Pluripotent Stem Cell-based Platform to Study SARS-CoV-2 Tropism and Model Virus Infection in Human Cells and Organoids. *Cell Stem Cell* **27**, 125–136.e7 (2020).

6. Choi, S. W. *et al.* Antiviral activity and safety of remdesivir against SARS-CoV-2 infection in human pluripotent stem cell-derived cardiomyocytes. *Antiviral Res* **184**, 104955 (2020).
7. Li, Y. *et al.* SARS-CoV-2 induces double-stranded RNA-mediated innate immune responses in respiratory epithelial-derived cells and cardiomyocytes. *Proceedings of the National Academy of Sciences* **118**, e2022643118 (2021).
8. Marchiano, S. *et al.* SARS-CoV-2 Infects Human Pluripotent Stem Cell-Derived Cardiomyocytes, Impairing Electrical and Mechanical Function. *Stem Cell Reports* **16**, 478–492 (2021).
9. Navaratnarajah, C. K. *et al.* Highly Efficient SARS-CoV-2 Infection of Human Cardiomyocytes: Spike Protein-Mediated Cell Fusion and Its Inhibition. *Journal of Virology* **95**, e01368-21 (2021).
10. Yang, L. *et al.* Cardiomyocytes recruit monocytes upon SARS-CoV-2 infection by secreting CCL2. *Stem Cell Reports* **16**, 2274–2288 (2021).
11. Bojkova, D. *et al.* SARS-CoV-2 infects and induces cytotoxic effects in human cardiomyocytes. *Cardiovascular Research* (2020) doi:10.1093/cvr/cvaa267.
12. Tani, H. & Tohyama, S. Human Engineered Heart Tissue Models for Disease Modeling and Drug Discovery. *Frontiers in Cell and Developmental Biology* **10**, (2022).
13. Simmons, G., Zmora, P., Gierer, S., Heurich, A. & Pöhlmann, S. Proteolytic activation of the SARS-coronavirus spike protein: Cutting enzymes at the cutting edge of antiviral research. *Antiviral Research* **100**, 605–614 (2013).
14. Hoffmann, M. *et al.* SARS-CoV-2 Cell Entry Depends on ACE2 and TMPRSS2 and Is Blocked by a Clinically Proven Protease Inhibitor. *Cell* **181**, 271-280.e8 (2020).
15. Su, H., Cantrell, A. C., Zeng, H., Zhu, S.-H. & Chen, J.-X. Emerging Role of Pericytes and Their Secretome in the Heart. *Cells* **10**, (2021).
16. Chen, L., Li, X., Chen, M., Feng, Y. & Xiong, C. The ACE2 expression in human heart indicates new potential mechanism of heart injury among patients infected with SARS-CoV-2. *Cardiovascular Research* **116**, 1097–1100 (2020).
17. Bocci, M. *et al.* Infection of Brain Pericytes Underlying Neuropathology of COVID-19 Patients. *Int J Mol Sci* **22**, 11622 (2021).
18. Katsoularis, I., Fonseca-Rodríguez, O., Farrington, P., Lindmark, K. & Connolly, A.-M. F. Risk of acute myocardial infarction and ischaemic stroke following COVID-19 in Sweden: a self-controlled case series and matched cohort study. *The Lancet* **398**, 599–607 (2021).
19. Bilaloglu, S. *et al.* Thrombosis in Hospitalized Patients With COVID-19 in a New York City Health System. *JAMA* **324**, 799–801 (2020).
20. Kunutsor, S. K. & Laukkanen, J. A. Incidence of venous and arterial thromboembolic complications in COVID-19: A systematic review and meta-analysis. *Thromb Res* **196**, 27–30 (2020).

21. Tavazzi, G. *et al.* Myocardial localization of coronavirus in COVID-19 cardiogenic shock. *European Journal of Heart Failure* **22**, 911–915 (2020).
22. Ackermann, M. *et al.* Pulmonary Vascular Endothelialitis, Thrombosis, and Angiogenesis in Covid-19. *New England Journal of Medicine* **383**, 120–128 (2020).
23. Varga, Z. *et al.* Endothelial cell infection and endotheliitis in COVID-19. *The Lancet* **395**, 1417–1418 (2020).
24. Volz, K. S. *et al.* Pericytes are progenitors for coronary artery smooth muscle. *eLife* **4**, e10036.
25. Ni, W. *et al.* Role of angiotensin-converting enzyme 2 (ACE2) in COVID-19. *Critical Care* **24**, 422 (2020).
26. Kurmann, L. *et al.* Transcriptomic Analysis of Human Brain-Microvascular Endothelial Response to -Pericytes: Cell Orientation Defines Barrier Function. *Cells* **10**, (2021).
27. Bestion, E., Halfon, P., Mezouar, S. & Mège, J.-L. Cell and Animal Models for SARS-CoV-2 Research. *Viruses* **14**, 1507 (2022).
28. Elshafei, A., Khidr, E. G., El-Husseiny, A. A. & Gomaa, M. H. RAAS, ACE2 and COVID-19; a mechanistic review. *Saudi Journal of Biological Sciences* **28**, 6465–6470 (2021).
29. Niu, Z. *et al.* N501Y mutation imparts cross-species transmission of SARS-CoV-2 to mice by enhancing receptor binding. *Sig Transduct Target Ther* **6**, 1–3 (2021).
30. Chen, R. E. *et al.* Resistance of SARS-CoV-2 variants to neutralization by monoclonal and serum-derived polyclonal antibodies. *Nat Med* **27**, 717–726 (2021).
31. Bailey Adam L. *et al.* SARS-CoV-2 Infects Human Engineered Heart Tissues and Models COVID-19 Myocarditis. *JACC: Basic to Translational Science* **6**, 331–345 (2021).
32. Basso, C. *et al.* Pathological features of COVID-19-associated myocardial injury: a multicentre cardiovascular pathology study. *European Heart Journal* **41**, 3827–3835 (2020).
33. Nikitina, E., Larionova, I., Choinzonov, E. & Kzhyshkowska, J. Monocytes and Macrophages as Viral Targets and Reservoirs. *Int J Mol Sci* **19**, 2821 (2018).
34. Zheng, J. *et al.* Severe Acute Respiratory Syndrome Coronavirus 2–Induced Immune Activation and Death of Monocyte-Derived Human Macrophages and Dendritic Cells. *J Infect Dis* **223**, 785–795 (2020).
35. Niles, M. A. *et al.* Macrophages and Dendritic Cells Are Not the Major Source of Pro-Inflammatory Cytokines Upon SARS-CoV-2 Infection. *Frontiers in Immunology* **12**, (2021).
36. Hui, K. P. Y. *et al.* Tropism, replication competence, and innate immune responses of the coronavirus SARS-CoV-2 in human respiratory tract and conjunctiva: an analysis in ex-vivo and in-vitro cultures. *The Lancet Respiratory Medicine* **8**, 687–695 (2020).
37. Junqueira, C. *et al.* FcγR-mediated SARS-CoV-2 infection of monocytes activates inflammation. *Nature* **606**, 576–584 (2022).
38. Long, Q.-X. *et al.* Antibody responses to SARS-CoV-2 in patients with COVID-19. *Nat Med* **26**, 845–848 (2020).

39. Bajpai, G. *et al.* The human heart contains distinct macrophage subsets with divergent origins and functions. *Nature Medicine* **24**, 1234–1245 (2018).
40. Bajpai, Geetika *et al.* Tissue Resident CCR2⁻ and CCR2⁺ Cardiac Macrophages Differentially Orchestrate Monocyte Recruitment and Fate Specification Following Myocardial Injury. *Circulation Research* **124**, 263–278 (2019).
41. Lin, K. L., Suzuki, Y., Nakano, H., Ramsburg, E. & Gunn, M. D. CCR2⁺ Monocyte-Derived Dendritic Cells and Exudate Macrophages Produce Influenza-Induced Pulmonary Immune Pathology and Mortality¹. *The Journal of Immunology* **180**, 2562–2572 (2008).
42. Epelman, S. *et al.* Embryonic and Adult-Derived Resident Cardiac Macrophages Are Maintained through Distinct Mechanisms at Steady State and during Inflammation. *Immunity* **40**, 91–104 (2014).
43. Revelo, X. S. *et al.* Cardiac Resident Macrophages Prevent Fibrosis and Stimulate Angiogenesis. *Circ Res* **129**, 1086–1101 (2021).
44. Nalbandian, A. *et al.* Post-acute COVID-19 syndrome. *Nature Medicine* **27**, 601–615 (2021).